



HAL
open science

Fuel discharge towards the core catcher in sodium-cooled fast reactor under severe accident conditions with mitigation devices

Eszter Csengeri

► **To cite this version:**

Eszter Csengeri. Fuel discharge towards the core catcher in sodium-cooled fast reactor under severe accident conditions with mitigation devices. Génie civil nucléaire. Université Grenoble Alpes [2020-..], 2022. English. NNT : 2022GRALI022 . tel-03685272

HAL Id: tel-03685272

<https://theses.hal.science/tel-03685272>

Submitted on 2 Jun 2022

HAL is a multi-disciplinary open access archive for the deposit and dissemination of scientific research documents, whether they are published or not. The documents may come from teaching and research institutions in France or abroad, or from public or private research centers.

L'archive ouverte pluridisciplinaire **HAL**, est destinée au dépôt et à la diffusion de documents scientifiques de niveau recherche, publiés ou non, émanant des établissements d'enseignement et de recherche français ou étrangers, des laboratoires publics ou privés.

THÈSE

Pour obtenir le grade de

DOCTEUR DE L'UNIVERSITÉ GRENOBLE ALPES

Spécialité : MEP : Mécanique des fluides Energétique, Procédés

Arrêté ministériel : 25 mai 2016

Présentée par

Eszter CSENGERI

Thèse dirigée par **Elsa MERLE**, Professeur, Université Grenoble Alpes

et codirigée par **Laurent TROTIGNON**

et co-encadrée par **Andrea BACHRATA**, CEA

préparée au sein du **Laboratoire CEA Cadarache**

dans l'**École Doctorale I-MEP2 - Ingénierie - Matériaux, Mécanique, Environnement, Energétique, Procédés, Production**

Cheminement du combustible vers le récupérateur en situation de mitigation d'accident grave dans un réacteur à neutrons rapides à caloporteur sodium

Fuel discharge towards the core catcher in sodium-cooled fast reactor under severe accident conditions with mitigation devices

Thèse soutenue publiquement le **24 mars 2022**,
devant le jury composé de :

Monsieur Sevostian BECHTA

PROFESSEUR, KTH Royal Institute of Technology, Rapporteur

Monsieur Yoël FORTERRE

DIRECTEUR DE RECHERCHE, CNRS, Rapporteur

Madame Andrea BACHRATA

INGENIEUR-CHERCHEUR, CEA, Encadrante

Monsieur Yves DELANNOY

PROFESSEUR DES UNIVERSITES, Grenoble INP, Président du jury

Monsieur Florian FICHOT

INGENIEUR HDR, IRSN, Examineur

Monsieur Christophe JOURNEAU

DIRECTEUR DE RECHERCHE, CEA, Invité

Monsieur Simone MASSARA

EXPERT SÛRETÉ NUCLÉAIRE, IAEA, Examineur

Madame Elsa MERLE

PROFESSEUR DES UNIVERSITES, Grenoble INP, Directrice de thèse

Madame Nathalie SEILER

DIRECTEUR DE RECHERCHE, CEA, Invitée

Monsieur Laurent TROTIGNON

DIRECTEUR DE RECHERCHE, CEA, Co-directeur de thèse



To my father with the love he left behind

Acknowledgements

Throughout the preparation of this thesis work, I have received a great deal of support and assistance. I am especially grateful to my two supervisors Andrea Bachrata and Laurent Trotignon. You both have provided me not only excellent technical guidance during the three years of the PhD but also many invaluable advices that contributed to my professional and personal development. Andrea, thank you in particular for your efforts in finding me the best opportunities (and cheering together when it was successful) and for encouraging me always to stay positive and trust in my competencies in every aspects of life. Laurent, thank you for always being available to discuss with me (sometimes to help making sense of my confusions), and for enriching this work and extending my scientific viewpoint by your continuously evolving ideas.

I would like to thank to my director Elsa Merle for accepting to supervise this work, providing insightful suggestions and essential support in dealing with university affairs. I would like to express my sincere appreciation to Manuel Saez who welcomed me at SESI as head of laboratory and invested a great amount of assistance into my integration. I acknowledge the valuable time of Pierre Gubernatis that he spent on helping me grasp the mysteries of the SIMMER code.

I would like to thank to all my colleagues who made my stay at CEA enjoyable. Paolo with whom we become friends during the resolution of several linguistic issues over the past 2 years as officemates. Alessandro who always had a large supply of delicious Italian sweets, which was impossible to refuse and made up most part of my sugar intake during an entire year. The climbing champi(gn)ons Sebastian and Charly with whom I shared a lot of fun exploring routes up to 6a+ and some plank challenge torture after. Also Elisabetta whose encouragements were sometimes crucial.

I would like to express my gratitude to my previous supervisor Dr. Kis Dániel Péter who enlightened me the first glance of research and launched me on the field of nuclear energy.

I cannot end this paragraph without mentioning the support from my friends. Thanks to my biggest cheerleader Elena who was always there for me no matter if celebrating the thrills or helping to navigate through the struggles. I am grateful to share the PhD experience with a Hungarian friend. Thank you Dóri for your patience in supporting me through the difficult times. Special thanks should also go to my flat mate Anne who played an important role in making me feel at home in France. Thank you Anne for being my family here. I would also like to thank to all my friends who brought me joyful distractions to rest my mind outside of the work.

Lastly, my deepest gratitude to my mother for her unconditional love and wholehearted support that gave me strength to chase my dreams. Anya, köszönöm azt a sok szeretet, támogatást és törődést ami erőt adott abban, hogy merjek az álmaim után menni és ezáltal boldog emberré válni.

The numerical results obtained in this manuscript are thanks to the access to the HPC resources of TGCC (Très Grand Centre de calcul du CEA - <http://www-hpc.cea.fr/en/complex/tgcc-curie.htm>) under the allocation A0091010087 and A0071007070 made by GENCI (Grand Equipement National de Calcul Intensif - <http://www.genci.fr>).

I acknowledge the opportunity the I was given by the European Nuclear Education Network (ENEN+ mobility grant) to perform a research exchange at the Japan Atomic Energy Agency (JAEA). Even though the outbreak of the COVID19 disease made it impossible to carry out the mobility action, I am thankful for all the fruitful technical exchanges with the Japanese colleagues.

Table of Content

Acknowledgements.....	i
Nomenclature.....	iv
List of figures.....	viii
List of tables.....	xii
Résumé en français.....	xiii
Introduction.....	xxiii
<i>Chapter I. CONTEXT.....</i>	<i>1</i>
I.1 The ASTRID project.....	2
I.1.1 The most developed Generation IV reactor design: SFR.....	2
I.1.2 The ASTRID technological demonstrator.....	5
I.2 Severe accidents in SFRs.....	7
I.2.1 Safety study approach.....	8
I.3 Mitigation by design.....	10
I.4 Thesis objectives.....	12
<i>Chapter II. PARTICULATE FLOW INSIDE THE TRANSFER TUBES.....</i>	<i>15</i>
II.1 Discharge phenomena inside the transfer tubes.....	16
II.1.1 Origin and properties of particulate matter.....	17
II.2 State-of-the-art numerical modelling of reactor debris.....	19
II.3 Departure from the effective fluid approach.....	22
II.4 Reactor debris as granular media.....	24
II.4.1 Hydrodynamics forces.....	25
II.4.2 Particle interactions.....	26
II.4.3 Granular regimes and their physical modelling.....	28
II.5 Phenomena identification-ranking table.....	33
II.5.1 PIRT evaluation context.....	33
II.5.2 Methodology.....	33
<i>Chapter III. MODEL DEVELOPMENT FOR PARTICLE DYNAMICS.....</i>	<i>37</i>
III.1 Numerical environment: SIMMER-V code.....	38
III.1.1 SIMMER overall framework.....	38
III.1.2 Momentum conservation and its solution procedure.....	39
III.2 Statement of the modelling context.....	43
III.3 Identification of transfer tube regions.....	45
III.4 Momentum exchange terms for particles.....	45
III.4.1 Interphase momentum exchange.....	45
III.4.2 Momentum exchange of particles with structures.....	47
III.5 Particle-particle interaction forces.....	47
III.5.1 $\mu(I)$ dense granular rheology.....	48
III.5.2 Numerical implementation.....	56
III.5.3 Continuity considerations.....	59
III.6 Discussion on fluid pressure.....	60

III.7	Synthesis of developed models	61
<i>Chapter IV. SIMPLIFIED TEST CASES</i>		63
IV.1	Basis for simplified test cases.....	64
IV.2	Jammed particle pile.....	65
IV.2.1	Stress distribution.....	66
IV.2.2	Jamming transition	69
IV.3	Bin discharge	71
IV.4	Flow through porous media	74
IV.5	Fluidization and fluidized state.....	77
IV.6	Sedimentation under gravity	82
IV.6.1	Terminal velocity of a quasi-single particle	82
IV.6.2	Settling velocity of a dense particle ensemble	84
IV.6.3	Terminal velocity of a cloud of different particulate components	88
IV.7	Hydraulic conveying.....	90
IV.8	Synthesis of results.....	94
<i>Chapter V. INTEGRAL EFFECT TEST</i>		97
V.1	Experimental programs on degraded core behavior.....	98
V.2	Synthetic description of EAGLE-1 tests.....	99
V.3	Modelling the test section in SIMMER-V	101
V.4	Simulation results of EAGLE-1 ID1 and FD with SIMMER-V	101
V.5	Comparison of discharged mass	104
V.6	Particle rheology in EAGLE-1 FD test	107
V.7	Sensitivity study	109
V.8	Discussion and perspectives	113
<i>Chapter VI. REACTOR SCALE APPLICATION</i>		115
VI.1	ASTRID conceptual design in SIMMER-V	116
VI.1.1	Reactor at nominal state	118
VI.2	ULOF transient in SIMMER-V.....	119
VI.2.1	Primary phase	119
VI.2.2	Transition phase.....	121
VI.2.3	Secondary phase	123
VI.2.4	Relocation phase in SIMMER-V_vpd.....	124
VI.3	Discharge performance by different SIMMER versions.....	127
<i>Chapter VII. CONCLUSIONS AND PERSPECTIVES</i>		131
VII.1	Summary and conclusions.....	131
VII.2	Perspectives	134
References.....		137

Nomenclature

Acronyms

<i>AFDM</i>	Advanced Fluid-Dynamics Model
<i>ASTRID</i>	Advanced Sodium Technological Reactor for Industrial Demonstration
<i>CDA</i>	Core Disruptive Accident
<i>CEA</i>	French Commission for Atomic Energy and Alternative Energy
<i>CFV</i>	Coeur Faible Vidange
<i>CRGT</i>	Control Rod Guide Tubes
<i>DCS-M-TT</i>	Complementary Safety Device for Mitigation – Transfer Tube
<i>EAGLE</i>	Experimental Acquisition of Generalized Logic to Eliminate recriticalities
<i>EOS</i>	Equation Of State
<i>FAIDUS</i>	FUel subassembly with Inner DUct Structure
<i>FAJ</i>	Fuel Assembly Jacket
<i>FCI</i>	Fuel-Coolant Interaction
<i>FD</i>	Fuel Discharge
<i>GIF</i>	Generation IV International Forum
<i>GFR</i>	Gas-cooled Fast Reactor
<i>ID</i>	Integral Demonstration
<i>JAEA</i>	Japan Atomic Energy Agency
<i>KTGF</i>	Kinetic Theory of Granular Flows
<i>LFR</i>	Lead-cooled Fast Reactor
<i>MSR</i>	Molten Salt Reactor
<i>PIRT</i>	Phenomena Identification-Ranking Table
<i>R&D</i>	Research and Development
<i>ULOF</i>	Unprotected Loss Of Flow
<i>UTOP</i>	Unprotected Transient Over Power
<i>USAF</i>	Unprotected SubAssembly Fault
<i>SFR</i>	Sodium-cooled Fast Reactor
<i>SIMMER</i>	Sn Implicit Multiphase Multicomponent Eulerian Recriticality
<i>SIMMER-V_vpd</i>	SIMMER version with newly implemented particle dynamics models
<i>SIMMER-V_vo</i>	SIMMER original version
<i>SCWR</i>	Supercritical Water-cooled Reactor
<i>TMI</i>	Three Mile Island
<i>VHTR</i>	Very High Temperature Reactor
<i>V&V</i>	Validation and Verification

Latin letters

a_w, a_1	Dimensionless parameters of the shear rate equation	-
a_i, a_v	Coefficients of rheology in inertial and viscous regimes	-
A	Laminar term of momentum exchange function	kg/m ²
Ar	Archimedes number	-
b	Dilatancy law exponent	-
B	Turbulent term of momentum exchange function	kg/m/s
Ba	Bagnold number	-
c	Constant multiplier in the Beverloo law	-
c_i, c_v	Dimensionless parameters of dilatancy law in inertial and viscous regime	-

c_s	Dimensionless parameter of shear rate equation	-
c_p	Dimensionless parameter from percolation theory	-
C_D	Drag coefficient	-
C_{PJ}	Jamming model parameter	-
Co	Coulomb number	-
d, r	Diameter, Radius	m
D_h, R	Hydraulic diameter and radius	m
D_o	Outlet orifice diameter	m
D	Container diameter	m
e	Coefficient of restitution	-
e_M	Specific internal energy	J/kg
f_1, f_2	Particle viscosity factors	-
f_p	Particle friction factor	-
F_{Ba}	Basset force	N
F_{bu}	Buoyancy force	N
F_D	Drag force	N
F_{Ma}	Magnus force	N
F_N	Normal force	N
F_p	Single particle forces	N
F_p^m	Total force on a multi-particle system	N
F_{Pr}	Pressure force	N
F_{p-p}	Particle-particle interaction forces	N
F_{p-w}	Particle-wall interaction forces	N
F_{Saff}	Saffman lift force	N
F_T	Tangential force	N
F_{VM}	Virtual Mass force	N
F_{wl}	Wall lift force	N
g	Gravity	m/s ²
H	Height	m
H	Number of high ranks	-
$H(...)$	Heaviside function	-
I_0	Empirical coefficient of macroscopic friction coefficient	-
I_i, I_v	Inertial and viscous number	-
IL	Importance level	-
k	Empirical coefficient of Beverloo law	-
K	Momentum exchange function	kg/m ³ /s
K_p	Lateral to vertical pressure ratio	-
K_{PJ}	Particle jamming model	-
l	Flow behavior index	-
L	Number of low ranks	-
Le	Leighton number	-
m	Mass	kg
M	Number of medium ranks	-
n	Settling exponent	-
p	Pressure	Pa
p_p	Particle pressure	Pa

P	Power	W
Q	Volumetric flow rate	m^3/s
Q_{HT}	Energy interchanging rate for heat-transfer	W/m^3
Q_{MF}	Energy interchanging rate for melting or freezing	W/m^3
Q_N	Nuclear heating rate	W/m^3
Q_{VC}	Energy interchanging rate for vaporization or condensation	W/m^3
r	Density ratio	-
r_{small}	Regularization parameter	-
Re	Reynolds number	-
St	Stokes number	-
t	Time	s
u_1, u_2	Impact velocities of colliding particle 1 and 2	m/s
UL	Uncertainty level	-
v	Velocity	m/s
v_t	Sedimentation velocity	m/s
v_s	Terminal velocity	m/s
v_1, v_2	Post-collisional velocities of particle 1 and 2	m/s
V_p	Particle volume	m^3
VM	Virtual mass term	$kg/m^2/s^2$
x, y, z	Cartesian coordinates	-
r, θ, z	Cylindrical coordinates	-
(-)	Dimensionless quantities	-

Greek letters

α	Volume fraction	-
α_{PJmax}	Maximum volume fraction for solid particles in the jamming model	-
β_i, β_v	Multiplication factor for inertial and viscous regimes	-
β_{PJ}	Fraction of α_{PJmax} above which the jamming model is applied	-
$\dot{\gamma}$	Shear rate	1/s
Γ	Mass-transfer rate per unit volume	$kg/s/m^3$
δ	Internal angle of friction	$^\circ$
δv	Fluctuating velocity of grains	m/s
θ	Granular temperature	m^2/s^2
λ	Volume concentration function in Bagnold law	-
μ	Macroscopic friction coefficient of particle systems	-
μ_f, μ_l, μ_g	Dynamic viscosity of fluids, liquids or gases	Pa s
μ_1	Empirical dynamical friction coefficient	-
μ_{app}	Apparent viscosity	Pa s
μ_s	Static friction coefficient	-
μ_w	Wall friction coefficient	-
ρ	Density	kg/m^3
σ	Normal stress	N
σ_p	Solid particle stress tensor	N
τ	Shear stress	N
ϕ	Dimensionless shape of the velocity profile	-
Φ	Particle sphericity	-
χ	Multiplicative parameter of the Stokes number	-

Indices/exponents

<i>f</i>	Fluid
<i>i</i>	Inertial regime
<i>GL</i>	Gas and liquid interface
<i>l</i>	Liquid
<i>m</i>	Running parameter of density components
<i>mf</i>	Minimum fluidization
<i>M</i>	Running parameter of energy components
<i>MD</i>	Maximum packing fraction for defining the mixture viscosity
<i>MP</i>	Maximum packing
<i>p</i>	Particle ensemble
<i>p1, p2, p3, p4</i>	Particles of fuel, steel, control and chunk components
<i>q</i>	Running parameter of velocity components
<i>S</i>	Structure
<i>v</i>	Viscous regime
<i>w</i>	Wall

List of figures

Figure 1 Principe de fonctionnement des SFR de type pool [A Technology Roadmap for Generation IV Nuclear Energy Systems, 2002].....	xiii
Figure 2 Chemin de relocalisation des matériaux via des tubes de transfert d'atténuation par [Bertrand et al., 2018] (DCS-M-TT: Complementary Safety Device for Mitigation – Transfer Tube).....	xiii
Figure 3 Particules d'UO ₂ lisses (A) et fracturées (B) après trempe au sodium par [Singh, 2019] (en haut), Coupe axiale (E5 test) et radiale (E4 test) de la broche dans les expériences CABRI-2 par [Sato et al., 2004] (en bas).....	xiv
Figure 4 Interactions directes particule - particule : collision (à gauche) et frottement (à droite).....	xiv
Figure 5 Bilan de masse dans les trois régions principales pour le test EAGLE FD avec différentes versions SIMMER	xviii
Figure 6 Bilan temporel de la répartition de la masse de carburant et de l'évolution de la puissance par différentes versions de SIMMER	xix
Figure I.1 Degraded core inventory in TMI-2 (1,2 coolant inlets, 3 cavity, 4 loose core debris, 5 crust, 6 previously molten material, 7 lower plenum debris, 8 possible region depleted in uranium, 9 in-core instrument guide, 10 hole in baffle plate, 11 coating of previously-molten material on bypass region interior surfaces, 12, upper grid damage reactor) ["Three Mile Island accident," 2021]	xxiii
Figure I.1 ASTRID Project driver schedule by [Rouault et al., 2015]	2
Figure I.2 GEN-IV reactor concepts selected by GIF) [A Technology Roadmap for Generation IV Nuclear Energy Systems, 2002].....	3
Figure I.3 Operating principle of pool type SFRs [A Technology Roadmap for Generation IV Nuclear Energy Systems, 2002]	5
Figure I.4 Schematic view of the CFV core concept (radial cut) by [Varaine et al., 2012].....	6
Figure I.5 ASTRID core arrangement and fuel subassembly view after [Beck et al., 2017]	7
Figure I.6 Severe accident temporal evolution	8
Figure I.7 Conceptual figure and the upward ejection by the modified-FAIDUS concept by [Tobita et al., 2008]	11
Figure I.8 Material relocation path via mitigation transfer tubes by [Bertrand et al., 2018].....	12
Figure II.1 Schematic view of the discharge phenomena.....	17
Figure II.2 (a) Molten Al ₂ O ₃ porous debris formed in by the interaction with liquid sodium during FR-3 test by [Matsuba et al., 2016]. (b) Smooth (A) and fractured (B) UO ₂ particles following sodium quench reproduced by [Singh, 2019] after [Schins and Gunnerson, 1986]. (c) Typical shapes of the small particles after molten UO ₂ – sodium interaction by [Mizua, 1974]. (d) Axial (E5 test) and radial (E4 test) cut of the pin in CABRI-2 experiments by [Sato et al., 2004]	18
Figure II.3 Momentum allocation (5 velocity fields) of fluid components in SIMMER: state-of-the-art approach (left), new separate particle field approach (right)	23
Figure II.4 Examples of granular media: a Mineral transport; b Cereals; c Medicine drugs and pills d Landside; e Sand castle; f Audience on rugby match, g Oranges; h Stock of wood logs; i Traffic jam (pictures from https://www.freeimages.com)	24
Figure II.5 Particle - particle direct interactions: collision (left) and friction (right).....	26
Figure II.6 Particle trajectory (dotted line) affected by the fluid flow (solid line) for different Stokes numbers by [Benavides and van Wachem, 2008].....	27
Figure II.7 Methods to estimate particle pressure: grid measurement [Boyer et al., 2011] (left) and pore pressure measurement [Garland et al., 2013] (right) pictures are taken from [Guazzelli and Pouliquen, 2018]	28
Figure II.8 Granular states resembling to solid, liquid and gas by [Andreotti et al., 2013].....	29
Figure II.9 Illustration of frictional yield (compressive stresses are defined positive) [Schulze, 2007]	30
Figure II.10 Theoretical importance and SIMMER modelling uncertainty levels for dense and dilute particle flows resulting from the expert advice in the PIRT	35

Figure III.1 Overall framework of the SIMMER code series from [Maschek et al., 2003]	38
Figure III.2 Schematic diagram of four-step method	41
Figure III.3 Channel Flow Regime Map (CP: continuous phase, G: gas, Lk: k type liquid, Lm: m type liquid) from [Yamano et al., 2003]	42
Figure III.4 Plane shear configuration in r-z frame with wall normal particle pressure pp,r , flow cross-section normal particle pressure pp,z and wall shear stress τ_p after [Andreotti et al., 2013]	48
Figure III.5 Interpretation of macroscopic time scale of particle assembly deformation (left) and microscopic time scale of particle rearrangements (right) after [Andreotti et al., 2013]	49
Figure III.6 Flow regimes for immersed granular media on (St,r) plane and the corresponding definition of inertial number after [Cassar et al., 2005]	49
Figure III.7 Velocity distributions reproduced from Sumner [Sumner et al., 1991].....	53
Figure III.8 Velocity distributions with maximum and minimum values of Sumner [Sumner et al., 1991] and dimensionless shape of the velocity profile by Eq. III.19 with best fit $aw = 0.8$ and $a1 = 0.22$	53
Figure III.9 Flow regimes in terms of particle-particle interactions	55
Figure III.10 Eulerian staggered mesh in axial direction with j axial coordinate.....	56
Figure III.11 Continuity of particle pressure and shear stress in function of solid concentration (with arbitrary particle and flow properties)	60
Figure IV.1 Schematic view of static particle pile in gas (left) and in liquid sodium (right).....	67
Figure IV.2 SIMMER-V_vpd: (a) Particle volume fraction inside the pile, (b) particle volume fraction axial profile after stabilization, and (c) Inertial and viscous numbers	68
Figure IV.3 Particle pressure axial profile by SIMMER-V_vpd and by Janssen equation Eq. IV.1 ($\mu_w = \mu_s, Kp = 0.27$).....	68
Figure IV.4 Vertical momentum profile in the particle pile by SIMMER-V_vo (left) and by SIMMER-V_vpd (right)	69
Figure IV.5 Schematic view of jamming transition.....	70
Figure IV.6 Temporal variation of particle volume fraction above and velocity below the support plate by SIMMER-V_vo (left) and SIMMER-V_vpd (right)	71
Figure IV.7 Schematic view of bin discharge test case (SIMMER-V geometry is axisymmetric around the left boundary).....	72
Figure IV.8 Volumetric flow rate through different orifice diameters by Beverloo equation ($c = 0.55, k = 1$) and in SIMMER-V_vpd	73
Figure IV.9 Particle shear stress around the location of orifice	74
Figure IV.10 Schematic view of flow through porous media in gas (left) and in liquid sodium (right).....	75
Figure IV.11 Pressure drop inside the particle bed as a function of inlet gas velocity with SIMMER-V_vo (left) and with SIMMER-V_vpd (right) in comparison to Ergun equation Eq. IV.5.....	75
Figure IV.12 Pressure drop inside the particle bed in function of inlet sodium velocity with SIMMER-V_vpd	76
Figure IV.13 Vertical profile of particle momentum balance at different inlet sodium flows.....	76
Figure IV.14 Pressure drop and bed voidage in packed and fluidized beds from [Toomey, 2018].....	78
Figure IV.15 Schematic view of fluidization by gas (left) and by liquid sodium (right)	79
Figure IV.16 Pressure drop over the bed, gas volume fraction and bed expansion ratio as a function of inlet gas velocity in SIMMER-V_vo	79
Figure IV.17 Temporal oscillations of particle volume concentration inside the bed (left) and of fluid pressure drop across the bed (right) at $vinlet = 0.7 m/s$ with SIMMER-V_vo	80
Figure IV.18 Temporal oscillations of particle volume concentration inside the bed (left) and of fluid pressure drop across the bed (right) at $vinlet = 0.4 m/s$ with SIMMER-V_vpd	80
Figure IV.19 Pressure drop over the bed, gas volume fraction and bed expansion ratio as a function of inlet gas velocity in SIMMER-V_vpd	80
Figure IV.20 Pressure drop over the bed, fluid volume fraction and bed expansion ratio as a function of inlet velocity in SIMMER-V_vpd.....	81
Figure IV.21 Schematic view of the terminal fall a single particle	83

Figure IV.22 Comparison of semi-analytical equation with SIMMER-V_vo (left) and with SIMMER-V_vpd (right) results for particle velocity for three representative particle diameters in liquid sodium	83
Figure IV.23 Schematic view of particle sedimentation.....	85
Figure IV.24 Axial concentration and velocity profile after 3 seconds of sedimentation by SIMMER-V_vpd .	86
Figure IV.25 Comparison of settling velocities computed by SIMMER-V_vo (left) and by SIMMER-V_vpd (right) with correlations from literature in liquid sodium	86
Figure IV.26 Axial profile of particle concentration and particle momentum balance after 3 seconds of sedimentation by SIMMER-V_vpd.....	87
Figure IV.27 Schematic view of sedimentation with different particulate components in SIMMER-V	88
Figure IV.28 Settling velocities in multi-component particle system and their relative deviation from the mono-component case at 10% (top) and 40% (bottom) global concentration	89
Figure IV.29 Experimental setup, F: flowmeter, S: standpipe, P: wall probe location, DP: wall friction transducer after [Shook and Bartosik, 1994]	90
Figure IV.30 Schematic view of the hydraulic conveying	91
Figure IV.31 Experimental and SIMMER-V pressure drops with pure water	91
Figure IV.32 Frictional pressure drop with 10% (top left) and 40% (top right) concentration of 2.8 mm mono-disperse polystyrene ($\rho_p = 1045 \text{ kg/m}^3$) grains by experiment, SIMMER-V_vo and SIMMER-V_vpd.....	92
Figure IV.33 Frictional pressure drop with 10%, 30% and 40% concentration of 2.8 mm mono-disperse polystyrene grains by experiment, SIMMER-V_vo and SIMMER-V_vpd.....	93
Figure IV.34 Momentum terms influencing the pressure drop during hydraulic conveying by 5 m/s fluid velocity of 40% concentration of 2.8 mm mono-disperse polystyrene grains by SIMMER-V_vpd.....	94
Figure V.1 Principle of FD, ID1 and ID2 in-pile tests conducted within the EAGLE-1 program after [Konishi et al., 2007]	99
Figure V.2 Characteristic shape of power transient by IGR after [Konishi et al., 2007]	100
Figure V.3 r-z cut of test section ID1 (left) and FD (right) modelling in SIMMER-V (dark green areas are excluded from calculation). The symmetry axis is on the left side of each figure.	101
Figure V.4 Material distribution inside the FAJ in EAGLE-1 ID1 (left) and FD (right) tests by SIMMER-V_vpd just before duct failure	102
Figure V.5 First duct rupture view and wall temperature and thickness at this location by SIMMER-V_vpd in EAGLE ID1 (left) and EAGLE FD (right).....	103
Figure V.6 Material distribution at the end of simulation for (a) ID1 test by SIMMER-V_vo, (b) ID1 test by SIMMER-V_vpd, (c) FD test by SIMMER-V_vo and (d) FD test by SIMMER-V_vpd	104
Figure V.7 Mass balance in the three main regions for EAGLE ID1 (left column) and for EAGLE FD (right column) with different SIMMER versions.....	105
Figure V.8 Particle volume fraction, particle velocity and newly implemented rheology terms in SIMMER-V_vpd for EAGLE FD test.....	108
Figure V.9 Sensitivity study results for uncertain coefficients of the $\mu(I)$ rheology models	111
Figure V.10 Sensitivity study results for uncertain particle properties and their initial material composition	112
Figure VI.1 SIMMER-V illustration of ASTRID reactor with annotated regions.....	116
Figure VI.2 SIMMER-V illustration of ASTRID CFV core (radial-axial cut) with annotated regions.....	117
Figure VI.3 Transfer tube extension towards the core catcher: long before pump shutdown (left) and after sodium inflow to the core is negligible (right)	117
Figure VI.4 Sodium temperature profile across the core (left) Fuel internal energy axial profile (right).....	118
Figure VI.5 Core inlet sodium flow rate after pump shutdown in SIMMER-V.....	119
Figure VI.6 Reactivity and power evolution after ULOF onset (primary and transition phase)	120
Figure VI.7 Illustration of boiling/reflooding phenomena (black arrows indicate sodium velocity directions and magnitudes)	120
Figure VI.8 Core state at the end of the primary phase (74.3 seconds after ULOF onset).....	121
Figure VI.9 Reactivity and power evolution at the end of the primary and during the transition phase	122
Figure VI.10 Core state shortly before (76.2 s) and after (76.7 s) first prompt criticality.....	122

Figure VI.11 Reactivity and power evolutions during the secondary phase up to the transfer tube opening	123
Figure VI.12 Material distribution before the transfer tube opening	123
Figure VI.13 Material distribution around the first transfer tube opening in 4 th subassembly ring	124
Figure VI.14 Total evacuated fuel mass (sum of liquid, particle and chunk components) (left), evacuated fuel mass and in form of particles (sum of particle and chunk components) (right) via inner/outer transfer tubes	125
Figure VI.15 Illustration of the hydraulic diameter change in the transfer tube ring 4 th (left) and ring 20 th (right)	126
Figure VI.16 Total evacuated mass (top) and nuclear power (bottom) evolution	127
Figure VI.17 Temporal balance of fuel mass distribution and the total material distribution plot at the end of the simulation by different SIMMER versions	128

List of tables

Table 1 Matrice d'évaluation des cas de tests simplifiés (+ reproduit, - non reproduit, o non interprétable, x non analysé)	xvii
Table I.1 Main characteristic values of the 1500 MWth ASTRID reactor	6
Table II.1 Particle-size reactor debris properties	19
Table II.2 Example for the use of particle viscosity models in current state-of-the-art approach when the continuous phase is liquid fuel - fuel particle mixture with suspended particles of steel and fuel chunks (indexes $p1, p2, p4$ refer to fuel particle, steel particle, chunks respectively) (red terms mark the effect of omitting chunks from particle viscosity factors)	21
Table II.3 Granular regimes by [Coussot and Ancey, 1999].....	29
Table II.4 Phenomena Identification-Ranking Table	34
Table III.1 Momentum exchange coefficients between components (K_{ik} between fluid i and k , K_{iS} between fluid i and structure, x not computed because they belong to the same velocity field in our approach).....	42
Table III.2 Momentum exchange functions between velocity fields (K_{ik} between fluid i and k , K_{iS} between fluid i and structure).....	43
Table III.3 Rheology parameters adopted for $\mu(I)$ rheology up to and above 55 % particle concentration	52
Table III.4 Rheology parameters	52
Table III.5 Synthesis of the developed models for particle dynamics in SIMMER-V	62
Table IV.1 Particle and fluid properties in simplified test cases	64
Table IV.2 Evaluation matrix of simplified test cases	65
Table IV.3 Validity criteria for Beverloo law [Nedderman et al., 1982] when container diameter $D = 0.16\ m$ and particle diameter $d_p = 0.001\ m$ are fixed (outlet orifice diameter D_0 , thickness/height of granular bed H)	72
Table IV.4 Correlations for settling exponent in dense particle flows.....	85
Table IV.5 Evaluation matrix of simplified test cases (+ reproduced, - not reproduced, o not interpretable, x not analyzed)	95
Table V.1 Experimental programs related to fuel degradation.....	98
Table V.2 Sensitivity study parameters and their analyzed range of variation.....	110

Résumé en français

Introduction et contexte

Ce travail de recherche a été conduit dans le contexte des évaluations de sûreté des futurs Réacteurs à Neutrons Rapides refroidis au sodium (RNRNa) et plus précisément dans le cadre du projet ASTRID (Advanced Sodium Technological Reactor for Industrial Demonstration) en France (Figure 1). Le domaine des accidents graves (Core Disruptive Accidents, CDA) y fait l'objet d'une attention particulière, une sûreté accrue étant demandée pour les futures filières de réacteurs de Génération IV. Lors d'une séquence accidentelle non protégée hypothétique, le cœur d'un RNRNa peut évoluer vers des configurations fortement dégradées. Sous l'effet des hautes températures et des chargements mécaniques, les aiguilles de combustible (pastilles, gaines) et les structures (boîtiers hexagonaux) peuvent rompre, fondre voire être vaporisés. Ces matériaux fondus ou vaporisés vont se relocaliser (par condensation, gel, écoulement) dans le cœur de façon hétérogène, en fonction de l'évolution des champs de température et de pression. Au final, le cœur accidenté est progressivement envahi, et en partie remplacé, par un mélange complexe multi-phasique multi-composant de matériaux et de fluides. La distribution spatiale de ce mélange et de ses constituants, en particulier de la matière fissile, a un fort impact sur la réactivité du cœur accidenté et gouverne donc en grande partie l'évolution future de l'accident et ses conséquences. En vue de se conformer aux exigences accrues de sûreté des filières GENIV, le CEA (Commissariat à l'Energie Atomique et aux Energies Alternatives) a élaboré une stratégie innovante de mitigation des accidents graves pour son concept de Cœur à Faible Vidange (CFV) [Bertrand et al., 2018; Varaine et al., 2012]. Cette stratégie consiste à faciliter, par une conception mettant en oeuvre des tubes de transfert et un récupérateur de corium en cuve, la décharge passive hors du cœur du combustible fondu ou dégradé (Figure 2). En réduisant la quantité de matière fissile dans le cœur, il est ainsi possible de réduire la probabilité et l'amplitude de potentielles excursions de puissance qui solliciteraient la cuve principale. Lors de la séquence accidentelle, les tubes de transfert jouent leur rôle dès lors que les boîtiers hexagonaux des assemblages voisins perdent leur intégrité, permettant ainsi aux matériaux fondus de perforer la paroi des tubes. Il s'ensuit un transfert vertical des matériaux jusqu'au récupérateur situé dans le fond de la cuve primaire. Le rôle du récupérateur est de collecter les débris et les matériaux fondus, de faciliter leur étalement et leur refroidissement à long terme.

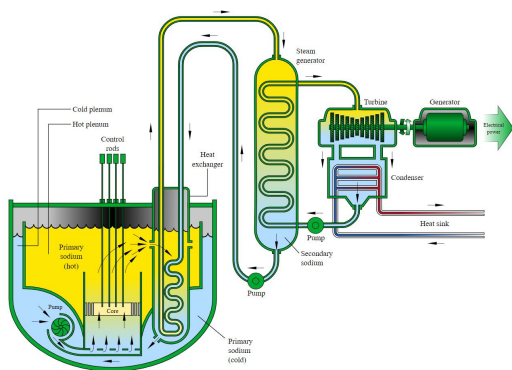
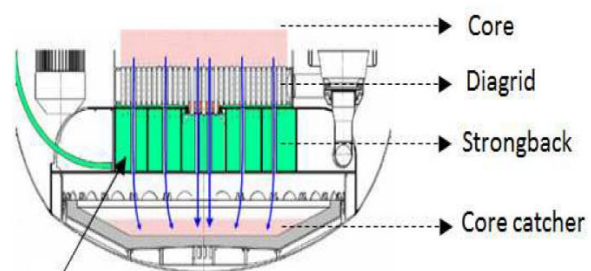


Figure 1 Principe de fonctionnement des SFR de type pool [A Technology Roadmap for Generation IV Nuclear Energy Systems, 2002]



Material discharge in 1 DCS-M-TT

Figure 2 Chemin de relocalisation des matériaux via des tubes de transfert d'atténuation par [Bertrand et al., 2018] (DCS-M-TT: Complementary Safety Device for Mitigation – Transfer Tube)

Ce dispositif de mitigation n'est efficace que si une quantité suffisante de combustible peut être extraite du cœur en un laps de temps le plus court possible. La performance d'extraction du combustible par un tube peut être évaluée à l'aide de programmes expérimentaux et d'outils de simulation. En l'état actuel de la recherche, la démonstration du scénario de mitigation s'appuie sur

l'outil numérique "best estimate" SIMMER (Sn Implicit Multiphase Multicomponent Eulerian Recriticality) [Maschek et al., 2003]. SIMMER, utilisé en France et au Japon, est un outil de calcul scientifique dédié à l'analyse des accidents graves dans les réacteurs nucléaires refroidis par des métaux liquides. Les simulations, avec SIMMER, de séquences accidentelles sur le concept de coeur CFV pour le prototype ASTRID ont indiqué qu'une fraction majoritaire du combustible dégradé se retrouve sous forme de particules solides. En conséquence, la performance de mitigation des tubes sera fortement affectée par l'écoulement et le transfert de matériaux à forte composante particulaire. Ainsi, en raison de l'importance de la dynamique des particules dans les futures évaluations de sûreté, ce travail de thèse est dédié à l'amélioration des modèles d'écoulement particulaire dans le code SIMMER-V. Ces améliorations ont été entreprises en considérant une nouvelle approche, distinguant les vitesses des particules et de leur liquide associé, et introduisant de nouveaux termes dans l'équation de Navier-Stokes décrivant la dynamique des particules.

Écoulements particulaires dans les Tubes de Transfert

L'état de l'art du traitement des écoulements particulaires dans le code SIMMER repose sur des modèles de viscosité apparente et de coefficients multiplicateurs afin de rendre compte de la présence de solides en suspension dans l'écoulement multi-phasique multi-constituant. Ces modèles supposent implicitement que les particules sont immergées dans la phase liquide ayant leur composition, avec laquelle elles s'écoulent en partageant un champ de vitesse commun. L'allocation d'un champ de vitesse spécifique aux particules n'est pas compatible avec ces hypothèses et modèles, d'où la nécessité d'élaborer une approche nouvelle permettant de décrire l'effet de la dynamique particulaire sur la relocalisation des matériaux. L'aspect physique de ces débris est illustré en Figure 3. La revue bibliographique dédiée aux milieux et écoulements granulaires secs et immergés (pris comme analogues des débris de combustible dans différents fluides) a permis d'identifier deux spécificités essentielles de leur physique, cruciales pour notre travail. En premier lieu, les systèmes granulaires exhibent des comportements dynamiques particuliers résultant principalement des chocs inélastiques et des frottements entre les grains (Figure 4).

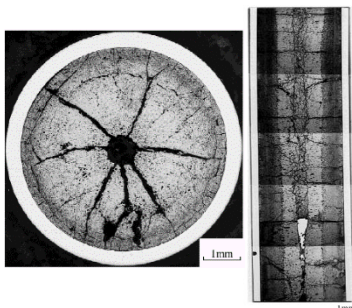
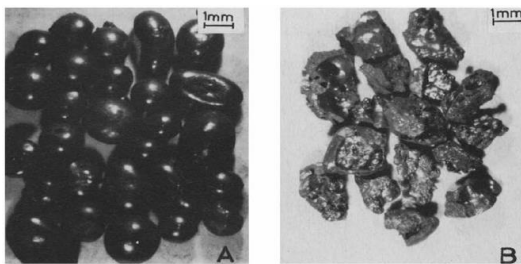


Figure 3 Particules d'UO₂ lisses (A) et fracturées (B) après trempe au sodium par [Singh, 2019] (en haut), Coupe axiale (E5 test) et radiale (E4 test) de la broche dans les expériences CABRI-2 par [Sato et al., 2004] (en bas)

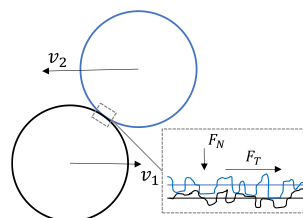
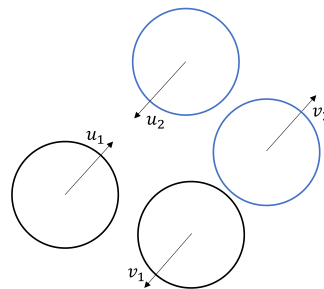


Figure 4 Interactions directes particule - particule : collision (à gauche) et frottement (à droite)

En second lieu, dans des configurations à forte concentration de particules, ces processus et interactions peuvent prédominer sur les autres forces gouvernant l'écoulement. Nous avons donc décidé d'incorporer, dans la simulation numérique faite par SIMMER, une représentation de ces interactions intergranulaires en vue de rendre la prédiction de la dynamique des débris, lors de leur décharge vers le récupérateur, plus réaliste et plus précise. Cette décision a pu être étayée grâce à un travail collectif de PIRT (Phenomena Identification-Ranking Table) que nous avons animé et dirigé, permettant de mettre en regard les incertitudes des modèles actuels de SIMMER et l'importance relative des processus physiques intervenant lors du transfert des débris dans les tubes de transfert.

Développement d'un modèle de dynamique particulaire

Cette partie représente le coeur de notre travail de recherche: le développement, dans l'environnement logiciel de SIMMER-V, d'un modèle de dynamique particulaire suffisamment général pour être appliqué, dans une large gamme de fraction volumique, aux situations et applications du domaine d'intérêt des réacteurs accidentés. Le modèle élaboré consiste à améliorer la formulation des termes d'échange de quantité de mouvement entre fluides et particules et à incorporer une description nouvelle des effets des interactions entre particules dans l'équation de bilan de quantité de mouvement des particules, Eq. 1.

L'amélioration de la loi constitutive de traînée interphase a consisté à renoncer à l'utilisation, inhérente à l'approche antérieure dans le modèle de mélange, de facteurs multiplicatifs pour évaluer la viscosité particulaire.. Elle a été réalisée en remplaçant la fonction d'échange de quantité de mouvement d'origine par la fonction de traînée de Gidaspow [Gidaspow, 1994]. L'équation de Gidaspow est une combinaison des corrélations de Wen & Yu et d'Ergun, Eq. 2. Cette dernière est largement reconnue pour être plus représentative des configurations ayant une forte fraction volumique de particules, où les corrélations telles que celle utilisée antérieurement dans SIMMER, sont la cause de fortes incertitudes.

La deuxième partie du développement du modèle a concerné la prise en compte des contacts directs particule-particule, interaction qui n'est pas modélisée dans les versions originales de SIMMER. Cela a été fait en introduisant un nouveau terme de contrainte mécanique, lié aux particules, dans l'équation de quantité de mouvement de SIMMER pour les particules. Les lois de comportement pour la contrainte solide (pression de particules et contrainte de cisaillement) ont été construites en suivant l'approche de la rhéologie granulaire dense $\mu(I)$ récemment développée par [Forterre and Pouliquen, 2009], Eq. 3 et Eq. 4. Sa capacité à décrire les régimes d'écoulements granulaires de type « fluide » dans lesquels les collisions inter-particulaires et les frottements ont une importance similaire, son adaptabilité permettant de formuler des lois constitutives en géométrie 1D, cohérentes avec la représentation dans SIMMER du transfert unidimensionnel dans les tubes, et le fait que les équations sont exprimées en termes de variables de champ macroscopiques ont motivé ce choix (pour plus de détails voir Chapter III).

$$\frac{\partial(\bar{\rho}_p v_p)}{\partial t} + \nabla(\bar{\rho}_p v_p v_p) = -\alpha_p \nabla p_f - \nabla \cdot \sigma_p + \bar{\rho}_p g + K_{pf}(v_p - v_f) \quad \text{Eq. 1}$$

$$K_{pf} = \left\{ \begin{array}{ll} \frac{3}{4} C_D \frac{\alpha_p \alpha_f \rho_f |v_p - v_f|}{\phi d_p} \alpha_f^{-2.65} & \text{if } \alpha_p < 0.2 \\ 150 \frac{\alpha_p^2 \mu_f}{\alpha_f \phi^2 d_p^2} + \frac{1.75 \alpha_p \rho_f |v_p - v_f|}{\phi d_p} & \text{if } \alpha_p \geq 0.2 \end{array} \right\} \quad \text{Eq. 2}$$

$$\frac{\partial \sigma_p}{\partial z} = \frac{\partial p_{p,z}}{\partial z} + \frac{4\tau_{p,rz}}{D_h} \quad \text{Eq. 3}$$

$$\tau_p = \begin{cases} 0.5\alpha_p\rho_p f_p v_p^2 & \text{if } \alpha_p < 0,3 \\ \mu(I_i) \left(\frac{c_i \alpha_p}{\alpha_{MP} - \alpha_p} \right)^2 \rho_p d_p^2 \dot{\gamma}^2 + \mu(I_v) \left(\frac{c_v \alpha_p}{\alpha_{MP} - \alpha_p} \right)^2 \mu_f \dot{\gamma} & \text{if } 0,3 \leq \alpha_p < 0,55 \\ \mu(I_i) \left(\frac{c_p}{\alpha_{MP} - \alpha_p} \right)^{2,8} \rho_p d_p^2 \dot{\gamma}^2 + \mu(I_v) \left(\frac{c_p}{\alpha_{MP} - \alpha_p} \right)^{2,8} \mu_f \dot{\gamma} & \text{if } 0,55 \leq \alpha_p < \alpha_{MP} \end{cases}$$

$$p_{p,z} = \begin{cases} 0 & \text{if } \alpha_p < 0,3 \\ \frac{1 + \sin\delta}{1 - \sin\delta} \left[\left(\frac{c_i \alpha_p}{\alpha_{MP} - \alpha_p} \right)^2 \rho_p d_p^2 \dot{\gamma}^2 + \left(\frac{c_v \alpha_p}{\alpha_{MP} - \alpha_p} \right)^2 \mu_f \dot{\gamma} \right] & \text{if } 0,3 \leq \alpha_p < 0,55 \\ \frac{1 + \sin\delta}{1 - \sin\delta} \left[\left(\frac{c_p}{\alpha_{MP} - \alpha_p} \right)^{2,8} \rho_p d_p^2 \dot{\gamma}^2 + \left(\frac{c_p}{\alpha_{MP} - \alpha_p} \right)^{2,8} \mu_f \dot{\gamma} \right] & \text{if } 0,55 \leq \alpha_p < \alpha_{MP} \end{cases} \quad \text{Eq. 4}$$

Le principal point fort de la mise en œuvre de la rhéologie granulaire dense $\mu(I)$ dans SIMMER est qu'elle se traduit par une rhéologie de friction dépendante du cisaillement à travers un coefficient de friction macroscopique dépendant du taux de cisaillement. De plus, cette rhéologie exprime la nature tridimensionnelle réelle des collisions et des frottements en corrélant les composantes normales et de cisaillement de la contrainte mécanique au sein du milieu granulaire. Ces deux caractéristiques permettent d'ajouter une physique entièrement nouvelle à la description originale de la dynamique des particules dans SIMMER. Contrairement à la description la plus simple de type continuum fluide/particules, le nouveau modèle fournit une description plus réaliste des écoulements de particules denses tout en tenant compte de l'hétérogénéité des contraintes solides et de la dépendance au taux de cisaillement.

Pour tenir compte des différents régimes d'écoulement dans les applications au cas des réacteurs, deux échelles de contrainte sont adoptées : dominante inertielle ou visqueuse. Contrairement à la carte topologique des écoulements dans la version antérieure de SIMMER, qui négligeait l'influence de la charge en particules, ce nouveau modèle ajoute une autre dimension à la topologie qui est désormais fonction de la concentration totale de particules. Tout en tenant compte davantage de l'effet de cette concentration particulière et en étendant le modèle aux interactions inter-particulaires, les équations de rhéologie granulaire dense $\mu(I)$ ont également été élargies, grâce à la théorie de la percolation (dans la formulation de la loi de dilatance), aux concentrations les plus élevées où se manifestent une transition vers un blocage de l'écoulement. À des concentrations faibles, où la rhéologie granulaire dense $\mu(I)$ n'est pas valide, la contrainte de cisaillement liée aux particules a été formulée suivant l'équation de Fanning conventionnelle avec un facteur de frottement solide que nous avons dérivé de la rhéologie granulaire dense $\mu(I)$ pour garantir la continuité. Globalement, ces choix rendent notre modèle multidisciplinaire.

Cas-tests simplifiés

Suite au développement du modèle, cette section présente leur validation en utilisant des cas-tests simplifiés. Tous les cas-tests considérés dans ce travail sont des configurations unidimensionnelles, purement dynamiques, sans transfert de chaleur ni de masse, à deux phases (particule-liquide ou particule-gaz) et intégrant une structure latérale frottante ou confiante. Ils correspondent à des conditions représentatives dans lesquelles une concentration élevée de débris solides est susceptible d'influencer la dynamique de décharge des matériaux du cœur via les tubes de transfert. Les cas de test comprennent : le lit sédimentaire statique, la décharge de silo, l'écoulement à travers un milieu poreux, la fluidisation et la sédimentation. Les calculs sont effectués d'une part avec SIMMER-V_vo, c'est-à-dire avec les équations originales et les options de modélisation par défaut et, d'autre part, avec SIMMER-V_vpd, intégrant le nouveau modèle de dynamique particulaire développé dans ce travail. Les résultats des deux simulations pour chaque cas-test sont comparés

à des solutions analytiques ou à des corrélations empiriques permettant d'évaluer la qualité des résultats. Les résultats sont synthétisés dans la Table 1.

Table 1 Matrice d'évaluation des cas de tests simplifiés (+ reproduit, - non reproduit, o non interprétable, x non analysé)

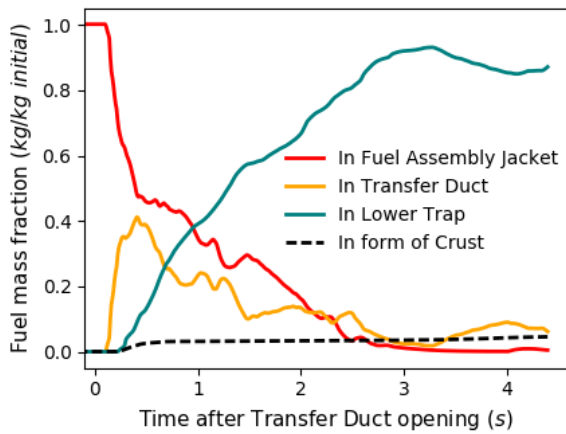
Cas de test	Figure du mérite	Comportement attendu de la figure du mérite	Version de SIMMER_V			
			vo		vpd	
			Gas	Liquid	Gas	Liquid
Tas de particules coincé (situation particulière)	Répartition des contraintes	Le profil de pression partielle est en accord avec la prédiction de Janssen	-	x	+	x
		Les contraintes de particules soutiennent le poids flottant des particules	x	-	x	+
	Transition de brouillage	Transition brouillage/débrouillage en fonction des contraintes spatiales	x	-	x	+
Décharge du bac	Débit refoulé	Débit constant en fonction de la granulométrie et de la variation de section d'orifice	-	x	+	x
Écoulement à travers les médias poreux	La chute de pression	Déclaration de Darcy : augmentation de la chute de pression du lit avec la vitesse du fluide d'entrée jusqu'à la fluidisation	+	-	+	+
Transition de fluidisation	Vitesse de fluidisation minimale	La vitesse du fluide d'entrée à laquelle le poids flottant du lit est contrebalancé par la force de traînée	-	o	+	+
	La chute de pression	Passage du lit tassé au lit fluidisé lorsque la perte de charge s'éloigne de la loi d'Ergun	-	o	+	+
Sédimentation	Vitesse terminale	Une vitesse constante est atteinte après une certaine distance pendant la chute libre d'une seule particule et elle correspond quantitativement à la solution analytique	x	+	x	+
	Taux de règlement	Taux de décantation constant à fraction solide constante et correspond quantitativement aux résultats expérimentaux	x	+	x	+
	Taux de sédimentation des différents composants	Retrouver le même taux de décantation que pour un seul composant si densités et tailles sont identiques	x	-	x	+
Convoyage hydraulique	Perte de pression par friction	La perte de pression par friction augmente avec la vitesse en vrac et la concentration solide	x	+	x	+

D'après les résultats présentés en Table 1 nous pouvons conclure que l'application de ce nouveau modèle de dynamique des particules produit des résultats encourageants. Le comportement physique correct est reproduit pour chaque cas-test. Les calculs avec SIMMER-V_vpd montrent des améliorations remarquables par rapport à SIMMER-V_vo, notamment en cas de fluidisation par le sodium liquide, cas-test pour lequel les résultats de SIMMER-V_vo ne sont pas interprétables, et en cas de blocage de particules où les modèles de SIMMER-V_vo, ne décrivant pas les contraintes mécaniques, ne permettent pas de capturer le comportement attendu du milieu granulaire.

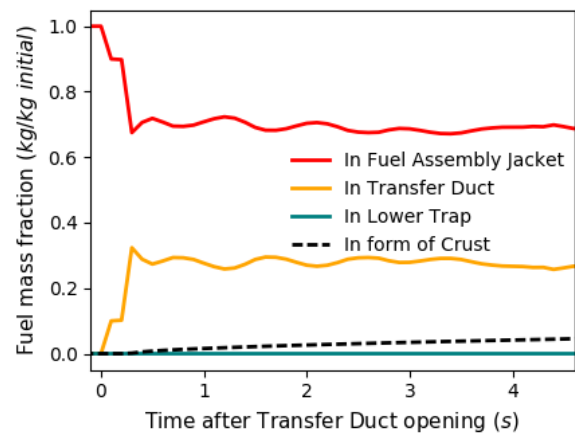
Essais intégraux

Cette section est liée à la validation à l'échelle expérimentale. Ce chapitre compare à nouveau les résultats de SIMMER-V_vo et SIMMER-V_vpd (et avec également le calcul best estimate antérieur, exécuté antérieurement au CEA avec SIMMER-III). Le scénario étudié est complexe avec des processus de transfert de chaleur et de masse qui correspondent mieux aux phénomènes se produisant lors de la décharge dans un réacteur réel, cependant à échelles de masse et de dimension réduites. Les tests intégraux utilisés à cette fin ont été réalisés lors des programmes expérimentaux EAGLE 1 FD et ID1 conduits par JAEA sur le réacteur IGR au Kazakhstan. Nous avons pu retracer grâce à SIMMER-V_vpd les événements majeurs des essais et reproduire les observations expérimentales essentielles et pertinentes pour valider notre développement. Cela comprend notamment la décharge massive du combustible dégradé depuis l'assemblage combustible simulé, l'absence de blocage permanent à l'intérieur du conduit de décharge et l'arrivée

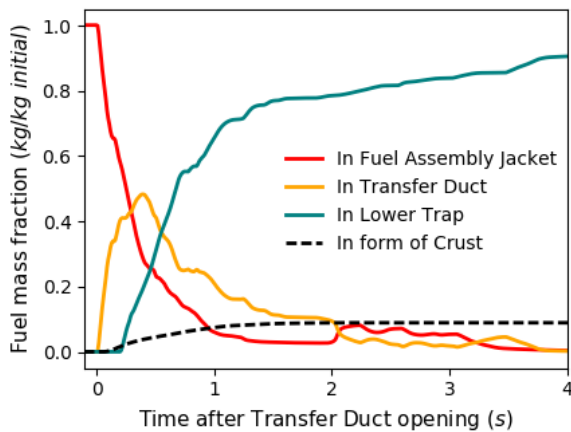
d'une grande partie de l'inventaire de combustible initial dans le piège inférieur, simulant le récupérateur. Les résultats de SIMMER-V_{vo} montrent des blocages permanents des particules et des mises en lévitation de matière non physiques qui ont empêché une relocalisation massive du combustible, en contradiction avec les résultats des tests FD et ID1. D'un autre côté, les résultats de SIMMER-V_{vpd} sont en bon accord avec la meilleure estimation numérique préconisée par le CEA (ce-dernier étant cependant réalisé avec une hypothèse multi-maillage du conduit non satisfaisante), tous deux prédisant bien l'observation post expérimentale de la distribution de masse de combustible pour les deux tests. Cependant, nous avons conclu à l'utilisation préférable de SIMMER-V_{vpd} puisque le conduit interne dans SIMMER-III était représenté dans une approche multi-maillage, contradictoire avec la topologie d'écoulement unidimensionnelle dans SIMMER. L'évolution temporelle de la distribution de masse pour le test EAGLE FD est montrée en Figure 5.



La meilleure estimation numérique préconisée par le CEA



SIMMER-V_{vo}



SIMMER-V_{vpd}

Figure 5 Bilan de masse dans les trois régions principales pour le test EAGLE FD avec différentes versions SIMMER

Afin de mieux comprendre le comportement des équations de rhéologie particulaire dans un environnement multi-phases et multi-composants complexe, une section est consacrée à l'analyse des termes de contraintes des particules en régime inertiel et visqueux. En comparant leur amplitude, nous avons confirmé notre hypothèse initiale sur leur additivité en postulant la prédominance forte de l'une sur l'autre. Sur la base de l'évolution spatiale et temporelle des contraintes normales et de cisaillement, nous avons déduit que leur dépendance vis-à-vis de la concentration en solide et la vitesse des particules est cohérente avec le comportement physique attendu. De plus, pour estimer l'effet de paramètres empiriques incertains des équations de rhéologie, une étude de sensibilité a été réalisée. L'analyse de sensibilité n'a mis en évidence qu'un

seul paramètre influent, le coefficient de proportionnalité entre le taux de cisaillement et la vitesse axiale moyenne qui a un effet considérable sur la dynamique de décharge des débris.

Application à l'échelle réacteur

La dernière section, constitue le troisième et le plus important niveau de conclusion lié à l'application de nos travaux à l'échelle réacteur. C'est en effet l'objectif de ce travail de thèse de prédire, grâce au développement du modèle de dynamique des particules, le scénario de décharge des débris du cœur fondu/dégradé avec une plus grande confiance et de contribuer ainsi à l'évaluation de la sûreté des futures générations de RNRNa. L'objectif de ce chapitre est donc d'évaluer l'impact des nouveaux modèles de dynamique des particules sur les performances (prédites numériquement) de la stratégie de mitigation des accidents graves. L'application à l'échelle du réacteur a été faite par une simulation de la séquence accidentelle non protégée de type ULOF, pour un cœur de référence CFV ASTRID et une représentation du réacteur en géométrie pseudo-3D. L'ensemble de la séquence accidentelle simulée avec SIMMER-V confirme le bon comportement naturel du cœur CFV, empêchant un dégagement important d'énergie mécanique lors de la phase accidentelle primaire. Ensuite, la décharge des matériaux via les tubes de transfert a été analysée avec SIMMER-V_vo, SIMMER-V_vpd et vis-à-vis des résultats du calcul de référence antérieur du CEA réalisé avec SIMMER-III (Figure 6).

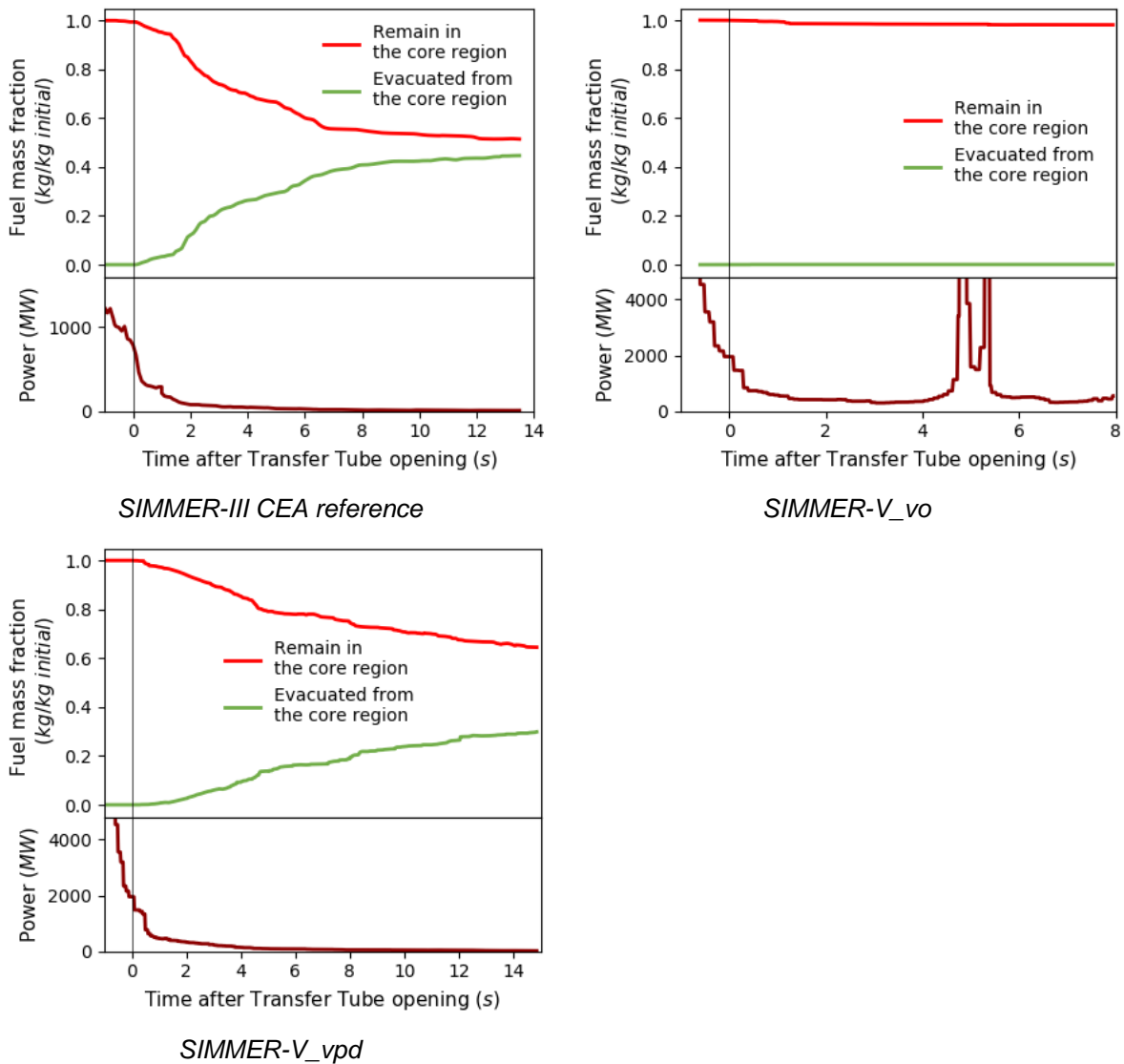


Figure 6 Bilan temporel de la répartition de la masse de carburant et de l'évolution de la puissance par différentes versions de SIMMER

Nous avons constaté qu'au cours de la simulation faite avec SIMMER-V_{vo}, la décharge des débris de combustible est fortement inhibée par la formation de blocages permanents, et peu réalistes, de particules à l'intérieur des tubes de transfert. Cela conduit à des puissances de cœur importantes, incompatibles avec le retour à l'état sûr du réacteur. Cependant, sur la base des prédictions inexactes de SIMMER-V_{vo} pour les cas de test simplifiés au chapitre IV et vis-à-vis des résultats des tests intégraux au chapitre V, nous pouvons estimer que les modèles originaux de dynamique des particules de SIMMER-V_{vo} doivent être modifiés pour pouvoir être appliqués selon l'approche de dynamique particulaire à champ de vitesse séparé. Cette affirmation est également étayée par les conclusions tirées de l'étude bibliographique sur les écoulements granulaires denses. D'autre part, l'étude comparative a montré que les résultats SIMMER-V_{vpd} sont en accord qualitatif avec le calcul de référence SIMMER-III CEA (ce dernier conservant la représentation du tube en 1D avec de premières modifications sur les termes de viscosité des particules, cependant loin du stade actuel de développement réalisé dans cette thèse). Les deux calculs ont démontré que grâce à l'extraction massive et rapide du combustible de la région centrale du cœur, le cœur revient dans un état fortement sous-critique, état favorable pour éviter d'autres re-criticités et les fortes excursions de puissance correspondantes à plus long terme. Cela implique que la stratégie de mitigation par un nombre et une conception adaptés des tubes de transfert peut être efficace au regard du principal critère de sûreté, qui est, dans un premier temps, de limiter la probabilité et l'amplitude de grands dégagements d'énergie mécanique. Le fait que le cœur ait été amené dans un état fortement sous-critique après un CDA est en effet la première étape avant que d'autres dispositifs d'atténuation n'entrent en action (récupérateur, dispositifs de refroidissement passifs, etc.). Une analyse plus poussée serait donc à conduire pour conclure sur l'atteinte d'un état final sûr du réacteur et traduire nos résultats en chargements thermique et mécanique des barrières de confinement et du récupérateur de corium. De telles évaluations, même si elles comportent actuellement de grandes incertitudes, sont d'un intérêt décisif pour les concepteurs de la chaudière.

Conclusions et perspectives

Notre travail, en comparaison des calculs de référence conduit antérieurement avec SIMMER, conduit à une prédiction numérique basée sur une physique améliorée et une meilleure estimation des performances de mitigation. La description détaillée du comportement dynamique des particules rend compte de manière plus réaliste de l'effet de la concentration en particules et de l'impact nouvellement intégré au modèle des interactions entre particules. Même si l'approche mise en œuvre est partiellement empirique et nécessite des raffinements supplémentaires, le nouvel outil de modélisation s'inscrit bien dans le domaine des accidents nucléaires graves, où l'on n'entend pas résoudre les phénomènes à l'échelle la plus fine mais fournir un niveau de prédiction suffisant pour obtenir une évaluation quantitative de la performance. Dans cette optique, l'ensemble des modèles développés dans cette thèse apporte une démonstration plus robuste des scénarios d'accidents graves RNRNa et, par conséquent, marque une étape importante dans les analyses de sûreté des réacteurs. Sa valeur ajoutée pour la communauté des réacteurs peut être encore étendue et accrue par les perspectives futures suivantes.

Les perspectives de ce travail de thèse sont organisées en trois niveaux, à savoir le niveau modélisation physique, le niveau expérimental et le niveau de l'application réacteur. En ce qui concerne le niveau de développement du modèle, nous identifions les sujets suivants qui pourraient être investis à l'avenir. Une partie d'entre eux découlent des lacunes de connaissance sur la physique et partant, de la modélisation. On peut en trouver dans les coefficients empiriques des équations de rhéologie. Ces coefficients ont été déduits d'expériences utilisant des particules et des fluides aux propriétés spécifiques. Par conséquent, l'applicabilité de ces coefficients pour la description des débris de réacteur peut être incertaine. Cette catégorie comprend la connaissance préalable et la formulation du taux de cisaillement pour adopter un traitement numérique unidimensionnel. En guise d'approche préliminaire, nous avons implémenté une corrélation simple, qui n'est fonction que de la vitesse axiale moyenne basée sur le comportement pseudo-plastique.

Pour améliorer l'équation du taux de cisaillement et proposer des coefficients empiriques spécifiques pour les débris de réacteur, nous suggérons des investigations supplémentaires et des programmes expérimentaux dédiés. Le deuxième domaine proposé pour les travaux futurs est lié au comportement rhéologique des écoulements multi-composants multiphasiques. Une difficulté vient du fait que la mise à l'échelle des contraintes dans la rhéologie granulaire dense $\mu(I)$ est établie par analyse dimensionnelle des systèmes à seulement deux composants et deux phases. Cependant, nous sommes contraints par derrière le peu de connaissances expérimentales disponibles et l'approche de modélisation développée spécifiquement pour les écoulements multi-composants multiphasiques. Si à l'avenir des approches et des corrélations bien établies seraient disponibles pour de tels systèmes, les équations mises en œuvre pourront être revisitées et améliorées. Le troisième point qui mérite l'attention la plus immédiate concerne la mise en œuvre numérique du gradient de pression des particules. Il a été mis en œuvre avec un traitement temporel explicite et une projection aval du premier ordre des variables de bord de cellule comme première approche. Même si nous avons expérimenté divers schémas numériques de discrétisation spatiale, nous n'avons pas réussi à en trouver un qui fournisse une solution stable dans toutes les configurations considérées. Par conséquent, nous avons appliqué une technique de régularisation numérique qui limite l'amplitude du gradient et résout les problèmes de stabilité. Concernant la discrétisation temporelle, nous n'avons pas le choix car le système d'équations de la quantité de mouvement dans SIMMER est résolu par élimination gaussienne du premier ordre complétée par une itération de Newton pour les termes d'ordre supérieur. La méthode matricielle itérative résout localement les vitesses des phases à un emplacement donné. L'inclusion d'un terme de gradient implicite dépendant de la vitesse (évaluation de la vitesse à différents endroits) dans ce système est une tâche numérique difficile et dépasse les limites de ce doctorat. Cependant, cela apporterait l'avantage de rendre cohérent le schéma temporel pour la pression particulaire avec celui pour le terme de contrainte de cisaillement, et nous postulons que cela pourrait résoudre les problèmes d'instabilité. Par conséquent, nous suggérons de mettre en œuvre un traitement en temps implicite pour la pression normale des particules. Dans ce but, un stage est proposé récemment au CEA (visant également à approfondir la question de l'interprétation de la pression des fluides dans SIMMER).

Outre les mesures correctives, l'autre volet des améliorations au niveau de la modélisation physique concerne la montée en gamme des capacités de modélisation, par exemple en intégrant les phénomènes de transfert de chaleur dans les systèmes particuliers ou en étendant la dynamique au 3D. Le premier point est nécessaire car la dissipation d'énergie est un processus en deux étapes, et pour en tenir compte de manière appropriée, les mécanismes de transfert de chaleur dans SIMMER-V doivent peut-être être revisités et reconsidérés. En prolongeant les modèles actuellement unidimensionnels en modèles tridimensionnels, ils pourraient être appliqués à l'ensemble de la région du cœur du réacteur et au récupérateur. En réalisant une telle extension, nous bénéficierions d'une approche cohérente de la dynamique des particules et vraisemblablement d'un comportement plus physique des débris sur l'ensemble du domaine de simulation. L'avantage de l'approche utilisant la rhéologie granulaire dense $\mu(I)$ est que les lois constitutives des contraintes solides sont relativement facilement adaptables à la modélisation 3D à la suite des travaux de (Jop et al., 2006). Le sujet de stage mentionné précédemment prévoit également cette direction. De plus, nous soulignons que l'application des modèles de dynamique des particules développés dans ce travail ne se limite pas aux RNRNa, ils peuvent être applicables à d'autres types de réacteurs où les écoulements de solides particuliers peuvent être importants.

Les perspectives au niveau expérimental comprennent la validation plus complète des modèles SIMMER-V_vpd par des tests d'effets séparés et intégrés. Concernant les tests d'effets séparés portant sur des phénomènes physiques élémentaires, les premiers tests de la plateforme PLINIUS2 (nom à confirmer) sont prévus. Pour la construction de la plateforme expérimentale prototypique new PLINIUS, il y a actuellement un investissement considérable réalisé au CEA, avec actuellement

deux propositions de tests à effets séparés à petite échelle. Ils pourraient être complétés par un nouveau test impliquant le seul écoulement vertical de débris denses à l'intérieur d'une structure tubulaire (au sein d'une section chauffée pour éviter les perturbations liées aux transferts de chaleur et de masse) visant à valider la dynamique frictionnelle et collisionnelle de rhéologie granulaire. Des calculs préliminaires de SIMMER-V_vpd peuvent aider à dimensionner la section expérimentale. Concernant les tests intégraux, il existe d'autres programmes expérimentaux adaptés pour examiner la dynamique des débris aux côtés d'autres phénomènes concomitants au réacteur. Par exemple, les essais hors pile EAGLE 1 pour lequel des bilans de masse plus précis sont disponibles, ou les futurs essais en pile EAGLE 2/3 et SAIGA-1 dédiés à l'étude des phénomènes de décharge. Cependant, de manière similaire à EAGLE 1 étudié dans ce travail, ils considèrent la décharge à l'échelle de quelques aiguilles de combustible. Pour la validation intégrale de l'effet des modèles de dynamique des particules nouvellement implémentés, nous sommes plus favorables au test en pile TR (Corium Relocation in Discharge Tubes) à grande échelle prévu sur la plate-forme PLINIUS2. C'est parce qu'il utilise des matériaux prototypiques et que la géométrie du test est plus représentative de la conception du tube de transfert : la longueur et la section transversale du canal de décharge seront proches de l'échelle 1. La mise en œuvre d'une instrumentation dédiée pour suivre la composition (distribution de taille et de forme) du combustible dégradé, les profils radiaux de vitesse et de concentration volumique, et les caractéristiques de relocalisation (débit massique, apparition/disparition des blocages) contribueraient à la validation des modèles de SIMMER-V_vpd. D'un autre point de vue, SIMMER-V_vpd peut être utilisé pour des calculs de dimensionnement pré-test et d'analyse post-test. Dans la phase de pré-conception actuelle, les résultats de simulation peuvent aider à approuver ou reconsidérer des configurations précédemment établies. Toutes ces expériences (test à effets séparés ou intégraux) peuvent être exploitées non seulement à des fins de validation mais aussi pour affiner les propriétés des débris et mieux ajuster les paramètres empiriques du modèle.

Le troisième niveau de perspectives concerne l'application à l'échelle réacteur. Dans nos simulations de réacteurs, les nouveaux modèles de dynamique des particules ont été appliqués uniquement aux régions du tube de transfert. Cependant, il est évident que la décharge du combustible à l'intérieur des tubes guide de barres de contrôle (CRGT) a également un effet de réactivité significatif. Dans le but de mieux évaluer l'effet de la dispersion des débris solides depuis le centre du cœur, nous proposons l'application des nouveaux modèles pour les régions du cœur occupées par les CRGT. Cela peut être fait par de simples modifications du fichier d'entrée utilisateur, les modèles sont facilement applicables. Une autre amélioration de la simulation du réacteur est de simuler la séquence accidentelle non protégée ULOF en coordonnées cartésiennes tridimensionnelles dans SIMMER-V, configuration pour laquelle des travaux sont déjà en cours (la modélisation de la dynamique des particules est en l'état actuel applicable à la sous-géométrie 1D des tubes). Ce calcul peut résoudre plusieurs des limitations géométriques des approches pseudo-3D, en particulier le fait que les tubes de transfert au même emplacement radial peuvent être traités séparément. En éliminant l'effet de cohérence résultant de la cylindrisation des couronnes d'assemblages combustibles, les résultats préliminaires montrent des enthalpies de combustible plus faibles et par conséquent une fraction plus élevée de débris solides. Par conséquent, cette configuration 3D soulignerait encore plus l'impact d'un nouveau traitement dynamique des particules par rapport aux exécutions pseudo-3D. De plus, elles sont étendues aux régions CRGT de sorte qu'un nouveau périmètre d'analyse peut être ouvert. Malheureusement, ce calcul est extrêmement long (en raison du grand nombre de mailles), nous n'avons donc pas eu l'occasion de présenter les résultats en cours de calcul dans ce travail.

Par ailleurs, il est prévu d'examiner l'évolution d'autres séquences accidentelles (ULOF, USAF), et d'étudier d'autres configurations ou conceptions (changement d'emplacement, de nombre ou de géométrie des tubes) si cela est jugé nécessaire par le projet ASTRID.

Introduction

In nuclear safety studies, the domain of severe accidents is addressed with a high importance. During a severe accident scenario of a nuclear power plant, the core may exhibit a strongly destructed configuration. Fuel pellets, cladding and internal structures may break apart, melt or evaporate under very high temperature and forceful mechanical load. Solidification, refreezing and condensation of these materials can take place in-homogeneously in the core according to the local temperature evolution. As a global result, a complex multi-phase multi-component mixture can develop inside the core. The spatial redistribution of this mixture, in particular of the reactive fissile fuel, is a crucial concern of safety regarding further accident evolution and its consequences. By analyzing and predicting the progression of fuel relocation, one can identify which phenomena and design features can be involved in the control.

Since the appearance of nuclear power generation, there has been several nuclear accident reported with varying impact. Among the most severe ones, we mention the Three Mile Island (TMI-2 1979, USA), Chernobyl (1986, Ukraine), and the Fukushima accident (2011, Japan).

The TMI-2 event was attributed to the combined effect of inappropriate operator action, design deficiencies, and component failures that led to core-meltdown as a consequence of a loss of coolant transient. The accident involved one reactor of 800 MWe Generation II Pressurized Water Reactor (PWR). During TMI-2 scenario a large pool of solid debris and molten materials developed. The pool lower surface solidified when it reached the water-steam interface forming a bowl shaped thick crust all around. Due to the presence of such lower crust hindering coolant flow, the center of the debris bed pool was not coolable. It heated up and the pool grew towards the top of the core through the gradual melting of the fragments. Eventually, the crust periphery failed and caused 20 tons of molten materials to flow down to the lower plenum, see the illustration in Figure I.1 left graph. After several hours, reactor vessel was able to solidify and retain the molten materials without its failure. The TMI-2 accident provided many lessons: it has demonstrated the importance of defense in-depth and human factors, alongside with the previously unknown possibility of core meltdown (large fraction of the TMI-2 core was severely damaged and redistributed in the reactor pressure vessel [Jacquemain, 2015]).

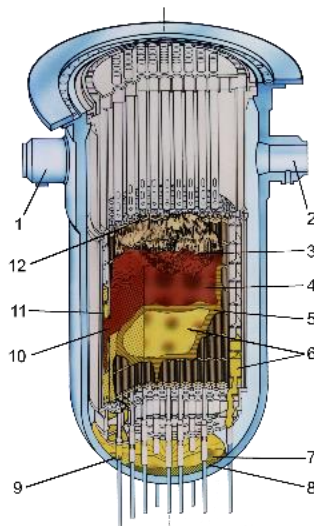


Figure I.1 Degraded core inventory in TMI-2 (1,2 coolant inlets, 3 cavity, 4 loose core debris, 5 crust, 6 previously molten material, 7 lower plenum debris, 8 possible region depleted in uranium, 9 in-core instrument guide, 10 hole in baffle plate, 11 coating of previously-molten material on bypass region interior surfaces, 12, upper grid damage reactor) [“Three Mile Island accident,” 2021]

The Chernobyl reactor was a Generation II type graphite-moderated, water-cooled channel-type boiling water reactor (RBMK designed by the Soviet Union) but with intrinsically different safety features from the commercial water-moderated cores. Therefore, the accident did not affect significantly the regulation of the western-type light water reactors. Although personnel and organizational errors contributed largely to the development of the Chernobyl disaster, the primary cause was attributed to the fundamental shortcomings of the RBMK reactor design. In the specific course of events, the active safety measures (recognized to be inadequate by current nuclear safety culture) were insufficient to prevent large reactivity insertion by coolant voiding. Consequently, several power excursions took place and led to clad melting, fuel destruction and complete core degradation. The uncontrolled course of violent explosions destroyed the reactor building and allowed the spreading of large quantity of radioactive materials into the environment (even if the reactor had a containment building, there exist no design in the world that could sustain such magnitude of mechanical load). The Chernobyl disaster is the stringing example of how serious consequences can emerge from the inherently large positive reactivity feedbacks accompanied by inappropriate core design parameters and various operator errors. It also highlights the importance of accident prevention and mitigation [Malko, 2016].

The Generation II type Boiling Water Reactors at Fukushima Daiichi nuclear power plant experienced a complete loss of power (offsite, onsite emergency diesel, and station battery) due to an earthquake and the following tsunami bigger than the design basis. By the loss of core and spent fuel pool cooling function, the Fukushima Daiichi accident involved three reactors and four spent fuel pools. In reactor 1, 2 and 3 the insufficient cooling eventually initiated meltdowns. It is assumed that molten corium penetrated through pressure vessel and is currently resting on the bottom of the primary containment vessel. The exact location and distribution of molten nuclear fuel within the containment buildings is unknown [Internationale Atomenergie-Organisation, 2015]. The Fukushima accident led to the recognition of gaps in nuclear safety and initiated a global review of nuclear facilities currently in operation or under construction. Extensive international level research activities have been launched with the objective of improving the flexibility and diversity in response to extreme conditions, the robustness of safety functions, the organizational behavior and the long-term accident management. New requirements for specific plant improvements has been established by national regulatory authorities [OECD/NEA, 2016].

The findings from past nuclear accidents and lessons learned provide guidelines for developing scenarios for possible severe accident evolutions. In general, for Generation II & III reactors, the impact of degraded fuel propagation is directly related to hydrogen production and direct containment heating which both challenge radioactivity confinement. In Generation IV reactors, the relocation of molten/degraded fuel is strongly associated to the risk of reactivity initiated large mechanical energy releases that challenges the confinement of radioactive matter. In the frame of France-Japan collaboration (2014-2019 and 2020-2024), a large Research and Development (R&D) program is launched at the French Commission for Atomic Energy and Alternative Energy (CEA) and at Japan Atomic Energy Agency (JAEA). It includes experimental programs, accident scenario definition and model development dedicated to Generation IV Sodium-cooled Fast Reactors (SFR). In the frame of model development, specific work is devoted to the understanding of degraded fuel relocation during severe accidents. The incentive for this thesis work has been conceived within the aforementioned research direction.

Chapter I.

CONTEXT

This thesis is defined in the context of a large R&D program launched at CEA in the frame of the ASTRID project. In the first section, the goal and the current status of the ASTRID project is described. The ASTRID reactor being the technological demonstrator of Generation IV type Sodium-cooled Fast Reactors, this part contains the enhanced safety requirements for Generation IV nuclear systems. Related to SFR safety studies, the French methodology to characterize severe core disruptive accidents is explained in the second section of this chapter. To comply with the higher safety standards, the third section exposes innovative strategies to mitigate the consequences of such severe accidents. The last section highlights the motivations behind the thesis topic and states the objectives for the outcome of this work.

I.1	The ASTRID project.....	2
I.1.1	The most developed Generation IV reactor design: SFR	2
I.1.2	The ASTRID technological demonstrator.....	5
I.1.2.1	The CFV core concept	5
I.2	Severe accidents in SFRs	7
I.2.1	Safety study approach	8
I.2.1.1	Primary phase	8
I.2.1.2	Transition and secondary phase	9
I.3	Mitigation by design	10
I.3.1.1	Japan FAIDUS concept.....	11
I.3.1.2	Mitigation transfer tubes	12
I.4	Thesis objectives	12

I.1 The ASTRID project

I.1 THE ASTRID PROJECT

This thesis work is defined in the frame of the ASTRID (Advanced Sodium Technological Reactor for Industrial Demonstration) project. The genesis of the project was created in the course of the French Act of 28 June 2006 on sustainable management of radioactive materials and wastes, in which the French Government entrusted CEA to conduct design studies on an SFR technological demonstrator, named ASTRID. The objective of the ASTRID program is to develop a prototype SFR to demonstrate on an industrial scale the relevance and performance of innovations dedicated to comply with requirements for 4th generation reactors. The project itself was launched in late 2009 in collaboration between CEA and its industrial partners (French: EDF, AREVA etc. and international: JAEA, GE, etc.). The roadmap showing the originally scheduled completion of milestones is shown in Figure I.1. This schedule was initially set for a 600 MWe ASTRID reactor. However, an intermediate project review in 2017 reconsidered the project objectives and led to a new ASTRID design with a reduced power of 150 MWe. The studies were then ongoing in parallel for both concepts.

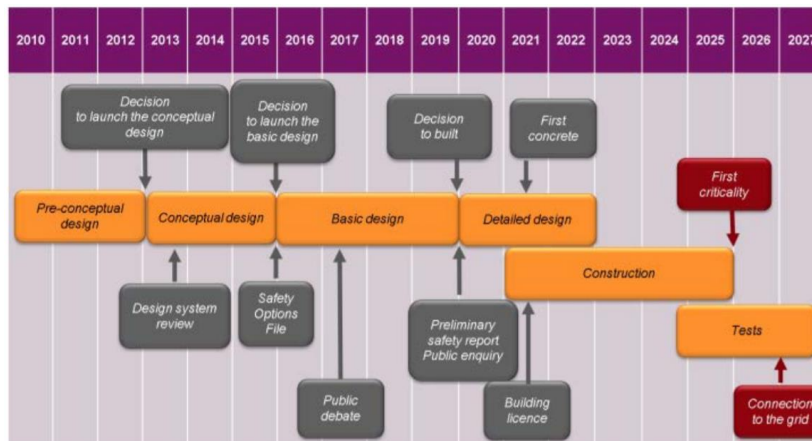


Figure I.1 ASTRID Project driver schedule by [Rouault et al., 2015]

From 2010 to 2019, the pre-conceptual, conceptual and the basic design phases have been completed. However, in 2018, CEA with its industrial partners and the French State concluded that the perspective of the industrial deployment of fast reactors is more distant. Completing the closure of nuclear fuel cycle is maintained as a long-term sustainability objective, and consequently the construction of the ASTRID reactor has been postponed to the second half of the 21st century. In the same time, the R&D work on the sodium technology is maintained in order to preserve competences, progress on technological barriers and further develop know-how [Rodriguez et al., 2020].

I.1.1 The most developed Generation IV reactor design: SFR

The ASTRID project is part of the large international initiative on promoting nuclear systems of the future as established by the Generation IV International Forum (GIF) in 2001. The GIF launched a collaborative international research and development frame aiming to study the feasibility and performance of a new generation of nuclear reactors, and to make them available for commercial deployment by 2030.

The main objectives in the development of these reactors are:

- sustainability (e.g. more efficient use of uranium),
- economic competitiveness with other energy sources,
- reduced nuclear waste production,
- improved safety,

- proliferation resistance and physical protection.

The GIF then identified six different reactor concepts over around the 120 potentially able to fulfil these goals: Gas-cooled Fast Reactor (GFR), Lead-cooled Fast Reactor (LFR), Sodium-cooled Fast Reactor (SFR), Very High Temperature Reactor (VHTR), Supercritical Water-cooled Reactor (SCWR) and Molten Salt Reactor (MSR) [A Technology Roadmap for Generation IV Nuclear Energy Systems, 2002], see Figure I.2.

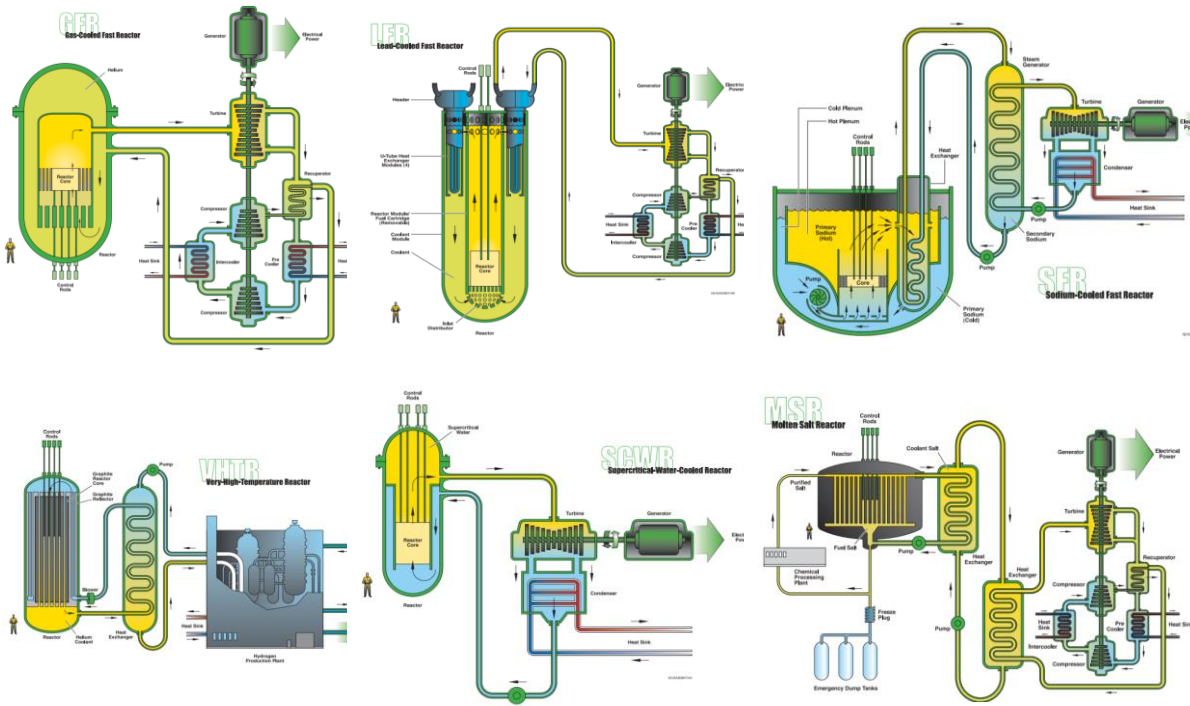


Figure I.2 GEN-IV reactor concepts selected by GIF [A Technology Roadmap for Generation IV Nuclear Energy Systems, 2002]

Among these technologies proposed by the GIF, SFRs are chosen as reference systems in many countries partially due to the most extensive industrial experience and operational feedback available for this technology, and partially because of its top-ranked sustainability features involving closed fuel cycle, the excellent potential for actinide management and good performance in terms of the other objectives.

Several past and present examples of industrial, experimental and demonstrator SFRs exist. SFRs built worldwide most notably in Russia (BOR-60, BN-600/800), India (PFBR), USA (EBR-I/II, FFTF and others), UK (DFR, PFR), Japan (JOYO, MONJU), China (CEFR), South Korea (PGSFR) and France [CEA Nuclear Energy Division, 2012]. In France, three sodium monitoring and experimental programs have been carried out in Rapsodie, Phenix and Superphenix reactors over more than forty years. Even though these reactors are all shutdown and dismantled, CEA acquired an important experience and knowledge based on which France is currently heavily involved and plays a leading role in SFR R&D programs.

The exceptional sustainability aspects of SFRs are attributed mainly to the fast neutron spectrum operation (typical not only to SFRs but to all fast breeder reactors), which brings about three major advantages.

I.1 The ASTRID project

- Burn all types of uranium

In conventional Light Water Reactors such as PWRs utilizing thermal neutron spectrum, the natural uranium (containing only 0.7% fissile¹ ²³⁵U but 99.3% fertile² ²³⁸U isotope) has to be enriched in order to increase its fissile content. In fast neutron spectrum, it is possible to transform ²³⁸U into fissile ²³⁹Pu by capturing a fast neutron. It allows to use not only uranium ore in its natural state without enrichment but also depleted uranium resulting from enrichment processes for PWRs as well as reprocessed uranium extracted from PWR spent fuel. This isotope transformation is known as breeding (i.e. the reactor produces more fissile material than it consumes) and it brings about an almost inexhaustible fuel supply for SFRs. The capability of recycling used fuel of currently operational PWRs, SFRs provide the possibility to close the fuel cycle and resolve economic issues associated with uranium resources.

- Recycle plutonium multiple times

The decades-long operation of PWRs has led to the accumulation of large amounts of ²⁴⁰Pu and ²⁴²Pu isotopes that cannot be used anymore as fuel in thermal reactors (they make part of the long-term disposal of spent fuel). In fast neutron spectrum, these elements are fissile favoring multiple plutonium recycling. The more efficient employment of plutonium enhances non-proliferation and contributes to better waste management.

- Reduce the radiotoxicity and lifetime of ultimate waste

The third important advantage is related to the minor actinide burning/transmuting ability of SFRs. Minor actinides are heavy elements, mainly neptunium, americium and curium, produced during fuel irradiation in both PWRs and SFRs by the consecutive neutron capture in U and Pu. Even though their amount is quite small in comparison to other elements, they are responsible for the major part of long-term radiotoxicity and heat generation of spent nuclear fuel. Therefore, minor actinide transmutation (i.e. reducing their inventory by transforming them into other elements) in SFRs helps to lower the thermal load of waste packages in final spent fuel repositories as well as to achieve a given level of radiotoxicity in a shorter time.

Apart from the sustainably matters attributed to fast neutron spectrum, the real preference towards SFR system arise from the use of sodium as coolant. The use of sodium brings about several advantageous safety aspects of pool type³ SFRs. Sodium bears an excellent compatibility with structural materials and it has superior thermal hydraulic properties such as high heat capacity, good thermal conductivity and broad range of liquid state at atmospheric pressure. It allows unpressurized primary system (also true for other Generation IV systems for example LFRs or MSR) with high thermal inertia and large temperature margin from sodium boiling. All of which permit better accident management by longer intervention time and less violent phase transition problems in case of the loss of pumping power. The benefit of pool type architecture is that initiates early and efficient natural convection. Besides, it minimizes and simplifies reactor structures.

On the whole, SFR technology offers several intrinsic advantages, but raises also various problematic areas that still lack the knowledge to resolve. The most crucial aspect regarding the debated safety issue is related to the reactivity⁴ characteristic of the sodium-cooled core. While

¹ Fissile: nucleus that can undergo fission by the effect of a collision with a neutron of any energy (thermal or fast)

² Fertile: nucleus that is not itself fissionable by thermal neutrons, but it can be converted into fissile by absorbing neutrons

³ Two concepts are conceived for SFRs: loop or pool type. Small-size reactors are mainly loop-type whereas large-size reactors tend to be pool-type. In addition, the pool configuration is better mastered in France for power reactors.

⁴ Reactivity is the measure of the core's relative departure from a critical state in which the nuclear chain reaction can be sustained. Reactivity is positive when a reactor is supercritical, zero at criticality, and negative when the reactor is subcritical.

Doppler effect⁵, fuel expansion and dispersal provide negative feedback, the strong positive contribution of sodium voiding still challenges the effective negative product. In addition, fast solid-fuel reactor cores are not in their most reactive geometrical configuration meaning that fuel compaction provokes reactivity insertion. Such hazardous features have to be tackled in order to establish a safety assessment that would allow the commercialization of the SFR design.

I.1.2 The ASTRID technological demonstrator

The technological demonstrator developed in the frame of the ASTRID project is a pool type SFR with 1500 MW_{th} thermal (and approximately 600 MWe electrical) power. The reactor operating principle is explained through Figure I.3.

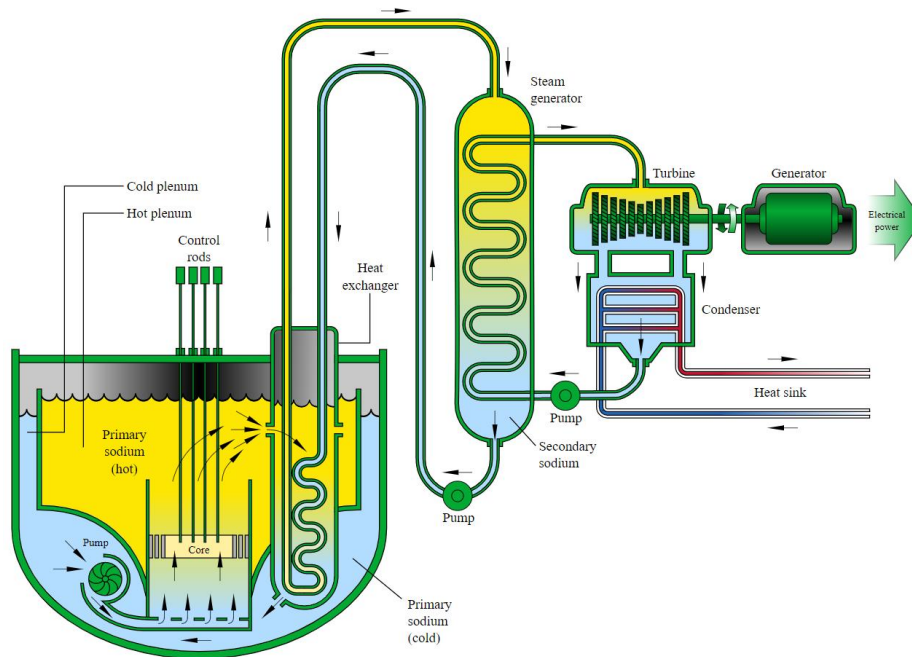


Figure I.3 Operating principle of pool type SFRs [A Technology Roadmap for Generation IV Nuclear Energy Systems, 2002]

The nuclear heat generated by the fuel subassemblies in the core heats up the sodium coolant passing in upward direction through the core. The hot sodium enters into the primary heat exchanger and by transferring its heat to the secondary sodium circuit, it leaves with a lower temperature (~150 K less). The primary pump directs this colder sodium back to the core. The secondary or intermediate sodium circuit is necessary to avoid the reaction between radioactive primary sodium and water/steam of the power conversion system. Such reactor involves radiological hazard combined with chemical risk in case of a potential heat exchanger tube rupture. In addition, without the intermediate circuit, any leakage in between the primary and the power conversion system (the latter being highly pressured) would cause massive water inflow that would generate severe reactivity accident. The secondary sodium exchanges its heat with the water of the power conversion system inside the steam generator. After this, the process is a standard Rankine cycle for power generation.

I.1.2.1 The CFV core concept

The reference core configuration for the ASTRID reactor design considered in CEA studies between 2010-2018 is called CFV (Coeur Faible Vidange). The CFV is the French acronym for a core with low void worth effect (net zero or small positive reactivity effect in case of sodium drainage). The

⁵ The Doppler effect expresses the reactivity variation due to the impact of a change in the fuel temperature on the reaction cross-sections.

I.1 The ASTRID project

core is comprised of an axially heterogeneous arrangement of fissile and fertile zones, illustrated in Figure I.4.

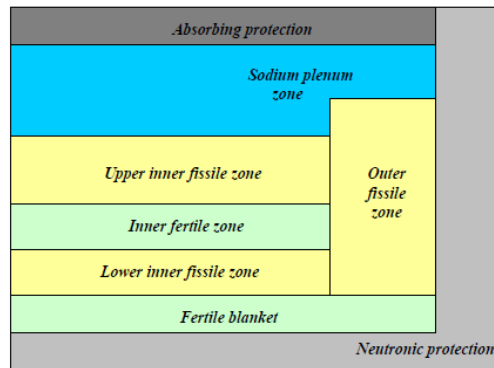


Figure I.4 Schematic view of the CFV core concept (radial cut) by [Varaine et al., 2012]

To explain the logic behind this arrangement, one has to understand the influence of sodium voidage on reactivity (i.e. sodium void worth). The void reactivity effect is the combination of three phenomena: the positive contributions of neutron spectrum hardening (1) and reduced neutron capture (2), and the negative contribution of increased neutron leakage (3) acting as a stabilizing feedback. In this principle, the CFV core aims to augment the negative contribution from neutron leakage, by adapting geometrical design measures. The upper sodium plenum enhances neutron leakage in case of sodium boiling at the top of the core, where the margin to boiling is minimum. The differential height between inner and outer core has the same function of further amplifying neutron leakage when sodium voiding occurs. The use of an internal fertile blanket shifts the highest neutron flux towards the upper surface for the core. It means that losing neutrons from this zone has a more pronounced reactivity reduction effect. Since sodium voiding around the upper core leads to enhanced neutron leakage due to the presence of upper plenum, the loss of high reactivity worth neutrons in the proximity has an additional stabilization effect. This arrangement is found to be an optimum combination to exploit the best natural behavior during transients [Varaine et al., 2012]. The main reactor parameters are listed in Table I. 1.

Table I.1 Main characteristic values of the 1500 MWth ASTRID reactor

Nominal thermal power (MWth)	1500
Nominal electrical power (MWe)	600
Core inlet/outlet temperature (°C)	400/550
Core flow rate (kg/s)	7900
Inner fissile zone height (lower / upper) (cm)	25 / 35
Outer fissile zone height (cm)	90
Inner fertile zone height (cm)	20
Inner zone radius (cm)	133.5
Outer zone radius (cm)	162.6
Sub-assembly pitch (cm)	17.5
Number of fuel subassemblies inner/outer core	180 / 108
Fuel pin diameter	9.7 mm
Number of pins per subassembly	217
Fissile zones PuO ₂ enrichment (Inner / Outer) (%vol.)	22.95 / 19.95

The whole core is built-up of hexagonal subassemblies containing multiple fuel pins. The fuel pins are composed of an annular steel cladding holding the fuel in the form of annular pellets. The

reference fuel in the ASTRID core is mixed oxide (U, Pu)O₂ in the fissile and uranium oxide UO₂ in the fertile zone with cladding material 15-15 Ti work-hardened austenitic steel AIM1 [CEA Nuclear Energy Division, 2012]. The core configuration, the subassemblies and the fuel pins are shown in Figure I.5.

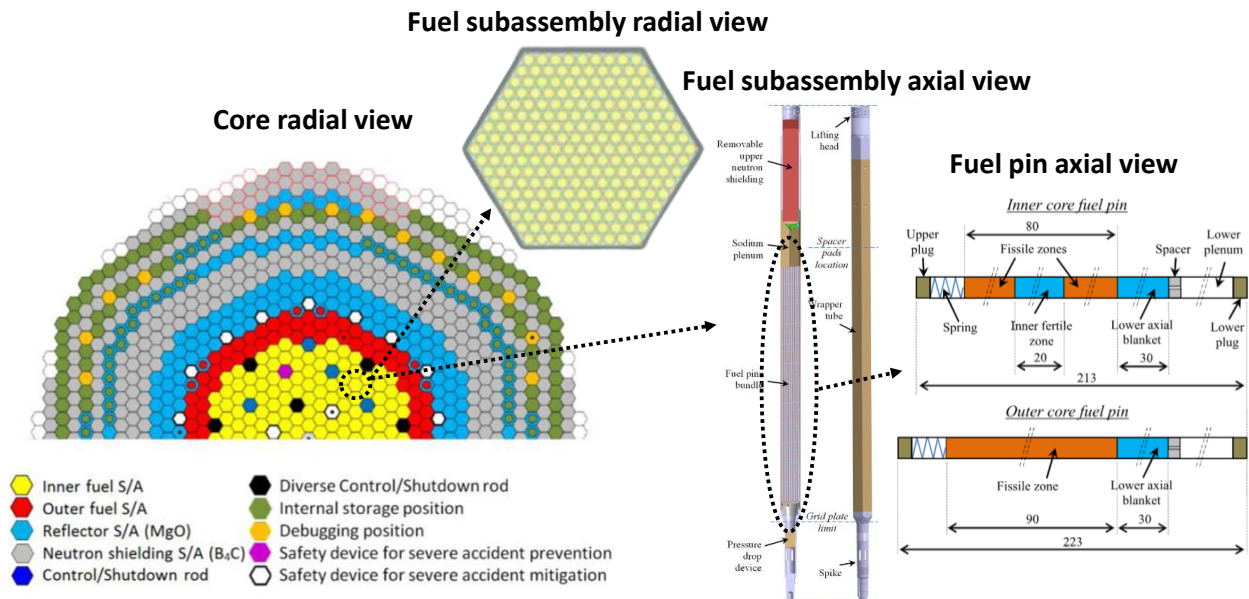


Figure I.5 ASTRID core arrangement and fuel subassembly view after [Beck et al., 2017]

In the design of the CFV core, special concern has been dedicated to severe accident prevention and mitigation measures (in Figure I.5 core radial view, one can see that some subassemblies are replaced by Complementary Safety Devices). It is necessary because severe core disruptive accidents (CDA) modify the core internal geometry by the relocation of molten/degraded materials providing the possibility for fuel compaction, which inserts positive reactivity in SFRs. In an event of reaching prompt criticality⁶, rapid heating and vaporization of the fuel and steel components take place. It produces high pressure that disassembles core materials and the corresponding severe mechanical energy release has the potential to damage reactor vessel and challenge containment integrity. Therefore, core disruptive accidents are treated as major issue in the safety evaluation of SFRs.

I.2 SEVERE ACCIDENTS IN SFRs

Severe core disruptive accidents are considered to be extremely low probability scenarios that can take place only by the simultaneous or subsequent failure of protection systems. Even through their occurrence is highly unlikely during the lifetime of a reactor (their frequency is less than 10⁻⁶ per reactor year [Tentner et al., 2010]), due to their potentially large harmful impact on humanity and environment, they have to be considered in the design process. By analyzing the unfolding of such events through safety studies, phenomena and design features are identified to be involved in the development of control strategies. Control strategies can be preventive: preventing the progression of transient sequences, or mitigative: mitigating the consequences of severe accidents. To ultimate purpose is to ensure that any transient terminates with a safe core state. Safe state implies that the integrity of containment is preserved, the radioactive release to the environment is kept within acceptable limits, and that long-term cooling and re-criticality control are assured [Kim et al., 1997].

⁶ Prompt criticality is the core condition when criticality is achieved with prompt neutrons alone and does not rely on delayed neutrons.

I.2.1 Safety study approach

Safety study approach of future generation of SFR in France is based on identification of different severe accident families according to [Bertrand et al., 2018]. Severe accident families are grouped into three categories according to the initial transient that can result in severe core degradation:

- reactivity insertion accident (unprotected transient overpower, UTOP),
- local default accidents due to scram failure spreading over the whole core (unprotected subassembly fault, USAF),
- core cooling failure accident (unprotected loss of flow, ULOF).

Reactivity insertion can occur from the inadvertent withdrawal of one or several control rods, from localized sodium drainage (gas bubble moving through the core) or from any fuel compacting movement. Local default accidents are associated to localized blockages that prevent subassembly sodium inflow. Core cooling failure accidents arise from the global decrease of sodium flow by the loss of electrical power supplying the primary pumps. These families of sequences refer to the initiating event combined always with reactor scram failure.

Each family can be decomposed into four accidental phases (primary, transition, secondary and post-accidental) which permits to better understand the transient evolution and to point out the driving phenomena, see Figure I.6.

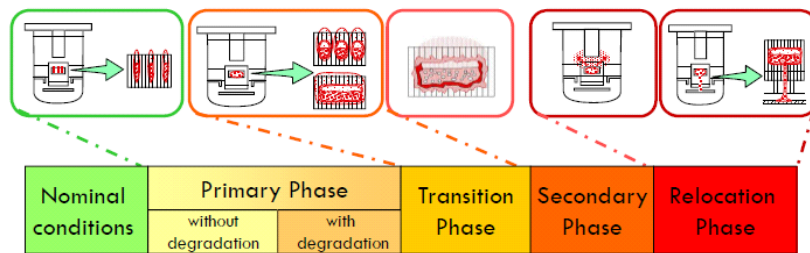


Figure I.6 Severe accident temporal evolution

In this principle, the different phases of the ULOF accident family are described in the followings. The ULOF accident is the scope of the PhD work. Generally, the accident evolution strongly depends on the core characteristics. The description applies for the reference CFV ASTRID core and follows the phenomenology of [Bertrand et al., 2018] supplemented by observations of [Lazaro et al., 2014] and [Tentner et al., 2010].

I.2.1.1 Primary phase

Unprotected loss of flow accident is initiated by the simultaneous coast-down of all primary pumps. It causes the primary sodium flow at the core entrance to drop according to the pump halving time (10 s in design specification). Without scram failure, there would be a sufficient time delay due to pump inertia to activate the shutdown systems before sodium boiling and to accomplish safe reactor condition. However, for a core disruptive accident to occur, safety studies in SFRs are carried out with the assumption on the instantaneous malfunction of all safety system.

In the absence of forced convection provided by the primary pumps, sodium mass flow rate decreases and natural circulation develops. The characteristic of the buoyancy driven convection is strongly related to the specific primary system design. The neutron chain reaction is still ongoing such that the coolant mass flow rate is insufficient to extract nominal nuclear heat generation. The mismatch between generated and extracted heat induces fuel, structure and sodium heat-up. From this point on, the energetic progression of events is governed by the competition between positive and negative reactivity effects, which result in phase change of one or more of the core materials and irreversible changes in the core geometry. The fuel temperature increase activates immediately

negative reactivity feedbacks such as the Doppler and the fuel expansion effect. Structure temperature increase induces other stabilizing effects most importantly control rods thermal expansion and axial penetration into the core. The effect of sodium density reduction (by temperature increase) is twofold. From one hand, it lowers the number of scattering neutron collisions and thus shifts towards higher neutron flux and increased core reactivity, and from the other hand it allows more neutrons to escape from the core and thus decreases reactivity. Altogether, the net reactivity and the power are expected to slightly decrease in the first instants of ULOF transient.

However, this power decrease is insufficient to stop sodium heat-up such that at some point after ULOF initiation, sodium reaches boiling temperature (~1200 K at atm. pressure). The onset of sodium voiding takes place around the upper region of the hottest fuel assemblies (smallest margin from boiling also in normal operation). In a CFV core, sodium void worth has an inhomogeneous spatial distribution. Boiling gives a negative feedback at the periphery and at the upper regions thanks to the enhanced neutron leakage contribution (sodium plenum on the top core). On the other hand, the effect is positive in the major center part of the reactor due to the loss of neutron absorption in liquid sodium. In this principle, sodium boiling in proximity of the upper plenum and around the upper fissile zone brings about a net negative reactivity, which further reduces the power. As boiling front penetrates into the fissile region, it inserts positive reactivity; the power ceases to fall or starts to rise. It leads to boiling at the upper region of other subassemblies that makes the power to decline again. In parallel, some boiling fronts are diminished by sodium reflooding from the large reservoir of upper plenum. As a global result, power oscillations establish but overall, the power decreases gradually (typically to 30/40 % of the nominal power for ASTRID design).

When boiling propagates into the high power density region, boiling crisis occurs. The abrupt reduction of the heat transfer from the dry cladding surface to the biphasic sodium brings about rapid rise in local peak cladding temperature. Eventually, cladding melts down and starts to relocate axially around the pins. Clad relocation generally has a positive reactivity effect (disappearance of neutron moderation, increase in fast neutron flux). However, dedicated neutronic studies concluded that the favorable timing and redistribution pattern of steel components in CFV core design brings a small positive or even negative reactivity insertion [Bertrand et al., 2016]. Following clad melting, fuel pellets are expected to undergo degradation as well due to the loss of their physical confinement. Since it occurs at low power, fuel degradation is likely to manifest mainly in mechanical fragmentation. Fuel melting is expected to be less pronounced. In accordance with power/temperature profiles, the location of first degradations is expected to be inside the hottest subassemblies at the height of the upper fissile zone. Following, the local failures propagate axially and radially within individual subassemblies.

When cladding integrity is lost, liquid fuel and/or steel come in contact with liquid sodium. This encounter is referred as fuel-coolant interaction (FCI). The physical contact between very high temperature molten fuel or cladding and relatively cold liquid sodium induces rapid thermal-to-mechanical energy conversion. Depending on the mass of the phases, the temperature differences and their confinement, there could develop a highly energetic reaction with explosive pressure generation, which affects the passage from primary to transition phase.

Overall, the primary phase consists of pin degradation by fuel and/or clad melting, axial and radial propagation of molten materials within individual subassemblies. Studies for the CFV design show that the natural behavior of the core most likely prevents large power depositions and significant mechanical energy releases during the primary phase. The primary phase typically lasts from around 60 s to more than 100 s depending on core design.

1.2.1.2 Transition and secondary phase

The transition phase begins with the loss of hexagonal tube integrity by melting, mechanical breach or by the combined effect of both. It allows degraded materials within individual subassemblies to

I.3 Mitigation by design

merge. In a slowly evolving accidental scenario, the transition phase evolves progressively according to power over flow rate ratio of each subassembly (P/Q specific to subassemblies), meaning that degradations and hexcan openings happen in-homogeneously across the core. When the core geometry is lost, the materials are free to relocate radially. Since SFRs are not in their most reactive configuration, the relocation brings about fuel compaction triggering large positive reactivity insertion. Reaching prompt criticality⁷, power excursion occurs. The magnitude of the power excursion strongly depends on the current neutronics state of the core. It can be very powerful such that fuel and steel components melt excessively or even vaporize, sub-assembly wall lose integrity in a large scale arriving almost immediately into secondary phase. If the power burst is less energetic, fuel and clad melting takes place in central assemblies without the immediate failure of hexagonal tubes. In this case, the melting process creates an internal cavity containing a pressurized mixture of molten fuel and fission gases. The cavity expands both radially and axially. The radial expansion and the high internal pressure induce eventually cladding failure. When it occurs, the molten fuel in the cavity is accelerated towards the location of the failure. As clad opening tends to be around the high neutron flux region, the reactive molten fuel moves toward higher reactivity region inducing an additional reactivity insertion. The violent ejection and dispersal of molten fuel into the coolant channel initiate a large dominant negative feedback, which terminates the power burst. As a result, large part of the fuel and clad are melted/fragmented. Globally, the transition phase is characterized by continued degradation processes, the consecutive losses of hexagonal tubes integrity, and the transition into extensive radial material motion.

The secondary phase starts with the accumulation of large quantity of core materials into one big or several smaller molten/degraded pools. The degraded mixture stays confined inside the core in form of these pools because the axial downward relocation is limited by the presence of intact fertile blanket below, axial upward motion is restricted by the upper neutron protection, while radial expansion is constrained either by intact core periphery subassemblies or by the side neutron protection. The sustained state of compact pool configuration involves the likelihood of further re-criticalities without the possibility of external cooling and control. A postulated re-criticality at this condition would end with excessive dispersal of core materials towards the primary vessel on which it would impose an enormous load what the safety barrier cannot be ensured to withstand. In order to avoid such course of transient scenario, severe accident management involving prevention and mitigation strategies are developed already in the reactor design phase.

I.3 MITIGATION BY DESIGN

Within the scope of defense in depth fundamental safety principle, the purpose of severe accident management is to ensure the safe termination of a postulated core degradation event without any significant radiological release to the environment. Safe termination includes the capability of long-term cooling and excludes the occurrence of re-criticalities. It is achieved through maintaining the integrity of the main safety barriers such as primary reactor and safety vessel by reducing the possibility and/or consequence of energetic power excursions. To comply with this purpose, prevention and mitigation strategies are developed.

Preventive measures bringing the possibility to prevent further accident progression encompass mostly the control over the reactivity feedbacks in the early stage of the accident. As it was discussed in paragraph I.1.2.1, the CFV core concept optimizes the behavior of reactivity feedbacks by geometrical design measures such that the core is inherently resistant to large positive variations. Another prevention strategy consists of implementing hydraulic and/or magnetic prevention rods that

⁷ The reactor state when the chain reaction is self-sustained only by prompt fission neutrons without relying on delayed neutrons.

drop into the core when primary flow rate decreases and/or sodium outlet temperature increases respectively to a design threshold [Marie et al., 2021].

Mitigation refers to all measures and actions that limit the consequences of a complete core meltdown. The mitigation of accident consequences for Generation IV reactors is envisaged by intrinsic design approach. The concept is to reduce the amount of fissile/fertile fuel in the reactive core region where the formation of large reactive pools are the most likely in order to limit the likelihood and the amplitude of further power excursions. It is achieved by the controlled fuel evacuation at the early stage of the accident. The evacuation circumvents the formation of core-wide molten pools and core compaction that could lead to prompt criticality and large mechanical energy release. Up to now, there are two proposals conceived for the physical implementation of the controlled discharge concept: the French and Japanese approach. The discharge process in both cases is inherently passive and considered at a few pin scale or at the subassembly level after the formation of assembly internal pool.

1.3.1.1 Japan FAIDUS concept

The Japanese approach developed by JAEA is referred as the FAIDUS concept (FUEl subassembly with Inner DUCT Structure). It is a modified fuel assembly, in which an internal sodium channel replaces some fuel pins. The original FAIDUS contains the duct in the center of the subassembly while, in a modified upgraded version, the duct is placed adjacent to the hexagonal wall. The duct wall is fabricated thinner than the hexagonal tube wall in order to facilitate its opening by either melting or mechanical failure. When the duct wall fails, the available path for the molten material to escape is mainly upwards due to the absence of upper plug inside the duct and considering that downward relocation is limited by the lower core structures. The upward ejection is illustrated in Figure I.7 [Tobita et al., 2008].

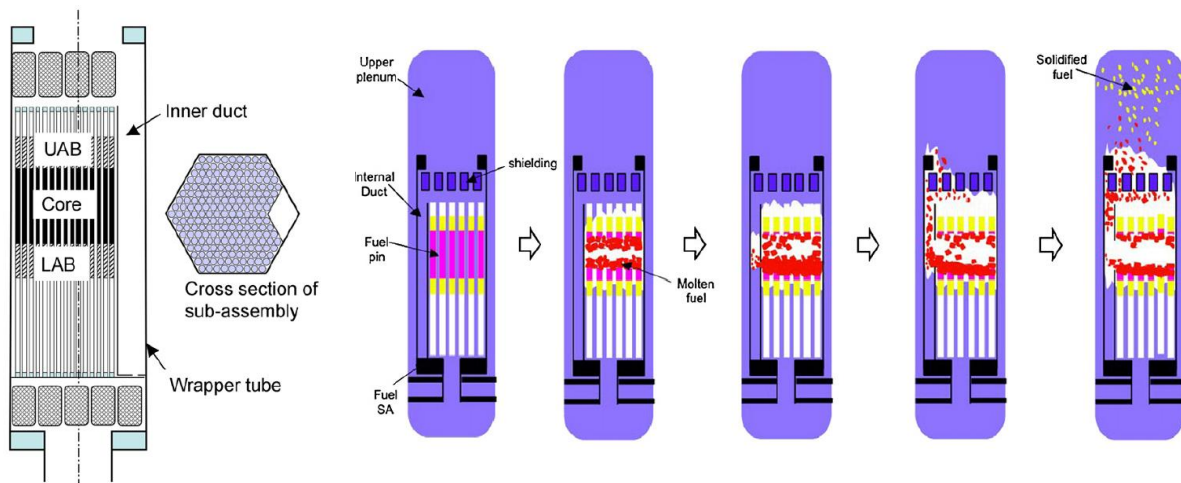


Figure I.7 Conceptual figure and the upward ejection by the modified-FAIDUS concept by [Tobita et al., 2008]

This concept is based on the principle that after a prior power excursion, which melted high fraction of fuel, the liquid fuel is evacuated quickly from the fuel assembly zone upwards via the FAIDUS duct. The driving force for upward discharge is the pressure in the disrupted subassembly due to fission gas releases, sodium vapor partial pressure and fuel-coolant interaction. The early molten fuel discharge from the core zone region is anticipated to guarantee the mitigation of energetic primary phase.

For the longer-term molten material relocation, the control rod guide tubes (CRGT) are taken into account in Japanese safety studies. In this case, small fraction of degraded core will be discharged,

I.4 Thesis objectives

after hexagonal tube opening, through control guide tubes to the lower part of the core. Core-catcher and in-vessel melt retention strategies are applied in addition.

I.3.1.2 Mitigation transfer tubes

The French concept developed by CEA consists of mitigation transfer tubes (Complementary Safety Device for Mitigation – Transfer Tube DCS-M-TT) and a core catcher. Compared to JAEA approach, the transfer tubes are envisaged to evacuate the molten material from the core region only after hexagonal tube opening in the transition or in the secondary phase. This mitigation approach postulates that the primary phase of the accident is less energetic such that the first power excursion following prompt-criticality does not lead to large energy deposition. Therefore, limiting the amount of fissile material in the core center region decreases the probability and amplitude of further power excursions that would impose large mechanical load on the safety barriers.

The transfer tubes have the shape of a regular fuel assembly (hexagonal tube) filled with quasi-stagnant liquid sodium during normal operation⁸. The tubes run through the whole core, cross the diagrid, penetrate the strong back and open to the lower plenum where the core catcher is located (Figure I.8). Their total length is approximately 10 m.

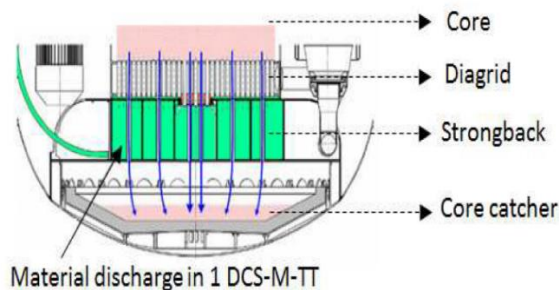


Figure I.8 Material relocation path via mitigation transfer tubes by [Bertrand et al., 2018]

Regarding the number of tubes, parametric safety studies at CEA concluded that maximum 3 tubes can be placed into the inner core due to their penalizing effect in terms of core performance. The number of tubes at the core periphery is more adaptable. It was found that 18 tubes spatially distributed around the core is the optimum to prevent radial molten material propagation towards the inner core and favor the kinetics of the relocation [Bertrand et al., 2018].

During severe accident evolution, the transfer tubes start to perform their function when the neighboring hexagonal walls of surrounding subassemblies lose integrity and allow the enclosed high temperature mixture to come in contact and eventually melt the wall of the transfer tubes. Following, the tubes promote material relocation downwards to the core catcher in the primary vessel. The role of the core catcher is to collect the arriving melt from the transfer tube, facilitate its spreading and provide long-term cooling.

The success of the mitigation depends on whether sufficient fraction of fissile material can be evacuated in sufficiently short time from the reactive core region. The time lag for the discharge is an important parameter due to its impact on reactivity besides ongoing neutronics. For the estimation of the discharge performance inside individual tubes, experimental programs and numerical simulation tools are available.

I.4 THESIS OBJECTIVES

As explained in the previous sections, a new 4th generation of nuclear reactors is under development. The most promising candidate to fulfil the requirement in terms of sustainability, safety, economic

⁸ There are still ongoing studies to define the exact design of transfer tubes.

competitiveness, reduced nuclear waste production and proliferation resistance is the SFR concept. In this context, the ASTRID project is launched at CEA. At present moment, the ASTRID project involves large R&D investments aiming to demonstrate the relevance and performance of innovative technological breakthroughs on an industrial scale. One of these breakthroughs is an innovative severe accident mitigation strategy developed principally for the ASTRID reactor CFV core design. The mitigation is achieved by implementing special design mitigation transfer tubes into the core and an in-vessel core catcher. The transfer tubes are envisaged to evacuate the mixture of reactive molten materials from the core region and thus decrease the probability and amplitude of further energetic power excursions.

For the pre-conceptual phase of French Generation IV SFR program, it is necessary to have a robust demonstration of the performance of the mitigation devices in order to reduce uncertainties influencing the safety assessment. The theoretical demonstration is currently based on best-estimate calculations with the mechanistic reference computer code SIMMER [Maschek et al., 2003]. Previous reactor calculations for the ASTRID pre-conceptual design on severe accident scenarios with mitigation strategy have demonstrated that the discharge of degraded core inventory via transfer tubes may be efficient [Bachrata et al., 2019]. On the other hand, SIMMER simulations highlighted uncertainties linked to the degraded core motion, in particular solid debris components inside the transfer tubes. The consideration of solid particles is of high importance in CFV concept where the low energetic natural behavior of the core prevents massive fuel melting and enhances the production of fuel debris from pellet fragmentation.

In this context, the thesis focuses on the relocation mechanism of the degraded core inventory via the mitigation transfer tubes in the frame of the SIMMER code. The objective is to improve SIMMER modelling of particle-size solid debris dynamics, in order to predict the scenario of molten/degraded core discharge with a higher confidence and to contribute therefore to the safety evaluation of future generation SFRs.

The thesis work constitutes the development and validation of a comprehensive modelling set for the dynamics of dense (high volume fraction) particulate flows in the SIMMER-V code. The structure of this document unfolds as follows. After the exposure in this chapter of the general context in which the thesis work has been defined, the second chapter focuses on the localized physical phenomena taking place during the discharge process via the transfer tubes and its current state-of-the-art numerical modelling by SIMMER code. In contrast to the state-of-the-art approach, the main outcomes of the bibliographic review around solid particle dynamics are presented. Concluding on this, the third chapter introduces the developed models (inspired by granular flow theory correlations) and their numerical implementation into the SIMMER-V code environment. The fourth chapter demonstrates the impact of such models compared to the original SIMMER-V particle approach through simplified test cases for which analytical or empirical solutions exist. In the fifth main part of this document, the performances of the new models are studied for an integral effect test together with a sensitivity study highlighting the influence of uncertain modelling parameters. The sixth chapter returns to the initial motivation of the thesis work. It contains the simulation of the whole reactor in case of the ULOF reference accidental scenario. Following the entire transient evolution, the mitigation performance applying the newly developed particle dynamics models is assessed. Lastly, the conclusions are summarized, and perspectives for future research on continuation of this work are outlined in the seventh chapter.

Chapter II.

PARTICULATE FLOW INSIDE THE TRANSFER TUBES

In this chapter, we highlight the phenomena related to the relocation of degraded core materials via the mitigation transfer tubes in ASTRID CFV core. Firstly, the complexity of the discharge phenomena itself is explained with a special focus on the origin and characteristic of particulate matter. Afterwards, the state-of-the-art numerical modelling of such reactor debris in the context of reactor safety studies is presented. Following, we establish the analogy between solid degraded core debris and granular matter. In this frame, different approaches and the main concepts in the physical modelling of granular media are reviewed from the literature. Lastly, we examine the state-of-the-art numerical approach in contrast to the relevant physical phenomena identified by the bibliographic study. It is carried out through a Phenomena Identification-Ranking Table (PIRT).

II.1	Discharge phenomena inside the transfer tubes	16
II.1.1	Origin and properties of particulate matter	17
II.2	State-of-the-art numerical modelling of reactor debris.....	19
II.3	Departure from the effective fluid approach.....	22
II.4	Reactor debris as granular media.....	24
II.4.1	Hydrodynamics forces.....	25
II.4.2	Particle interactions.....	26
II.4.2.1	Interpretation of particle pressure	28
II.4.3	Granular regimes and their physical modelling	28
II.4.3.1	Granular solid.....	30
II.4.3.2	Granular gas	31
II.4.3.3	Granular liquid.....	32
II.5	Phenomena identification-ranking table.....	33
II.5.1	PIRT evaluation context.....	33
II.5.2	Methodology.....	33

II.1 DISCHARGE PHENOMENA INSIDE THE TRANSFER TUBES

The initiating event for the discharge process is the thermal or mechanical failure of the transfer tube wall. It takes place after the degradation of one or several sub-assemblies surrounding the transfer tubes. Thermal failure occurs when the hexagonal walls of neighboring subassemblies lose integrity and allow the enclosed high temperature mixture to come in contact and eventually melt the surface of the transfer tubes [Bachrata et al., 2019]. Mechanical failure occurs under forceful mechanical load and/or large pressure differences between core and transfer tubes regions⁹. The sequence of events leading to the degraded core state before tube opening has been described in detail in section I.2. Concerning the discharge phenomena, the importance of prior degradation manifests in the surface area of the opening and the instant of wall failure, which influences the composition of entering materials. Regarding the opening surface, it is straightforward to conclude that the size and perimeter over which wall integrity is lost directly depend on the number of degraded subassemblies around the tube. Higher fraction of surrounding subassemblies is degraded, larger surface area of the tubes wall is expected to disintegrate. The instant of the failure plays a role in the consecutive discharge process through the material composition (fraction of molten to particulate) inside the degraded fuel sub-assemblies that will flow into the tube eventually. If late opening takes place (meaning larger energy deposition inside the fuel), it is more likely that the major part of the pins is in liquid state. In this scenario, the entering degraded core mixture features higher mobility, which facilitates downward motion. In case of early tube opening and/or at low energetic core regions, the incoming mixture is expected to contain a high fraction of solid fragments (the origin of such fragments will be discussed in paragraph II.1.1). The exact composition and state of entering materials strongly depends on the accident evolution and on the given tube location (it may be significantly different from one tube to another). In essence, it is a mixture of fission gases, vapor, molten steel, molten fuel and solid fragments of fuel and steel reactor components. The material composition has a significant influence on the discharge phenomena.

The transfer tubes start to perform their function when one of them open to accommodate and guide the entering degraded core mixture downwards to the core catcher. During the relocation process, several complex physical phenomena take place due to the large temperature and pressure differences.

Just after the tube opening, energetic fuel-coolant interaction is expected to occur [Berthoud, 2000]. FCI is characterized by a large thermal energy transfer within a short time that causes significant mechanical energy output, excessive fragmentation and solidification of high temperature liquid and drainage of sodium bulk via its vaporization close to the aperture location¹⁰. It follows that core materials relocate in gas bulk around the core height inside the tubes. In this region, the downward thrust arising from FCI provides the driving force for downward¹¹ motion. When the pressure gradient is diminished, the relocation becomes gravitational.

Considering ongoing nuclear heat generation of fissile components, typical temperature values in the core region (upper tube region) range below ~1730 K for steel and ~3100 K for fuel particles, between ~700-1300 K for liquid sodium (tube bulk before opening), between ~1200-3200 K for fission gases and vapor, above ~3100 K for liquid fuel and above ~1730 K for liquid steel. The large heat flux between these materials and structures leads to massive mass transfer. Mass transfer includes freezing/melting and vaporization/condensation of reactor components along the flow path, in-homogeneously according to the local temperature evolution. Arising from the interaction between the molten mixture and tube wall, solid fuel crust can build up on the wall surface. At lower tube

⁹ In severe accident calculations, transfer tube rupture is generally due to thermal failure, mechanical loading is not evaluated.

¹⁰ FCI is likely manifest at any location where high temperature liquids are exposed to each other.

¹¹ Upwards motion is also expected but since the tube is closed at the top according to current design, it is not favored.

locations, the large volume of bottom sodium reservoir in core catcher provides cold (370 K) sodium supply. Consequently, the discharge well below the core region continues in liquid sodium and at lower temperatures. A schematic sketch of the discharge process is shown in Figure II.1.

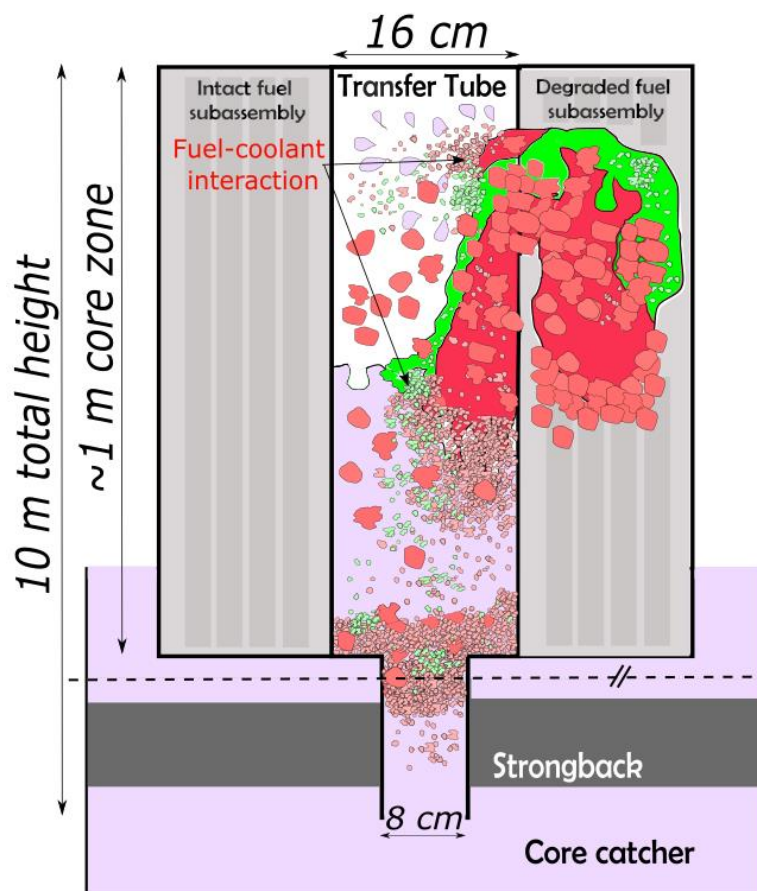


Figure II.1 Schematic view of the discharge phenomena

The view of Figure II.1 emphasizes that some fuel assemblies surrounding the transfer tubes are intact while the discharge from degraded ones is ongoing. It is because the degradation occurs according to the spatial distribution of P/Q ratio between subassemblies (see the explanation in paragraph I.2.1.2) meaning that not all fuel assemblies melt and fragment at the same moment. Overall, Figure II.1 intends to highlight the complexity of phenomena taking place during the material removal; one can assume large heterogeneities, high spatial gradients along the flow path and rapid changes in time.

II.1.1 Origin and properties of particulate matter

This paragraph describes the origin and properties of particulate reactor debris. Solid debris during the severe accident progression are produced in several ways [Singh, 2019]:

- from fragmentation/mechanical breakup of fuel pellets, cladding and other internal components with typical size range between 1- 4 mm,
- rapid freezing due to FCI producing smaller, around 0.05 - 0.1 mm particles,
- from (slow) re-solidification of previously liquidized components (size not predictable).

Figure II.2 illustrates some examples for debris: the typical size distribution of prototyping alumina (a), particles of uranium dioxide produced from FCI (b) and (c), and pin fragmentation characteristic (d).

II.1 Discharge phenomena inside the transfer tubes

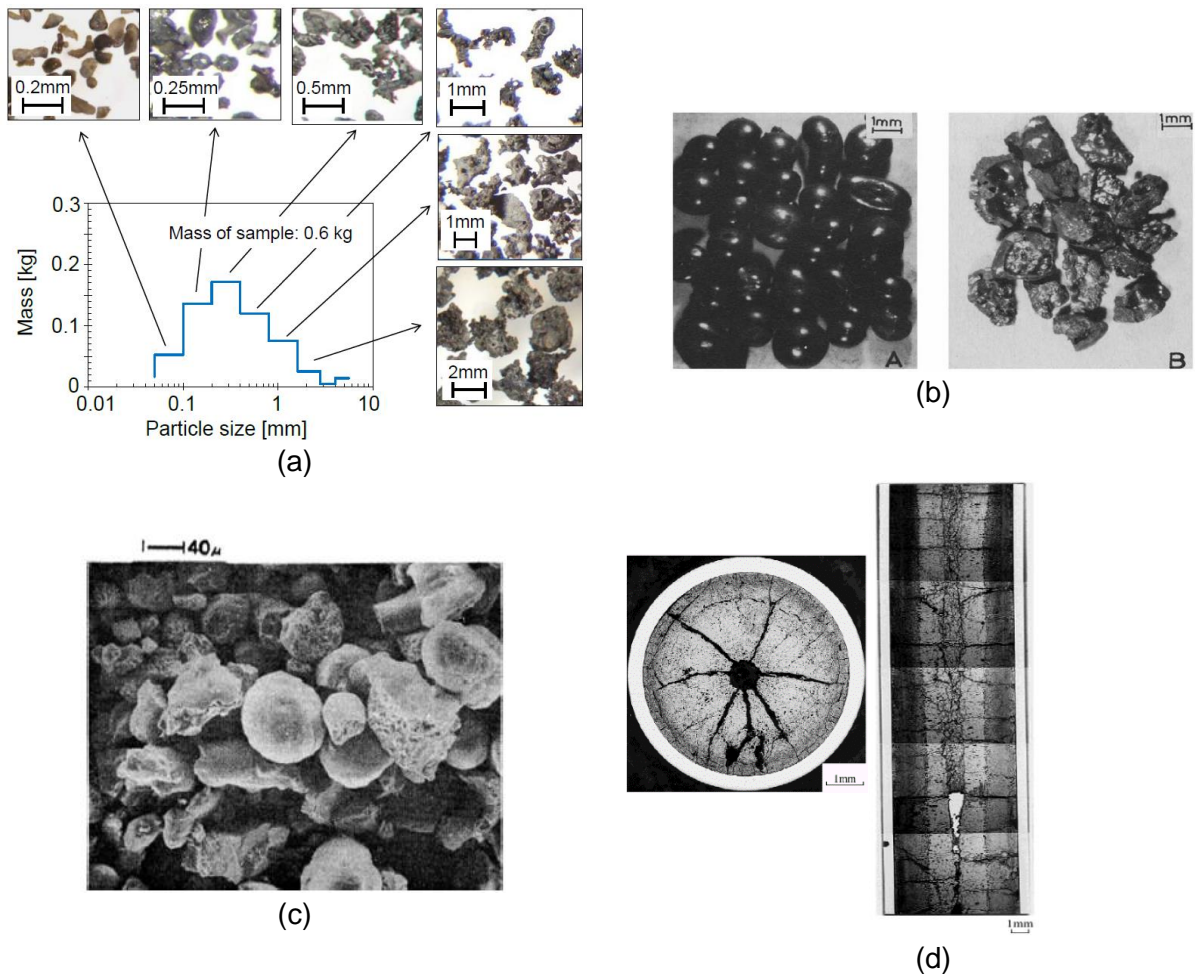


Figure II.2 (a) Molten Al_2O_3 porous debris formed in by the interaction with liquid sodium during FR-3 test by [Matsuba et al., 2016]. (b) Smooth (A) and fractured (B) UO_2 particles following sodium quench reproduced by [Singh, 2019] after [Schins and Gunnerson, 1986]. (c) Typical shapes of the small particles after molten UO_2 – sodium interaction by [Mizua, 1974]. (d) Axial (E5 test) and radial (E4 test) cut of the pin in CABRI-2 experiments by [Sato et al., 2004]

The presence of particulate debris is especially pronounced for the CFV core in which the low energetic natural behavior of the core prevents massive fuel melting and enhances the production of solid fuel debris. Furthermore, the fertile layer of the inner core may provide additional fertile fuel fragments. Therefore, the degraded core matter inside the transfer tube is expected to be abundant in solid particles, in particular fuel fragments [Bachrata et al., 2019].

Assigning dimensions and features for particles created from slow freezing/re-solidification mechanism is a difficult challenge since it can vary largely depending on the exact configuration. It is possible that the liquid freezes as global and does not transform into particles but becomes directly one solid body. Such transition is a longer-term issue and therefore out of the PhD scope.

The other above-mentioned particle sizes are average values derived from post-experimental observations. The distribution of particle size around the average is subject of research. A recent review of current state of knowledge can be found in [Singh et al., 2018]. In the same study, particles produced from the rapid solidification of the molten fuel (via FCI) are found to be rather smooth and very close to be spherical. We are aware of no investigation focusing on the mechanical fragmentation of fuel pellets. However, one can reasonably postulate that cylindrical fuel pellets of dimensions of 8 mm diameter and 10 mm height disintegrate into asymmetrical pieces of around 1 - 4 mm diameter on average. The surface roughness of pellet fragments presumably corresponds to their internal microscopic grain structure, which depends on burn-up history. Similarly, there is no

conclusive study on the fragmentation of annular steel cladding. Moreover, steel components are mainly found to be in form of liquid in reactor studies especially after the first criticality.

The density of reactor debris with negligible uncertainty is around 7000 and 11000 kg/m³ (depending on their temperature) corresponding to steel components and mixed (U-Pu) oxide fuel. The properties of reactor debris are summarized in Table II.1.

Table II.1 Particle-size reactor debris properties

Production mode	Size (mm)	Shape	Surface property	Density (kg/m³)
Fuel-coolant interaction	0.05 - 0.1	Spherical	Smooth	~7000 if steel ~11000 if fuel
Mechanical fragmentation	1 - 4	Asymmetrical	Rather rough	~7000 if steel ~11000 if fuel

Considering other properties of degraded reactor debris, such as elasticity, plasticity, conductivity, hardness etc., we recognize again the lack of available data. Future experimental programs, such as the PLINIUS-2 platform [Journeau et al., 2019], may provide more information on debris properties that can refine their numerical description and consequently improve the estimation of the mitigation strategy involving the controlled discharge of particle rich degraded reactor mixture via the mitigation transfer tubes. In the next paragraph, the state-of-the-art numerical approach for reactor debris is presented.

II.2 STATE-OF-THE-ART NUMERICAL MODELLING OF REACTOR DEBRIS

Reference severe accident studies and safety evaluation of future generation SFRs are carried out with the SIMMER (Sn Implicit Multiphase Multicomponent Eulerian Recriticality) [Maschek et al., 2003] code in France and Japan. Likewise, SIMMER is used as reference scientific tool in France for the theoretical evaluation of the mitigation scenario. SIMMER is an advanced safety analysis computer code series dedicated to investigate postulated core disruptive accidents in liquid-metal fast reactors. Currently available code versions include SIMMER-III two-dimensional, SIMMER-IV three-dimensional [Maschek et al., 2003] and the most recent SIMMER-V incorporating the possibility for two and three-dimensional treatment in Cartesian XYZ and cylindrical $RZ\theta$ coordinates [Serre et al., 2015]. At present, physical models in all code versions are identical. Therefore, the state-of-the-art particle-size debris treatment described in this paragraph is general to all SIMMER code series. In line with the scope of this work, we focus solely on dynamic aspects expressed by the balance of momentum. The overall SIMMER framework will be presented in more detail in section III.1 in the context of model development.

The numerical representation of degraded solid debris applies several simplifications, partially to save computational time but mostly because of the lack of available knowledge on real reactor debris. Solid particulate components in the SIMMER code comprise fuel particles, steel particles, control particles (B_4C) and fuel chunks. Fuel chunks are distinguished from fuel particles in order to account for their different origin: chunks are produced from fuel pin mechanical fragmentation while fuel particles are created from FCI, on analogy to Table II.1. In current SIMMER versions, there are specific dynamics models for chunks to take into account blockages due to one single large chunk and bridge formations due to a pair of chunks. These models do not affect the simulation of transfer tubes because of the large tube (0.16 m) to particle diameter (0.1 – 4 mm) ratio. Particle components are different in their densities (material specific) but each of them is assumed to be spherical and

II.2 State-of-the-art numerical modelling of reactor debris

has a user defined diameter that is uniform for all particles of the given type. Particle size can differ between different components if the user modifies default settings¹².

In SIMMER, being a multi-velocity field code, the approach for particle dynamics is a user choice as well. However, the code validation is realized with specific recommendations. The state-of-the-art description assumes that particles are suspended in their corresponding liquid phase. To confirm the applicability of this approach for severe accident transient analyses, the underlying hypothesis was validated via water sloshing experiments carried out in the frame of the first code validation phase [Maschek et al., 1992]. In these experiments, solid particles of similar density to water and with specific size remained intimately mixed in the flow. Creating the correspondence with the case of fuel particles in liquid fuel and steel particles in liquid steel, momentum balances in SIMMER are written as mixture equations for particles and their liquid phase (except for fuel chunks that are allocated into a different velocity field allowing it to move independently from the liquid fuel).

The mixture approach implies that particles always move at the same speed as their carrying liquid form and no transfer of momentum is computed within them. Momentum exchange is considered between the liquid-particle mixture and structure components, and between the liquid-particle and other momentum fields. Following the multi-component feature of the code, other momentum fields comprise liquid sodium, gases, chunk field and additional liquid-particle mixtures (more details about the momentum partition of SIMMER material components will be given in section II.3). Closure relations for momentum exchange functions describing interactions between continuous-discontinuous fluids (discontinuous fluid can be solid particle, dispersed liquid or vapor/gas bubble) $K_{qq'}$ ($kg/s/m^3$) and fluid-structure K_{qS} ($kg/s/m^3$) are written as Eq. II.1 and Eq. II.2 [Aoyagi et al., 2018]. For the momentum exchange function between two discontinuous phases, only a turbulent term B is considered proportional to a constant drag coefficient, the average density and their contact surface area [Yamano et al., 2003]. The full form of the momentum equation will be given in section III.1

$$K_{qq'} = f_1 A_{qq'} (\mu_{app}) + B_{qq'} |v_{q'} - v_q| \quad \text{Eq. II.1}$$

$$K_{qS} = f_2 A_{qS} + f_2 B_{qS} v_q \quad \text{Eq. II.2}$$

Where v is the momentum field velocity (m/s), and subscripts q , q' stand for different momentum fields and S for structure components. Coefficients A and B represent laminar and turbulent contributions respectively. The presence of solid bodies in such interactions is taken into account through modified viscosity terms, namely μ_{app} ($Pa \cdot s$) apparent viscosity and particle viscosity factors/multipliers f_1, f_2 ($-$). These terms account for the apparent increase of viscosity in liquid-solid suspension compared to the viscosity of the liquid alone. If no hydrodynamic force is applied on the dispersed solid particles (valid for neutrally buoyant bodies), the increase is attributed to the flow disturbance generated by the resistance of the non-deforming solid bodies to the straining component of the shearing flow. The rotational component creates no disturbance [Guazzelli and Pouliquen, 2018]. The concept of apparent viscosity for neutrally buoyant suspension has been widely recognized and used up to now since firstly introduced by Einstein [Einstein, 1906] and further developed by many researchers over the years. The terms expressing apparent increase of viscosity in SIMMER are formulated by Eq. II.3 following Ishii's work [Ishii and Hibiki, 2010] and by Eq. II.4, Eq. II.5 following the adaptation of Russel's equation [Russel, 1983].

¹² The default setting is between minimum $d_p = 0.1 \text{ mm}$ and maximum $d_p = 20 \text{ mm}$ diameters without cumbersome details on how the exact value is chosen.

$$\mu_{app} = \mu_f \left(1 - \frac{\alpha_{pi}}{\alpha_{DM}} \right)^{-2.5\alpha_{DM} \frac{\mu_{pi} + 0.4\mu_f}{\mu_{pi} + \mu_f}} \quad \text{Eq. II.3}$$

$$f_1 = \frac{\alpha_l}{\alpha_l + \alpha_{pk}} + \frac{5 \alpha_{MP} \alpha_{pk}}{\alpha_{MP}(\alpha_l + \alpha_{pk}) - \alpha_{pk}} \quad \text{Eq. II.4}$$

$$f_2 = 1 + \frac{5 \alpha_{MP} \alpha_p}{\alpha_{MP}(1 - \alpha_s) - \alpha_p} \quad \text{Eq. II.5}$$

Where α_{MP} is the maximum packing fraction for defining the particle viscosity (–) (0.62 by default), α_{DM} is the maximum packing fraction for defining the mixture viscosity (–) (1.0 by default) and μ is the dynamic viscosity [Liu et al., 2006]. The subscripts l, f, pi, pk, p refer to liquid, fluid (can be liquid or gas), particles interacting directly, particles not interacting directly and all particles irrespective of their velocity fields. Eq. II.3 applies fluid index because it is used in the exchange terms of both liquids and gases, while Eq. II.4 and Eq. II.5 are applied only in liquid suspensions. Even though μ_{app}, f_1, f_2 express the same physical effect, separate formulations are adopted due to the multi-component, multi-velocity field feature of the SIMMER code. To better understand the use of particle viscosity models, we demonstrate an example for the interactions between liquid fuel-fuel particles mixture, steel particles, chunks and structures in Table II.2.

Table II.2 Example for the use of particle viscosity models in current state-of-the-art approach when the continuous phase is liquid fuel - fuel particle mixture with suspended particles of steel and fuel chunks (indexes $p1, p2, p4$ refer to fuel particle, steel particle, chunks respectively) (red terms mark the effect of omitting chunks from particle viscosity factors)

	Part of the continuous phase Fuel particles $p1$ $K_{qq'}$	Dispersed phase Steel particles $p2$ $K_{qq'}$	Dispersed phase Chunks $p4$ $K_{qq'}$	Structures K_{qs}
Continuous phase Liquid fuel	Same velocity field	$\mu_{app}(\alpha_{p2})$ $f_1(\alpha_{p1}, \alpha_{p4})$	$\mu_{app}(\alpha_{p4})$ $f_1(\alpha_{p1}, \alpha_{p2})$	$f_2(\alpha_{p1}, \alpha_{p2}, \alpha_{p4})$
Part of the continuous phase Fuel particles $p1$		No friction model	No friction model	$f_2(\alpha_{p1}, \alpha_{p2}, \alpha_{p4})$
Dispersed phase Steel particles $p2$			No friction model	$f_2(\alpha_{p1}, \alpha_{p2}, \alpha_{p4})$
Dispersed phase Chunks $p4$				$f_2(\alpha_{p1}, \alpha_{p2}, \alpha_{p4})$

Recent code development efforts on blockage formations due to freezing by [Aoyagi et al., 2018] identified inconsistencies between physical phenomena and numerical modelling. These inconsistencies were related to the treatment of fuel chunks. It was found that including the effect of chunks in the particle volume fraction to simulate freezing behavior is inappropriate since the loss of fluidity is caused by the generation of solid nuclei, fuel particles solely. In addition, the friction resistance of large unmolten chunks on structure surfaces is as well independent of surrounding fluid

II.3 Departure from the effective fluid approach

viscosity and vice versa, friction resistance of solid-liquid mixture on structure is independent of the presence of chunks. Therefore, a new user option was created to omit chunk effects from particle viscosity factors. By activating this option, dependencies marked in red disappear in Table II.2.

In addition, multi-phase flow models in SIMMER code include a jamming model as well. The purpose is to simulate the blockage formation of molten materials when penetrating into a structure channel. The jamming model is added to the particle-structure momentum exchange function with a form of K_{PJ} (the summation assures that jamming is accounted for even in pool flows where the effect of structure is negligible). The mathematical formulation of the jamming model writes as Eq. II.7.

$$K_{PJ} = \max \left\{ 1 - \frac{\max(\alpha_p - \alpha_{PJmax}\beta_{PJ}, 0)}{\alpha_{PJmax}(1 - \beta_{PJ})}, 0.1 \right\}^{-C_{PJ}} - 1 \quad \text{Eq. II.6}$$

Where $\alpha_{PJmax} = 0.7$ is the maximum volume fraction for solid particles (–), $\beta_{PJ} = 0.95$ is the fraction of α_{PJmax} above which the particle jamming model is activated (–), and $C_{PJ} = 10$ is a model parameter (–) [Liu et al., 2006]. This form expresses an exponential increase when particle content approaches the maximum packing fraction. When the solid content is less than the minimum, $\alpha_{PJmax}\beta_{PJ}$ here, K_{PJ} is zero.

II.3 DEPARTURE FROM THE EFFECTIVE FLUID APPROACH

As it was stated previously, the velocity field allocation of different material components in SIMMER is a user option. The state-of-the-art particle dynamics models are developed in conjunction with one specific velocity field concept that considers one momentum equation with averaged quantities for solid particles and for their corresponding liquid phase. In this approach, the mixture is seen as an effective Newtonian fluid with apparent viscosity being the function of solid concentration only (leading a non-Newtonian mixture behavior [Journeau et al., 2006]). Consequently, rheological properties arising from the presence of particles depend solely on solid concentration. However, as we shall see in next II.4 section, approaching higher solid concentrations particle-particle interaction forces start to play a role and the effect of such interactions should be included into the equation of motion. This contribution can be accounted for by considering second order terms $O(\alpha_p^2)$ in the apparent viscosity formulation [Guazzelli and Pouliquen, 2018]. Another problematic issue related to the apparent viscosity approach is the fact that reactor debris particles are not neutrally buoyant considering in particular that they relocate in a multi-phase multi-component environment with varying densities. Since measuring apparent viscosity in settling systems (velocity of suspended particles is different from the carrying liquid) is problematic, the apparent viscosity correlations are derived from measurements in neutrally buoyant configurations. Applying such correlations for differential liquid-particle motion is therefore ambiguous. In addition, large particles do not increase liquid phase viscosity [Bartosik, 2020], as it was also pointed out in the SIMMER development for chunk components by [Aoyagi et al., 2018].

In recent years, a new interest appeared at CEA towards a different velocity field allocation that groups all particulate components of SIMMER (fuel particles, steel particles, control particles (B₄C) and fuel chunks) into an individual momentum field. This approach is encouraged for the analysis of the CFV French core design including also the evaluation of the mitigation strategy. In low energetic CFV core, transients are characterized by less reactivity insertion and lower power escalations, see paragraph I.2.1. This prevents massive fuel melting and enhances the production of solid fuel debris. When only minor fraction or even no corresponding liquid phase is present, solid particles form alone a momentum field. Another motivation is to improve the reliability of the SIMMER code in simulating particle movement after FCI. During an FCI (expected at the location of tube opening), solidified particles accelerate rapidly away from their liquid phase. Resolving such relative motion between

particles and liquid of the same material is only possible by defining a separate velocity field for particles in SIMMER. Figure II.3 demonstrates the state-of-the-art and the new momentum field allocation, and illustrates it through an example flow configuration for both. We note that, in case of slow dynamic process, both velocity field approaches are expected to converge in space and time to the same solution.

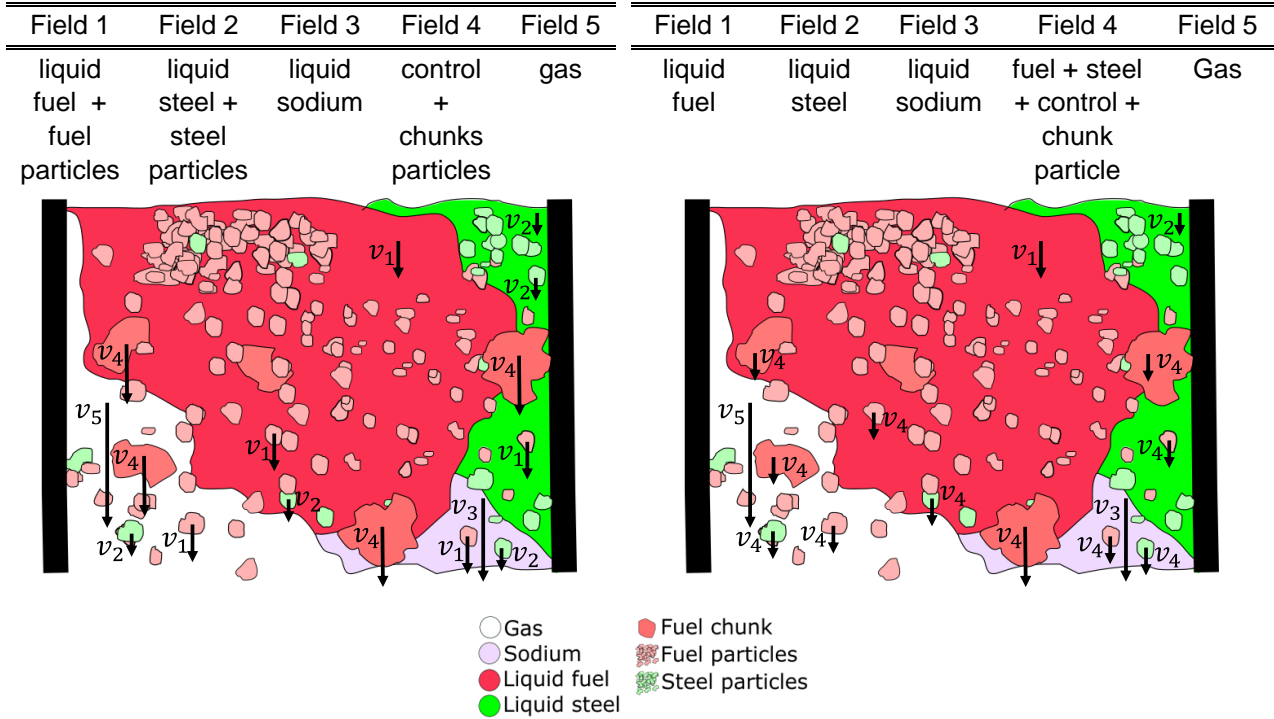


Figure II.3 Momentum allocation (5 velocity fields) of fluid components in SIMMER: state-of-the-art approach (left), new separate particle field approach (right)

In this new frame, the particle ensemble is treated as an Eulerian continuum phase in the multi-phase multi-component environment. Other fluid components in SIMMER constitute as well momentum fields analogue to the state-of-the-art approach. This fluid dynamics modelling corresponds to a multi-fluid approach, in which the system is seen as several interpenetrating continuous phases according to their representative volume fractions. The governing integral balance equations describe each momentum phase in an average sense by averaged quantities: density, velocity. We mention that, in order for the continuum approach for macroscopic particles to be valid, the spatial domain over which averaging is performed has to contain a sufficiently large number of particles but still has to remain smaller than the length scale of global flow variations. The main challenge of multi-fluid models is to define closure relationships for interface momentum exchanges and stresses of each phase. Interface exchanges are formulated by transfer laws describing the interaction between the phases. Stresses are interpreted by constitutive laws specifying how the physical parameters of a phase interact with each other. Constitutive and transfer relations are needed to close the system of equations providing that the number of averaged unknown variables is larger than the number of balance equations [Enwald et al., 1996]. Since the separate particle velocity approach (scope of the PhD work) is different from the state-of-the-art SIMMER momentum concept, it is necessary to reconsider current SIMMER particle dynamic models (constitutive relations) by performing a bibliographic review specific to the separate particle treatment. In lack of three or more-phase interaction models, closure laws in multi-fluid approach are generally constructed by multiple two-phase terms, similarly to SIMMER models at present. Correspondingly, in the following sections, we focus on the dynamic behavior of particle ensemble in a two-fluid framework.

II.4 REACTOR DEBRIS AS GRANULAR MEDIA

The purpose of this section is to deeper understand the dynamic behavior of large population of discrete solid bodies that can be associated to degraded core debris encountered during the severe accident mitigation scenario in SFRs. The collection of rigid, non-Brownian¹³ (non-colloidal) macroscopic particles is entitled as granular matter or granular suspension in the literature. The term granular media usually applies for dry grains in air or in gaseous environment. The case of particles immersed in liquid is commonly cited as granular suspension. Identifying the unique features of granular matter is fundamental to the modelling of particle abundant degraded core relocation.

The study of granular media/granular suspensions has long been the scope of interest in several fields. The principal motivation arises from the fact that granular media is the second most employed type of material in industry and that it encompasses a major domain of geophysics, examples being illustrated in Figure II.4. Examples for industrial sectors handling particulate matter include mining (transport, extraction of minerals), civil engineering (concrete, bitumen and asphalt), pharmaceutical industry (medicine powders, pastilles), food industry (cereals, candies, coffee, rice etc.), glass production (sand powder), petroleum industry (coal, plastic) and several others. The geophysical importance is attributed mainly to soil mechanics (landslides, snow avalanches, pyroclastic volcanic flows) but extends up to the orbital ice particles of the Saturn's ring [Andreotti et al., 2013].



Figure II.4 Examples of granular media: a Mineral transport; b Cereals; c Medicine drugs and pills d Landslide; e Sand castle; f Audience on rugby match, g Oranges; h Stock of wood logs; i Traffic jam (pictures from <https://www.freeimages.com>)

¹³ The particles are large enough (i.e. their radius is much greater than a micrometre) for the effects of thermal fluctuations (Brownian motion) to be neglected [Guazzelli and Pouliquen, 2018]. Large particle are also considered to be non-colloidal. Colloids refers to two-component systems in which the dispersed phase is too small to be easily observed by an optical microscope [Mewis and Wagner, 2011].

In the following, we do not attempt to present an exhaustive review of granular phenomena being an extremely broad multidisciplinary domain and subject of active research. We also note that in spite of the importance of granular matter not only in several engineering applications but also in shaping our everyday life (see for example the dynamics of traffic jams), there are still unsettled questions resisting the complete understanding of such materials. At current state of research, it exists no unifying theoretical framework covering all variety of granular configurations encountered under various conditions. Difficulties arise from (1) the complexity of grain level interactions, (2) the lack of scale separation between grain level and flow scale, (3) the multi-phase nature of the flows, (4) the wide range of coexisting solid concentrations, and (5) the fact that granular media exhibits different forms of matter (i.e. a particulate system under certain conditions displays similar properties to solid, liquid and gas). As a global result of these features, the rheology (the science of material deformation) of granular media can be complex, nonlinear, non-uniform and unsteady [Andreotti et al., 2013; Jaeger et al., 1996]. Difficulties mentioned here are non-exhaustive because they are often inherent to the given problem, modelling approach etc.

Such peculiar and unique nature of granular materials comes from two particularly important aspects. First, the role of ordinary temperature (manifestation of thermal energy) is negligible. Contrary to real fluids in which viscous effects dissipate mechanical energy directly into heat, the energy dissipation is a two-step process in granular systems. Viscous dissipation by the fluid phase produces random fluctuating motion firstly that transforms into thermal heat in the second step. Second, interactions between the grains are highly dissipative. Besides hydrodynamic forces (when interstitial fluid is present), these interactions have a major impact on the macroscopic flow dynamics especially at higher solid concentrations [Gidaspow, 1994]. In the next parts of this chapter, we review firstly hydrodynamic forces acting on the fluid - particle interface and secondly, we focus on particle-particle interactions.

II.4.1 Hydrodynamics forces

Hydrodynamic forces exerted on the surface of dispersed particle by the surrounding fluid are based on Newton's second law of motion pertaining particle trajectory. The equation of motion of a single particle falling through a viscous fluid is expressed by the generalized Boussinesq–Basset–Oseen equation, see Eq. II.7 in presence of a confining wall inducing shear [Kleinstreuer and Feng, 2013]:

$$m_p \frac{dv_p}{dt} = F_{bu} + F_{VM} + F_D + F_{pr} + F_{Ba} + F_{Saff} + F_{Ma} + F_{wl} + (F_{p-w} + F_{p-p}) \quad \text{Eq. II.7}$$

where the left-hand side expresses the acceleration of the particle with the mass m_p (kg) and the terms on the right-hand side stand for body forces such as buoyancy and virtual mass, and surface forces such as drag, pressure, Basset, Saffman lift, Magnus and wall lift forces. The last two terms come from particle-wall and particle-particle interaction forces that will be detailed in the next paragraph. Buoyancy force arises from the suspended weight of the particle that causes a pressure difference between the bottom and top of an object. The virtual mass (or added mass) force is attributed to the fluid acceleration induced by the accelerating particle. The drag force (combination of skin friction and form drag) is the fluid resistance to the relative motion between the particle and fluid. The pressure force involves the effect of the local pressure distribution. The Basset force addresses the temporal delay in the boundary layer development around the particle in a viscous flow, also referred as history force or memory effect. The Saffman lift force is due to local flow velocity gradients that direct the particle laterally away from the wall. The Magnus force originates from the asymmetric pressure distribution around a solid body due to its angular rotation. The wall lift force is due to the formation of a low-pressure region in the gap between the wall and the relocating particle. The low-pressure gap appears because the presence of the wall distorts the wake vorticity field around the particles, and because of the higher relative flow acceleration on the wall side of the particle [Kleinstreuer and Feng, 2013; Zhang et al., 2016].

II.4 Reactor debris as granular media

These forces have been identified in the hydrodynamic modeling of particulate phase by many authors [Caulet et al., 1996; Delannay et al., 2017]. For the motion of a single spherical body, analytical expressions, with very few empiricisms, exist for the magnitude of these forces. The total force on a multi-particle system F_p^m (interest of the Eulerian continuum approach) can be derived from the sum of forces exerted on a single particle $\sum F_p = F_{VM} + F_D + F_{Ba} + F_{Saff} + F_{Ma} + F_{wl}$ if the medium is homogeneous, meaning that the particles are distributed uniformly across the flow cross-section, by Eq. II.8 [Ishii and Hibiki, 2010]. The pressure force is excluded because, in the Eulerian approach it coincides with the fluid pressure gradient term. In addition, buoyancy effect in multi-fluid continuum treatment is taken into account in standard way by including the gravity term in each momentum balance and coupling them through the pressure.

$$F_p^m = \frac{\alpha_p}{V_p} \sum F_p \quad \text{Eq. II.8}$$

We note, that more sophisticated methods exist to develop hydrodynamic forces in dense particle clouds [Marshall and Li, 2014]. Expressions differ for each force and they are not detailed here.

II.4.2 Particle interactions

Particle-wall and particle-particle interactions are complex processes subject to various mechanisms at the microscopic level (influenced by grain level properties). The macroscopic behavior depends also on the variations of individual grain properties within the particulate system. If particles are poly-disperse or have a non-uniform density distribution segregation occurs (i.e. grains with different size tend to separate axially). If grains are irregularly shaped, their maximum volume concentration can vary largely with the sample preparation. Non-convex grains are even more complex as they can interlock and form clusters at any solid volume fraction.

Although, such microscopic origin of particle interactions is interpreted in many research works, the general approach is to describe them in terms of macroscopic laws. In this paragraph, we adapt the description of [Ancy et al., 1999]. An incomplete list of grain level interactions includes frictional, collisional, electrostatic, adhesive, capillary cohesive, lubrication and solid bridge contacts etc. In this work, we focus on direct mechanical contacts comprising brief quasi-instantaneous collisions and sustained frictional contacts between spherical particles. These contacts are identified as the two main dissipative processes of particle-size reactor debris in line with the granular analogy. The schematic view of two-body collision and friction are illustrated in Figure II.5.

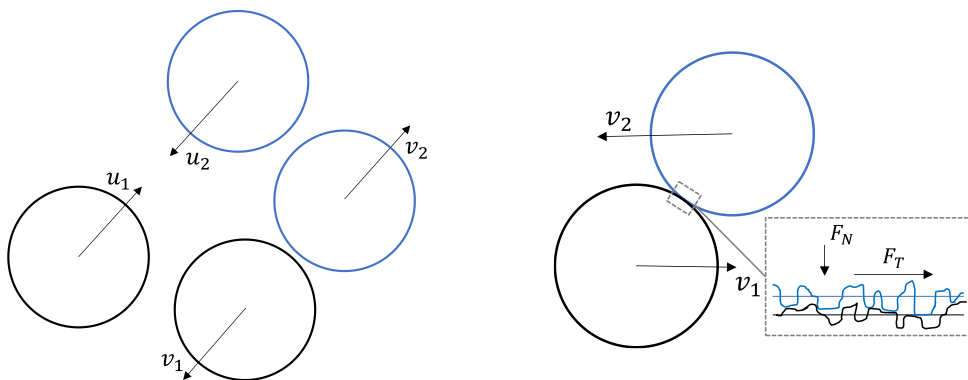


Figure II.5 Particle - particle direct interactions: collision (left) and friction (right)

The collision between dry particles, between particles in suspensions or between particles and solid surfaces is always inelastic. An evident real-life example is the bouncing of a football on the ground: the ball never reaches its original height and after a number of bumps, it stops. In a two-particle case, the colliding bodies lose part of their kinetic energy and move away from each other with a

reduced velocity. The relation between impact and post-collisional velocities is expressed by the restitution or inelasticity coefficient e , expressed by Eq. II.9.

$$v_1 - v_2 = e(u_1 - u_2) \quad \text{Eq. II.9}$$

Where v_1, v_2 and u_1, u_2 refer to the post-collisional and impact velocities of particle 1 and 2 respectively. In the simplest view of collisions, the two-body restitution coefficient can be used as the measure of momentum transfer. More complicated collisional mechanisms, for example involving three particles, are still open questions and thus not discussed here.

If particles remain in contact, the interaction is referred as frictional. The microscopic origin of friction arises from the surface roughness of the particles, particles with perfectly smooth surfaces cannot undergo frictional interaction. Depending on the velocity at the point of contact, one can distinguish between rolling without slipping (velocity is zero) and with slipping friction (velocity is non-zero). The process of inter-particle friction is described generally by the Amontons-Coulomb law of friction. This law writes as Eq. II.10 and it states that the tangential F_T and normal F_N components of the contact force are proportional through the coefficient of friction μ . The friction coefficient characterizes the condition (roughness) of the two contact surfaces.

$$F_T = \mu F_N \quad \text{Eq. II.10}$$

The importance of inter-granular collisions and friction in contrast to hydrodynamics forces can be estimated through the dimensionless Stokes number St expressing the ratio between particle response time and characteristic flow time, Eq. II.11. Even though Eq. II.11 is derived for the motion of a single particle, it is assumed to be valid for concentrated suspensions by means of a multiplicative parameter depending on the solid concentration alone $\chi(\alpha_p)$.

$$St \cong \chi(\alpha_p) \frac{\rho_p d_p^2 \dot{\gamma}_f}{\mu_f} \quad \text{Eq. II.11}$$

Where ρ_p is the particle density (kg/m^3), d_p is the particle diameter (m) and $\dot{\gamma}_f$ is the fluid shear rate ($1/s$). This definition of Stokes number can be used as an indication of to which extent particles interact with the fluid flow,

- $St \gg 1$ the particle motion can be considered independent from the interstitial fluid flow, the global dynamics is governed by particle-particle interactions;
- $St \approx 1$ two-phase behavior with mutual phase dependence manifests, similar importance of hydraulic and particle interaction forces;
- $St \ll 1$ particle inertia is sufficiently small for its trajectory to follow the fluid stream lines, particles behave as an integral part of the fluid mixture and the global behavior is governed purely by hydrodynamics.

The dependence of particle trajectory on fluid flow in function of the Stokes number is pictured in Figure II.6.

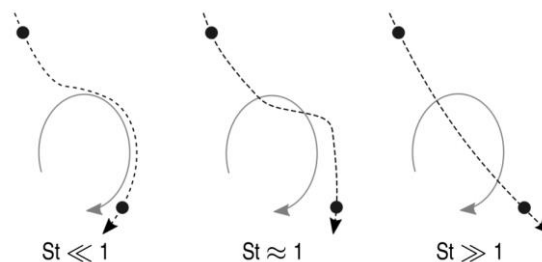


Figure II.6 Particle trajectory (dotted line) affected by the fluid flow (solid line) for different Stokes numbers by [Benavides and van Wachem, 2008]

II.4 Reactor debris as granular media

II.4.2.1 Interpretation of particle pressure

Direct particle-particle (or particle-wall when the grains are surrounded by structures) interactions transmit stresses in every direction due to the three-dimensional nature of collisions and frictional contacts. This gives rise to shear τ and normal σ stresses of different magnitude. The normal component of particle stresses is referred as particle pressure, the pressure coming from the particle phase. The existence of such pressure has been identified in several early works [Enwald et al., 1996; Jenkins and Savage, 1983; Lun et al., 1984]. [Enwald et al., 1996] refer to the role of the particle collisional pressure-gradient as responsible to keep particles apart such that that particle concentration does not exceed the maximum attainable concentration (maximum packing limit). The physical understanding behind the “pressure” notion is provided by more recent experimental studies, following the configurations of Figure II.7.

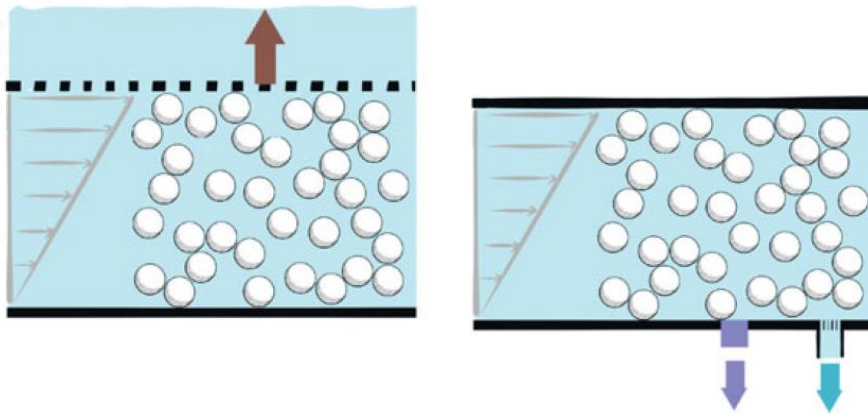


Figure II.7 Methods to estimate particle pressure: grid measurement [Boyer et al., 2011] (left) and pore pressure measurement [Garland et al., 2013] (right) pictures are taken from [Guazzelli and Pouliquen, 2018]

The left plot of Figure II.7 shows a uniformly sheared annular cell filled with a mixture of particles and liquid. The top plate above the suspension is perforated allowing the fluid to exit and retaining the particles below (openings are smaller than the grain dimensions). The analysis of this configuration by [Boyer et al., 2011] showed that a force appears on the perforated surface. Since the liquid is free to escape through the plate and thus does not impose any normal load on it, this force originates from shear-induced granular interactions. The second configuration of Figure II.7 is studied by [Garland et al., 2013]. It is a Couette cell in which the pure fluid pressure is measured through small holes drilled into the outer cylinder and protected from particles by means of membranes and grids. Subtracting this value from the total pressure of the suspension measured by other pressure sensors, the pressure contribution coming from particle-particle interactions can be estimated.

These experimental findings provide proof and basic understanding for the concept of granular pressure. However, some areas still remain to be explored, for instance whether there is a critical volume fraction below which the particle pressure diminishes. It is not detailed here but both previously presented works determine the shear components as well, and their relation to normal stresses. As it was explained before, the fundamental issue in modelling the dynamic behavior of granular media in the frame of Eulerian continuum approach is to define constitutive equations for granular stresses arising from such grain level interactions.

II.4.3 Granular regimes and their physical modelling

Granular regimes in the literature are constructed with the purpose of identifying the predominating interaction type that allows reducing the complexity of mathematical modelling (including constitutive equations) by eliminating the negligible contributions.

Historically, the first attempt for the classification of liquid-solid suspensions is attributed to Bagnold [Bagnold, 1954]. Based on experimental observations, he labeled two characteristic regimes. The grain inertia regime where the measured normal and tangential stresses arise from permanent contacts and periodic collisions between particles-particles and particles-wall, and the macro-viscous regime where stresses are associated to interstitial fluid effects. The prevailing mechanism is controlled by a dimensionless number that is referred as Bagnold number and writes in form of Eq. II.12.

$$Ba = \frac{\rho_p d_p^2 \lambda^{0.5} \dot{\gamma}}{\mu_f} \quad \lambda = 1 / \left[(\alpha_{MP} / \alpha_p)^{1/3} - 1 \right] \quad \text{Eq. II.12}$$

He argues that both normal and the tangential stresses in macro-viscous regime ($Ba < 40$) scale linearly proportional to the liquid viscosity μ_f , to the shear rate $\dot{\gamma}$ and to a function of the solid concentration λ . On the other hand, stresses in grain inertia regime ($Ba > 450$) are independent of fluid viscosity and vary with the square of shear rate $\dot{\gamma}^2$, with the square of particle diameter d_p^2 , linearly to the particle density ρ_p and as function of the solid concentration λ . In between $40 < Ba < 450$, there is a transition regime.

Another conceptual categorization of rheophysical regimes for neutrally buoyant monodisperse granular suspensions is proposed by [Coussot and Ancey, 1999]. The classification uses three dimensionless numbers (Bagnold number Ba , Coulomb number Co^{14} , Leighton number Le^{15}) to express the relative importance of collision, friction and lubricated contact. In a simplified view, granular regimes are distinguished by Table II.3.

Table II.3 Granular regimes by [Coussot and Ancey, 1999]

Frictional regime	Collisional regime	Hydrodynamic regime
$Co \ll 1$	$Co \gg 1$	$Le \gg 1$
$Le \ll 1$	$Ba \gg 1$	$Ba \ll 1$

Based on our bibliographic review, the most popular and presumably the most straightforward way of distinguishing granular regimes is based on the solid concentration. It is analogous to statement (5) in section II.4 according to which granular matter manifests in different forms of matter depending mostly on the particle volume fraction [Andreotti et al., 2013]. The solid, liquid and gas-like behaviors are illustrated in Figure II.8.

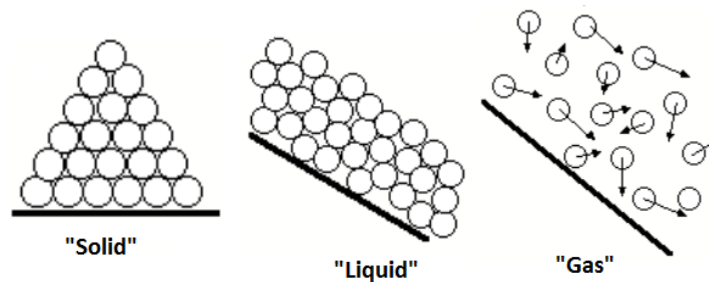


Figure II.8 Granular states resembling to solid, liquid and gas by [Andreotti et al., 2013]

Approaches to derive constitutive relations are specific to solid, liquid and gas-like regimes. Constitutive relations describe how the internal forces between particles impose changes on the global continuum flow behavior of particle phase. Attributed to their different physical origins, modelling discontinuities appear at the transition between the regimes. Such phase transitions

¹⁴ Coulomb number expresses the magnitude of collisional to frictional contacts.

¹⁵ Leighton number expressed the ratio between hydrodynamic repulsive force and normal force.

II.4 Reactor debris as granular media

remain to be resolved up until now. The following part of this chapter describes the main features and modelling approaches in view of such regimes.

II.4.3.1 Granular solid

The granular matter can be regarded as solid when particles are packed densely enough to create a static structure. This situation develops when the particle volume fraction exceeds a critical limit, referred previously as maximum packing limit α_{MP} . Theoretically, there is a maximum volume concentration of particles because two grains cannot occupy the same space. The critical value depends on the internal structure of the assembly, the shape of grains, their size distribution, their surface properties (i.e. friction) and several other parameters with minor importance. Considering uniform spherical particles, to describe the compactness of the granular assembly one can talk about random loose packing, random close packing and regular close packing depending on the preparation history of the granular pile. Random loose packing refers to the solid concentration obtained by pouring a collection of grains into a container ($\alpha_p \cong 0.55 - 0.6$). Random close packing is obtained by shaking the loosely filled container until the highest packed configuration is reached ($\alpha_p \cong 0.62 - 0.64$). Regular close packing is achieved when particles are arranged into a face-centered cubic lattice ($\alpha_p \cong 0.74$) [Scott and Kilgour, 1969; Song et al., 2008].

Inside the static pile, particles are in contact with several of their neighbors forming a network of enduring contacts due to inter-granular friction forces. The system of frictional contacts can resist applied stresses without deformation (granular elasticity) resulting in a mechanically quasi-stable jammed state. The jammed state is quasi-stable because in most configurations a stability criterion exists above which the structure undergoes irreversible deformation (granular plasticity). In terms of frictional description, friction being the dominant grain level interaction, the simplest criterion is formulated through the relation between shear and normal stresses. The granular matter yields and suffers plastic deformation if the shear stress τ in any segment of the granular structure exceeds a threshold value that is proportional to the normal stress σ . The condition writes as Eq. II.13 [Andreotti et al., 2013], similar to Eq. II.10.

$$\tau = \mu\sigma \quad \text{Eq. II.13}$$

Figure II.9 shows an example of yield behavior in case of a solid bulk resting on a plane surface [Schulze, 2007]. In the first case (a), the normal force is perpendicular to the plane creating no shear stress. When the plane is inclined (b) by an inclination angle α , shear stress appears between the wall and the solid. If the force transferred through the shear stress is larger than the force pulling the bulk solid downwards, the material remains at rest. If the inclination is increased above a critical value (c), the transferable stress becomes smaller than the normal stress and eventually the solid slides downwards.

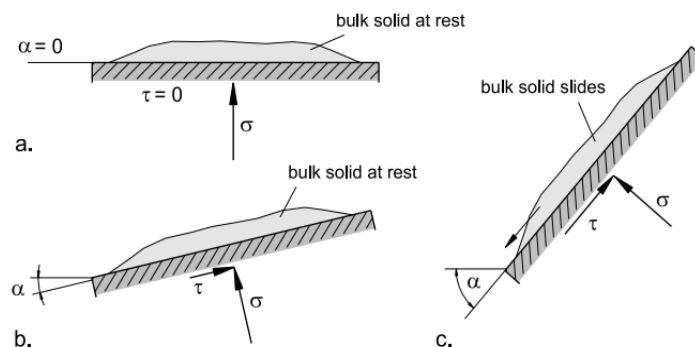


Figure II.9 Illustration of frictional yield (compressive stresses are defined positive) [Schulze, 2007]

Higher-level descriptions take into account for example the effect of volume fraction (critical-state theories). It allows modelling dilatancy and contractancy effects: depending on the initial volume, the granular assembly dilates or contracts under an applied stress and converges towards the critical concentration. More complex models (Cam-clay model) incorporate the variation of critical concentration with applied stress attributed to the compressibility of the particles at the contact points [Campbell, 2006]. Different expressions exist also for the yield criterion such as Mohr-Coulomb or Drücker-Prager failure criterion. The description of such concepts is not the scope of this work. In addition, most of these refined soil mechanics models are formulated by extending the rudimentary relation of Eq. II.13 to derive constitutive laws for granular solids. Constitutive laws in soil mechanics and geophysics are intended to describe the criterion and the transition itself from a mechanically stable particulate structure to slowly deforming configuration.

In reactor severe accident applications, the solid-like regime is identified to be of high importance as it corresponds to postulated blockage formation inside the transfer tube. The blockage corresponds to a jammed state of matter for which the yield criterion and plasticity models can be applied. The adaption of soil mechanics constitutive laws into the continuum hydrodynamic description is possible but applicable only for very limited ranges of configurations depicting jamming transitions.

II.4.3.2 Granular gas

In the opposite limit of particle concentration in which particles are widely spaced, strongly agitated and free to move in any direction, the granular matter behaves similar to gases. Particles in granular gases are assumed to interact via binary, instantaneous and uncorrelated collisions. The analogy between rapid and dilute granular media and the molecules of the gases provides the basis for the development of modified gas kinetic theories, referred as Kinetic Theory of Granular Flows (KTGF). The modification is essential to account for the dissimilarities of a system of macroscopic solid particles from a classical molecular gas. Dissimilarities arise mostly from the inelastic nature of the collisions and the physical dimensions of grains and molecules [Shi et al., 2017].

The first step towards the gas-like description of granular matter was the notion of granular temperature (or pseudo-thermal energy) by Ogawa [Ogawa, 1978]. The granular temperature is the statistical measure of the fluctuating component of the particles' kinetic energy around the average, computed as the mean square root of the random velocities by Eq. II.14. Contrary to thermodynamic temperature, it has no relation with the thermal state of the grains.

$$\Theta = \langle \delta v_p^2 \rangle \quad \text{Eq. II.14}$$

Where Θ is the granular temperature (m^2/s^2) and δv is the fluctuating velocity of the grains (m/s). The later is defined as the difference between the average flow and instantaneous particle velocities. Granular temperature is central concept in KTGFs since it governs the intermediate state in the two-step energy dissipation (see section II.4). Its main source of production comes from the viscous dissipation of the solid phase, while the highest dissipation is attributed to inelastic collisions. Other early works applying the elementary concepts of KTGF include Umemura & Oshima [Ogawa et al., 1980], Shen [Shen and Ackermann, 1982] and Haff [Haff, 1983]. More recent and comprehensive studies are performed by Jenkins & Savage [Jenkins and Savage, 1983], Lun [Lun et al., 1984] and Gidaspow [Gidaspow, 1994].

The idea behind granular kinetic theories is to estimate the collisional momentum and energy transfer between the particles by considering a distribution function for the motion of a single particle. It is feasible by imposing that the number of particles is large enough to adapt statistical mechanics. The formal analysis is based on the Boltzmann transport equation (describing the temporal evolution of the single-particle distribution function) with a modified collision kernel (inelastic Enskog-Boltzmann equation) accounting for the instantaneous, binary, uncorrelated and inelastic nature of hard-sphere collisions. The derivation of macroscopic fluid dynamics equations is beyond the scope of this work.

II.4 Reactor debris as granular media

The final hydrodynamic equations obtained by KTGF models resemble the conventional Navier–Stokes equations except for the additional balance equation for the evolution of granular temperature [Gidaspow, 1994]. Constitutive laws in these equations are constructed by relating the exact micromechanical grain-level properties, such as coefficient of restitution and individual grain velocities, to global hydrodynamic variables [Andreotti et al., 2013; Iwashita and Oda, 1999]. This provides one of the biggest advantages for the use of constitutive equations by KTGF. In the frame of particle dynamics, our interest is towards the constitutive laws for solid stresses. In the KTGF approach, solid stresses are decomposed into a kinetic and a collisional transfer term. The kinetic (or translational) part reflects the continuous and chaotic motion of the grains and the resulting transport of momentum during the free flight of grains. The collisional part accounts for the transfer from one particle to another during a binary instantaneous contact [Dartevielle, 2004].

The main limitation of such equations is the assumption on the nature of collisions. At higher solid concentrations, collisions can no more be considered to be nor binary, nor instantaneous and nor uncorrelated in space. Particles in dense suspensions interact with several of their neighbors. The velocity of individual grains after collisions cannot be purely controlled by the two-body restitution coefficient because their spatial freedom is reduced due to the proximity of other particles. In addition, the effect of friction comes into play when particles are forced into longer duration contact with each other. Even though, there are attempts to extend the kinetic granular treatment to higher concentrations, in a rigorous way the KTGF can only be used up to a certain particle concentration ($\alpha_p < 0.4$ by [Schneiderbauer et al., 2012]). Another problematic of KTGF model is related to its application for immersed granular media in which interstitial fluid effects appear. Little literature is available on this subject mainly because rapid collisional particle flows in viscous fluid are rarely encountered in practical applications.

II.4.3.3 Granular liquid

The last liquid-like regime is apparent when the system yields and flows under applied stress. This regime lays between the gaseous and solid-like state and it combines features of both since particles in rather dense configurations interact via mutual collisions and inter-particle friction. The momentum exchange is therefore described by the combined effect of frictional forces (and resulting permanent solid contacts) and particle-particle collisions [Andreotti et al., 2013]. The theoretical framework describing the liquid-like regime is the recently developed $\mu(I)$ dense granular rheology [GDR MiDi, 2004]. This approach constitutes a major advancement in defining universal constitutive laws for dense granular flows since it extends from collisional up to quasi-static flows.

We identify $\mu(I)$ dense granular rheology as the most promising approach for modelling the effect of particle-particle interactions shaping the dynamic behavior of degraded solid debris during the severe accident mitigation scenario. The motive towards this approach lays in the following aspects:

- Covering the range of particle-size debris concentrations that are interest of the model development
- Being a very recent approach incorporating the most available knowledge on particulate matter
- Encompassing dry and suspension granular regimes
- Constitutive relations reflect interactions occurring at the particle level
- Provides constitutive laws in term of averaged hydrodynamics variables
- Adaptability to the Eulerian continuum models of SIMMER-V

$\mu(I)$ dense granular rheology models will be discussed in the chapter of model development. Before, in light of the outcomes of the bibliographic review on granular flows, current SIMMER particle dynamic models are evaluated through a Phenomena Identification-Ranking Table (PIRT)

II.5 PHENOMENA IDENTIFICATION-RANKING TABLE

The objective of the PIRT is to classify the importance of the physical phenomena relevant to the dynamic behavior of particulate flows (identified in paragraphs II.4.1 and II.4.2) and to estimate the uncertainty of associated SIMMER models. The figure of merit is the particle phase velocity in the frame of a one-dimensional two-fluid Eulerian approach. One-dimensional velocity resolution is required to comply with SIMMER channel flow models inside the vertical transfer tubes that will be discussed in detail in paragraph III.1.1. The phenomena labelled with high theoretical importance and high SIMMER modelling uncertainty are in our primary interest for improvement and development.

II.5.1 PIRT evaluation context

We recall from section II.1 that the relocation of the degraded core mixture during severe accident progression is extremely complex. It is difficult to partition different scenarios in space and time. Fuel or steel particles of different sizes may traverse co- or counter-current through gas, liquid sodium, liquid steel and/or liquid fuel under gravity and/or pressure force. These configurations may as well coexist in close proximity. Therefore, the evaluation criterion for this first iteration of the PIRT is general concerning all foreseen accidental scenarios.

The numerical modelling context in which the PIRT is evaluated is the case when all solid particulate components are assigned into one momentum field, corresponding to the approach described in section II.3. The effect of heat and mass transfer is excluded from the PIRT analysis in order to target purely dynamic aspects. The phenomena considered in the PIRT include all physical processes that influence the motion of solid bodies in the previously explained general accidental context. It covers interaction forces of the particle ensemble with other fluids, interactions of particles with bounding walls following paragraph II.4.1, and interactions within the particulate phase following paragraph II.4.2. Other phenomena listed in the PIRT, namely interfacial area tracing and turbulence modelling, are based on multi-phase theories by [Ishii and Hibiki, 2010]. Interfacial area tracing is considered as it defines contact surfaces through which momentum transfer can occur. The effect of turbulence is evaluated due to the momentum coupling between fluid phase turbulent eddies and particle traverse motion, which can induce damping or amplification of one or the other.

Each phenomenon is classified into high, medium or low theoretical importance and SIMMER modelling uncertainty (only where the phenomenon is modelled in the code). The ranking is subdivided between dilute and dense regions according to the particle volume fraction. The separation of these two regimes is necessary to highlight the varying importance of the different transport phenomena. One can find different boundary values in the literature [Elghobashi, 1994] but, in our investigation, dilute simply refers to the regime that is governed by fluid-dynamic transport of particles, while dense is when inter-particle collisions and long-duration particle contacts influence the transport process.

II.5.2 Methodology

Phenomena evaluation was performed in the frame of a PIRT meeting by a panel of experts, each of whom has experience with the SIMMER code or expertise in multiphase particulate flow modelling. A three-scale ranking is adopted by high (phenomenon has dominant impact on the figure-of-merit), medium (phenomenon has moderate impact on the figure-of-merit) or low (phenomenon has small or no impact on the figure-of-merit) votes. The final importance IL and uncertainty UL levels for each phenomenon were determined by averaging the panelists' votes according to Eq. II.15 [OECD-NEA, 2018]:

$$IL, UL = \frac{1.0H + 0.5M + 0.0L}{H + M + L} \quad \text{Eq. II.15}$$

II.5 Phenomena identification-ranking table

where H is the number of high ranks is, M is the number of medium ranks and L is the number of low ranks. The PIRT results are displayed in Table II.4. Based on section II.2, we note that the effect of wall friction-collision and particle-particle friction are incorporated through the particle viscosity models in the closure laws of SIMMER.

Table II.4 Phenomena Identification-Ranking Table

		Theoretical importance					SIMMER uncertainty											
		Particle volume fraction					Particle volume fraction											
		Dilute			Dense		Dilute			Dense								
		H	M	L	IL	H	M	L	IL	H	M	L	UL	H	M	L	UL	
Physical Phenomena	Interaction between particles and other phases	Buoyancy force	2	1	5	0,31	2	6	0	0,63	0	0	5	0,00	0	2	3	0,20
		Drag force	6	1	1	0,81	6	2	0	0,88	1	1	4	0,25	4	1	1	0,75
		Added mass force	0	5	3	0,31	1	5	2	0,44								
		Magnus force	1	0	6	0,14	0	0	7	0,00								
		Basset force	0	0	8	0,00	0	0	8	0,00								
	Wall interactions	Friction - collision	1	4	3	0,38	6	1	1	0,81	1	4	0	0,60	4	1	0	0,90
		Saffman lift force	0	3	4	0,21	1	1	5	0,21								
		Wall induced lift force	0	4	3	0,29	1	1	4	0,25								
	Particle-particle interactions	Collision	1	0	7	0,13	4	4	0	0,75								
		Kinetic transport	0	4	3	0,29	1	2	4	0,29								
		Friction force	0	1	7	0,06	6	2	0	0,88					4	0	0	1,00
	Interfacial area tracking		5	2	0	0,86	4	2	1	0,71	0	3	1	0,38	2	3	0	0,70
	Turbulence		5	3	0	0,81	4	2	1	0,71								

Summarizing the results of the PIRT on Table II.4, there are several physical phenomena that are currently not modelled in SIMMER. Many of these phenomena, such as the effect of kinetic transport, added mass, Magnus and Basset history force are ranked with relatively low theoretical importance in both dilute and dense configurations. The same is concluded for particle-wall interactions that induce transverse motion such as Saffman lift and wall induced lift force. Consequently, one can assume that neglecting these effects in current state of numerical modelling results in a minor impact on particle phase velocity in one-dimensional Eulerian continuum approach. On the other hand, among the not modelled phenomena, the expert panel recognizes particle-particle collisions for dense flows and fluid turbulence¹⁶ with high theoretical importance. It implies that further research should be dedicated to evaluate the associated modelling shortcomings. Regarding the phenomena currently taken into account by SIMMER, the graphical representation correlating theoretical importance and SIMMER modelling uncertainty levels are shown in Figure II.10.

¹⁶ Turbulent effects in SIMMER can be taken into account via specific models activated by user options (not default). These options are not review in the scope of the PhD. In lack of sufficient knowledge, turbulence is considered as not modelled phenomena in SIMMER.

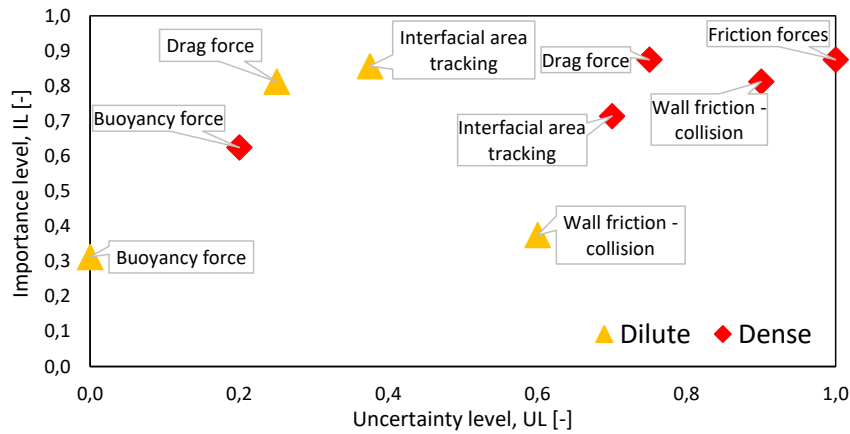


Figure II.10 Theoretical importance and SIMMER modelling uncertainty levels for dense and dilute particle flows resulting from the expert advice in the PIRT

Concluding on Figure II.10, the three highest uncertainties of SIMMER modelling and highest theoretical importance phenomena include particle-wall direct interactions, interphase drag forces and frictional forces between particles in dense particle flows. Interfacial area tracking follows closely. Regarding that it defines the contact surface through which momentum transfer occurs between the phases, interfacial area models in SIMMER play a role in interphase drag and particle-wall momentum transfer processes. Thanks to such dependency, the uncertainty of interface area tracking can be treated together with wall and particle friction forces.

Overall, we conclude that the numerical modelling of dense particles flows in SIMMER requires the improvement of interphase and particle-wall momentum exchange terms and the new incorporation of inter-particle collisions. The associated model development efforts are presented in the next chapter.

Chapter III.

MODEL DEVELOPMENT FOR PARTICLE DYNAMICS

To analyze situations wherein the particles and the fluid have different motions (our scope of interest), it is necessary to go beyond the SIMMER state-of-the-art effective-fluid description [Guazzelli and Pouliquen, 2018]. Since the original SIMMER-V momentum equations are developed for fluids, the fundamental differences between fluid and solid particulate behavior have to be incorporated into the numerical description of particle motion. This chapter describes the collection of physical models that has emerged from the bibliographic review on the dynamics of particulate systems. The modelling set constitutes a comprehensive framework for the numerical representation of dense particle flows, corresponding to the relocation mechanism of particle-size reactor debris through the mitigation transfer tubes. The model development is carried out in the SIMMER-V code.

III.1	Numerical environment: SIMMER-V code	38
III.1.1	SIMMER overall framework	38
III.1.2	Momentum conservation and its solution procedure	39
III.2	Statement of the modelling context	43
III.3	Identification of transfer tube regions	45
III.4	Momentum exchange terms for particles	45
III.4.1	Interphase momentum exchange	45
III.4.2	Momentum exchange of particles with structures	47
III.5	Particle-particle interaction forces	47
III.5.1	$\mu(I)$ dense granular rheology	48
III.5.1.1	Closures for solid volume fraction law	50
III.5.1.2	Closures for macroscopic friction coefficient	52
III.5.1.3	Area-averaged vertical pressure	52
III.5.1.4	Radial velocity profile	53
III.5.1.5	Particle density	54
III.5.1.6	Fluid viscosity	55
III.5.1.7	Limits of the rheology	55
III.5.2	Numerical implementation	56
III.5.2.1	Regularization	58
III.5.3	Continuity considerations	59
III.6	Discussion on fluid pressure	60
III.7	Synthesis of developed models	61

III.1 NUMERICAL ENVIRONMENT: SIMMER-V CODE

As it was said in section II.2, the SIMMER code is used as reference numerical tool in France for the safety evaluation of future generation SFRs. Currently available code versions include SIMMER-III two-dimensional, SIMMER-IV three-dimensional and the most recent SIMMER-V. SIMMER-V is derived from SIMMER-IV with identical physical models at present. The main motivation towards SIMMER-V is that it is able to follow the entire accident evolution including initiating, transition and secondary phase, thanks to recent code developments at JAEA and CEA. SIMMER-V takes advantage of parallel computing by domain decomposition and by improving memory management. Another advantage of SIMMER-V is that it is possible to be coupled with other codes such as GERMINAL (for fuel pre-irradiation phase) or in the future: APPOLO3 (CEA code for neutronics) and CATHARE (CEA code for system-scale thermal-hydraulics) via the SEASON platform (under CEA development). In this PhD project, SIMMER-V serves as the numerical environment for model development on particle dynamics. The code version used as reference in our work is the SIMMER-V 1.B release. SIMMER is a large and complex code combining different disciplines (multiphase thermal hydraulics, neutronics etc.) and offering numerous options for their modelling. Therefore, we do not intend to provide an exhaustive code description. Following, the general SIMMER-V (analogous to SIMMER-III and SIMMER-IV) approach is presented with details only on the parts relevant to particle dynamics and the associated model development.

III.1.1 SIMMER overall framework

The main objective behind the SIMMER code architecture is to provide a mechanistic simulation of event progression during a severe core disruptive accident by following material redistributions inside the reactor core. The material distributions are obtained by solving the basic conservation equations in the fluid-dynamics module of the code. The fluid-dynamics section is integrated with a structure model, predicting the time dependent disintegration of structural materials by heat and mass transfer calculations through their surfaces. The neutronics feedback of the material dispersion is computed by the space-, time- and energy-dependent neutron kinetics model. The neutronics module determines the nuclear heat source from fission reactions based on the mass and energy distributions given by the fluid dynamics and the structure modules. The conceptual framework of SIMMER describing the interplay between these three modules is illustrated in Figure III.1.

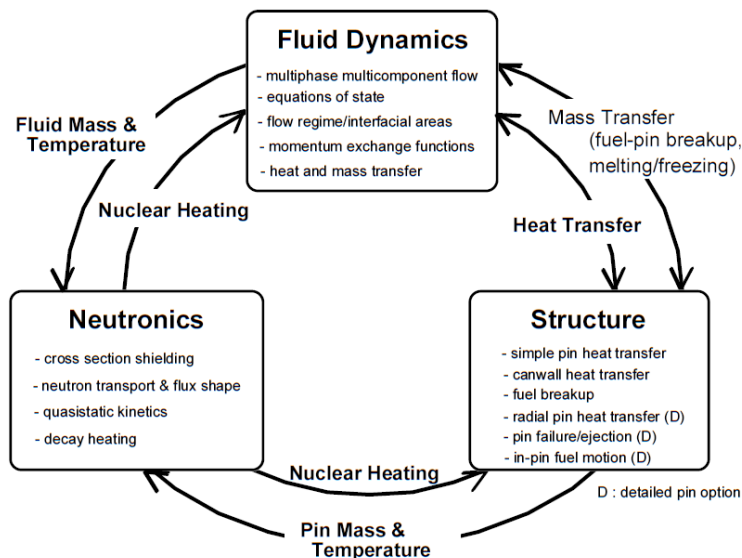


Figure III.1 Overall framework of the SIMMER code series from [Maschek et al., 2003]

Core materials in SFR application include fuel, steel, coolant, control and fission gas. These materials exist in different physical states during an accident evolution. For example, fuel can be

present in form of fabricated pins, particle-size debris from the mechanical fragmentation of pins, liquid fuel after reaching melting temperature, solid crust refrozen on structures, or vapor after reaching saturation temperature. In the SIMMER context, it relates to the definition of several structure, liquid (including solid particles) and gas components¹⁷ [Maschek et al., 2003]. Structures are immobile but they can fragment or melt, and transform (fragment) into movable fluids. The spatial redistribution of movable fluids are determined by the fluid-dynamics module of the code. It contains the differential conservation equations for mass, momentum and energy, see Eq. III.1 - Eq. III.3. The form of these balance equations are inherited from precedent Advanced Fluid-Dynamics Model (AFDM) code [Wilhelm, 1990]. The system of equations is defined for density components m , velocity fields q and energy components M .

$$\frac{\partial \bar{\rho}_m}{\partial t} + \nabla(\bar{\rho}_m \mathbf{v}_q) = -\Gamma_m \quad \text{Eq. III.1}$$

Where $\bar{\rho}_m$ is the average density (kg/m^3), t is time (s), \mathbf{v}_q is the velocity (m/s) and Γ_m is the mass transfer rate ($kg/s/m^3$).

$$\begin{aligned} \frac{\partial(\bar{\rho}_q \mathbf{v}_q)}{\partial t} + \sum_{m \in q} \nabla(\bar{\rho}_m \mathbf{v}_q \mathbf{v}_q) + \alpha_q \nabla p - \bar{\rho}_q g + K_{qS} \mathbf{v}_q - \sum_{q'} K_{qq'} (\mathbf{v}_{q'} - \mathbf{v}_q) - \mathbf{VM}_q \\ = - \sum_{q'} \Gamma_{qq'} [H(\Gamma_{qq'}) \mathbf{v}_q + H(-\Gamma_{qq'}) \mathbf{v}_{q'}] \end{aligned} \quad \text{Eq. III.2}$$

Where α_q is the volume fraction ($-$), p is the locally averaged pressure (Pa), K_{qS} is the momentum exchange function between the velocity field q and structure ($kg/s/m^3$), $K_{qq'}$ is the momentum exchange function between the velocity fields q, q' ($kg/s/m^3$), \mathbf{VM}_q is the virtual mass term ($kg/s^2/m^2$) and $H(x)$ is the Heaviside unit function.

$$\begin{aligned} \frac{\partial(\bar{\rho}_M e_M)}{\partial t} + \sum_{m \in M} \nabla(\bar{\rho}_m e_m \mathbf{v}_q) + p \left[\frac{\partial \alpha_M}{\partial t} + \nabla(\alpha_M \mathbf{v}_q) \right] \\ - \frac{\bar{\rho}_M}{\bar{\rho}_q} \left[\sum_{q'} K_{qq'} (\mathbf{v}_q - \mathbf{v}_{q'}) (\mathbf{v}_{q'} - \mathbf{v}_{qq'}) + K_{qS} \mathbf{v}_q (\mathbf{v}_{q'} - \mathbf{v}_{qS}) \right. \\ \left. - \mathbf{VM}_q (\mathbf{v}_{q'} - \mathbf{v}_{GL}) \right] = Q_N + Q_{MF}(\Gamma_{MF}) + Q_{VC}(\Gamma_{VC}) + Q_{HT} \end{aligned} \quad \text{Eq. III.3}$$

Where e_M is the specific internal energy (J/kg), \mathbf{v}_{GL} is the velocity at the interface of gas and liquid phases (m/s), Q is rate of energy interchange (W) due to N nuclear heating, MF melting/freezing, VC vaporization/condensation and HT heat transfer.

III.1.2 Momentum conservation and its solution procedure

Since this work focuses on the dynamics of particle flows, we center our attention on the momentum balance equation without virtual mass, heat and mass transfer terms. The effect of the last two will be discussed in the next sections. The virtual mass term is computed between real liquids and gas

¹⁷ Fuel: MOX, UO₂, MSRE (Molten Salt Reactor Experiment), MSBR (Molten Salt Breeder Reactor)

Steel: SUS316, SUS316

Coolant: Sodium, Water, Lead, LBE (Lead-Bismuth Eutectic)

Control: B₄C

Gas: Xenon, Air

III.1 Numerical environment: SIMMER-V code

components that is not in the scope of our work. In SIMMER, the number of velocity fields (number of momentum equations) and the allocation of fluid components (namely liquid fuel, liquid steel, liquid sodium, fuel particles, steel particles, control particles, fuel chunks and gas) into each field are user options. Even though it would be possible to define a momentum equation for each one, the best practice based on SIMMER Validation and Verification (V&V) experience for SFRs is to apply five velocity fields, on analogy to section II.3. In this context, Eq. III.2 rewrites as Eq. III.4, a system of five differential equations with $q = 1 \dots 5$.

$$\frac{\partial(\overline{\rho}_q \mathbf{v}_q)}{\partial t} + \sum_{m \in q} \nabla(\overline{\rho}_m \mathbf{v}_m \mathbf{v}_q) = -\alpha_q \nabla p + \overline{\rho}_q g - K_{qs} v_q + \sum_{q'} K_{qq'} (\mathbf{v}_{q'} - \mathbf{v}_q) \quad \text{Eq. III.4}$$

Eq. III.4 states that the change of momentum with time is equal to the net rate of momentum transferred by convection, acceleration due pressure gradient, gravity force, interphase momentum exchange though drag force, and momentum transfer to structures. These terms are identified to be the dominant dissipation mechanisms in reactor severe accident studies by [Wilhelm, 1990].

The differential equation system of Eq. III.4 is discretized in space and time. The spatial discretization (in cylindrical or Cartesian coordinates) is done on an Eulerian staggered mesh¹⁸ in which velocities are defined on cell faces while densities and pressure are evaluated at cell centers [Bohl, 1990]. Spatial boundary conditions are treated using boundary cells and ghost cells out of the real domain boundaries. For the discretization scheme, there are two options implemented in SIMMER: first order donor cell or higher (2nd) order finite difference method [van Leer, 1979]. By default, higher order finite differencing scheme is used in multi-phase reactor severe accident calculations in order to reduce numerical diffusion. The temporal discretization involves the integration of every term in differential momentum equations over a time step. The transient term is resolved by first order method. Other spatially discretized terms are evaluated by implicit time scheme, except for the convection term for which explicit treatment is used. The time step size is strictly controlled by several physical criteria (Courant condition etc.) allowing a stable and accurate numerical calculation and at the same time taking into account computational cost that can be considerable for a 3D full reactor geometry [Yamano et al., 2003]. The typical time step size in reactor severe accident application varies in the range of $10^{-6} - 10^{-3}$ second. The space and time discretized form of Eq. III.4 in axial direction in cylindrical coordinates writes as Eq. III.5 with $A_{qq'}$, A_{qs} and $B_{qq'} |\mathbf{v}_{q'} - \mathbf{v}_q|$, $B_{qs} |\mathbf{v}_q|$ laminar and turbulent contributions respectively. Spatial discretization in Cartesian coordinates is not detailed here.

$$\begin{aligned} & \frac{\overline{\rho}_{q\xi}^{n+1} \mathbf{v}_{q\xi}^{n+1} - \overline{\rho}_{q\xi}^n \mathbf{v}_{q\xi}^n}{\Delta t} + \frac{1}{r \Delta r_i} \left[\langle \overline{\rho}_q r \mathbf{u}_q \rangle^n_{i+\frac{1}{2}, j+\frac{1}{2}, k} \mathbf{v}_{q, i+\frac{1}{2}, j+\frac{1}{2}, k}^n - \langle \overline{\rho}_q r \mathbf{u}_q \rangle^n_{i-\frac{1}{2}, j+\frac{1}{2}, k} \mathbf{v}_{q, i-\frac{1}{2}, j+\frac{1}{2}, k}^n \right] \\ & + \frac{1}{\Delta z_{j+\frac{1}{2}}} \left[\langle \overline{\rho}_q \mathbf{v}_q \rangle^n_{i, j+1, k} \mathbf{v}_{q, i, j+1, k}^n - \langle \overline{\rho}_q \mathbf{v}_q \rangle^n_{i, j, k} \mathbf{v}_{q, i, j, k}^n \right] \\ & + \frac{1}{\Delta \theta_k} \left[\langle \overline{\rho}_q \mathbf{w}_q \rangle^n_{i, j+\frac{1}{2}, k+\frac{1}{2}} \mathbf{v}_{q, i, j+\frac{1}{2}, k+\frac{1}{2}}^n - \langle \overline{\rho}_q \mathbf{w}_q \rangle^n_{i, j+\frac{1}{2}, k-\frac{1}{2}} \mathbf{v}_{q, i, j+\frac{1}{2}, k-\frac{1}{2}}^n \right] \\ & = -\alpha_{q\xi}^{n+1} \frac{p_{i, j+1, k}^{n+1} - p_{i, j, k}^{n+1}}{\Delta z_{j+\frac{1}{2}}} + \overline{\rho}_{q\xi}^{n+1} g - (A_{qs, \xi}^n + B_{qs, \xi}^n |\mathbf{v}_{q, \xi}^n|) \mathbf{v}_{q, \xi}^{n+1} \\ & + \sum_{q'} (A_{qq', \xi}^{n+1} + B_{qq', \xi}^{n+1} |\mathbf{v}_{q', \xi}^n - \mathbf{v}_{q, \xi}^n|) (\mathbf{v}_{q', \xi}^{n+1} - \mathbf{v}_{q, \xi}^{n+1}) \end{aligned} \quad \text{Eq. III.5}$$

¹⁸ The typical mesh size in reactor severe accident application is around 10 cm, but can vary within reactor regions.

Where u, v, w are the radial, axial and theta velocity components (m/s); $\Delta r, \Delta z, \Delta \theta$ are the radial, axial and theta oriented mesh dimensions; i, j, k are the radial, axial and theta coordinates, $\xi = i, j + 1/2, k$ location, superscript $n, n + 1$ refers to values at two consecutive time steps and $\langle \rangle$ notation indicates the evaluation of multiple variables at given spatial coordinates.

The overall fluid-dynamics solution algorithm, including Eq. III.5, is based on a time-factorization approach. It is a four-step method developed originally for the AFDM code, in which intra-cell transfers (interfacial area source terms, heat and mass transfer) are determined separately from inter-cell fluid convection, see Figure III.2. The physical pretext behind splitting inter-cell convection from intra-cell heat and mass transfer lays in the prior knowledge on the relaxation mechanisms and their characteristic times after a thermodynamic disequilibrium. It is considered that the characteristic time for heat and mass transfer in response to phase and/or thermal local disequilibrium and the characteristic time of macroscopic fluid motion in response to global mechanical disequilibrium are of the same order of magnitudes. Separating these two permits a strong simplification. Accordingly, in SIMMER, intra-cell heat and mass transfer is solved by the STEP1 algorithm, followed by the calculation of fluid convection in the STEP2 algorithm.

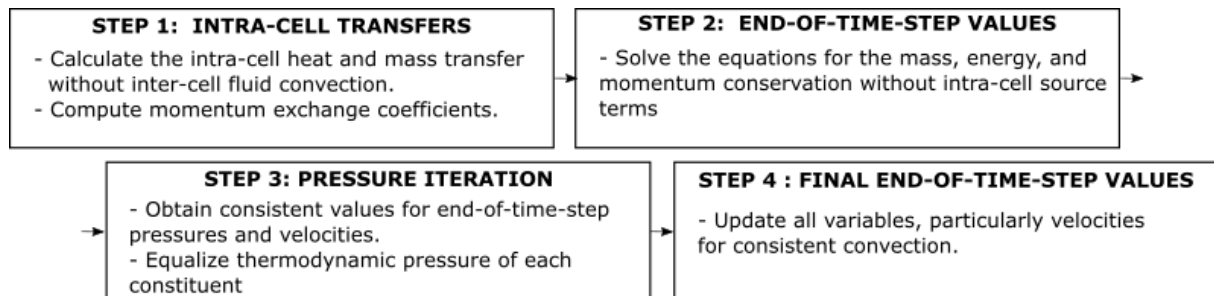


Figure III.2 Schematic diagram of four-step method

The third time scale in the SIMMER application domain corresponds to the local response of the system to a pressure disequilibrium. This relaxation time is very short compared to the previous two and thus instantaneous mechanical equilibrium is assumed on a local scale. It means that there is a homogenized and common pressure for all the fluid components within a computational cell. Correspondingly, this pressure has to satisfy all momentum equations for consistent pressure-flow field relation as well as the Equation Of State (EOS) of each constituent to ensure thermodynamic local equilibrium. As the pressure is not recalculated in STEP1 and STEP2, during which both the thermodynamic state and the flow field of constituents are modified, the next algorithm (STEP3) is dedicated to obtain the consistent pressure. STEP3 applies an iterative process to minimize six residuals, namely the difference between cell and EOS pressure, four momentum densities and one gas energy residual. These residuals represent the deviation between end of STEP2 values and stabilized state values. Stabilized state at the end of STEP3 signifies that the pressure within each mesh satisfies the EOS of every constituents and all transport equations, and that the volume of constituents fills the total free volume of the cell after all adjustments (momentum densities) during STEP3. The last step (STEP4) is a repeated fluid convection calculation that readjusts velocities according to modified pressure and densities at the end of STEP3.

In order to close the system of momentum conservation equations, closure laws are defined for the interphase $K_{qq'}$ and the structure K_{qs} momentum exchange functions. Their formulations are based on engineering correlations of steady-state two-fluid flows. Two-fluid correlations are used because both theoretical and experimental knowledge at the time of SIMMER development was limited for multi-fluid multi-phase flows. In the SIMMER-V multi-component context, momentum exchange functions are first computed between each component (fluids belonging to different velocity fields and structures) present inside the computational mesh. The default method of defining exchange coefficient between the 8 transportable fluid components and structures with the new velocity field

III.1 Numerical environment: SIMMER-V code

allocation, according to section II.3, is shown in Table III.1. The formulation of component-component exchanges is given in section II.2

Table III.1 Momentum exchange coefficients between components (K_{ik} between fluid i and k , K_{iS} between fluid i and structure, x not computed because they belong to the same velocity field in our approach)

	Liquid fuel 1	Liquid steel 2	Liquid sodium 3	Fuel particle 4	Steel particle 5	Control particle 6	Chunk 7	Gas 8	Structure S
Liquid fuel 1		K_{12}	K_{13}	K_{14}	K_{15}	K_{16}	K_{17}	K_{18}	K_{1S}
Liquid steel 2			K_{23}	K_{24}	K_{25}	K_{26}	K_{27}	K_{28}	K_{2S}
Liquid sodium 3				K_{34}	K_{35}	K_{36}	K_{37}	K_{38}	K_{3S}
Fuel particle 4					x	x	x	K_{48}	K_{4S}
Steel particle 5						x	x	K_{58}	K_{5S}
Control particle 6							x	K_{68}	K_{6S}
Chunks 7								K_{78}	K_{7S}
Gas 8									K_{8S}

The interfaces (contact areas between fluid-fluid and fluid-structure components) through which momentum transfer takes place are postulated based on a one-dimensional steady-state flow regime map. It describes the topology of the multiphase flow in channel and pool configurations; Figure III.3 displays channel flows topologies (used also for heat and mass transfer processes). The effective void fraction considers the ratio of gas volume compared to the total volume of gas and real liquids (liquid fuel, liquid steel and liquid sodium) inside a mesh. In addition, SIMMER can perform interfacial area convection to take better account of highly transient flows [Tobita, 1991; Yamano et al., 2003].

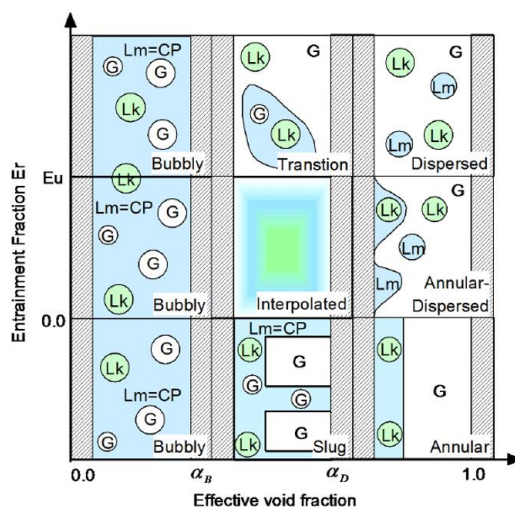


Figure III.3 Channel Flow Regime Map (CP: continuous phase, G: gas, Lk: k type liquid, Lm: m type liquid) from [Yamano et al., 2003]

After having computed each individual component to component coefficients in Table III.1, they are lumped into the final $K_{qq'}$ and K_{qs} momentum exchange function in accordance with the components' attribution into velocity fields by geometric averaging and arithmetic summation. Without details on the heavy mathematical operations in obtaining averaged functions, Table III.2 indicates the general summation rule.

Table III.2 Momentum exchange functions between velocity fields (K_{ik} between fluid i and k , K_{iS} between fluid i and structure)

	Field 1	Field 2	Field 3	Field 4	Field 5	Structure
Field 1	X	K_{12}	K_{13}	$K_{14} K_{15} K_{16} K_{17}$	K_{18}	K_{1S}
Field 2	X	X	K_{23}	$K_{24} K_{25} K_{26} K_{27}$	K_{28}	K_{2S}
Field 3	X	X	X	$K_{34} K_{35} K_{36} K_{37}$	K_{38}	K_{3S}
Field 4	X	X	X	X	$K_{84} K_{85} K_{86} K_{87}$	$K_{4S} K_{5S} K_{6S} K_{7S}$
Field 5	X	X	X	X	X	K_{8S}

In this default SIMMER-V procedure of defining momentum exchange coefficients, interactions between particle components are not taken into account (coefficient between particulate components are not computed in Table III.1). Moreover, simply including such coefficients would only symbolize momentum transfer in between two groups of particle components. However, interactions (collisions and friction) can occur among all particles independently of their material type. Supported by the conclusions drawn in section II.4, such particle-level interactions give rise to a new source of stress that influences the macroscopic behavior of the multi-fluid system. Incorporating these effects into SIMMER-V is one of the main objectives of the model development described in the next sections.

III.2 STATEMENT OF THE MODELLING CONTEXT

In this section, the assumptions, simplifications and constraints that comprise the framework for further development are listed. We highlight that the model development for particle dynamics concerns only the motion of reactor debris inside the transfer tubes.

Momentum allocation of particles

As it was explained in paragraph II.1.1, the degraded core inventory is expected to be highly abundant in solid fragments due to the low energetic behavior of the CFV core design in case of an ULOF scenario. Consequently, the dynamics of solid debris is expected to influence the relocation mechanism inside the mitigation transfer tubes. To have a better representation of the discharge flow and to be able to account for the specific physics of particulate matter, it is encouraged to treat the ensemble of particles as a distinct momentum field in SIMMER-V, following the statement on the scope of the thesis work in section II.3. The five momentum groups, out of which one is reserved for particulate components only, were defined by Figure II.3 right plot.

The ensemble of particles forms a separate momentum field in the frame of the Eulerian two-fluid approach.

Transfer tube representation in SIMMER

We have seen in paragraph I.3.1.2 that transfer tubes in reality are hexagonal channels and identical to regular fuel assemblies except that they are longer aiming to reach the lower sodium plenum. Due to the insufficient experimental and theoretical knowledge available about the effect of the flow cross section shape on the global motion of particle ensemble, the transfer tubes are simply characterized

III.2 Statement of the modelling context

by an equivalent hydraulic diameter and an internal surface area that can be computed for different geometries (analogous to current SIMMER approach for channels).

In the SIMMER-V code architecture, the one-dimensional flow topology map for channel flows determines the interphases not only for momentum exchanges but also for heat and mass transfer processes. Heat and mass transfers bring about vaporization, condensation, melting and freezing phenomena that are of high importance in reactor severe accident scenarios. In line with the 1D flow topology map, heat transfer correlations are intra-cell models developed as well for 1D geometries. This imposes the constraint to represent mitigation transfer tubes in 1D by a single radial and tangential cell. Changes occur along the flow path only in axial direction.

Transfer tubes are modelled as one-dimensional vertical cylindrical channels.

Particle properties

Regarding the particle properties, paragraph II.1.1 exposed that debris size and shape distribution can vary largely with different scenarios in different accidental stages. Simplifications applied for the numerical representation of degraded solid debris in SIMMER-V were detailed in section II.2. In the model development, we adapt to such constraints and therefore they are shortly recalled here.

Particle components (fuel, steel, control and fuel chunks) in SIMMER-V are spherical and have a user defined diameter, which is uniform for all particles of the given type. Even through, real reactor debris is far from being mono-sized or spherical, it is a common practice in numerical simulations to assume uniform particle size distribution or equivalently to use an average diameter representative for a collection of polydisperse asymmetrical particles [Clavier et al., 2015].

In addition, we note that unmolten fuel debris might dilate/swell significantly due to the presence of inter-granular gaseous fission products. Theoretically, they could be modelled as soft particles that undergo large plastic deformations without rupture. Their ability to change volume by varying their shape and size leads to enhanced space filling compared to hard particles and thus impacts the maximum packing limit. For realistic modelling of soft-particle materials at large deformations, it is necessary to combine an Eulerian continuum and a Lagrangian discrete representation of particles [Nezamabadi et al., 2015]. In addition, in most of these models, particles remain geometrically rigid, and their deformation is taken into account via specific force models. This combined Eulerian-Lagrangian approach is out of the PhD scope since SIMMER is a purely Eulerian continuum code. Following, particle components are modelled as not deformable hard spheres.

Particles of all components are considered to be spherical, rigid and represented by a volume averaged diameter.

Effect of heat and mass transfer

In order to focus solely on dynamic aspects, heat and mass transfer processes are not considered in the model development. However, in reactor severe accident scenarios, the momentum transfer is complemented with massive heat and mass transfer. Due to the high temperature differences between reactor components and the ongoing nuclear heat generation of fissile components, the impact of heat and mass transfer on the discharge performance has to be addressed.

Heat transfer inside the fluid phases affects the discharge velocity through variations in fluid (density and viscosity) and particle (density) properties with temperature. It is taken into account in SIMMER-V by recalculating densities and viscosities meshwise in each time step. Mass transfer involves freezing/melting and vaporization/condensation of reactor components along the flow path. Arising from the interaction between the molten mixture and tube wall, fuel crust can build up on the wall surface. Reaching boiling temperature in sodium bulk produces vapor bubbles that can detach from the particle/wall surfaces and mix with the flow or form a vapor film on the particle surface. Both modify the flow field around the particles and, presumably, alter the discharge velocity. Some of

these phase transition phenomena have the potential to interfere with the relocation process. The upward product of FCI (rapid heat transfer between high and low temperature liquid components), the loss of flow mobility due to excessive solidification, crust formation or their combined effect reduce the mixture mobility and hinder material removal. Consequently, only a part of the entering molten mass may arrive to the lower exit of the tube and being discharged to the core catcher. We conclude that heat and mass transfers have a substantial impact on the discharge performance. However, revisiting these models and evaluating of the resulting velocity perturbations is not the scope of this work (future R&D is proposed recently at CEA).

In a particulate system, besides conventional heat transfer, there is another type of heat generation. It is a two-step process with an intermediate energy dissipation state: firstly, the production of random fluctuating motion by viscous dissipation by the fluid phase, and secondly the dissipation of this fluctuating velocity into thermal heat mostly by inelastic collisions between grains. This process is neglected because conventional heat generation, through convection and conduction, is assumed to be dominant in reactor severe accident application in contrast to the heat produced by granular interactions.

The effect of heat and mass transfer on the particle velocity field is not the scope of model development. Heat generation due to granular collisions and interactions is neglected.

III.3 IDENTIFICATION OF TRANSFER TUBE REGIONS

The model development concerns the relocation of solid debris inside the transfer tubes. Accordingly, the improvements and new momentum terms presented in next sections will only be applied to transfer tubes regions in SIMMER. Thus, the meshes representing these regions have to be identified. With this purpose, a new input parameter, called RHEOLREG, is created. RHEOLREG defines three-dimensional rectangular regions by $(i, k, j)_{min}, (i, k, j)_{max}$ and labels the contained meshes as “transfer tubes” in which original SIMMER equations are replaced by new correlations. In order to remain consistent with the one-dimensional approach, the left i_{min} and right i_{max} radial and the circumferential k_{min} and k_{max} mesh coordinates of RHEOLREG region have to be identical. It is possible to specify several transfer tubes by multiple RHEOLREG parameters. It is an important feature in reactor simulations where the 21 mitigation devices are spatially distributed in the core.

III.4 MOMENTUM EXCHANGE TERMS FOR PARTICLES

In this section, we focus on the current momentum exchange processes, namely the interphase drag and the structure momentum exchange. In the frame of separate particle momentum approach, new improved closure terms are proposed. These terms aim to avoid the use of mixture viscosities, see section II.2, and to better describe the behavior of dense particle configurations.

III.4.1 Interphase momentum exchange

The momentum transfer between a multi-particle system and a surrounding fluid phase is derived from the generalization of single particle interaction forces. The dynamics of a single particle traveling through a bulk fluid involves several mechanisms following paragraph II.4.1. Among these, the drag and buoyancy force have been identified as dominant contribution to the interphase momentum exchange by several researchers [Clift et al., 2005]. As buoyancy is computed in standard way (by coupling the momentum equations through the pressure, see Eq. II.9) with negligible modelling uncertainty, we focus on the formulation of the drag force.

Generally, there are two types of formulas developed for fluid-solid drag. One type of correlations is based on the terminal velocity of a single particle in fluidized or settling beds. It assumes that the drag acting on a single particle is identical for all particles in the flow and thus the total drag acting on a particle ensemble is simply a multiplication of single drag forces. Following, the correlations are expressed as function of void fraction and single particle Reynolds number. This approach is

III.4 Momentum exchange terms for particles

encouraged for low particle contents [Ishii and Zuber, 1979]. The other branch of correlations for high particle concentrations is derived from packed-bed pressure drop experiments and expressed in the form of Ergun equation. These equations have to be supplemented by correlations for low values of the solid volume fraction.

The most widely referenced and validated model combining both types of correlations is the Gidaspow drag model, see Eq. III.6 written in term of particle-fluid momentum exchange function K_{pf} [Gidaspow, 1994]. The Gidaspow drag function is comprised of the Ergun and Wen & Yu equations:

$$K_{pf} = \begin{cases} \frac{3}{4} C_D \frac{\alpha_p \alpha_f \rho_f |\mathbf{v}_p - \mathbf{v}_f|}{\phi d_p} \alpha_f^{-2.65} & \text{if } \alpha_p < 0.2 \\ 150 \frac{\alpha_p^2 \mu_f}{\alpha_f \Phi^2 d_p^2} + \frac{1.75 \alpha_p \rho_f |\mathbf{v}_p - \mathbf{v}_f|}{\Phi d_p} & \text{if } \alpha_p \geq 0.2 \end{cases} \quad \text{Eq. III.6}$$

$$C_D = \frac{24}{Re_p} (1 + 0.15 Re_p^{0.687})$$

$$Re_p = \frac{\alpha_f \rho_f d_p |\mathbf{v}_p - \mathbf{v}_f|}{\mu_f}$$

where C_D is the drag coefficient (–), Re_p is the particle Reynolds number (–), Φ is the particle sphericity (–), and subscript p, f refer to particle and fluid phase.

The Ergun equation, Eq. III.6 when $\alpha_p \geq 0.2$, expresses that the pressure loss over a packed bed is caused simultaneously by viscous and kinetic energy losses. The viscous part is the Blake–Kozeny equation. It models the fluid motion through a packed bed as laminar flow inside a collection of curved passages (capillary tubes) crossing the particle bed. It applies Poiseuille's law to describe the laminar flow in circular pipes with a modified empirical constant taking into account that the capillary flow is not straight but zigzag around the particles. The kinetic contribution, when the flow is highly turbulent and dominated by inertial forces, is the Bruke-Plumer equation. It uses another empirical constant describing the flow tortuosity and a constant friction factor [Pal, 2019]. Even though the Ergun equation is originally developed for static particle bed, Gidaspow and others claim its validity for fluidized conditions [Gidaspow, 1994]. The extrapolation to fluidized conditions entails that particles do not interact between themselves. The derivation of the Wen & Yu equation, Eq. III.6 when $\alpha_p < 0.2$, is the extrapolation of the single sphere drag force. The multi-particle nature of system is taken into account through an empirical voidage function based on the experimental results of Richardson & Zaki [Lundberg and Halvorsen, 2008]. We note that the transition between Ergun and Wen & Yu equations at 20% particle volume fraction is discontinuous. In order to avoid such discontinuous behavior, smoothing functions can be introduced, for example the Huilin-Gidaspow model [Huilin and Gidaspow, 2003].

We choose to implement the Gidaspow correlation into SIMMER-V because it is valid in a wide range of particle concentrations and because it provides a sound physical description of particle-fluid friction in dense debris flows characteristic of a degraded CFV core. Another main interest towards the Gidaspow model comes from the fact that it is derived from experiments where particles and fluid have different velocities, which conforms to the separate particle momentum approach in SIMMER-V. Followig, Eq. III.6 is applied in the transfer tube regions for fluid-particle momentum exchange terms. Smoothing operation is not implemented providing that the code architecture defines K_{pf} exchange term already as an averaged product of different particle component terms, as it was explained in section III.1.2, such that the effect of a discontinuous transition can be assumed negligible in a multi-component system.

III.4.2 Momentum exchange of particles with structures

The structure momentum exchange of particles in SIMMER represents the frictional pressure loss due to particle interactions with the flow boundary. Since the one-dimensional momentum equations are obtained by the integration over the flow cross-sectional area of the axisymmetric Navier-Stokes equations, the only momentum dissipation term due to particle shearing, termed as $\tau_{w,p}$ (Pa), appears on the wall surface. The physics of particle-wall interactions depends on the nature of granular system and the flow conditions. For this reason, the formulation of the wall shear stress term is function of particle properties and volume concentration. The behavior of dense configurations will be discussed in the next sections.

In this chapter, we focus on the description of dilute particle flows in which the particle-fluid slip velocity is not negligible compared to bulk fluid velocity. Due to the settling motion of particles, they do not increase the liquid phase viscosity [Bartosik, 2020]. Correspondingly, mixture viscosities via the particle viscosity models in the structure momentum terms of real liquids are eliminated. The particle contribution to the frictional pressure loss in dilute systems is commonly approximated by the conventional Fanning friction equation assuming that the mobile particulate phase follows the general frictional force of fluid mechanics. This approach is derived from experimental observations on the vertical pneumatic and hydraulic transport of dilute particles [Garić-Grulović et al., 2014; Leung and Jones, 1986; Matsen and Grace, 2012]. The particle-structure momentum exchange is formulated as Eq. III.7.

$$K_{ps}\mathbf{v}_p = \frac{4\tau_{w,p}}{D_h} = \frac{4}{D_h} 0.5\alpha_p\rho_p f_p \mathbf{v}_p^2 \quad \text{Eq. III.7}$$

Where f_p is the solid particle friction factor (–) and D_h is the tube hydraulic diameter (m). For the friction factor, there are several empirical expressions proposed in the literature for different flow characteristics. The formulation we choose to implement into SIMMER-V will be discussed in paragraph III.5.3.

III.5 PARTICLE-PARTICLE INTERACTION FORCES

As it was demonstrated in paragraph II.4.2, the dynamic behavior of dense particulate suspensions is strongly influenced by particle-particle interactions such as inter-particle collisions, friction and permanent solid contacts. These mechanisms generate significant momentum transfer within the particulate phase and manifest in peculiar granular behavior, especially when approaching the jamming transition. Therefore, taking into account particle level interactions is crucial to the modelling of dense particulate systems. As it is currently not modelled in SIMMER-V (or indirectly through the apparent viscosity formulation that is used beyond its validity range and is therefore discarded in our work), this section is dedicated to investigate the modelling of particle-particle interactions.

The general concept to account for the effect of in-phase particle contacts (instantaneous collisions and longer duration friction) is to introduce a solid stress tensor σ_p in the particles' equation of motion [Jackson, 2000], see Eq. III.8:

$$\frac{\partial(\bar{\rho}_q \mathbf{v}_q)}{\partial t} + \sum_{m \in p} \nabla(\bar{\rho}_m \mathbf{v}_m \mathbf{v}_q) = -\alpha_q \nabla p_f - \nabla \cdot \sigma_p + \bar{\rho}_q g + \sum_{q'} K_{qq'} (\mathbf{v}_q - \mathbf{v}_{q'}) \quad \text{Eq. III.8}$$

$$\sigma_p = p_p \delta + \boldsymbol{\tau}_p \quad \text{Eq. III.9}$$

where p_f corresponds to fluid pressure (Pa) and σ_p solid stress tensor is composed of an isotropic normal pressure p_p (Pa) and a shear stress $\boldsymbol{\tau}_p$ (Pa) term, as in Eq. III.9 with δ being the Kronecker

operator (indicating that the pressure is on the diagonal of the tensor). Solid particle stresses are included with a negative sign because grains repel from high interaction rate regions and flow towards the negative gradients.

We note that the necessity to include particle phase stresses to account for the unique granular behavior has been recognized by JAEA as well. Correspondingly, model development to include shear and normal stresses has been realized by [Tagami and Tobita, 2014]. The development concerns the self-leveling phenomena of debris bed taking place in the lower plenum of SFRs. It is different from our case because it is a three-dimensional model, which aims to improve the bed's radial spreading and thus the estimation of bed thickness in quasi-static situations.

Following on our one-dimensional modelling and the channel geometry (with equivalent diameter D_h) of transfer tubes, the expression for solid stress tensor simplifies by considering that variations are only in axial z direction, that the flow is axisymmetric such that quantities are independent of θ , and that the shear stress appears on the wall surface [Leung and Jones, 1986].

$$\frac{\partial \sigma_p}{\partial z} = \frac{\partial p_{p,z}}{\partial z} + \frac{4\tau_{p,rz}}{D_h} \tag{Eq. III.10}$$

In order to have a closed set of equations, constitutive relation for σ_p in the form of Eq. III.10 has to be provided. We only consider empirical closures following the discussion on explicit formulations in paragraph II.4.3.2. However, the quantitative measurement of particle phase stresses is not so straightforward firstly because of the little experimental evidence that bears directly on the form of σ_p , and secondly because of the difficulties in appointing the measured stress between particles and fluid [Guazzelli and Pouliquen, 2018; Jackson, 2000].

III.5.1 $\mu(I)$ dense granular rheology

Concluding on the bibliographic study on granular systems in section II.4 and considering that our interest is to describe dense liquid-like particle configurations, we adopt constitutive equations for $p_{p,z}$ and $\tau_{p,rz}$ ($\tau_{p,rz}$ is denoted by τ_p in the following) based on $\mu(I)$ dense granular rheology [GDR MiDi, 2004]. The $\mu(I)$ rheology describes the rheological behavior of particle systems in which the frictional nature of the particle assembly becomes as important as the collisional. It is a phenomenological approach derived from a steady plane shear configuration of rigid, spherical particles immersed in viscous fluid, see in Figure III.4. Even though the simple shear origin of $\mu(I)$ rheology, it has been widely applied in recent years and proved accurate for other, more complex flow configurations such as bed load transport, sediment columns, granular collapse etc. [Maurin et al., 2016].

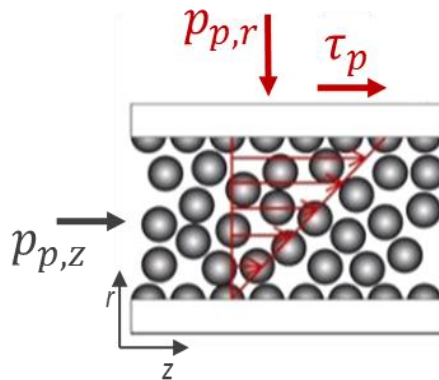


Figure III.4 Plane shear configuration in r - z frame with wall normal particle pressure $p_{p,r}$, flow cross-section normal particle pressure $p_{p,z}$ and wall shear stress τ_p after [Andreotti et al., 2013]

The shear cell in Figure III.4 can describe free surface flows, referred to as pressure–controlled shear, if particles are sheared at a constant rate $\dot{\gamma}$ and the pressure $p_{p,r}$ imposed on the top plate. Under these conditions, the volume fraction freely adjusts depending on the pressure and shear rate. Another shear cell configuration, referred to as volume-imposed, is the case when the distance between the plates is fixed and the medium is sheared at constant volume fraction. Under these conditions, the pressure $p_{p,r}$ and shear stress τ_p adjusting with the control parameters are the unknowns. This is well suited to investigate confined flows and therefore focus of interest regarding the model development for debris discharge through the transfer tubes.

Dimensional analysis shows that the rheology is controlled by a single dimensionless parameter, the inertial number I . The inertial number can be interpreted as the ratio between microscopic time scale of particle rearrangements and macroscopic time scale of flow deformation, illustrated in Figure III.5.

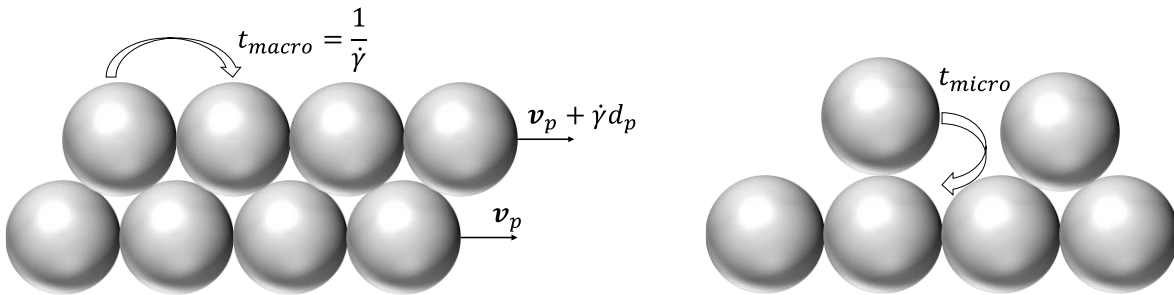


Figure III.5 Interpretation of macroscopic time scale of particle assembly deformation (left) and microscopic time scale of particle rearrangements (right) after [Andreotti et al., 2013]

The time scale of macroscopic granular deformation is linked to the mean shear rate in the flows, while the microscopic rearrangement varies with flow regimes. Flow regimes for immersed granular media are classified via the fluid-particle density ratio r and Stokes number St (comparing the free fall time to the viscous time) and distinguish viscous, free fall or grain inertia and turbulent particle flows. The motion of one particle to over another, Figure III.5 right plot, is governed by the viscous drag of displaced fluid in viscous regime; the unhindered free acceleration in grain inertia regime, and the turbulent drag in turbulent regime. Respectively the inertial number is formulated as shown in Figure III.6 [Cassar et al., 2005]. In the followings, we consider only viscous and grain inertia regimes because particles are heavier than fluids and C_D is generally smaller than one in reactor application, such that r is generally greater than unity.

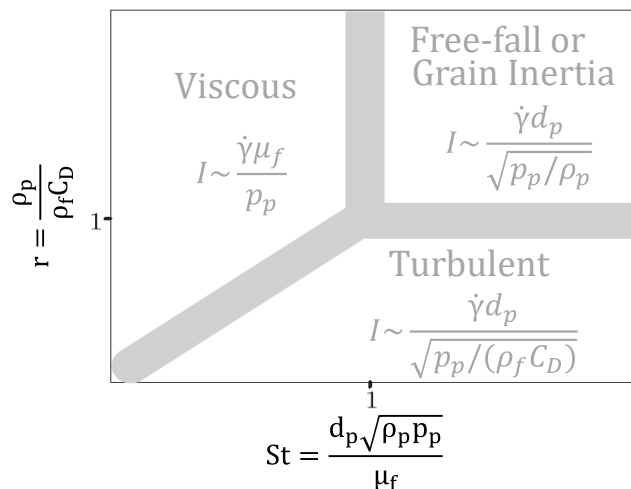


Figure III.6 Flow regimes for immersed granular media on (St,r) plane and the corresponding definition of inertial number after [Cassar et al., 2005]

III.5 Particle-particle interaction forces

Based on dimensional analysis, the $\mu(I)$ dense granular rheology states that the local shear stress is proportional to the local normal stress through the macroscopic friction coefficient μ that is function of I only. This friction law relates to Eq. III.11 with notations of Figure III.4.

$$\tau_p = \mu(I) p_{p,r} \quad \text{Eq. III.11}$$

The rheology is local in a sense that stresses depend only on the local variables. Contrary to the hydrodynamics of simple fluids, where the origin of non-locality is the pressure transmitted at the speed of sound, stresses inside a granular assembly establish locally due to the shorter range of collisional and frictional particle interactions. At the scale of mesh dimensions around 10 cm, corresponding to reactor studies with SIMMER-V and particles of a few millimeters, the locality of granular stresses is a reasonable assumption. Intra-mesh non-local effects due to radial particle migrations are neglected in line with the radially averaged momentum terms.

In volume-imposed shear, both τ_p and $p_{p,r}$ are unknown. The same dimensional reasoning imposes that stresses scale linearly with shear rate $\dot{\gamma}$ and fluid viscosity μ_f in viscous regime. In inertial flows, stresses scale quadratic with shear rate $\dot{\gamma}$ and grain size d_p , and proportional to particle density ρ_p , on analogy with Bagnold's law in paragraph II.4.3. Postulating that the dissipation due to viscous effects and due to grain binary interactions are additive [Trulsson et al., 2012], one being always negligible compared to the other, the granular shear stress and pressure are formulated by Eq. III.12 [Andreotti et al., 2013].

$$\begin{aligned} \tau_p &= \tau_p^i + \tau_p^v = \frac{\mu(I_i)}{I_i(\alpha_p)^2} \rho_p d_p^2 \dot{\gamma}^2 + \frac{\mu(I_v)}{I_v(\alpha_p)} \mu_f \dot{\gamma} \\ p_{p,r} &= p_{p,r}^i + p_{p,r}^v = \frac{1}{I_i(\alpha_p)^2} \rho_p d_p^2 \dot{\gamma}^2 + \frac{1}{I_v(\alpha_p)} \mu_f \dot{\gamma} \end{aligned} \quad \text{Eq. III.12}$$

Where subscripts i, v refer to inertial and viscous regimes and superscripts s, n refer to shear and normal components. Eq. III.12 can serve as constitutive law for solid stresses arising from particle-particle interactions if expressions are provided for:

- solid volume fraction law describing $I(\alpha_p)$ variations,
- macroscopic friction coefficient $\mu(I)$,
- shear rate $\dot{\gamma}$ in 1D configuration,
- transformation of radial to vertical pressure ($p_{p,z}$ instead of $p_{p,r}$ in Figure III.4),
- particle density (in the context of 4 particulate components in SIMMER-V),
- fluid viscosity (in the context of multiple fluid components in SIMMER-V).

These expressions are detailed in the six following sub-sections III.5.1.1 to III.5.1.6. The last sub-section III.5.1.7 is dedicated to some considerations on the limits of $\mu(I)$ rheology.

III.5.1.1 Closures for solid volume fraction law

The variation of solid fraction with inertial number $\alpha_p(I)$ is described by dilatancy laws. Assuming that dilatancy laws is monotonic, they can be inverted to obtain expression for the variation of inertial number with solid volume fraction $I(\alpha_p)$. Dilatancy laws are most often modelled as power functions of I based on experimental data and best-fitted numerical results of discrete-element simulations. The commonly used dilatancy equation writes as Eq. III.13 [Maurin et al., 2016] and after inversion, the solid volume fraction law has the form of Eq. III.14:

$$\alpha_p(I) = \frac{\alpha_{MP}}{1 + cI^b} \quad \text{Eq. III.13}$$

$$I(\alpha_p) = \left(\frac{\alpha_{MP} - \alpha_p}{c\alpha_p} \right)^{1/b} \quad \text{Eq. III.14}$$

where α_{MP} stands for the maximum packing limit (–) and c, b are dimensionless rheology parameters specific to the considered system. The validity of Eq. III.13 [Boyer et al., 2011] is for volume fractions ranging from 40% to 58.5%, but found to accurately reproduce experimental measurements down to 30% by [Deboeuf et al., 2009]. Therefore, we establish 30% as the lower applicability limit of dense granular rheology. Below this concentration, particle-particle interaction forces are generally modelled by the KTGF, see paragraph II.4.3.2.

Towards higher concentrations, the dynamics becomes controlled by permanent contact networks between particles and increasingly correlated in space. Close to the maximum packing limit, the rheology results from geometrical constraints and interlocking between the particles. In this extreme regime of concentration, a phase transition from mobile to jammed particle system takes place, the suspension jams into an “amorphous” solid. The characteristics of the phase transition are displayed by the percolation theory. Percolation describes the connectivity of large number of objects that possess spatial extent, and their spatial relationships are statistically prescribed [Hunt et al., 2014]. A core concept of percolation theory applied to granular media is that the constitutive relations are singular at maximum packing limit α_{MP} . The singularity of rheological properties at $\alpha_{MP} \cong \alpha_p$ is inherent to particulate systems representing jamming transition in which flow is inhibited. It is equivalent to the divergence of τ_p and $p_{p,r}$ with $(\alpha_{MP} - \alpha_p)$ on the power of $1/b$ or $2/b$ (viscous and inertial) predicted by Eq. III.12 and Eq. III.14. However, the percolation theory provides a different dilatancy law and a different exponent governing the rigidity transition. The theoretical description of this exponent is built on the cluster properties of permanent contacts and on the analysis of possible deformation modes of the granular packing close to jamming [Düring et al., 2016; Guazzelli and Pouliquen, 2018]. Accordingly, a different scaling is applied for the dilatancy laws by Eq. III.15 and after inversion Eq. III.16.

$$\alpha_p(I) = \alpha_{MP} - cI^b \quad \text{Eq. III.15}$$

$$I(\alpha_p) = \left(\frac{\alpha_{MP} - \alpha_p}{c} \right)^{1/b} \quad \text{Eq. III.16}$$

We assume that particle-particle contact networks start to appear on a large scale above random loose packing. Random loose packing corresponds to the particle concentration that is obtained by allowing particles to freely settle and fill the available space. For monodispersed spherical particles, it is around 55% [Onoda and Liniger, 1990]. Therefore, the transition from Eq. III.14 to Eq. III.16 at which percolation theory becomes well-founded is set to be at ~55% particles concentration. The rheology parameters considered for inertial and viscous regimes below and above percolation threshold are shown in Table III.3. In case of inertial flows at high particle concentrations, there is no clear consensus on the value of exponent b . It originates from the fact that inertial flows appear to be strongly affected by characteristics of inter-particle friction [DeGiuli et al., 2015]. From the range of values displayed in Table III.3, we apply 0.71 because it is close to the mean and leads to the same divergence of stresses as in viscous regime due to its inverse square value in Eq. III.12 by $1/0.35 = 2/0.72 = 2.8$.

III.5 Particle-particle interaction forces

Table III.3 Rheology parameters adopted for $\mu(I)$ rheology up to and above 55 % particle concentration

	Inertial regime from [Chauchat, 2018] up to 55% particle concentration ¹⁹	Viscous regime from [Boyer et al., 2011] up to 55% particle concentration ²⁰	Inertial regime from [DeGiuli et al., 2015] above 55% particle concentration ²¹	Viscous regime from [DeGiuli et al., 2015] above 55% particle concentration
	Eq. III.14		Eq. III.16	
c	0.67	1	1	1
b	1	0.5	[0.35-0.87] 0.71	0.35

III.5.1.2 Closures for macroscopic friction coefficient

The experimentally fitted form of macroscopic friction coefficient writes as Eq. III.17. This formulation of $\mu(I)$ is found not to vary with grain microscopic properties such as the coefficient of restitution or the inter-particle friction [Forterre and Pouliquen, 2009].

$$\mu(I) = \left(\mu_s + \frac{\mu_2 - \mu_s}{1 + I_0/I} \right) \quad \text{Eq. III.17}$$

Where μ_s is the static friction coefficient (–), μ_2 is the empirical dynamical friction coefficient (–) and I_0 is an empirical parameter of the rheology. Eq. III.17 reflects the experimentally observed saturation of macroscopic friction coefficient toward μ_s for quasi-static flows where $I \rightarrow 0$, and the convergence towards μ_2 for rapid flows where $I \rightarrow \infty$. The experimentally fitted values for inertial and viscous regime are given in Table I.1.

Table III.4 Rheology parameters

	Inertial regime from [Jop et al., 2005] ²²	Viscous regime from [Boyer et al., 2011]
μ_s	0.38	0.7
μ_2	0.64	0.32
I_0	0.3	0.005

We remark that the derivations of solid fraction laws in III.5.1.1 and macroscopic friction coefficient closures are purely phenomenological. The microscopic physical explanation behind is still subject of active research. Therefore, the precise rheological description of phenomena determined by the microstructural characteristics of the system is beyond the scope of $\mu(I)$ dense granular rheology. This is the case for jamming transition, whose complete understanding is still not fully developed. With the here presented dilatancy laws, we intend to reproduce a global rheological behavior of a particle assembly.

III.5.1.3 Area-averaged vertical pressure

In order to comply with the one-dimensional solid stress model of Eq. III.10, the normal stress acting on the tube wall $p_{p,r}$ has to be expressed by the area-averaged vertical normal stress $p_{p,z}$. It can be

¹⁹ Numerical simulation of unidirectional sheet flow and its comparison to experimental data on irregularly shaped PMMA particles of $d_p = 3 \text{ mm}$ in air and on sand/plastic spheres of $d_p = 0.16 - 1.7 \text{ mm}$ in water

²⁰ Experiment: pressure-imposed annular shear cell. Granular matter/fluid: PMMA spheres of $d_p = 1.1 \text{ mm}$ water zinc chloride mixture and polystyrene spheres of $d_p = 0.58 \text{ mm}$ in polyethylene glycol

²¹ Theoretical framework based on percolation theory

²² Experiment: particles released from hopper. Granular matter/fluid: glass beads of $d_p = 0.5 \text{ mm}$ in air

done by measuring the principal stresses in a triaxial apparatus (a soil specimen confined in a pressurized cylindrical cell), and applying Mohr-Coulomb condition to relate the maximum and minimum principal stresses to the internal friction angle δ . The maximum principal stress corresponds to the vertical stress in the direction of the cylinder axis, while the minimum equals to the wall normal stress components [Khamseh, 2014]. With the terminology of Figure III.4, it writes as Eq. III.18. This expression is applied to fluidized conditions as well by [Leung and Jones, 1986].

$$p_{p,r} = \frac{1 - \sin\delta}{1 + \sin\delta} p_{p,z} \quad \text{Eq. III.18}$$

The value of internal friction angle depends on soil properties and material preparation. In lack of such information in reactor scenarios, we chose $\delta = 35^\circ$ as an average for metallic powders [Zegzulka et al., 2018].

III.5.1.4 Radial velocity profile

In the one-dimensional transfer tube problem with a single radial mesh resolution, the shear rate $\dot{\gamma} = \partial v / \partial r$ remains unknown due to the integration of the axial velocity over the flow cross-section. To resolve this issue, we apply the classical 1D closure hypotheses of decomposing the velocity $v(r, z)$ into a dimensionless shape of the velocity profile ϕ (depending only on $\bar{r} = r/R$) and the average axial velocity $v(z)$ computed by the 1D momentum balance via Eq. III.19 [Ghigo et al., 2018].

$$v(r, z) = \phi(r)v(z) \quad \text{Eq. III.19}$$

It is now the dimensionless shape of the velocity profile, which is lost by the integration process. Implementing an a priori assumption on ϕ , the shear rate can be computed. To do so, we take advantage of the experimentally obtained particle velocity profiles of [Sumner et al., 1991]²³. In this experiment, the strongest radial gradient of axial velocity is measured near the wall due to particles' tendency to migrate towards the center. The velocity distributions normalized to the mean bulk velocity are plotted in Figure III.7 (no information is provided by [Sumner et al., 1991] about the error bars of the experimental data).

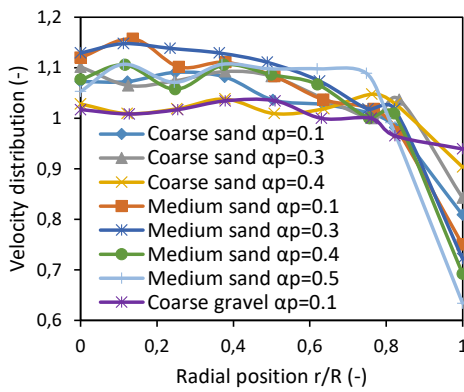


Figure III.7 Velocity distributions reproduced from Sumner [Sumner et al., 1991]

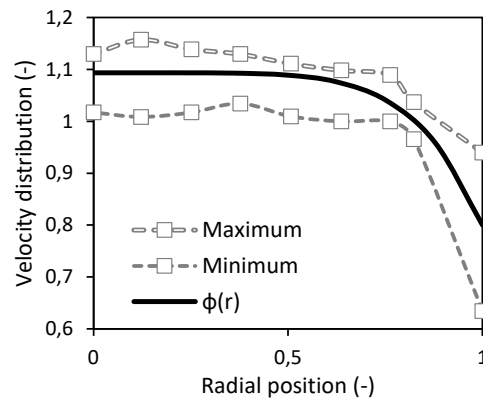


Figure III.8 Velocity distributions with maximum and minimum values of Sumner [Sumner et al., 1991] and dimensionless shape of the velocity profile by Eq. III.19 with best fit $a_w = 0.8$ and $a_1 = 0.22$

²³ Transport of dense slurries in vertical water flow circuit. Particles of coarse sand $d_p = 0.78$ mm, medium sand $d_p = 0.47$ mm, coarse gravel $d_p = 1.7$ mm

III.5 Particle-particle interaction forces

Next, we apply a modified form of the general fluid power law for circular ducts by Eq. III.20 [Simpson and Janna, 2008], and fit it between the maximum and minimum velocity values of Sumner. The addition of a_w is necessary to account for the sliding motion of particles along the wall (particle velocity at the wall is different from zero), while the inclusion of a_1 is convenient to reproduce flatter distributions.

$$\phi(r) = a_w + a_1 \frac{3l+1}{l+1} \left[1 - \left(\frac{r}{R} \right)^{\frac{l+1}{l}} \right] \quad \text{Eq. III.20}$$

Where l is the flow behavior index indicating the degree of non-Newtonian characteristics of the fluid: Newtonian $l = 1$, dilatant or shear-thickening $l > 1$, or pseudo-plastic or shear-thinning $l < 1$ behaviors. Figure III.8 shows the best fitted curve achieved by $l = 0.2$ pseudo-plastic behavior, $a_w = 0.8$ and $a_1 = 0.22$. Computing the derivative of Eq. III.20 by ∂r and taking its value on the wall, we arrive to Eq. III.21 for the shear rate:

$$\dot{\gamma} = a_1 \frac{6l+2}{l} \frac{v(z)}{D_h} = c_s \frac{v(z)}{D_h} \quad \text{Eq. III.21}$$

where the c_s dimensionless parameter is used in SIMMER-V to express velocity shear rate proportionality ($c_s = 3.52$ with best-fitted experimental data). We recognize that the a priori choice of velocity profile, the averaging procedure cancelling out radial fluctuations of the axial velocity and consequently the magnitude of shear rate through c_s significantly affects particle dynamic behavior. It is straightforward that a unique value of c_s cannot be representative to a wide range of flow configurations and thus, at current state of model development, we consider c_s as an adjustable parameter.

To improve the simulation of particle dynamics by $\mu(I)$ rheology by refining the shear rate equation, a first step should aim at incorporating the dependence of velocity profile on solid concentration. It is commonly recognized that particles migrate cross-stream across the pipe especially in highly inertial flows. Particles tend to move away from the wall creating a sharp concentration profile near the wall and a peak or plateau concentration towards the center. Increasing the particle content, the plateau expands radially because of more particles to pack geometrically in the same space around the center. Since the local particle velocity is function of local concentration, the radial velocity profile and so the shear rate vary with average particle concentration [Han et al., 1999]. In addition to the effect of solid concentration, precise knowledge on transfer tube wall roughness (and its potential surface degradation during accident evolution) and reactor debris properties is necessary to improve shear rate prediction. At current state of research, we lack this information. Overall, we consider the form of Eq. III.21 as a fairly good approximation for the particle shear rate.

III.5.1.5 Particle density

In SIMMER-V, four particle components with varying density are grouped into one velocity field. Namely, fuel particles of $\rho_{p,1} \approx 10000 \text{ kg/m}^3$, steel particles of $\rho_{p,2} \approx 7 - 8000 \text{ kg/m}^3$, control particles of $\rho_{p,3} \approx 2500 \text{ kg/m}^3$ and chunks of $\rho_{p,4} \approx 10000 \text{ kg/m}^3$ typical density. In constitutive law for inertial regime in Eq. III.12, the particle density appearing can be considered as an average value by Eq. III.22.

$$\rho_p = \frac{\rho_{p,1}\alpha_{p,1} + \rho_{p,2}\alpha_{p,2} + \rho_{p,3}\alpha_{p,3} + \rho_{p,4}\alpha_{p,4}}{\alpha_{p,1} + \alpha_{p,2} + \alpha_{p,3} + \alpha_{p,4}} \quad \text{Eq. III.22}$$

We note that control particles are generally not used in current reactor calculations by SIMMER-V mainly because control pin degradation into particles is not considered following conservatism²⁴. Excluding the density of control particles reduces the averaging error. In addition, the particle density is the only control parameter in inertial regime that is encountered mainly in gaseous environment where the density difference between particle ensemble and fluid is considerably higher than the difference within particle components.

III.5.1.6 Fluid viscosity

The constitutive law for viscous regime by Eq. III.12 contains the fluid viscosity. In the multiphase multicomponent phenomenon of degraded core relocation, the definition of fluid viscosity is not straightforward. Fluid surrounding the particles can be liquid fuel lf , liquid steel ls , sodium s or gas with very different associated viscosities. At this point, we adapt to the standard SIMMER-V approach of defining average liquid and gas viscosities by Eq. III.23 corresponding to bubbly and dispersed flow regimes, see Figure III.3.

$$\mu_f = \left\{ \begin{array}{ll} \frac{\alpha_{lf} + \alpha_{ls} + \alpha_s}{\frac{\alpha_{lf}}{\mu_{lf}} + \frac{\alpha_{ls}}{\mu_{ls}} + \frac{\alpha_s}{\mu_s}} & \text{in bubbly regime with liquid continuous phase} \\ \mu_g & \text{in dispersed regime with gas continuous phase} \end{array} \right\} \quad \text{Eq. III.23}$$

To distinguish between bubbly and dispersed regimes, we follow the original concept of flow topology by Figure III.3, and adapt the separation²⁵ illustrated in Figure III.9.

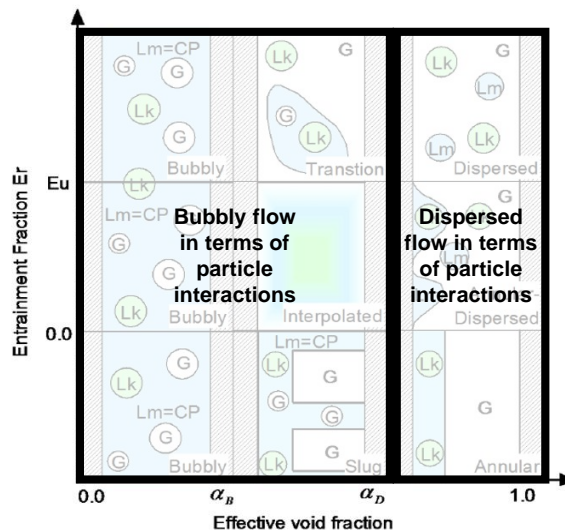


Figure III.9 Flow regimes in terms of particle-particle interactions

III.5.1.7 Limits of the rheology

The $\mu(I)$ dense granular rheology is a current research area with several aspects still remaining to be explored. In this paragraph, we describe briefly the limitations relevant to our application. The description follows [Forterre and Pouliquen, 2009].

²⁴ Conservatism in nuclear safety implies assuming the worst-case scenario. Since control particles entering into the core center would reduce reactivity and power, a conservative approach neglects their effect.

²⁵ We are obliged to eliminate the interpolated regimes between α_B and α_D because the standard SIMMER-V method of averaging momentum coefficients over the bubbly and dispersed fractions of the mesh would cause inconsistencies in defining global particle volume fractions and their distance from maximum packing concentration (being a global value independent of flow regime).

One challenge lays in relating the mechanics of the particle interactions at the microscopic scale to the macroscopic properties based on which constitutive equations are defined. This indicates that the complete rheological behavior of phenomena that requires the thorough understanding of grain scale interactions is still challenging. An example is the jamming transition. In the frame of $\mu(I)$ dense granular rheology, it is described by a simple Coulomb criterion through a unique friction angle μ_s ($\mu(I) = \mu_s$ when $I \rightarrow 0$). In reality, the transition is more complex and depends on several other aspects, for instance history of previous deformations or hysteresis effects, that are not taken into account by the $\mu(I)$ rheology. In addition, the distinction between viscous and inertial regimes is not clearly established when jamming occurs.

Another limitation concerns the description of quasi-static flows. In very dense and slow flows, non-local effects often play a role on the macroscopic dynamic behavior. Non-local effects are related to local rearrangements that influence the stress distribution far from the initial location. These effects are mainly encountered in quasi-static flows. However, the case of the jamming transition can be mentioned here as well, due to the large spatial extension of particle clusters.

The third limitation addresses the transition into dilute fast flows dominated by instantaneous collisions. The dilute regime is commonly studied through the KTGF. The KTGF provides constative equations for normal and shear granular stresses based on the fluctuating kinetic energy of individual grains. Even through this approach is well developed and widely investigated, there is little research in the literature on the reconciliation between dense collisional-frictional and dilute binary collisional-kinematic stresses. In lack of such information, we consider a simplified expression for shear stress (see section III.4.2) and vanishing particle pressure at the dilute limit below 30% solid content (see paragraph III.5.1.1).

III.5.2 Numerical implementation

In this part, the numerical implementation of particle pressure gradient and shear stress term into SIMMER-V is presented. The spatial discretization is performed on an Eulerian staggered mesh on analogy with other momentum terms detailed in section III.1.2. The one-dimensional axial mesh resolution is illustrated in Figure III.10. Cell centers are denoted by $j - 1$, j and $j + 1$, and cell edges by $j \pm 1/2$. In the following, radial and theta coordinates are not displayed and the p index referring to the particle phase variables is dropped for simplicity.

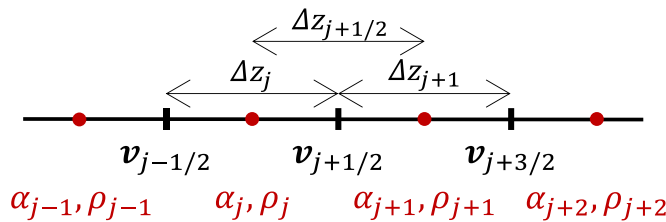


Figure III.10 Eulerian staggered mesh in axial direction with j axial coordinate

The temporal discretization is designated by superscripts n , $n + 1$. In order to simplify the discretized equation, we define the parameters of Eq. III.24 that group only cell center variables.

$$a_i = \frac{\rho_p d_p^2}{I_i(\alpha_p)^2} \left(a_1 \frac{6n + 2}{nD_h} \right)^2$$

$$a_v = \frac{\mu_f}{I_v(\alpha_p)} a_1 \frac{6n + 2}{nD_h}$$

Eq. III.24

With Eq. III.24, the spatial and temporal discretized shear stress writes as Eq. III.25.

$$\tau_{j+1/2}^{n+1} = \langle \mu(I_i) a_i \rangle_{j+1/2}^{n+1} |v_{j+1/2}^n| v_{j+1/2}^{n+1} + \langle \mu(I_v) a_v \rangle_{j+1/2}^{n+1} v_{j+1/2}^{n+1} \quad \text{Eq. III.25}$$

The form of shear stress is based on the already existing particle-wall momentum exchange term in SIMMER-V, with a semi-implicit time discretization. A fully implicit treatment is not feasible in SIMMER-V since the velocity solution algorithm currently applies a linear Gaussian elimination method.

$$\langle \mu(I) a \rangle_{j+1/2}^{n+1} = \langle \mu(I) a \rangle_{j+1/2}^n \frac{\bar{\rho}_p^{n+1}}{\bar{\rho}_p^n} \quad \text{Eq. III.26}$$

Cell center variables are projected to cell faces considering downstream values through Eq. III.27. The downstream projection is not a common practice due to its unstable nature. Although, for staggered meshes where the velocity is defined on the upper cell face, this method permits to restrict particle inflow into meshes that are closely packed. Following on the higher numerical stability (in comparison to conventional upstream implementation) observed in our simulations with SIMMER-V, we pragmatically implement downstream projection by Eq. III.27. Additionally, a “no projection” method through Eq. III.28 is implemented because it provided higher numerical stability in reactor simulations. We note that the two method are identical for downward relocation, being the scope of interest.

$$\langle \mu(I) a \rangle_{j+1/2} = \begin{cases} \langle \mu(I) a \rangle_{j+1} & \text{if } v_{j+1/2} > 0 \\ \langle \mu(I) a \rangle_j & \text{if } v_{j+1/2} < 0 \end{cases} \quad \text{Eq. III.27}$$

$$\langle \mu(I) a \rangle_{j+1/2} = \langle \mu(I) a \rangle_j \quad \text{Eq. III.28}$$

The numerical implementation involves the modification of current A_{ps}^n and B_{ps}^n momentum coefficients on condition that the particle fraction is higher than 30%. The dependence of $\mu(I)$ on I and consequently on p_p (according to the definition of I for inertial and viscous regime in Figure III.6) is taken into account explicitly, meaning that the macroscopic friction coefficient is function of particle pressure at the same location and at the same time step.

Regarding the gradient of the particle pressure, the time and spatially discretized form at location $j \pm 1/2$ writes as Eq. III.29. The particle pressure gradient is computed in a new subroutine.

$$\begin{aligned} \frac{p_{j+1}^n - p_j^n}{\Delta z_{j+1/2}} &= \frac{1 + \sin\delta}{1 - \sin\delta} \left[a_{i,j+1}^n |v_{j+1}^n| v_{j+1}^n - a_{i,j}^n |v_j^n| v_j^n \right] \\ &\quad + \frac{1 + \sin\delta}{1 - \sin\delta} \left[a_{v,j+1}^n v_{j+1}^n - a_{v,j}^n v_j^n \right] \end{aligned} \quad \text{Eq. III.29}$$

The formulation of the particle pressure gradient follows the method used for the particle shear stress term except for the explicit time treatment. In terms of modelling consistency, a semi-implicit treatment identical to the shear stress would be more appealing. However, the semi-implicit temporal discretization of a spatial gradient requires a complex numerical treatment that is out of the PhD scope. Since coefficients a_i and a_v are evaluated at cell centers, only particle velocities have been approximated in Eq. III.29 to obtain cell center values from cell face quantities. As a result of several trial and error analyses on different spatial discretization schemes, we found that the simplest projection by Eq. III.30 provides the best compromise in terms of numerical stability and physical consistency between shear and normal particle stresses.

III.5 Particle-particle interaction forces

$$\begin{aligned} v_{j+1}^n &= v_{j+1/2}^n \\ v_j^n &= v_{j-1/2}^n \end{aligned} \tag{Eq. III.30}$$

III.5.2.1 Regularization

When implementing $\mu(I)$ dense granular rheology into SIMMER-V, regularization techniques have to be introduced in order to overcome convergence problems near singularities and numerical precision errors. The latter is necessary to comply with SIMMER-V floating-point arithmetic settings on dealing with small and large quantities.

Singularities appear when the particles assembly becomes fully packed. In this case, the inverse of solid volume fraction closures (Eq. III.14 and Eq. III.16) diverges with $(\alpha_{MP} - \alpha_p) \rightarrow 0$, parallel to the singularity in the macroscopic friction coefficient closure with $I \rightarrow 0$ in Eq. III.17. As it was explained in section III.5.1.1, the divergence ensures the existence of a flow threshold being a characteristic feature of granular matter. Numerically it can be treated by implementing a regularization technique. To do so, we apply a simple maximum function comparing the value of interest with a regularization parameter r_{small} . Conclusive to our test simulations, we consider $r_{small} = 10^{-8}$ sufficiently small to reproduce the divergent behavior in SIMMER-V. We note that there are other more complex and probably higher accuracy regularization techniques in the literature, see for example the work of [Chauchat and Médale, 2014]. Following, the regularized form of Eq. III.17 writes as Eq. III.31. Similarly, Eq. III.14 and Eq. III.16 after regularization become Eq. III.32 where $k = 1$ in viscous regime and $k = 2$ in inertial regime.

$$\mu(I) = \left(\mu_s + \frac{\mu_2 - \mu_s}{1 + I_0 / \max(I, r_{small})} \right) \tag{Eq. III.31}$$

$$\frac{1}{I(\alpha_p)^k} \cong \left(\frac{1}{\max(\alpha_{MP} - \alpha_p, r_{small})} \right)^{k/n} \tag{Eq. III.32}$$

In packed particle beds, after reaching flow threshold, particle stresses are saturated at their maximum value. From test simulations, we observe that particle shear stress reaches stable maximum value which satisfies the momentum balance at static conditions. Particle pressure behaves as expected by Eq. III.1, proportional to the shear stress. However, large gradients appear in the proximity of bed interface during the numerical convergence into a packed state. It is presumably due to the combined effect of large mesh sizes and explicit time treatment of particle pressure which produces abrupt variations between meshes filled up with particles close to maximum packing limit. Attributed to the asymptotic increase of particle pressure within these meshes, even a small change in solid concentration causes large jumps in the particle pressure gradient. Such increases lead to instabilities in the calculation. We conclude that it does not originate from the spatial discretization of particle pressure gradient, since instabilities were detected in case of each discretization technique tested during the PhD work. At the current state of model development, we do not have a more sophisticated option to resolve this issue than limiting the value of particle pressure gradient to $10^4 Pa/m$ (value deduced from test runs). We mention also that interface problems are commonly observed in SIMMER-V owing to the velocity evaluation at the upper edge of the computational cells. Consequently, further investigation on this subject is proposed.

Numerical precision errors are related to divisions by the equivalent hydraulic diameter in pool regimes. In SIMMER-V, the hydraulic diameter is computed in standard way when structure

components are present inside the mesh. When there is no structure indicating that the mesh is part of an open pool, the hydraulic diameter has a large value, around $10^{20} m$. This feature of hydraulic diameter computation also assures that particle wall shear stress disappears when structures are lost due to the inverse proportionality of stresses with D_h . Even though $\mu(I)$ dense granular rheology equations are exclusively defined at the beginning of the calculation for vertical channels housed by structure components, situations during the severe accident evolution can develop in which tube walls disintegrate such that a mesh is seen as a pool by the code. In these meshes, dividing by the power of D_h brings about numerical precision errors. The division appears in Eq. III.10 through the definition of wall shear rate and in the constitute equation for 1D shear rate in Eq. III.21. Therefore, we implement a regularization functions for the hydraulic diameter. The regularized form writes as Eq. III.33 with regularization parameters $r_{small} = 10^{-20}$ and $r_{large} = 10^{20}$. These values correspond to the smallest and largest numbers that SIMMER-V floating-point arithmetic effectively manages.

$$D_h = \min[\max(D_h, r_{small}), r_{large}] \quad \text{Eq. III.33}$$

III.5.3 Continuity considerations

Having defined all parameters in the constitutive equations describing the shear dependent frictional rheology, shear and normal solid stresses write as Eq. III.34. Eq. III.34 incorporates wall shear stress at solid concentrations where particle-particle interactions are negligible, based on Eq. III.7.

$$\tau_p = \begin{cases} 0.5\alpha_p\rho_p f_p v_p^2 & \text{if } \alpha_p < 0,3 \\ \mu(I_i) \left(\frac{c_i\alpha_p}{\alpha_{MP} - \alpha_p} \right)^2 \rho_p d_p^2 \dot{\gamma}^2 + \mu(I_v) \left(\frac{c_v\alpha_p}{\alpha_{MP} - \alpha_p} \right)^2 \mu_f \dot{\gamma} & \text{if } 0,3 \leq \alpha_p < 0,55 \\ \mu(I_i) \left(\frac{c_p}{\alpha_{MP} - \alpha_p} \right)^{2,8} \rho_p d_p^2 \dot{\gamma}^2 + \mu(I_v) \left(\frac{c_p}{\alpha_{MP} - \alpha_p} \right)^{2,8} \mu_f \dot{\gamma} & \text{if } 0,55 \leq \alpha_p < \alpha_{MP} \end{cases} \quad \text{Eq. III.34}$$

$$p_{p,z} = \begin{cases} 0 & \text{if } \alpha_p < 0,3 \\ \frac{1 + \sin\delta}{1 - \sin\delta} \left[\left(\frac{c_i\alpha_p}{\alpha_{MP} - \alpha_p} \right)^2 \rho_p d_p^2 \dot{\gamma}^2 + \left(\frac{c_v\alpha_p}{\alpha_{MP} - \alpha_p} \right)^2 \mu_f \dot{\gamma} \right] & \text{if } 0,3 \leq \alpha_p < 0,55 \\ \frac{1 + \sin\delta}{1 - \sin\delta} \left[\left(\frac{c_p}{\alpha_{MP} - \alpha_p} \right)^{2,8} \rho_p d_p^2 \dot{\gamma}^2 + \left(\frac{c_p}{\alpha_{MP} - \alpha_p} \right)^{2,8} \mu_f \dot{\gamma} \right] & \text{if } 0,55 \leq \alpha_p < \alpha_{MP} \end{cases}$$

Where c_i, c_v, c_p refer to dimensionless coefficient of dilatancy laws for inertial, viscous and percolation theory regimes respectively. Eq. 1.33 reflects the distinction between three granular regimes according to the value of solid concentration. Such discretization of physics brings about continuity issues when switching from dilute $\alpha_p < 0.3$ to moderately dense $0.3 < \alpha_p < 0.55$ and from moderate dense to dense $\alpha_p > 0.55$ regimes. The discontinuity is not physical and therefore additional consideration is required to smoothen the transition. In this context, we introduce continuity parameters to comply with the numerical and physical consistency. These operations ensure the smooth transition between granular regimes preserving the scaling behavior in each.

The transition between dilute and moderately dense regimes is matter of concern in the particle shear stress term. The equations of these regimes are deduced from different physical bases and so their transition is not evident. To resolve this issue, we take advantage of the solid friction factor. By imposing equality of shear stress expression just below 30% described by the conventional Fanning equation and just above 30% described by the $\mu(I)$ dense granular rheology, we obtain an expression for solid friction factor as Eq. III.35.

III.6 Discussion on fluid pressure

$$f_p = \mu(I_i) \left(\frac{c_i}{\alpha_{MP} - 0.3} \right)^2 \frac{0.3d_p^2 c_s^2}{0.5D_h^2} + \mu(I_v) \left(\frac{c_v}{\alpha_{MP} - 0.3} \right)^2 \frac{0.3\mu_f c_s}{0.5\rho_p D_h |v_p|} \quad \text{Eq. III.35}$$

In section III.4.2, we have seen that there is a considerable uncertainty on the formulation of solid friction factor. Equations in the literature show no clear consensus on the parameters and their proportionality influencing the evolution of solid friction factors. Thus we assume that, as long as the characteristic form of Eq. III.7 is preserved, such arbitrary formulation of f_p by Eq. III.35 brings no physical inconsistency. We also note that unifying granular rheology over the whole range of volume fractions is challenge of current research as it was highlighted in paragraph II.4.3.

The transition between moderately dense and dense regimes appear in the formulation of both particle pressure and shear stress terms. The discontinuity arose from the switch from 2 to 2.8 exponent at 55% solid concentration. To resolve this issue, we introduce a multiplication factor β when $\alpha_p > 0.55$. The factor is derived by equating the expressions just below and just above the transition point (for inertial and viscous part of stresses separately) and substituting $\alpha_p = 0.55$. Following the multiplication factor writes as Eq. III.36 with subscript $k = i, v$ referring to the coefficients in inertial and viscous regimes respectively.

$$\beta_k = \frac{(0.55c_k)^2}{c_p^{0.8}} (\alpha_{MP} - 0.55)^{0.8} \quad \text{Eq. III.36}$$

Following, Figure III.11 illustares the charecteristic shape of particle pressure and shear stress after applying contiunity corrections.

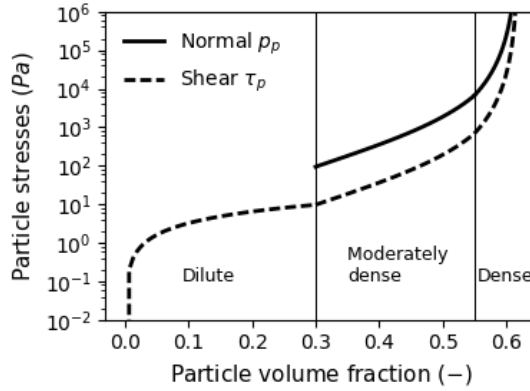


Figure III.11 Continuity of particle pressure and shear stress in function of solid concentration (with arbitrary particle and flow properties)

III.6 DISCUSSION ON FLUID PRESSURE

Following the derivation of constitutive equations for inter-particle stresses, we return to Eq. III.8 and open the discussion on the interpretation of pressure as fluid pressure in SIMMER-V. As it was explained in section III.1.2, the general SIMMER-V framework applies a locally homogenized pressure concept. The pressure inside each computational mesh satisfies from one hand the momentum equation of each velocity fields, and on the other hand the EOS of all fluids (including particles) in the cell. In the context of the SIMMER state-of-the-art mixture model, in which particles are part of their liquid form and occupy the same momentum field, the homogeneous shared pressure approximation is supported by the instantaneous mechanical equilibrium approximation between real liquid and gaseous components.

When the particle ensemble is treated as a separate momentum phase, the concept of pressure is interpreted separately for fluids and particles. Particle pressure is a measure of mutual collisions and frictional interactions between the grains, see paragraph II.4.2.1. While fluid pressure corresponds to the classical pressure definition arising from fluid motion, temperature changes etc. In SIMMER-V, the particles' EOS reflects their compressibility in direct functional relationship with temperature, for more information see [Morita and Fischer, 1998]. When reactor debris is modelled as granular media, the influence of particles' thermal temperature on the conventional fluid pressure is ambiguous. In this context, we know about no physical reason why SIMMER-V pressure (that we interpret as fluid pressure in Eq. III.8) should satisfy the EOS of particle components. Overall, we conclude on the future research need to exclude particles from the computation of common EOS pressure.

III.7 SYNTHESIS OF DEVELOPED MODELS

In line with the PhD objectives, a comprehensive modelling set for debris dynamics in SIMMER-V has been developed. The modelling set is applicable to a diverse set of 1D-flow configurations inherent to the discharge process via the mitigation transfer tubes. Part of the development concerns the modification of particle-fluid interphase momentum function better describing the drag force in dense configurations. The other part incorporates the physics of particle-particle interactions. These equations are mostly based on the $\mu(I)$ rheology that describes the granular medium as a frictional visco-plastic fluid with a shear rate dependent friction coefficient. The ensemble of developed models in the frame of the PhD work are summarized in Table III.5. In the code, they are activated by specific input options: MXFOPT(28) defines the projection of shear stress terms, MXFOPT(32) indicates the use of Gidaspow equation, MXFOPT(33) activates the use of shear stress term, MXFOPT(36) activates particle pressure calculation, and MXFOPT(34) and MXFOPT(37) switches off particle viscosity models in particle-fluid and fluid-structure momentum exchange terms respectively.

These equations do not concern heat and mass transfer processes. They remain to be accounted for by original SIMMER-V models without being interfered by the new models.

To track the progress of the development, the CEA SIMMER repository²⁶ of WebSVN online subversion repository browser was used [WebSVN, 2021]. The new branch of "SV_PARTICLE_RHEOLOGY" revision 1403 contains the final state of developed models. The SVN tool allows integrating and merging the thesis developments into newer code versions.

²⁶ <https://svn-ag.intra.cea.fr/>

Table III.5 Synthesis of the developed models for particle dynamics in SIMMER-V

	$\alpha_p < 0.2$	$\alpha_p > 0.2$	
Interphase momentum exchange	Wen & Yu equation in the Gidaspow drag [Gidaspow, 1994] $K_{pf}(\mathbf{v}_p - \mathbf{v}_f) = \frac{3}{4} C_D \frac{\alpha_p \alpha_f \rho_f \mathbf{v}_p - \mathbf{v}_f (\mathbf{v}_p - \mathbf{v}_f)}{\phi d_p} \alpha_f^{-2.65}$	Ergun equation in the Gidaspow drag [Gidaspow, 1994] $K_{pf}(\mathbf{v}_p - \mathbf{v}_f) = 150 \frac{\alpha_p^2 \mu_f}{\alpha_f \phi^2 d_p^2} (\mathbf{v}_q' - \mathbf{v}_q) + 1.75 \frac{\alpha_p \rho_f \mathbf{v}_p - \mathbf{v}_f (\mathbf{v}_p - \mathbf{v}_f)}{\phi d_p}$	
Particle-particle interaction forces & Particle-structure momentum exchange below 30% solid content	$\alpha_p < 0.3$ Particle – structure momentum exchange in the form of Fanning equation $\tau_p = 0.5 \alpha_p \rho_p f_p v_p^2$ with solid friction factor adjustment for continuity correction based on $\mu(l)$ dense granular rheology $f_p = \mu(I_i) \left(\frac{c_i}{\alpha_{MP} - 0.3} \right)^2 \frac{0.3 d_p^2 c_s^2}{0.5 D_h^2} + \mu(I_v) \left(\frac{c_v}{\alpha_{MP} - 0.3} \right)^2 \frac{0.3 \mu_f c_s}{0.5 \rho_p D_h \mathbf{v}_p }$ In lack of available data particle pressure is zero $p_p = 0$	$0.3 \leq \alpha_p < 0.55$ Shear and normal particle stress from $\mu(l)$ dense granular rheology [GDR MiDi, 2004] $\tau_p = \mu(I_i) \left(\frac{c_i \alpha_p}{\alpha_{MP} - \alpha_p} \right)^2 \rho_p d_p^2 \dot{\gamma}^2 + \mu(I_v) \left(\frac{c_v \alpha_p}{\alpha_{MP} - \alpha_p} \right)^2 \mu_f \dot{\gamma}$ $p_p = \frac{1 + \sin \delta}{1 - \sin \delta} \left(\frac{c_i \alpha_p}{\alpha_{MP} - \alpha_p} \right)^2 \rho_p d_p^2 \dot{\gamma}^2 + \frac{1 + \sin \delta}{1 - \sin \delta} \left(\frac{c_v \alpha_p}{\alpha_{MP} - \alpha_p} \right)^2 \mu_f \dot{\gamma}$	$\alpha_p > 0.55$ Shear and normal particle stress from $\mu(l)$ dense granular rheology [GDR MiDi, 2004] $\tau_p = \mu(I_i) \left(\frac{c_p}{\alpha_{MP} - \alpha_p} \right)^{2.8} \rho_p d_p^2 \dot{\gamma}^2 \beta_i + \mu(I_v) \left(\frac{c_p}{\alpha_{MP} - \alpha_p} \right)^{2.8} \mu_f \dot{\gamma} \beta_v$ $p_p = \frac{1 + \sin \delta}{1 - \sin \delta} \left(\frac{c_p}{\alpha_{MP} - \alpha_p} \right)^{2.8} \rho_p d_p^2 \dot{\gamma}^2 + \frac{1 + \sin \delta}{1 - \sin \delta} \left(\frac{c_p}{\alpha_{MP} - \alpha_p} \right)^{2.8} \mu_f \dot{\gamma}$
		Shear rate fitted after Sumner [Sumner et al., 1991] $\dot{\gamma} = c_s \frac{v_p}{D_h}$	Continuity correction by β_i, β_v Shear rate fitted after Sumner [Sumner et al., 1991] $\dot{\gamma} = c_s \frac{v_p}{D_h}$
		Dilatancy exponent from [Chauchat, 2018] and [Boyer et al., 2011] Macroscopic friction law by [Forterre and Pouliquen, 2009]. $\mu(I) = \left(\mu_s + \frac{\mu_2 - \mu_s}{1 + I_0/I} \right)$	Dilatancy exponent from percolation theory by [DeGiuli et al., 2015] Macroscopic friction law by [Forterre and Pouliquen, 2009]. $\mu(I) = \left(\mu_s + \frac{\mu_2 - \mu_s}{1 + I_0/I} \right)$
		Inertial and viscos numbers by [Andreotti et al., 2013] $I_i = \frac{\dot{\gamma} d_p}{\sqrt{p_p / \rho_p}}$ $I_v = \frac{\dot{\gamma} \mu_f}{p_p}$	Inertial and viscos numbers by [Andreotti et al., 2013] $I_i = \frac{\dot{\gamma} d_p}{\sqrt{p_p / \rho_p}}$ $I_v = \frac{\dot{\gamma} \mu_f}{p_p}$

Chapter IV. **SIMPLIFIED TEST CASES**

For the analysis of the new particle dynamics modelling set presented in the previous chapter, simplified test cases are considered as the first validation step. These test cases correspond to representative reactor conditions in which high concentration of particle-sized solid debris is likely to influence the dynamics of degraded core discharge via the mitigation transfer tubes. Since our focus is on the validation of particle dynamic models, heat and mass transfer processes are deactivated by user options in SIMMER-V for all test cases.

IV.1	Basis for simplified test cases.....	64
IV.2	Jammed particle pile.....	65
	IV.2.1 Stress distribution.....	66
	IV.2.2 Jamming transition.....	69
IV.3	Bin discharge.....	71
IV.4	Flow through porous media.....	74
IV.5	Fluidization and fluidized state.....	77
IV.6	Sedimentation under gravity.....	82
	IV.6.1 Terminal velocity of a quasi-single particle.....	82
	IV.6.2 Settling velocity of a dense particle ensemble.....	84
	IV.6.3 Terminal velocity of a cloud of different particulate components.....	88
IV.7	Hydraulic conveying.....	90
IV.8	Synthesis of results.....	94

IV.1 BASIS FOR SIMPLIFIED TEST CASES

During the discharge process, one can find largely different flow features along the approximately 10 m long relocation path. Particulate debris can be surrounded by various fluids in the same time, namely sodium (in the form of liquid or vapor), molten fuel, molten or vaporized steel and fission gases. Since the modelling set developed in this work is applicable for two-phase granular systems, particle dynamics in all test cases is elaborated in a single fluid being either gas or liquid sodium. These two are the most commonly encountered bulk fluids by the discharging reactor debris inside the transfer tubes. Varying concentration of particulate debris moves within a gaseous environment when previously occurring fuel-coolant interaction close to tube opening evaporated and/or pushed away the sodium bulk. The relocation of reactor debris in sodium is likely to manifest at lower tube regions in which liquid sodium is still present due to supply from the large volume of bottom sodium reservoir in the core catcher.

From a numerical point of view, physical models in SIMMER-V only differ between bubbly (continuous phase is liquid: either sodium, liquid fuel or liquid steel) and dispersed (continuous phase is gas) flow regimes, see section III.1. In this context, liquid sodium can be considered as a representative liquid, enveloping the dynamic behavior of other liquids (liquid fuel and liquid steel) in bubbly flow regime of SIMMER-V. In the following SIMMER-V simulations, particle size-reactor debris is modeled by fuel particle components (except for the analysis of multi-component flow). Examined particle diameters ranging from 0.5 mm to 2 mm are representative of reactor scenarios, but with a uniform size distribution (and spherical shape) according to the current modelling capability of SIMMER-V. The properties of fluid and particle components used in all test cases are given in Table IV.1.

Table IV.1 Particle and fluid properties in simplified test cases

Fuel particles		Gas		Liquid sodium	
d_p (mm)	ρ_p (kg/m ³)	ρ_g (kg/m ³)	μ_g (Pas)	ρ_l (kg/m ³)	μ_l (Pas)
0.5 - 2	10070	0.4	0.00004	797	0.00019

The particles in each test case are contained in a vertical cylindrical channel with dimensions similar to the current design of mitigation transfer tubes. The channel is modelled in cylindrical coordinate system with an internal radius of 8 cm, providing the cross sectional area similar to the conceptual design for transfer tubes. The test tube is represented by one radial and one azimuthal mesh in line with the one-dimensional SIMMER-V approach for channel configurations and the developed particle dynamics models. Applying a single azimuthal mesh means that the mesh extends over 360° in circumferential direction on a single cell. The symmetry axis is shown by the left boundary in all the "Schematic view" figures below. The tube walls are modelled by a 1 mm thick can wall structure. Even though transfer tubes are approximately 10 meter long, we focus only on a 2.5 m long section in the test cases covering completely and extending somewhat below the core region (the core height is around 1 m). The number of axial decompositions depends on the test case with mesh heights conforming to the typical mesh dimensions in reactor calculations by SIMMER-V.

The test cases considered in this work are listed in Table IV.2. The figure of merit and its expected behavior for each test are identified on the basis of a bibliographic review.

Table IV.2 Evaluation matrix of simplified test cases

Test case	Figure of merit	Expected behavior of the Figure of Merit
Jammed particle pile (special situation)	Stress distribution	Particle pressure profile in agreement with Janssen's prediction Particle stresses supporting the buoyant weight of particles
	Jamming transition	Jamming/unjamming transition as a function of spatial constraints
Bin discharge	Discharged flow rate	Constant flow rate as a function of particle size and orifice cross-section variation
Flow through porous media	Pressure drop	Darcy statement: increase of bed pressure drop with inlet fluid velocity till fluidization
Fluidization transition	Minimum fluidization velocity	The inlet fluid velocity at which the bed buoyant weight is counterbalanced by the drag force
	Pressure drop	Transition from packed to fluidized bed when the pressure drop breaks away from Ergun law
Sedimentation	Terminal velocity	Constant velocity reached after a certain distance during the free fall of single particle and its quantitative match with analytical solution
	Settling rate	Constant settling rate at constant solid fraction and its quantitative match with experimental results
	Settling rate of different components	Same settling rate as for a single component if densities and sizes are identical
Hydraulic conveying	Frictional pressure loss	Frictional pressure loss increases with bulk velocity and solid concentration

In the following subsections, each test case is described separately with respect to the figure of merit and its characteristic behavior. Simulations are carried out by SIMMER-V original version with equations of section II.2 and by SIMMER-V with the newly implemented particle momentum modelling set of section III.7. Results obtained by the SIMMER-V original equations with default options will be referred as SIMMER-V_vo (version original)²⁷, while results obtained by SIMMER-V with the particle dynamics models developed in the PhD work will be indicated by SIMMER-V_vpd (version particle dynamics). Test cases are analyzed separately for liquid and gas bulk fluid in order to account for bubbly and dispersed flow regimes in SIMMER-V. The outcomes of computations by SIMMER-V_vo and by SIMMER-V_vpd are compared to analytical solutions, where available, or empirical correlations.

IV.2 JAMMED PARTICLE PILE

The first test case addresses the situation of a jammed particle pile at rest. The fully static case is a special situation as it reaches the limits of $\mu(l)$ dense particle rheology. In a real static configuration, both particle velocity and shear rate vanish. Therefore, strictly speaking, constitutive laws depending on the average particle shear cannot describe the response of the systems. This regime is classically studied through principles of soil mechanics, described in paragraph II.4.3.1. In addition, experimental observations in the quasi-static regime show the appearance of non-local effects that

²⁷ We note that different option sets in original SIMMER-V version could improve the estimation of specific flow configurations. However, the purpose of this work is not to find the best fitting modelling options and parameters in SIMMER-V.

IV.2 Jammed particle pile

cause the basic assumption on locality, when formulating constitutive laws by $\mu(I)$ rheology, to fail [Bouزيد et al., 2015]. Even though the fully rigorous description of this regime cannot be captured by the $\mu(I)$ dense rheology models (see paragraph III.5.1.7 on the limits of the $\mu(I)$ rheology), we analyze whether the main characteristics of jammed configurations can be reproduced numerically by the equations of section III.7 in SIMMER-V. It is inevitable since static particle systems manifest in potential flow blockages inside the transfer tubes.

IV.2.1 Stress distribution

This test is dedicated to analyze the stress distribution inside a packed particle bed at rest. It is an important configuration because it underlines the different physics of bulk solids and fluids. Considering that the original momentum equations in SIMMER-V are derived for real fluids or fluid-solid mixtures, it is a good demonstration to highlight the impact of the newly implemented particle models in case of a purely particulate momentum field.

Unlike pressure in liquids or gasses, being an isotropic scalar quantity, stress in bulk solids is a tensor with normal and shear components. The shear stress in liquids at rest is always zero, whereas static friction between adjacent particles and particles and container sidewalls (with rough surface) brings about finite granular stresses. The stress scaling behavior of static granular packing is described by the pioneering work of Janssen [Sperl, 2006]. Janssen studied vertical storage tanks filled with corn and found that the pressure felt at the base of the system tends exponentially towards a finite upper limit above which further addition of granular matter is no longer felt at the bottom. The build-up of stresses with increasing depth is due to the shielding effect of contact forces between the grains redirecting their weight towards the sidewalls. Integrating the force balance on a differential slice of granular material subjected to normal pressure at the upper and lower surfaces, lateral friction force on the wall and gravity, Janssen derived an analytical equation for the granular pressure p_p distribution along the container depth by Eq. IV.1.

$$p_p(z) = \alpha_p \rho_p g z_c \left(1 - e^{-\frac{z}{z_c}}\right)$$

$$z_c = \frac{D_h}{4K_p \mu_w}$$

Eq. IV.1

Where α_p is the particle volume fraction (-), ρ_p is the particle density (kg/m^3), g is the gravitational acceleration (m/s^2), z_c is the characteristic depth (m), K_p is the lateral to vertical pressure ratio (-), μ_w is the friction coefficient on the wall and z is the vertical coordinate along the depth of the silo. The characteristic depth separates a linearly increasing pressure regime above z_c resembling to the hydrostatics of fluids, and a saturation region below. Although more than one hundred years old, the Janssen's theory it is still the most widely used analytical solution for the design of industrial granular systems. In addition, it forms the foundation of hourglass theory and allows measuring time with hourglass geometries.

Considering the two-phase nature of the system, we write the one-dimensional equation of motion for a fluid-particle field at static conditions ($v_f = v_p = 0$ and $\alpha_p \cong \alpha_{MP}$) by Eq. IV.2 [Andreotti et al., 2013].

$$0 = \alpha_f \frac{\partial p_f}{\partial z} + \alpha_f \rho_f g$$

$$0 = \frac{\partial \sigma_p}{\partial z} + \alpha_p \frac{\partial p_f}{\partial z} + \rho_p \alpha_p g$$

Eq. IV.2

Where subscripts p and f refer to particles and fluid respectively, p_f is the fluid pressure (Pa) and σ_p is the particle stress term (Pa). Rearranging Eq. IV.2, expressions are obtained for fluid and particle stresses as Eq. IV.3.

$$\frac{\partial p_f}{\partial z} = -\rho_f g$$

$$\frac{\partial \sigma_p}{\partial z} = -(\rho_p - \rho_f)\alpha_p g$$

Eq. IV.3

Eq. IV.3 indicates that the fluid weight is balanced by the fluid pressure, while particle buoyant weight is supported by the solid stress term.

To study stress behavior depicted by Eq. IV.1 and Eq. IV.3, the test case in SIMMER-V is a one-dimensional vertical cylindrical $D_h = 0.16 \text{ m}$ container filled with fuel particles ($d_p = 1 \text{ mm}$) up to around 2.2 m. Pressure boundary conditions with continuous inflow/outflow through the surface is set for the uppermost mesh to model atmospheric opening. Particles are surrounded by gas for the analysis of Janssen's theory, and submerged in sodium for the study of two-phase (liquid-solid) stress behavior. Since particle pressure and consequently the Janssen effect in original SIMMER-V_vo are not defined, the case of gas-particle system is studied only with SIMMER-V_vpd. For the liquid-solid two-phase stress behavior, both SIMMER-V_vo and SIMMER-V_vpd are compared to the analytical solution. The SIMMER-V visualization of such test cases and their schematic view is shown in Figure IV.1.

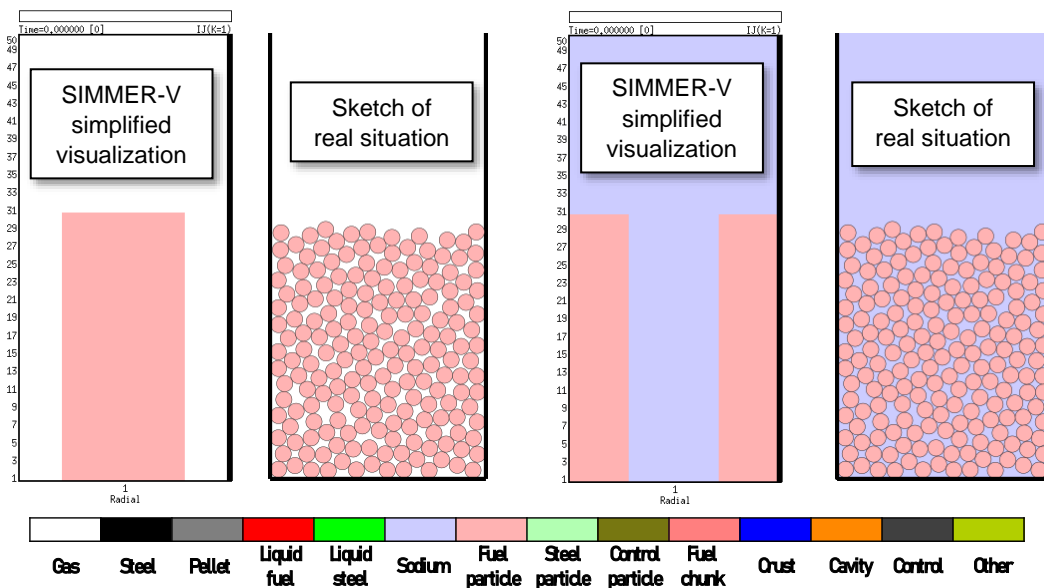


Figure IV.1 Schematic view of static particle pile in gas (left) and in liquid sodium (right)

The initial volume fraction of particles in both cases is set to 0.57. At the beginning of the calculation, the particle bed consolidates to reach the numerically predicted maximum packing limit that provides the true static configuration.

In case of gas bulk with SIMMER-V_vpd, the consolidation happens in 0.1 second during which a sharp increase of particle volume fraction towards maximum packing is observed in Figure IV.2 (a). After consolidation, the axial profile of particle concentration is well established. It is zero above the bed and close to 0.62 inside the particle pile, see Figure IV.2 (b). Parallel to the initial compaction, both inertial and viscous numbers are diminished as can be seen in Figure IV.2 (c). It is in agreement with the theory of $\mu(l)$ rheology predicting $I_v, I_i \rightarrow 0$ in quasi-static regime where $v_p \cong 0$, and consequently the rheology being independent of shear rate [GDR MiDi, 2004].

IV.2 Jammed particle pile

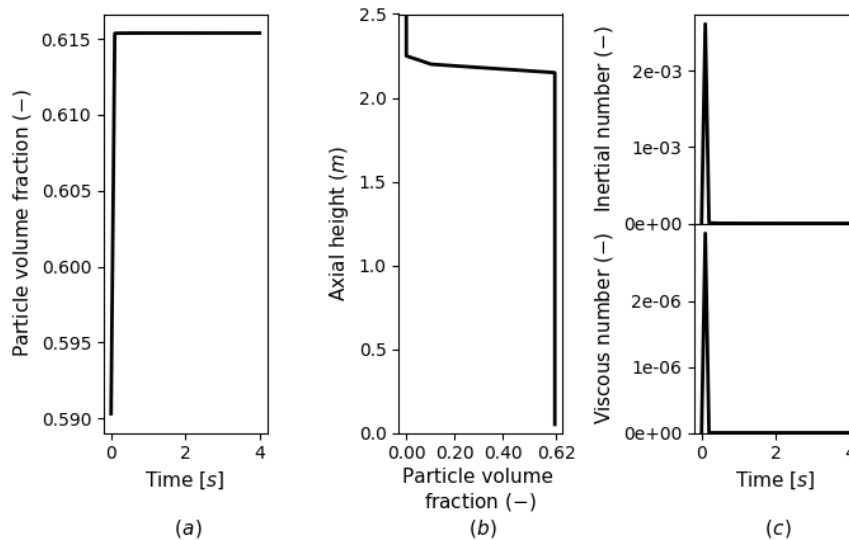


Figure IV.2 SIMMER-V_vpd: (a) Particle volume fraction inside the pile, (b) particle volume fraction axial profile after stabilization, and (c) Inertial and viscous numbers

Following the initial bed stabilization, the Janssen effect can be interpreted. The particle pressure axial profile computed by SIMMER-V_vpd is illustrated in Figure IV.3 in contrast to the Janssen prediction of Eq. IV.1.

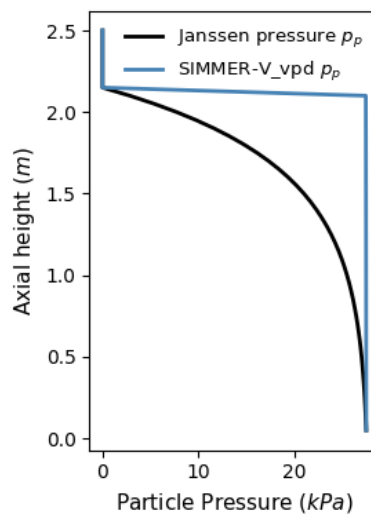


Figure IV.3 Particle pressure axial profile by SIMMER-V_vpd and by Janssen equation Eq. IV.1 ($\mu_w = \mu_s, K_p = 0.27$)

Examining Figure IV.3 from a generic point of view, we observe that the upper boundary condition of Janssen, stating that granular pressure at the bed surface is zero, is satisfied. Furthermore, Janssen's principle describing a constant granular pressure after a certain bed depth is recovered as well. In between, there is a saturation region in which granular pressure converges from zero to its constant maximum value. Unfortunately, SIMMER-V_vpd models are not able to reproduce this region of smooth transition; instead, a sharp step-like jump is simulated. We postulate that it is because of the velocity dependence of the particle pressure constitutive law by the $\mu(I)$ dense granular rheology that is not intended to describe purely static cases. To recover the Janssen profile, the static equilibrium of forces acting on the particle ensemble should be solved for the particle pressure as the only unknown variable (without defining a constitutive law for it). During the thesis work, we considered implementing such an algorithm into SIMMER-V (by identifying the jammed

meshes and applying the Janssen solutions for them), but we arrived to the conclusion that it is a challenging task considering that SIMMER-V is a dynamic code based on the concept of velocities. At the current state of research, we are satisfied with the stepwise jump being a more conservative prediction for the build-up of granular pressure.

The second case, when particles are suspended in liquid sodium is studied to describe the stress behavior in two-phase liquid-solid situations. The simulations are performed with sufficiently long time to overcome initial bed consolidation and numerical stabilization. In Figure IV.4 left plot, the axial pressure drop per unit length obtained by SIMMER-V_{vo} is compared to the particle buoyant and fluid weight as in the analytical expression Eq. IV.3. In SIMMER-V_{vo}, there is one pressure assumed to be homogeneous for all momentum fields within one computational mesh. It imposes that the pressure drop in a static particle bed should be equal to the mixture weight (sum of particle buoyant and fluid weight). It is true above the bed where only liquid sodium is present. However, one can observe from Figure IV.4 left plot that the pressure gradient reaches unreasonably large values and oscillates inside the particle bed. It is far from being in agreement neither with the prediction of an homogeneous pressure approach nor with the analytical solution for two-fluid granular systems.

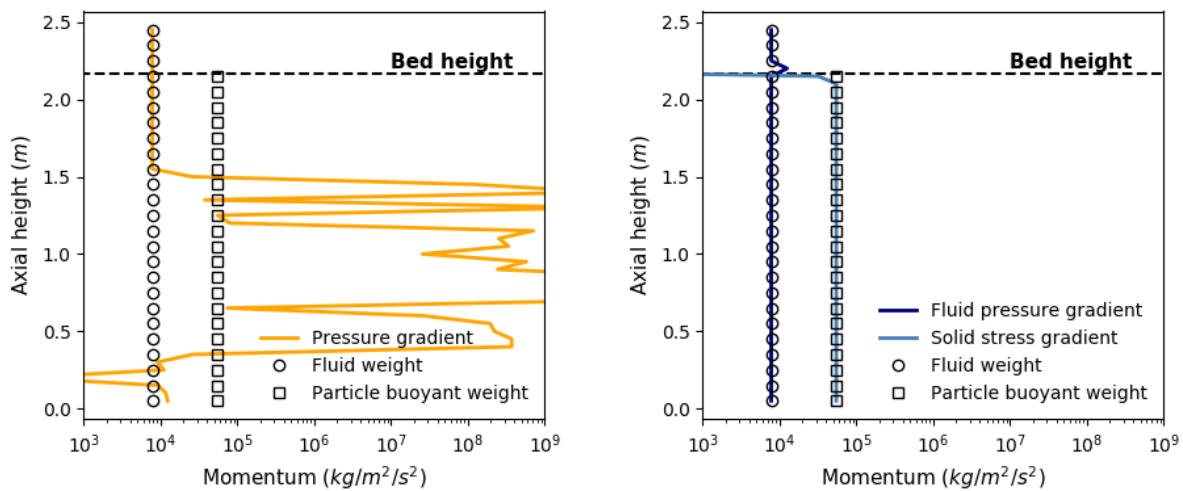


Figure IV.4 Vertical momentum profile in the particle pile by SIMMER-V_{vo} (left) and by SIMMER-V_{vpd} (right)

Applying the new particle modelling set by SIMMER-V_{vpd}, the fluid pressure and granular stress gradients are plotted in Figure IV.4 right plot. The fluid pressure drop corresponds to the fluid weight both inside and above the particle column, except a slight jump at the interface. The granular stress inside the bed balances the buoyant weight of particles. The only stress contribution here is the shear component. The particle pressure gradient is zero due to the constant solid volume fraction along the bed height in 1D approach (after sufficient simulation time). Overall, the results with the newly implemented particle stress terms into SIMMER-V_{vpd} reproduce the general principle of Janssen's theory and match well with the analytical solution of two-phase stress distribution according to Eq. IV.3.

IV.2.2 Jamming transition

The second test case addresses the transition from jammed to mobile state. The real transition is a complex multi-dimensional phenomenon including several microstructural effects, and it is still subject of active research. Our purpose here is to explore whether the passage from a previously jammed structure to a flowable state can be captured in SIMMER-V. It is of high importance in reactor scenarios because it assures that blockage/unblockage situations due to particle accumulation (if relevant in transfer tubes) are covered by the numerical modelling. In this section, we examine the

IV.2 Jammed particle pile

transition phenomenon from a purely geometrical point of view. Geometrical in a sense that there is no fully limiting spatial constraint on the jammed solid structure.

The simplest way is to imagine a granular pile resting on a support plate, which is removed after some time (after fully jammed state is established) allowing the particles to relocate downwards by gravity. Theoretically, if particles are cohesionless, spherical, rigid and their size is sufficiently small compared to the tube diameter to avoid arch formations, the only restriction against motion is geometrical. The disappearance of the support plate diminishes the geometrical constraint and thus particle clusters (contact grids) have then a new degree of freedom to break up and set the lower particle layer free to flow [Hunt et al., 2014]. Inside the mitigation transfer tubes, this scenario may correspond to the melting or mechanical breakup of large degraded reactor components blocking the downward flow and above which particles have accumulated previously.

The corresponding test case in SIMMER-V consists of the same vertical cylindrical tube as in section IV.2.1 but the particles are now placed above a virtual wall, which acts as a support plate. The virtual wall is deactivated in the code after 1.4 s. This time is necessary to ensure a stationary jammed state after initial consolidation.

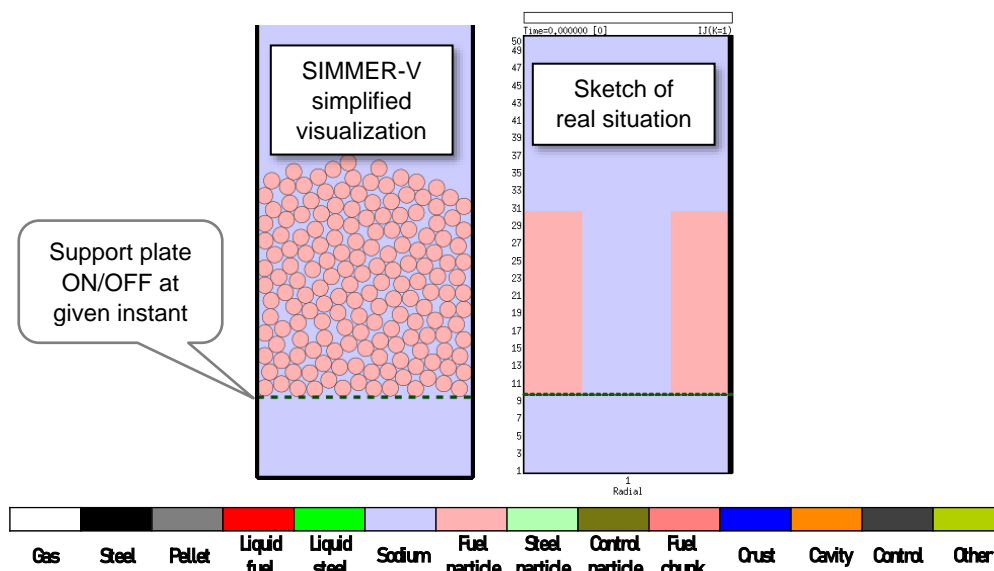


Figure IV.5 Schematic view of jamming transition

The temporal evolutions of the volume fraction and velocity of particles are plotted with SIMMER-V_vo default options and with SIMMER-V_vpd new particle modelling set in Figure IV.6. The calculation with SIMMER-V_vo predicts the solid volume fraction close to maximum packing limit that is constant in time and unchanged by the removal of the support plate. In addition, particle velocity remains zero long after opening the downward path. These observations imply that the particle bed stays jammed and levitates even if the geometrical constant is dismissed. Based on this, SIMMER-V original version with the default options²⁸ is not able to capture unjamming transition. In case of SIMMER-V with the new granular momentum modelling, the particle volume fraction above the support plate starts to decrease immediately after removing the plate. Particles start to relocate with a negative velocity when there is free space available to accommodate them. Therefore, we conclude that the modified particle-phase momentum equation can simulate the transition between jammed and unjammed states in this simple configuration. In line with our focus of interest in reactor

²⁸ Some tentative combination of user variables (affecting directly closure laws in SIMMER-V) may improve the modelling answer. However, approach that is more rigorous is represented while applying new SIMMER-V_vpd models presented in this thesis. It means that user does not need to search a combination of options to overpass the lack of modelling answer.

applications, the most important characteristics of granular piles, namely the stress distribution and jamming transition, are reproduced via the new particle dynamic models in SIMMER-V.

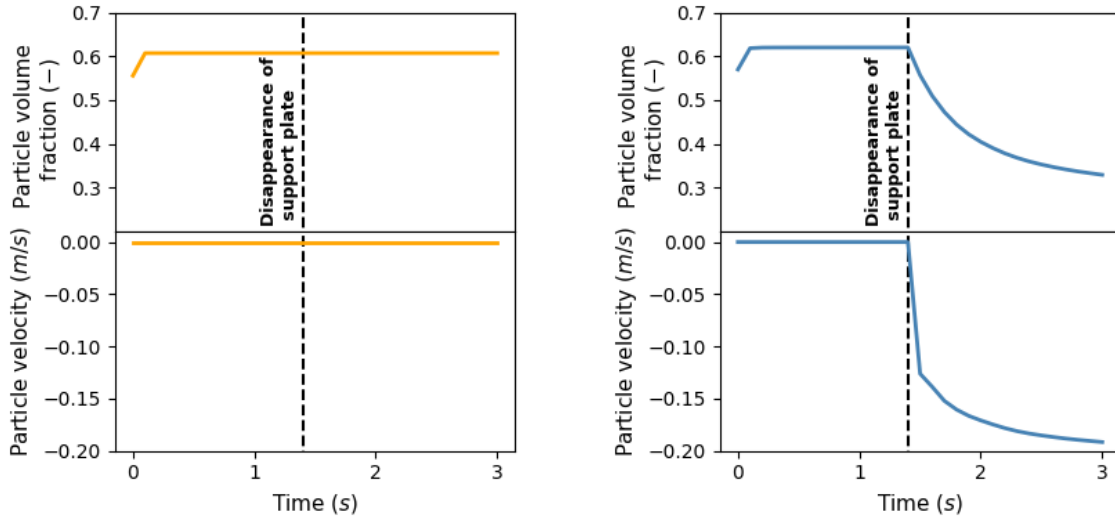


Figure IV.6 Temporal variation of particle volume fraction above and velocity below the support plate by SIMMER-V_vo (left) and SIMMER-V_vpd (right)

IV.3 BIN DISCHARGE

The next test case is similar to the jamming transition analysis of paragraph IV.2.2 but better adapted to practical applications and resembles more to severe accident scenarios. The case that we refer here as bin discharge covers a wide range of situations in which the outflow of particulate matter through an orifice is of high importance. Classical examples include the discharge from silos, hoppers, bins, chutes with different outlet geometries but in the same way, hourglass/sandpipe flows belong to this category as well. In reactor severe accident scenarios, one can find such bin discharge configurations at lower regions where transfer tubes cross the diagrid, strongback and other support structures via a cross-sectional restriction²⁹. Another bin discharge situation inside the core region can correspond to a flow area reduction due to excessive freezing of liquid steel or liquid fuel (crust) on the tube walls. Studying debris progression through apertures is therefore an essential element in estimating the discharge performance via the mitigation transfer tubes.

The basic principle of bin discharge phenomena is the independence between the height of the granular column and the discharge flow rate through the aperture. It is explained by frictional contacts between grains and sidewalls that redirect pressure towards the container walls and hence granular stresses saturate with filling height, as follows the Janssen effect described in paragraph IV.2.1. The widely accepted correlation predicting the discharge flow rate of cohesionless mono-sized grains through an orifice under gravity is the Beverloo law [Beverloo et al., 1961]. Providing that Janssen's pressure scaling is established, Beverloo law states that the orifice volume flow rate is constant in time and can be computed by Eq. IV.4.

$$Q = c\sqrt{g}(D_0 - kd_p)^{5/2} \quad \text{Eq. IV.4}$$

Where Q is the volume flow of particles (m^3/s), D_0 is the outlet orifice diameter (m), d_p is the particle diameter (m), c and k are dimensionless empirical discharge and shape coefficients respectively. Eq. IV.4 is obtained by dimensional analysis following the assumption that there is an arch of solid contacts just above the outlet. The arch acts as a shielding and separates the packed particle

²⁹ According to current design, the tube diameter is reduced by half at this location.

IV.3 Bin discharge

structure from free-fall regime in which particles accelerate freely under gravity. In this region, particles accelerate from zero to a value equivalent to the free-fall velocity after traveling a distance proportional to the outlet size. Accordingly, the velocity varies with the square root of effective orifice diameter. This reasoning provides the physical interpretation for the 5/2 exponent when determining the flow rate, and the square relation with gravity [Mankoc et al., 2007]. Since Eq. IV.4 does not contain any information on the height and diameter of the granular system, it is only valid as long as the container dimensions do not influence the flow rate. In addition, particles have to be sufficiently small to avoid jamming at the aperture that could lead to flow intermittenencies. The geometrical conditions under which Eq. IV.4 is applicable are summarized in Table IV.3.

Table IV.3 Validity criteria for Beverloo law [Nedderman et al., 1982] when container diameter $D = 0.16\text{ m}$ and particle diameter $d_p = 0.001\text{ m}$ are fixed (outlet orifice diameter D_0 , thickness/height of granular bed H)

Statement	Condition	Criteria for the test case
Cohesionless granular media	$d_p > 0.0005\text{ m}$	0.001 m
Intermittenencies in the flow due to jamming are avoided	$D_0 > 6d_p$	$D_0 > 0.006\text{ m}$
Pressure at the bottom of the silo saturates due to the Janssen effect	$H > 1.2D$	$H > 0.192\text{ m}$
Flow rate is independent of container diameter	$D_0 < D/2.5$	$D_0 < 0.064\text{ m}$
	$D_0 < D - 30d_p$	$D_0 < 0.13\text{ m}$

Table IV.3 expresses the constraints on the orifice diameter D_0 and bed height H besides fixed particle d_p and container D diameters equivalent to average reactor debris size and transfer tube dimensions. These values are respected when constructing the test case in SIMMER-V. The schematic view of the test case dedicated to study the flow of particle-size reactor debris through a restriction in SIMMER-V is shown in Figure IV.7. The cylindrical tank filled with fuel particles discharges through a bottom circular outlet. The circular outlet is modelled by an increased structure volume (according to aperture size) in the mesh below the particle bed. To reproduce atmospheric conditions below and above the particle column, the domain is decomposed into two radial meshes and a pressure boundary condition is applied to both uppermost ones. The rest of the boundaries are considered as rigid walls. At the beginning of the simulation, a virtual wall is situated at the location of the orifice in order to allow the particle bed to consolidate to its maximum concentration. The virtual wall is deactivated after 0.5 s proving free path for the particles to discharge.

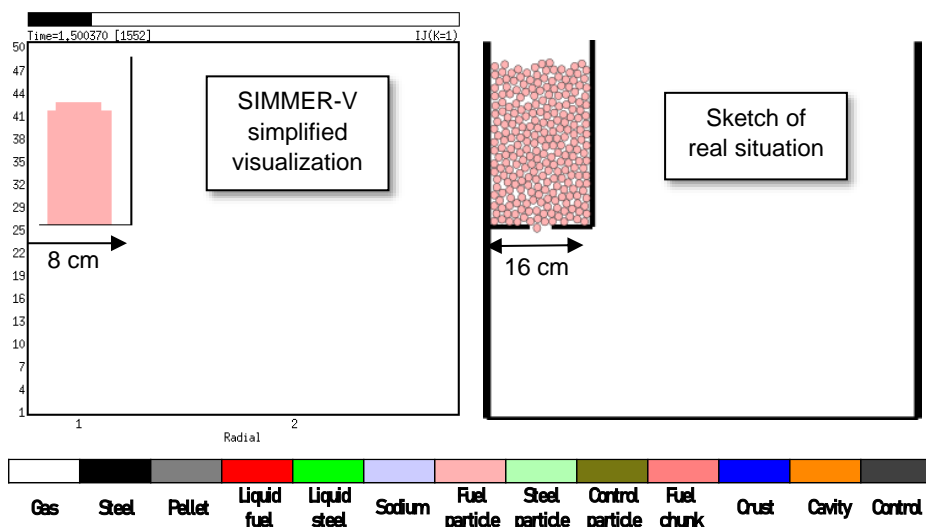


Figure IV.7 Schematic view of bin discharge test case (SIMMER-V geometry is axisymmetric around the left boundary)

The simulation of SIMMER-V_vo predicts no particle motion after the disappearance of virtual wall. Particles enter into the mesh with increased structure volume fraction representing the orifice but they do not advance further. It is presumably due to the upstream projection of particle-structure momentum exchange term. It is projected to the cell edge by taking the maximum of upper and lower mesh center values. The particle-structure momentum term is large in the orifice mesh because of the high particle content and the use of particle viscosity model. The projection of such large value for the mesh just below the orifice acts as a flow obstacle and avoids downward flow of particles.

The simulation with SIMMER-V_vpd predicts continuous outflow of fuel particles through the outlet. The amount of particles leaving the container is constant in time in agreement with experimental observations. The discharge rate is therefore straightforward. In line with Eq. IV.4 stating that the discharge flow is controlled by the orifice and particle diameter, simulations are performed with different outlet orifice diameters and with two particle sizes. The results are plotted in Figure IV.8 with orifice diameters respecting the constraints defined in Table IV.3. The last point is marked with red frame because it violates the assumption on flow rate independency on container diameter through $D_0 = D/2$. We included this case since it corresponds to the diameter reduction by a factor of two in lower transfer tubes regions.

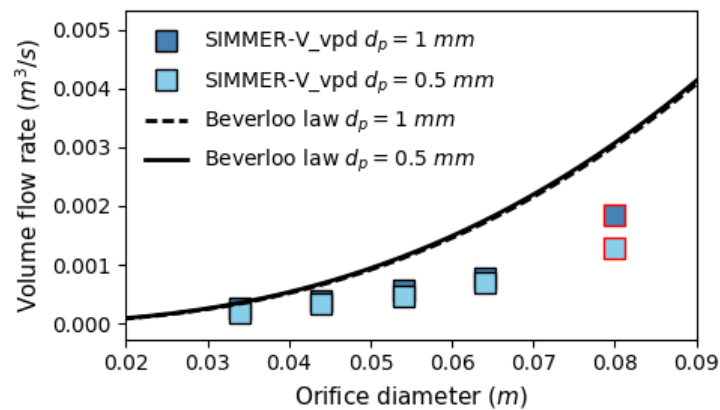


Figure IV.8 Volumetric flow rate through different orifice diameters by Beverloo equation ($c = 0.55$, $k = 1$) and in SIMMER-V_vpd

From Figure IV.8, one can see that the general trend of volumetric flow rate increase with orifice diameter is reproduced by SIMMER-V_vpd. In the validity range of Eq. IV.4, the flow rate with different particle sizes in SIMMER-V_vpd are very close to each other, which agrees well with the Beverloo's characteristic. Even through the last orifice diameter does not respect the assumptions behind Eq. IV.4, it seems to conform the general trends. However, SIMMER-V_vpd computes flow rates lower than the prediction of Beverloo. It is valid for both particle sizes and all orifice diameters. In the derivation of Beverloo law, particles are considered to undergo unhindered gravitational fall across the orifice. On the other hand, frictional and collisional particle-particle interactions are taken into account when particles cross through the orifice mesh in SIMMER-V_vpd.

Figure IV.9 shows the axial profile of particle shear stress representing such particle-particle interactions. One can see that shear stress is nonzero at the location of the cross-section reduction indicating that it plays a role in the discharge process. It hinders the discharge and brings about a reduced flow rate compared to the free fall case of Eq. IV.4 (the gravitational free fall will be scope of paragraph IV.6.1). The lower relocation speed is advantageous in terms of conservatism in reactor application.

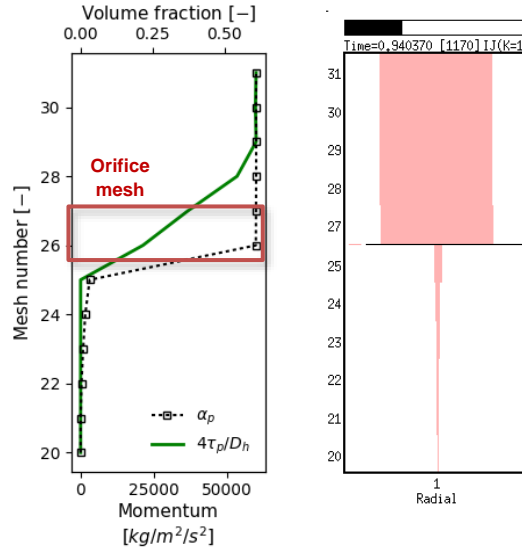


Figure IV.9 Particle shear stress around the location of orifice

Overall, we conclude that the qualitative behavior of bin discharge phenomena is well reproduced by SIMMER-V_vpd. The underestimation of discharge rate is due to hindering effect of particle-particle interaction forces at the location of the orifice.

IV.4 FLOW THROUGH POROUS MEDIA

The test case of flow through porous media belongs to the category of fluid-solid interaction type problems. It is dedicated to measure the fluid pressure drop through a porous media comprised of immobile particles. The pressure difference over a packed bed is an important feature of the two-phase granular systems since it describes the progression towards a flowable fluidized particle state. The fluidization transition itself will be studied in the next section.

As we have seen in paragraph IV.2.1, when particles are at rest in a stagnant fluid, their weight is supported against gravity by the combination of frictional forces exerted on the sidewalls and between the particles in contact, and buoyancy. If a viscous fluid passes through a bed of granular solids, it encounters a flow resistance and a resultant pressure drop. Following, the particle weight becomes partially supported by the drag force exerted on them by the fluid [Jackson, 2000]. The pressure gradient inside the fluid is equal to the drag on the particle bed and the fluid weight. It increases proportional to the flow rate according to the Darcy statement. The Darcy-like proportionality is generally expressed by the Ergun equation by Eq. IV.5, including the fluid weight [Gidaspow, 1994].

$$\frac{dp_f}{dz} = \rho_f g + 150 \frac{(1 - \alpha_f)^2 \mu_f}{\alpha_f^2 d_p^2} v_f + 1.75 \frac{(1 - \alpha_f) \rho_f}{d_p \alpha_f} v_f^2 \quad \text{Eq. IV.5}$$

The test case in SIMMER-V consists of a vertical cylindrical tube (with the same dimensions as in section IV.2 test cases) in which a particle bed is initialized at a certain height above the tube entrance, see Figure IV.10. The tube and the interstitial space between particles ($d_p = 0.5 \text{ mm}$) are filled with fluid (liquid sodium or gas). The fluid flow is introduced from the bottom with inlet velocity condition, and it leaves on the top with pressure condition after passing through the particle column. The flow onset is somewhat delayed at the beginning of each computation for the particle assembly to consolidate into a packed state. Afterwards, the inlet fluid velocity is kept constant in each simulation to obtain stationary conditions. In order to ensure that particles do not fall out of the calculation domain, a numerical restriction is applied on their downward velocity component in the

lowest bed mesh. In reality, particles in porous media flow experiments rest on a perforated plate. The numerical constraint on downward particle motion functions as a support plate. Leaving some distance between the particle column and the lower boundary cell is therefore needed in order not to interfere with boundary conditions. It is advantageous also because it provides a fully developed fluid flow below the bed.

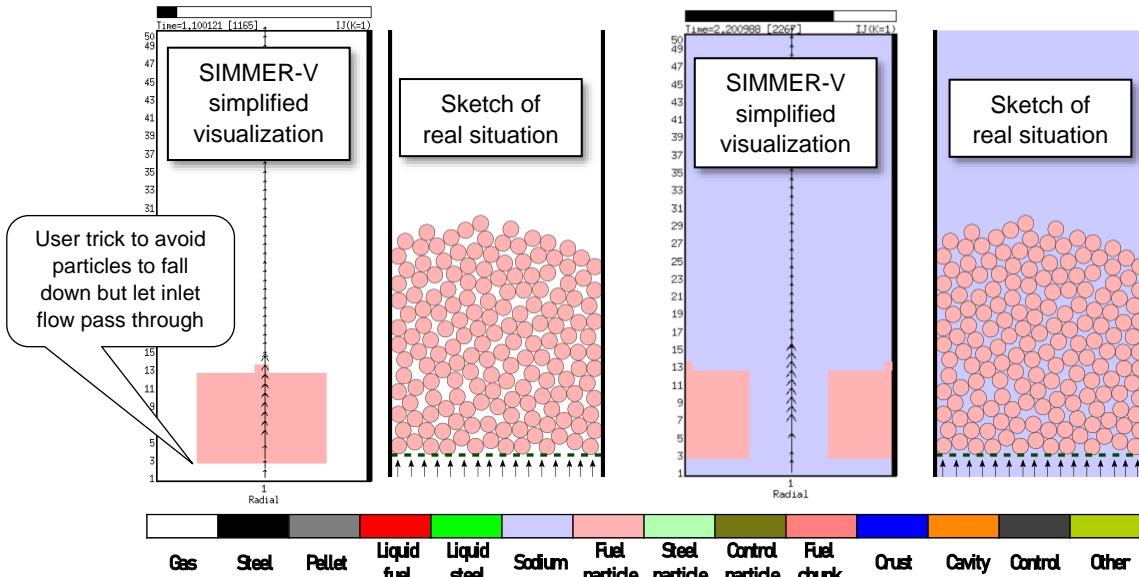


Figure IV.10 Schematic view of flow through porous media in gas (left) and in liquid sodium (right)

The pressure drops in gas obtained with different inlet velocities by SIMMER-V_{vo} and SIMMER-V_{vpd} are compared to the Ergun prediction in Figure IV.11. Velocity values are considered up to minimum fluidization condition (this will be detailed in the next section). For each inlet flow, a steady pressure drop is reached after initial bed consolidation, and these values are plotted in Figure IV.11.

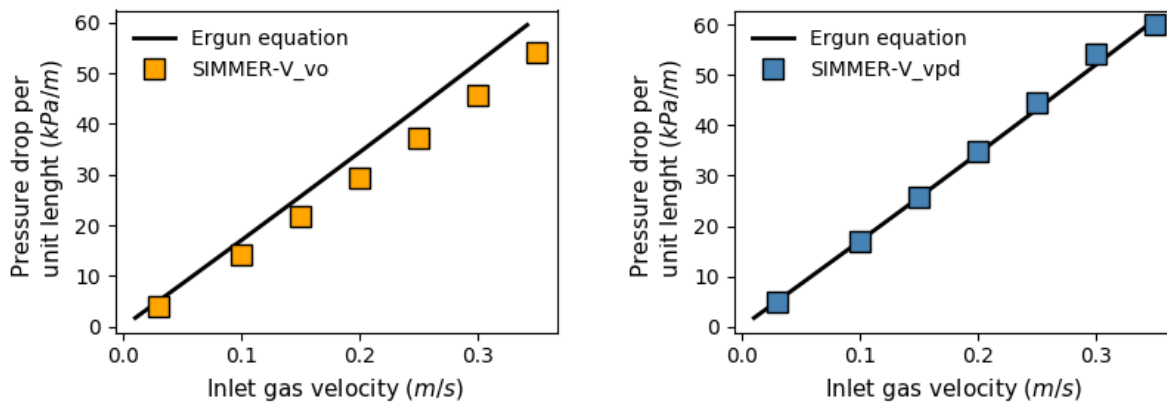


Figure IV.11 Pressure drop inside the particle bed as a function of inlet gas velocity with SIMMER-V_{vo} (left) and with SIMMER-V_{vpd} (right) in comparison to Ergun equation Eq. IV.5

The bed pressure drops computed by SIMMER-V_{vo} and SIMMER-V_{vpd} are both in close agreement with the empirical prediction of Ergun. SIMMER-V_{vo} results show increasing deviations with higher inlet velocities but it does not distort considerably the general trend. According to Eq. IV.5, the fluid pressure gradient is governed by the interphase friction between fluid and particle momentum field. Therefore, the discrepancy is due to the different formulation of the interphase drag function in SIMMER-V_{vo}. The exact match between Ergun equation and SIMMER-V_{vpd} pressure

IV.4 Flow through porous media

drops is attributed to the fact that the Gidaspow drag function above 20% particle concentration is indeed the Ergun equation.

In case of liquid sodium being the bulk fluid, the simulation of SIMMER-V_vo does not predict a stabilized bed pressure drop in time. We observe that sodium accumulates below the bed and causes a large pressure increase in the lowest meshes. It originates from the mixture viscosity model appearing in the structure momentum exchange function of liquid sodium. When particles are in a packed state, the mixture viscosity tends towards infinity and consequently the structure exchange term as well. The large wall friction of sodium inside the bed avoids further fluid mass to enter into the interstitial space of particles. The continuous sodium inflow imposed by the boundary condition brings about large pressure escalation below and across the bed and therefore unreasonably large and numerically unstable bed pressure drops. The SIMMER-V_vo computed pressure drops show no consistency with the inlet sodium velocity. For this reason, we do not analyze further this case. On the other hand, with SIMMER-V_vpd, we obtain stabilized pressure data at each inlet condition. The results of SIMMER-V_vpd are illustrated in Figure IV.12.

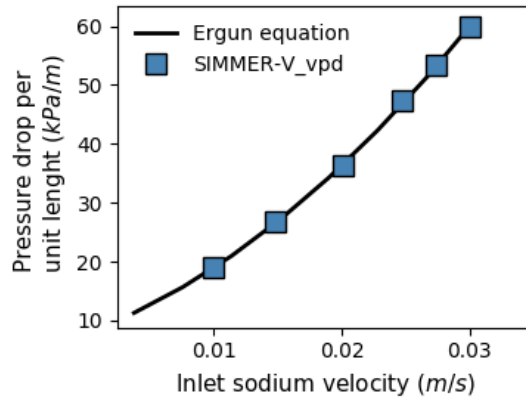


Figure IV.12 Pressure drop inside the particle bed in function of inlet sodium velocity with SIMMER-V_vpd

From Figure IV.12, we conclude that SIMMER-V_vpd pressure drop matches well with the empirically predicted curve in the regime of packed granular bed. Following Eq. IV.5, it is mainly associated to the Gidaspow drag function for interphase friction. To examine further the porous media flow in view of particle stress behavior by SIMMER-V_vpd, Figure IV.13 shows the variation of vertical momentum terms with inlet sodium velocities.

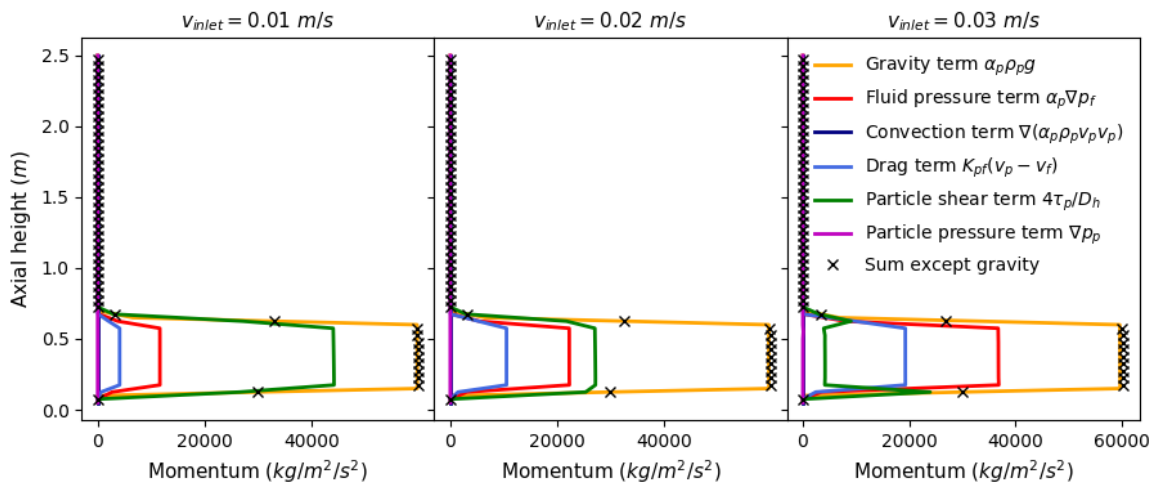


Figure IV.13 Vertical profile of particle momentum balance at different inlet sodium flows

The momentum balance in Figure IV.13, one can see that there are three dominant mechanisms balancing the gravity force, namely the drag, fluid pressure gradient and particle shear stress terms. Particle convection and pressure gradient are negligible since there is no spatial variation of particle velocity and volume fraction after flow stabilization. The ratio between the three dominant terms changes with increasing fluid flow. The competition is controlled by the drag force containing directly the effect of fluid velocity increase. The fluid pressure term varies proportionally to the drag as long as the particle volume fraction stays constant independently of the inlet flow. It is then the particle shear stress that adjusts to balance the gravity term at each inlet flow with the corresponding drag and fluid pressure terms. The physical interpretation of this behavior is that particles' weight is partially supported by inter-particle contacts and partially by the drag force exerted from the fluid. As fluid forces become larger, particles separate from each other such that the contact network breaks up and solid stresses diminish. The point at which particles become fully suspended in the flow is discussed in the next section.

IV.5 FLUIDIZATION AND FLUIDIZED STATE

In section IV.2.2, we have seen unjamming transition as a result of the disappearance of geometrical constraints. In reactor scenarios, it corresponds to the melting or mechanical breakup of any solid component supporting and blocking the downward passage of debris inside the transfer tubes. In this fluidization test case, we focus on the transition phenomenon due to fluid forces. Powerful fluid forces arise from large pressure differences inside the core or from fuel-coolant interactions in which the fluid is pushed away with a large inertia.

Following on the test case of porous media flow in section IV.4 where the packed particle bed maintained a static state by the action of gravity, the fluidization case describes how stationary solid particles are brought into motion. At fluidization point, the particle assembly is converted from a static solid-like to a dynamic fluid-like state. To achieve fluidization, the particle assembly has to be supported against gravity. The support is provided by the fluid flow imposing a pressure gradient by the drag force on the particles, as it was shown in section IV.4. Fluidization takes place when the fluid pressure gradient is sufficient to bear the buoyant weight of particles. It is expressed as Eq. IV.6, where the subscript mf refers to variables at minimum fluidization condition. The fluid velocity satisfying the balance is the minimum fluidization velocity computed as Eq. IV.7 with Ergun equation for interphase drag and with Ar being the Archimedes dimensionless number [Gidaspow, 1994].

$$(1 - \alpha_{f,mf})(\rho_p - \rho_f)g = 150 \frac{(1 - \alpha_{f,mf})^2 \mu_f}{\alpha_{f,mf}^2 d_p^2} v_{f,mf} + 1.75 \frac{(1 - \alpha_{f,mf}) \rho_f}{d_p \alpha_{f,mf}} v_{f,mf}^2 \quad \text{Eq. IV.6}$$

$$v_{f,mf} = \frac{\mu_f}{d_p \rho_f} \left[\sqrt{[42.85(1 - \alpha_{f,mf})]^2 + 0.57 \alpha_{f,mf}^3 Ar} - 42.85(1 - \alpha_{f,mf}) \right] \quad \text{Eq. IV.7}$$

$$Ar = \frac{d_p^3 g \rho_f (\rho_p - \rho_f)}{\mu_f^2}$$

Besides the extensively used Ergun type equation, there are a number of correlations available in the literature for the prediction of minimum fluidization velocity. These equations are mainly developed to take into account other factors influencing the fluidization transition, such as polydispersity or irregular particle shapes. In addition, large amount of experimental data can be found. The Ergun equation is evaluated by comparing to a wide range of experimental results, and so we consider it as an adequate approximation for minimum fluidization velocity.

Any additional increase in flow rate above minimum fluidization value causes the bed to dilate (particles separate from each other to accommodate the increased fluid flow) to a concentration at

IV.5 Fluidization and fluidized state

which sustained solid contacts are diminished. However, once particles are in motion in a fluidized state, they interact with one another by collision or by sliding friction generating dispersive stresses. It drives the particles apart and can amplify the fluidization by the so-called self-fluidizing effect [Campbell, 1989]. The resulting stress contribution is proportional to the particle shear rate. The shear rate in a stabilized fluidized column slightly above fluidization conditions, where particles are floating in the fluid flow with negligible averaged velocity, and therefore this effect is usually neglected in pressure drop analysis. With negligible granular stresses, particles are fully supported by the fluid flow such that the fluid pressure drop across the bed is equal to the particle-fluid mixture weight, as writes Eq. IV.8 [Gidaspow, 1994], with H being the bed height (m).

$$\Delta p_f = -gH(\alpha_p \rho_p - \alpha_f \rho_f) \quad \text{Eq. IV.8}$$

In reality, the fluidization process strongly depends on whether the fluidized medium is gas or liquid. In case of gas fluidization, several regimes are distinguished due to the high heterogeneity, aggregative and unstable nature of gas-particle mixtures. In the literature, we encounter bubbling, slugging, turbulent or fast regimes as a function of particle size and inlet flow rate. In liquid systems, particles are tend to disperse uniformly leading to a rather homogeneous stable behavior [Kwauk and Li, 1996]. Our interest in scope of SIMMER-V debris model is to investigate the general characteristics of fluidization process, which is identical for liquid and gas fluidizing medium depicted in Figure IV.14.

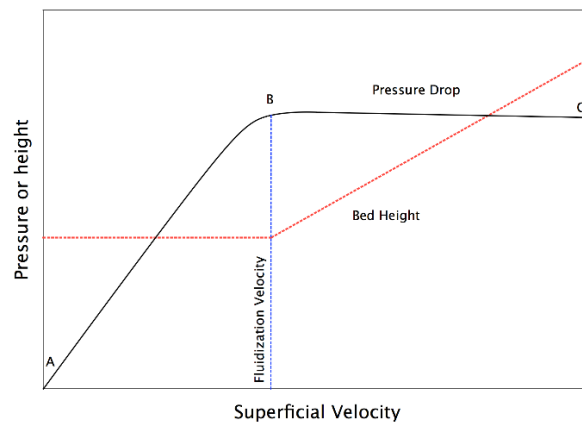


Figure IV.14 Pressure drop and bed voidage in packed and fluidized beds from [Toomey, 2018]

According to the global view of the transition phenomenon from packed bed to fluidized state in Figure IV.14, below fluidization velocity (between points A and B), particles remain static with a constant bed height independent of fluid velocity, see section IV.4. Parallel, the pressure drop over the bed increases proportionally as a function of inlet flow rate. At fluidization condition (point B), one observes a knickpoint in the pressure profile and the onset of bed expansion. After particles are fluidized (between point B and C), the bed pressure drop across the bed maintains a constant value while the bed height increases with inlet fluid velocity.

The fluidization test case in SIMMER-V is identical to the one on flow through porous media, see the schematic view in Figure IV.15, but with inlet fluid velocities increased to and above the minimum fluidization point.

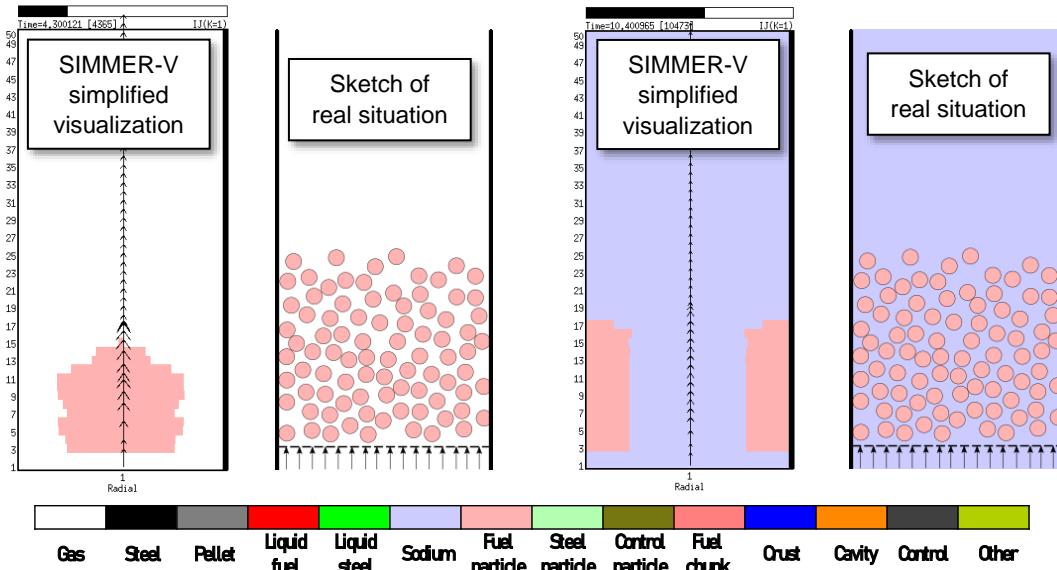


Figure IV.15 Schematic view of fluidization by gas (left) and by liquid sodium (right)

The pressure drop characteristic, fluid volume fraction and bed expansion ratio in gas bulk fluid obtained from SIMMER-V_{vo} simulations are plotted in Figure IV.16.

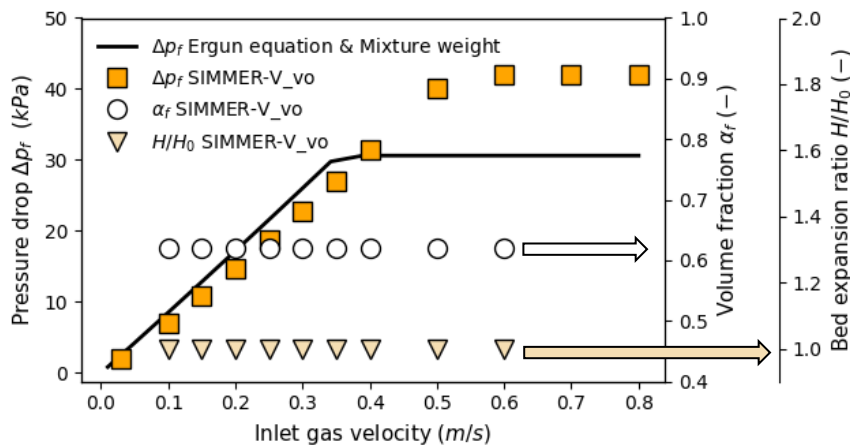


Figure IV.16 Pressure drop over the bed, gas volume fraction and bed expansion ratio as a function of inlet gas velocity in SIMMER-V_{vo}

From Figure IV.16, one can see that there no knickpoint point in the pressure drop profile around the empirically predicted minimum fluidization condition $v_{inlet} = 0.35 \text{ m/s}$. The pressure drop continues to increase with increasing inlet gas flow alongside an unchanged bed voidage and bed expansion ratio. It indicates that the particles assembly remains at rest. At $v_{inlet} = 0.7 \text{ m/s}$, the pressure drop begins to fluctuate. At the same time, the fluid volume fraction and bed height oscillates as well in such a way that we cannot extract an average value. Therefore, they are not plotted in Figure IV.16 above $v_{inlet} = 0.7 \text{ m/s}$. Further increasing the inlet velocity shows similar pressure and voidage oscillations, see Figure IV.17. This behavior can be regarded as a transition into a fluidized state. Although, the inlet gas velocity at which it takes place in SIMMER-V_{vo} is not in correspondence with the empirical value. The computation of gas-particle mixture in SIMMER-V_{vpd} shows similar instabilities as SIMMER-V_{vo} above $v_{inlet} = 0.7 \text{ m/s}$. However, they appear closely after the empirically predicted fluidization condition is met at $v_{inlet} = 0.4 \text{ m/s}$. At this velocity, fluctuations occur around the steady-state value corresponding to the mixture weight of Eq. IV.8, see in Figure IV.18.

IV.5 Fluidization and fluidized state

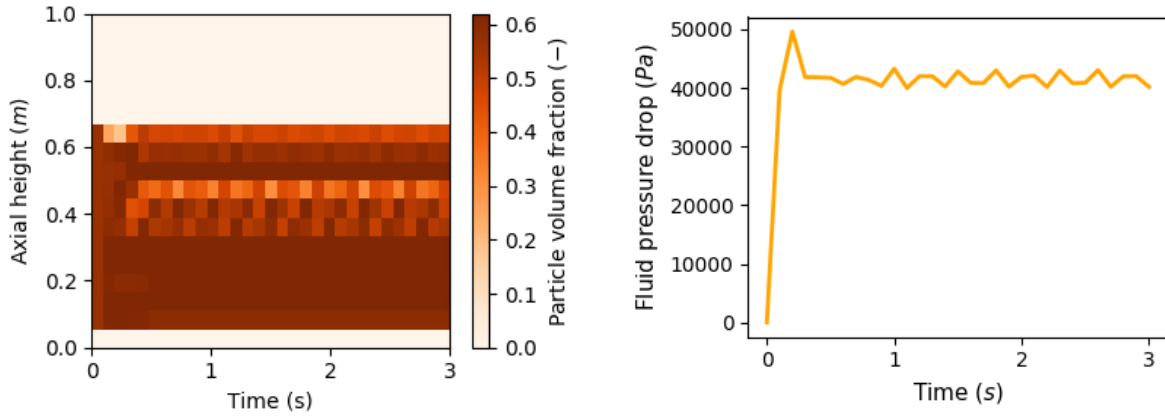


Figure IV.17 Temporal oscillations of particle volume concentration inside the bed (left) and of fluid pressure drop across the bed (right) at $v_{inlet} = 0.7 \text{ m/s}$ with SIMMER-V_vo

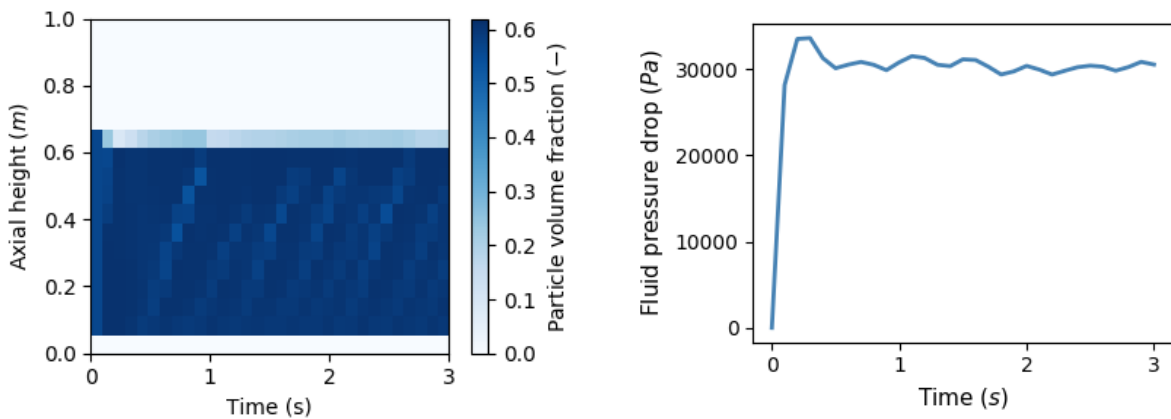


Figure IV.18 Temporal oscillations of particle volume concentration inside the bed (left) and of fluid pressure drop across the bed (right) at $v_{inlet} = 0.4 \text{ m/s}$ with SIMMER-V_vpd

The pressure drop profile covering the fluidization transition by SIMMER-V_vpd is illustrated in Figure IV.19. Bed voidage and expansion ratio are omitted because of their large fluctuations, likewise in SIMMER-V_vo.

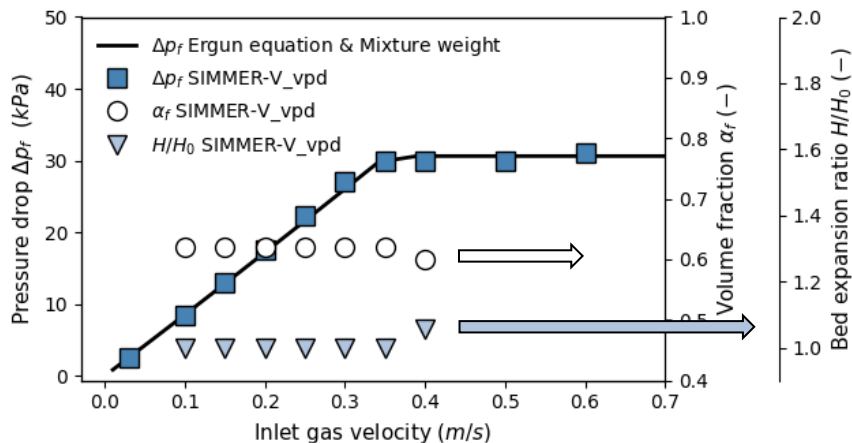


Figure IV.19 Pressure drop over the bed, gas volume fraction and bed expansion ratio as a function of inlet gas velocity in SIMMER-V_vpd

The reason behind the fluctuations observed at fluidized state in both SIMMER-V_vo and SIMMER-V_vpd can be twofold. From one side, gas fluidized beds are commonly considered heterogeneous with large asymmetries that gave way to chaotic transient behavior. The heterogeneity arises from

localized bubble formations and their periodic coalescence, as well as from particle aggregation leading to inhomogeneous rising of cavities inside the assembly. From the other hand, numerical issues are likely to appear because particles fall and rise from one mesh to another. It changes abruptly the magnitude of interphase drag and consequently the fluid pressure gradient meshwise. In addition, the relatively low spatial resolution in SIMMER-V (mesh size is 5 cm) brings about uncertainties on the exact bed height which in turn makes it difficult to determine the precise values of bed pressure drop.

The simulations for liquid sodium are only carried out with the new granular models in SIMMER-V_vpd. Since SIMMER-V original calculations have already failed to predict the behavior of flow through porous media. The pressure drop, fluid volume fraction and bed expansion ratio as a function of different inlet velocities are plotted in Figure IV.20.

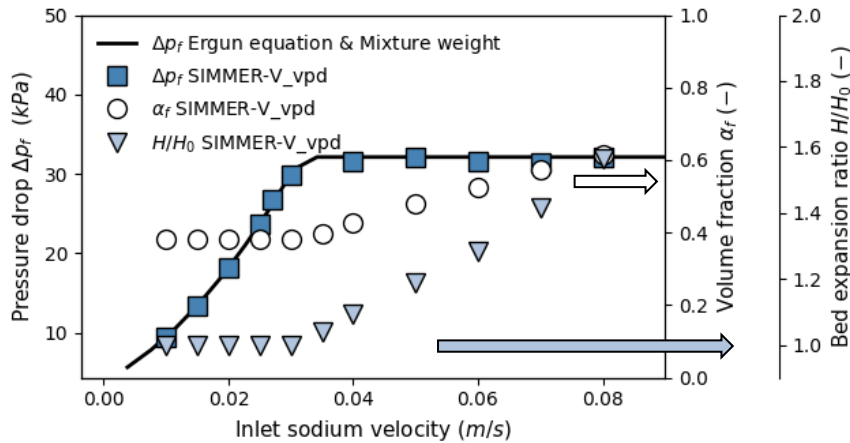


Figure IV.20 Pressure drop over the bed, fluid volume fraction and bed expansion ratio as a function of inlet velocity in SIMMER-V_vpd

At each computational point plotted in Figure IV.20, we reached a fully stabilized state, meaning that pressure profile and bed height do not vary in time. It is in agreement with the experimentally observed homogeneous fluidization characteristic of liquid fluidized beds [Rumpf, 1975]. As we have seen in section IV.4, the pressure drop below fluidization increases with sodium velocity while the bed remains at rest with solid concentration close to maximum packing limit, $\alpha_{MP} = 0.62$. Correspondingly, the sodium volume fraction in packed bed regime in Figure IV.20 is constant as well at around 0.38. The knickpoint point in pressure drop and volume fraction data indicating incipient fluidization is found to be around $v_{inlet} = 0.03 \text{ m/s}$. It matches well with the empirically predicted value of Eq. IV.7 $v_{inlet} = 0.032 \text{ m/s}$, with $\alpha_{f,mf} = 0.38$, $d_p = 0.5 \text{ mm}$ and particle/fluid properties equal to the ones of sodium and fuel debris in SIMMER-V. At higher inlet velocities, the bed loosens up and levels off at a higher steady-state position. This effect is shown by the bed expansion ratios reported in Figure IV.20. In parallel, the further increase of fluid velocity does not cause additional pressure variation. The constant pressure drop value after fluidization follows closely the mixture weight according to Eq. IV.8.

Altogether, we draw the following conclusions. SIMMER-V_vo resolves fluidization transition when the fluidizing medium is gas but its onset is somewhat higher than the empirical prediction. The bed pressure drop after fluidization is overestimated; it does not reflect the mixture weight of the bed. SIMMER-V_vo with liquid sodium flow is not investigated since the pressure convergence problems are encountered already well before fluidization. On the other hand, the fluidization onset and the main flow characteristics in its close proximity are well represented by the implementation of the new granular momentum modelling in SIMMER-V_vpd. It is true in both gas and liquid fluidizations.

IV.6 SEDIMENTATION UNDER GRAVITY

Continuing on the fluid-solid interaction type problems, the sedimentation test case addresses the situation when the whole particle assembly is in motion and settles downwards under the effect of gravity in a viscous suspension. The associated reactor scenario is the discharge process itself in absence of any significant pressure variation due to fluid motion or in other words the fall of fragmented core materials in quasi-stationary fluid environment under the influence of gravity. Gravitational settling inside the transfer tubes is typical at bottom tube regions where there is no source of large pressure escalation (mainly in liquid sodium), and around the core height after pressure equilibrium between transfer tubes and core region is established (mainly in gas). The discharge rate of fissile fuel particles, associated with the settling velocity, governs the reactivity removal time that is among the main safety parameters regarding the mitigation strategy.

The settling velocity is one of the important parameters in sedimentation studies because it plays a substantial role in various processes employed in many industries and in geosciences. Examples include deposition and diffusion processes in chemical engineering, or pipeline sediment transport in mining industry. Alternatively, the settling behavior of macroscopic granular systems has received a great attention over a long period. A number of experimental correlations and theoretical equations are available for the prediction of settling velocity under a wide range of different conditions. We note here that the settling phenomenon is equivalent to the fluidization process just viewed from a different frame of reference. The fluid velocity maintaining the particles at zero average velocity is expected to be the same as the settling velocity at which the particles fall when the fluid is stagnant [Dharmarajah, 1982].

In this section, we investigate the sedimentation phenomena in three stages. First, the terminal free-fall velocity of a single body is analyzed in SIMMER-V. It is necessary because many correlations for the behavior of a particle ensemble assume the priory knowledge on single particle kinematics. Following, the settling velocity of a multi-particle system is investigated through the concept of hindered settling in the second part. Lastly, we extend the analysis for a particle cloud that is composed of different particulate components in SIMMER-V.

IV.6.1 Terminal velocity of a quasi-single particle

The vertical sinking of a solid debris particle under gravity can be related to the concept of terminal fall velocity. It states that any object moving through a viscous fluid eventually reaches an asymptotic velocity when the upward product of buoyancy and drag forces exerted by the surrounding fluid counterbalances the downward gravity force such that the net force on the body becomes zero. It brings about zero acceleration and thus a constant rate of motion. The highest attainable speed in case of the gravity driven motion of suspended particles is referred as terminal fall velocity [Chhabra and Basavaraj, 2019, p. 6]. Since gravity and buoyancy are computed in standard way with negligible modelling uncertainties in SIMMER-V, the accuracy of the numerically predicted terminal velocity can be directly associated with the formulation of the drag force.

Theoretically, there are several analytical formulas proposed to calculate single body terminal velocity. The two most commonly used expressions are the Stokes law at $Re_p < 1$ and the Impact law at $Re_p > 1$ as writes Eq. IV.9, with $Re_p = d_p \alpha_f \rho_f |v_p - v_f| / \mu_f$ being the particle Reynold number.

$$v_p(t) = \left\{ \begin{array}{ll} v_t \left(1 - e^{-\frac{gt}{v_t}} \right) & v_t = \frac{(\rho_p - \rho_f) g d_p^2}{18 \mu_f} \quad \text{if } Re_p < 1 \\ v_t \tanh\left(\frac{gt}{v_t}\right) & v_t = \sqrt{\frac{4 d_p g (\rho_p - \rho_f)}{3 C_D \rho_f}} \quad \text{if } Re_p > 1 \end{array} \right\} \quad \text{Eq. IV.9}$$

Eq. IV.9 is valid when particles fall in an infinite fluid medium. In case the flow is confined by structures such as the case of cylindrical transfer tubes, the displacement of the particle volume creates additional retarding effect [Dharmarajah, 1982]. The wall effect depends on the ratio of sphere to tube diameter (d_p/D_h) and the particle Reynolds number. With values of reactor debris size and transfer tube diameter, the effect of bounding walls produces an insignificant contribution to the relocation speed. Therefore, it is neglected in further analysis. The test case in SIMMER-V is identical to the vertical cylindrical tube in previous cases. For the analysis of terminal fall velocity, low volume fraction of solid particles is introduced into the uppermost mesh of the calculation domain, see in Figure IV.21.

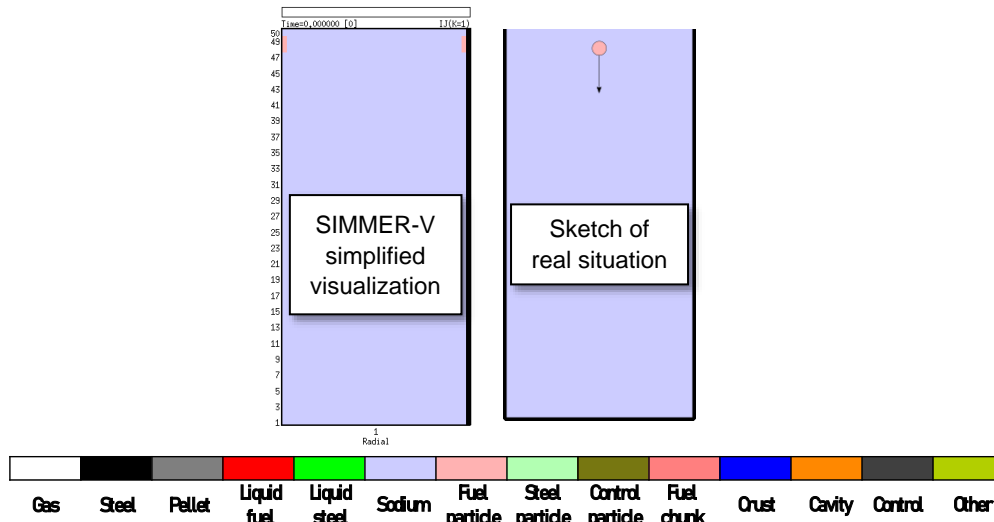


Figure IV.21 Schematic view of the terminal fall a single particle

At low particle concentration, the flow field perturbed by one particle of the loose cloud can be assumed not to counteract and distort the flow field around other lone particles [Dey et al., 2019], and therefore the concept of single body terminal velocity can be applied. Solid volume fraction of 5% was arbitrary chosen considering that it is sufficiently high to preserve the validity of SIMMER-V continuum approach and, in the same time, to associate the velocity of such particle cloud with the terminal fall velocity of a single particle. Simulations are performed solely in liquid sodium. In gas bulk, the large density difference between fluid and particles would require a very long tube to reach terminal velocity ($v_t \sim 10 \text{ m/s}$, $H > 70 \text{ m}$). The results for the quasi-single particle ($Re_p \sim 10^3$) and its temporal built-up by SIMMER-V_vo and SIMMER-V_vpd are shown in Figure IV.22.

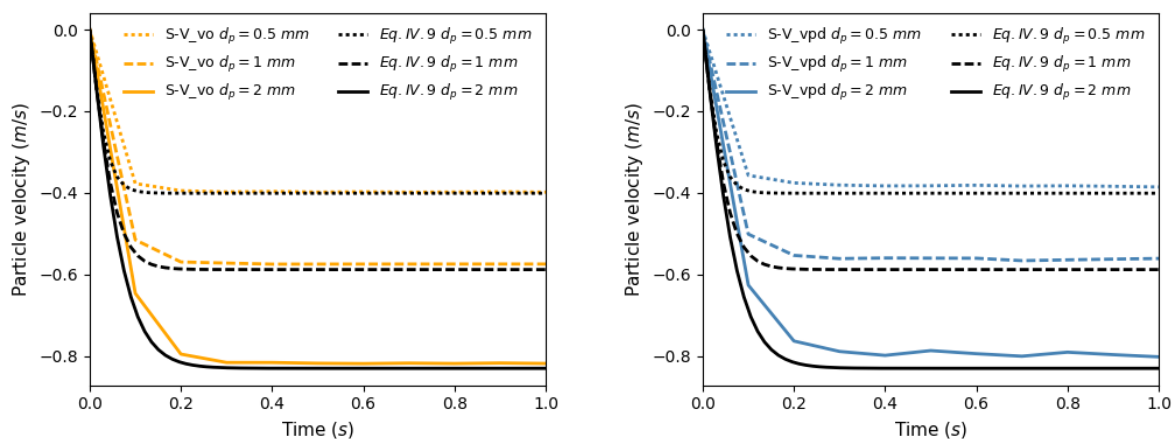


Figure IV.22 Comparison of semi-analytical equation with SIMMER-V_vo (left) and with SIMMER-V_vpd (right) results for particle velocity for three representative particle diameters in liquid sodium

IV.6 Sedimentation under gravity

The temporal variation of the particle velocities computed by both SIMMER-V_{vo} and SIMMER-V_{vpd} follow the semi-analytically predicted characteristic by Eq. IV.9. After an initial acceleration regime, the velocity stabilizes at constant value. The magnitude and the temporal built-up of the asymptotic velocity depend on the particle size through the drag force and particle weight. From one hand, increasing the particle diameter brings about heavier grains and leads to a stronger gravitational force. On the other hand, increasing the grain size amplifies the drag term being proportional to the surface area of the moving object. Due to the quadratic and cubic dependences of drag force and gravity respectively on the grain diameter, it takes longer time for the drag to offset the gravity for bigger particles. It allows them reaching higher velocities before equilibrium. Correspondingly, the absolute value of terminal velocity and the time required to reach it in Figure IV.22 increases with particle size. In addition, the magnitude of the asymptotic velocities matches well with the analytical solution for all particle diameters. This observation is valid for SIMMER-V_{vo} and SIMMER-V_{vpd} results as well. Although, one can see that the prediction of SIMMER-V_{vpd} is somewhat less precise compared to SIMMER-V_{vo}. It originates from the different definition of drag coefficients at low particle concentrations. Since the discrepancies are small and the underestimation of relocation velocity promotes conservatism in reactor application, we conclude that both SIMMER-V versions reproduce well the gravitational free fall of a quasi-single debris component.

IV.6.2 Settling velocity of a dense particle ensemble

In this section, we extend the analysis from the gravitational free fall of low solid contents to the settling behavior of dense particle clouds. Compared to the free fall of a single body, wherein particles are unencumbered by the hydrodynamics of other particles, additional hindering effects influence the sedimentation process of a system of particles. As a result of these hindering effects, the relocation velocity of a particle ensemble is lower than that of a single settling body [Kramer et al., 2019]. The accurate numerical computation of the relocation velocity plays a central role in estimating the discharge rate of dense fuel debris via the mitigation transfer tubes. For this reason, a separate analysis is performed to evaluate SIMMER-V modelling of dense particle sedimentation.

Theoretically, one can distinguish two main sources of retardation effects in the settling process of dense particle clouds. Indirect hydrodynamic particle-particle interaction forces arise from the modified flow field due to fluid displacement by the collection of particles. The motion of a single falling particle distorts the streamlines producing a return flow and a wake behind which hinders the motion of upstream particles affected by it. In addition, particles in dense suspensions are likely to interact directly with one another by collisions or sliding friction leading to an emerging contribution of contact stresses alongside the indirect hydrodynamic interactions [Landman and White, 1992]. In practice, the sedimentation phenomenon is most commonly described through empirical laws for the settling velocity. Empirical correlations are derived from experiments in which a particle fluid mixture contained in a vertical cylinder is agitated first to ensure a homogenous solid dispersion, and then it is let to adjust to its equilibrium concentration profile. If particles are heavier than the fluid, they settle downwards by gravity. The most frequently applied formula describing the rate of settling is the Richardson and Zaki equation [Richardson and Zaki, 1997]. It is the first pioneering analysis that correlates the sedimentation velocity in a dense sediment-laden fluid v_s to the terminal velocity of a single particle v_t in terms of particle volume concentration α_p by Eq. IV.10.

$$v_s = v_t(1 - \alpha_p)^n \quad \text{Eq. IV.10}$$

Where n stands for the settling exponent depending on the flow regime through the single particle terminal Re . The form of Richardson and Zaki equation is universally accepted: the majority of settling velocity correlations from the literature apply the same form except for the settling exponent. Attempts to improve the settling exponent include other empirically derived expressions (fitting to experimental data with varying conditions) such as [Garside and Al-Dibouni, 1977], hydraulic

analytical model [Kramer et al., 2019], purely mathematical derivations [Pal and Ghoshal, 2013] or probability based approaches [Zhu et al., 2019]. These correlations are listed in Table IV.4.

Table IV.4 Correlations for settling exponent in dense particle flows

Investigator	Expression for settling exponents in SI units
Richardson and Zaki [Richardson and Zaki, 1997]	$n = \begin{cases} n = 4.65 & Re_{p,t} < 0.2 \\ n = 4.4Re^{-0.03} & 0.2 < Re_{p,t} < 1 \\ n = 4.4Re^{-0.1} & 1 < Re_{p,t} < 500 \\ n = 2.4 & Re_{p,t} > 500 \end{cases}$
Garside and Al-Dibouni [Garside and Al-Dibouni, 1977]	$n = \frac{5.1 + 0.27Re_{p,t}^{0.9}}{1 + 0.1Re_{p,t}^{0.9}}$
Kozeny – Lewis model [Kramer et al., 2019]	$n = \frac{\ln\left(\frac{3}{4}\alpha\frac{Re_{p,t}^{\beta+1}}{180}\frac{\alpha_{mf}^3}{1-\alpha_{mf}}\right)}{\ln\alpha_{mf}} \quad \alpha = 10, \beta = -0.5$
Pal and Ghoshal [Pal and Ghoshal, 2013]	$n = \frac{\frac{4}{3}\ln(1-\alpha_p) - \ln\left(1 - \frac{\alpha_p}{\alpha_{MP}}\right) + 3\ln(f) - \frac{7}{8}\left[\frac{38.1 + 5.74f^{\frac{12}{7}}Re_{p,t}^{\frac{4}{7}}}{38.1 + 5.74Re_{p,t}^{\frac{4}{7}}}\right]}{\ln(1-\alpha_p)}$ $f = \left[\left(\frac{\rho_p}{\rho_f}(1-\alpha_p)^{\frac{\rho_p-\rho_f}{\rho_f}} - 1\right)\frac{\rho_f}{\rho_p-\rho_f}\left(1 - \frac{\alpha_p}{\alpha_{MP}}\right)^2(1-\alpha_p)^{-1}\right]^{\frac{1}{3}}$
Zhu and Wang [Zhu et al., 2019]	$n = -14.29 \left[0.15 - 0.14 \exp\left(-0.08\left(\frac{Re_{p,t}(\rho_p-\rho_f)}{\alpha_p\rho_f}\right)^{0.45}\right) \right]^{\frac{2}{3}} + 6.29$

To investigate the behavior of hindered settling in SIMMER-V, the same vertical tube described as in previous sections is used. It is filled with the homogeneous suspension of varying volume fraction of solid particles ($d_p = 1$ mm) and fluid. The calculations are performed with liquid sodium only, settling in gaseous environment is not analyzed because of the same reasoning as in section IV.6.1. The schematic view of the sedimentation test case is shown in Figure IV.23.

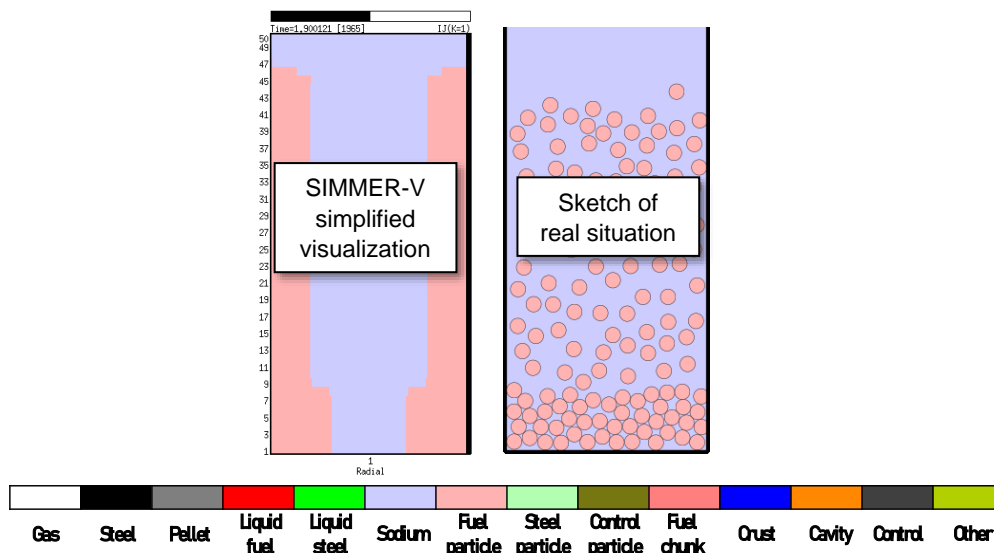


Figure IV.23 Schematic view of particle sedimentation

When the calculation begins, particles of the homogeneous suspension start to settle under gravity according to the density difference between particles and fluid. To examine the global settling behavior, the axial particle concentration and velocity profile are plotted on Figure IV.24 in case of 40% initial particle volume fraction as an example. The regions indicated on the graph correspond

IV.6 Sedimentation under gravity

to the three settling regimes identified experimentally by [Azizi et al., 1992]. One can see that, at the top of the setting column significant particle depletion takes place. Just below the clear fluid interface, particle velocity is the highest. In this transition regime, the system is adjusting itself to steady state. Below the clear fluid-suspension interface, there is a regime of constant settling where particle bed relocates at fixed volume fraction with a constant velocity. At the lower part of this region, particle concentration increases in parallel to the reduction of settling rate due to increased hindrance effects. At the container bottom, the dispersed phase forms a static packed bed with zero average velocity.

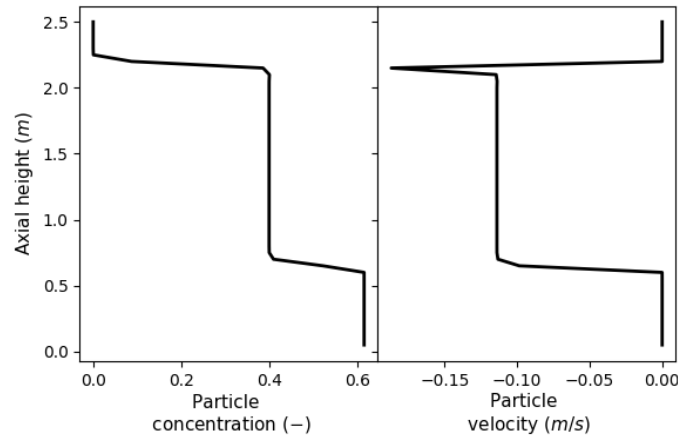


Figure IV.24 Axial concentration and velocity profile after 3 seconds of sedimentation by SIMMER-V_vpd

SIMMER-V_vo and SIMMER-V_vpd settling velocities are compared to equations from Table IV.4 in Figure IV.25. The graph shows the settling velocities measured in the regime of constant sedimentation rate with varying initial solid concentrations.

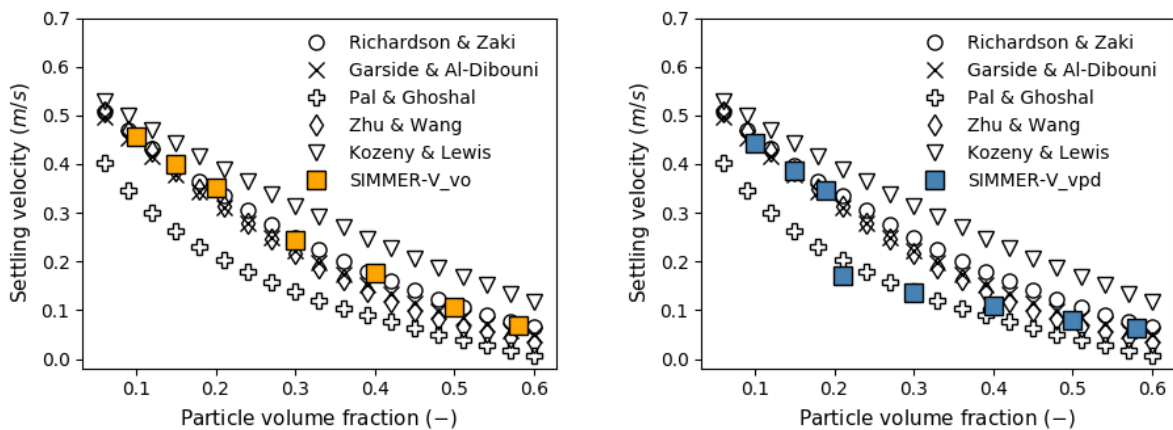


Figure IV.25 Comparison of settling velocities computed by SIMMER-V_vo (left) and by SIMMER-V_vpd (right) with correlations from literature in liquid sodium

Figure IV.25 shows that the global characteristics of SIMMER-V_vo and SIMMER-V_vpd computed settling velocities as a function of solid concentration are in agreement with empirical and theoretical equations. The higher the initial volume fraction of solid particles, the higher the drag force experienced by the particle ensemble, therefore the lower the maximum attainable speed. The hindered settling velocity decreases from the single particle terminal value nonlinearly with initial concentration and converges towards zero at maximum solid concentration.

SIMMER-V_vo results follow the closest the empirical prediction of Richardson & Zaki but also show good agreement with the equation of Garside & Al-Dibouni and Zhu & Wang on the full range of particle concentration. SIMMER-V_vpd computed velocities are also in perfect match with the same

three correlations below 20% particle concentration. At 20% solid volume fraction, there is an abrupt reduction in the settling velocity. It arises from the hybrid nature of the Gidaspow drag function switching discontinuously from Wen & Yu equation to Ergun's law. The sharp drop results in the underestimation of sedimentation rate approximately up to 40% particle fractions. In this regime, the assumption on tortuous capillary flow inside the interstitial grain space, being the fundamental concept of Ergun's law, seems inappropriate. Above 40%, SIMMER-V_vpd results become again in close agreement with Richardson & Zaki type equations. This behavior is expected, since packed bed pressure drop measurements used in the derivation of Ergun's law are performed generally above random loose packing around 40%.

The values of settling velocities from SIMMER-V_vo are taken at the first few time steps of the simulations, before a settled bed is formed at the bottom of the container. As it was demonstrated in paragraph IV.2.1, SIMMER-V_vo predicts unreasonably large pressure variations inside a static pile of particles, which brings about inconsistent and fluctuating sedimentation velocities after the appearance of a fully settled bed in this test case. On the contrary, the computations with SIMMER-V_vpd show stabilized behavior at each solid volume concentration. To investigate the impact of solid phase stresses during the sedimentation process, the balance of particle momentum terms in SIMMER-V_vpd is shown in Figure IV.26.

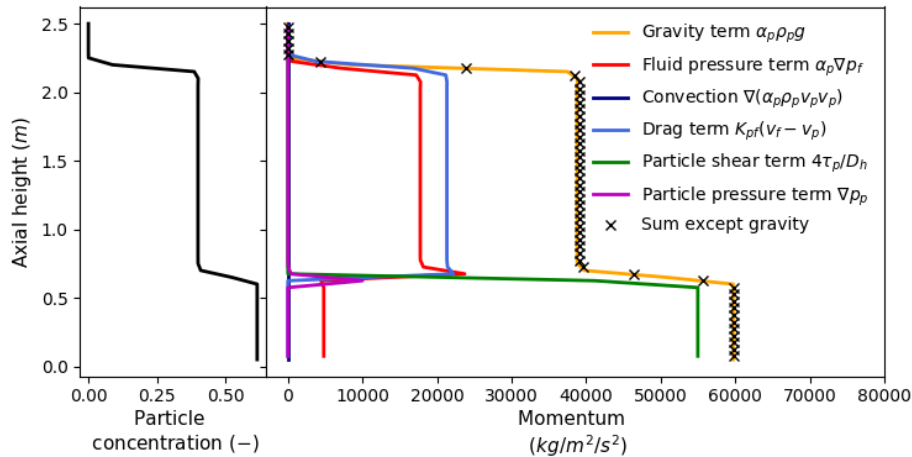


Figure IV.26 Axial profile of particle concentration and particle momentum balance after 3 seconds of sedimentation by SIMMER-V_vpd

We observe from Figure IV.26 that both particle pressure gradient and particle shear stress terms are negligible in the regime of constant settling (just below the clear fluid-suspension interface). In this region, the gravity weight of particles is balanced by the fluid pressure gradient and the interphase drag term. This supports the fact that the sedimentation process is governed by fluid-solid interphase exchanges. Particle pressure gradient appears exclusively at the interface between the settling and the settled bed. This is the only location where solid concentration changes significantly within the application limits of $\mu(I)$ dense granular rheology equations ($\alpha_p \geq 0.3$). Inside the settled bed, the vertical profile of solid concentration is constant and the velocity is zero. Therefore, the gradient of particle pressure is zero inside the bed. In this regime, the apparent weight of particles is fully supported by the shear stress term, while fluid weight is balanced by the gradient of fluid pressure. The behavior of packed particle bed is analogous to the test case of two-phase packed particle piles studied in section IV.2.

Based on the results presented in this section, we conclude that both SIMMER-V_vo and SIMMER-V_vpd predict well the sedimentation velocity of initially homogeneous dense particle clouds with varying uniformly sized particles settling under gravity. Although the results of SIMMER-V_vo are in

IV.6 Sedimentation under gravity

closer agreement with the empirical equations, it fails to provide a stable solution when particles come to rest at the base of the tube.

Despite the fact that results are presented for one single size of fuel particle components in SIMMER-V, the above conclusions are valid for each grain size. Simulations performed with different grain sizes within the range defined in Table IV.1 show identical behavior with both SIMMER-V_vo and SIMMER-V_vpd. In the next part, the analysis is extended for a multi-component system.

IV.6.3 Terminal velocity of a cloud of different particulate components

Reactor debris most commonly consist of varying fractions of different degraded core materials. Following the terminology of SIMMER-V, particle-size solid debris comprise fuel, steel and chunk particles. In this section, we analyze the effect of such multi-component nature of the particle assembly on the sedimentation phenomenon. The purpose is to verify the consistency of numerical modelling in SIMMER-V_vo and SIMMER-V_vpd for the case of multi-component particle assembly.

Theoretically, if all constituents possess identical physical properties, the mixture settles at same rate as a pure component at the same global concentration. In this way, equations of Table IV.4 can be used for comparison. The test case is identical to the one of paragraph IV.6.2, except that the dispersed phase contains not only fuel but also steel and chunk particles, see the schematic view in Figure IV.27. These components are grouped into the same momentum field in line with the scope of the thesis on unified particulate momentum allocation. The densities of steel and chunk are modified manually to match with the density of fuel and an equal size is imposed for all components.

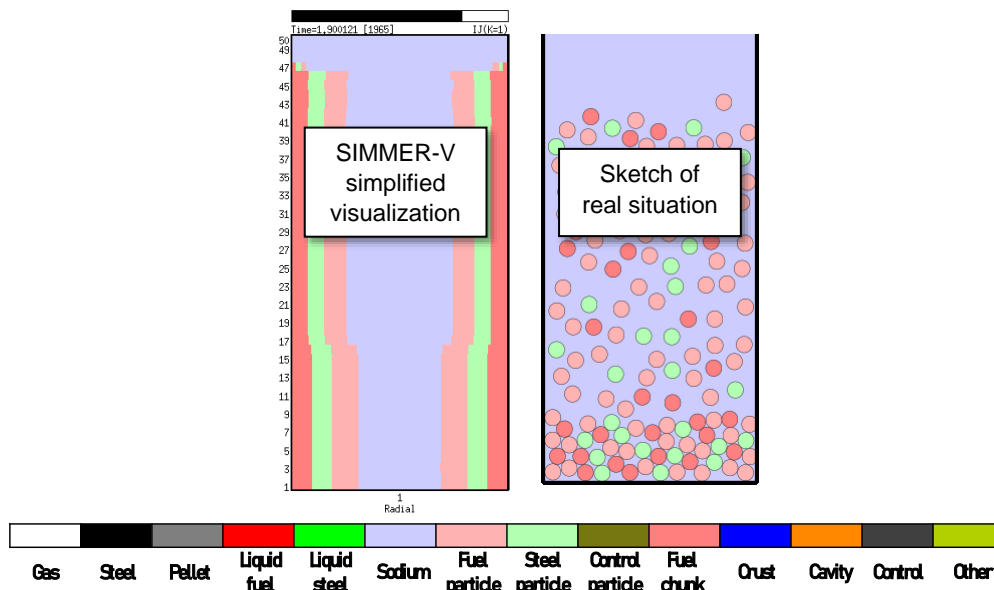


Figure IV.27 Schematic view of sedimentation with different particulate components in SIMMER-V

Simulations are performed with varying fraction of fuel, steel and chunk components homogeneously mixed in liquid sodium but keeping the global solid concentration always constant. The results obtained by SIMMER-V_vo and SIMMER-V_vpd at 10% and 40% solid concentration are presented in Figure IV.28. These two concentrations are analyzed to take into account both elements of the Gidaspow drag equation.

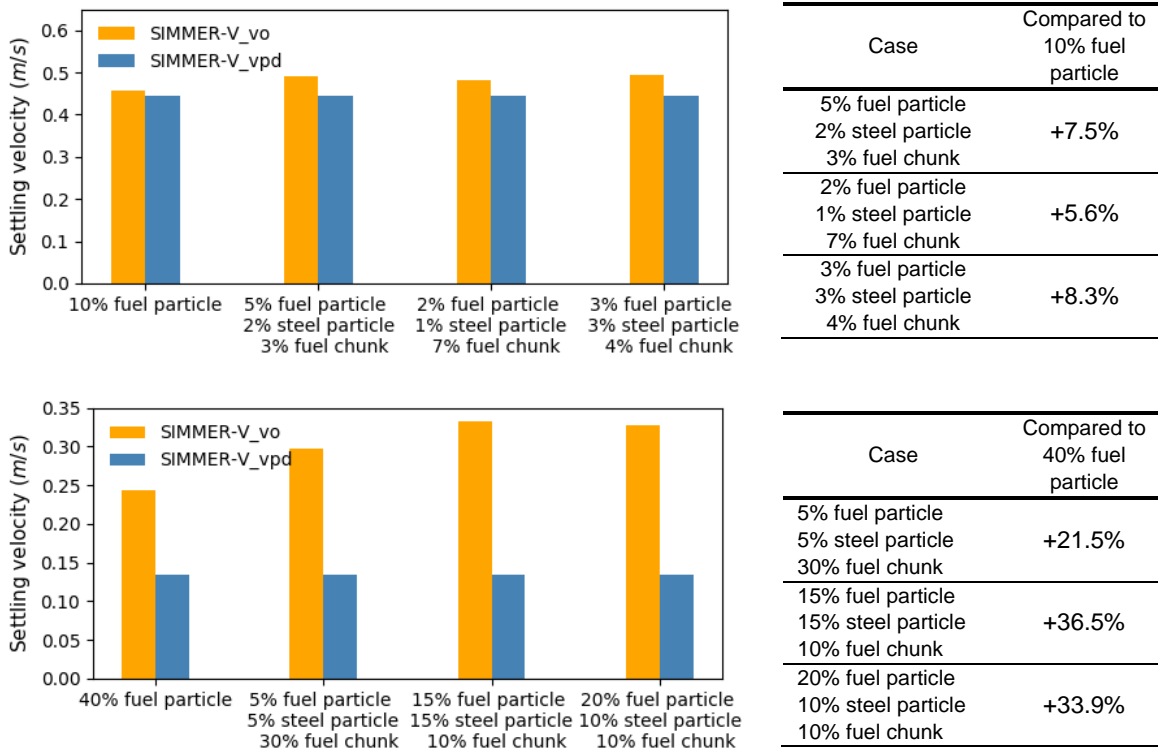


Figure IV.28 Settling velocities in multi-component particle system and their relative deviation from the mono-component case at 10% (top) and 40% (bottom) global concentration

Looking at the settling velocities with different fractions of particle components in contrast to the settling velocity of fuel particles alone in Figure IV.28, one observes different values simulated by SIMMER-V_vo. With 10% global particle content, the highest deviation from the mono-component value is around 8% indicating an overestimation of sedimentation rate. In case of 40% global particle content, this difference increases above 35% when the flow is comprised of relatively equal ratio of particulate components. The reason for these inconsistencies arises from the interfacial area modelling and its use in the formulation of interphase drag function. Since SIMMER-V_vo was originally developed on the mixture momentum approach for particles and fluid, interfacial areas (for both momentum and heat exchange) between particulate components are computed as a function of their concentration. However, there is no momentum exchange processes through inter-particle interfacial area when particles are grouped into the same velocity field. Consequently, the corresponding particle surface area is excluded from the fluid-particle exchange function, resulting in lower drag force and higher settling rates depending on the ratio of the components. This is inconsistent with the theoretically predicted behavior. Above all, such magnitude of inconsistent increases can have a significant impact on the discharge rate of reactor debris through the mitigation transfer tubes.

Calculations with SIMMER-V_vpd in Figure IV.28 show no dependency on the fraction of components comprising the particulate mixture. In the formulation of Gidaspow drag function, the interfacial area is included indirectly for each component, representing their real surface through which momentum exchange occurs. At both global concentrations, the settling velocity of particle mixtures is identical to the one of a single component, which is in agreement with the basic theoretical expectation.

Overall, we conclude that the settling velocity in an initially homogeneous dense particle cloud with varying fraction of uniformly sized and equally heavy particle components is well simulated by SIMMER-V_vpd while considerable inconsistencies are identified in SIMMER-V_vo calculations.

IV.7 HYDRAULIC CONVEYING

The last test case addresses the situation when both particle and fluid (liquid in particular) phases flow co-current relative to the confining structure in a vertical pipe under the effect of pressure difference. In reactor severe accident scenarios, one may expect that the unidirectional flow of particle-fluid mixture is encountered during the relocation process through the mitigation transfer tubes. Solid debris relocate together with liquid fuel or liquid steel typically around the core height (where FCI evaporated the sodium bulk of the transfer tubes). At lower tube regions, reactor debris can flow co-current within liquid sodium when the latter is drained down to the core catcher.

In the literature, this configuration corresponds to hydraulic conveying systems exploiting liquid flow and pressure differential to transport bulk solid material or powders through enclosed pipelines. Another type of conveying is pneumatic using gas as carried fluid. In this section, we focus on hydraulic transport only because the typical debris size and density difference between debris and sodium vapour or fission gases would require a very large gas mass flow to carry reactor particles. Such mass flows are unlikely to be encountered in reactor application. The dense phase particle transport by a carrier liquid is referred as slurry flow [Kalman et al., 2019]. Slurry flows are widely employed in industry and occurring in nature, examples include mixtures of coal/cement and water used in the petroleum industry, open-pit mining of phosphate, pyroclastic material composed of rocky debris and liquids produced in a volcanic eruption and the mixture of ice crystals and water. The main interest in studying slurry flows is to determine the pressure drop or head loss, which has to be compensated by the pumping power to maintain the material transfer through the pipeline and move particles from one location to another. Slurries are generally divided into non-settling (small particles typically less than 75 μm , neutrally buoyant particles flowing at the same speed as the liquid) and settling (large particles traveling at a different velocity than that of the fluid) types. In both cases, the presence of particles contributes to the frictional pressure loss but of different physical origin. For settling slurries, corresponding to reactor debris, it is attributed to particle-particle and particle-wall collisional and frictional interactions [Bartosik, 1996].

The experimental analysis to evaluate SIMMER-V particle dynamic models is an upward co-current vertical conveying of water-particle mixture, performed by [Shook and Bartosik, 1994]. The test section is a 26 mm diameter and 2.28 m long vertical cylindrical tube, shown in Figure IV.29. During the experiment, a constant fraction of solid particles is added to the recirculating water flow. Measurements for frictional head losses are performed with different grain types (sand, polystyrene and polyvinyl chloride) at varying solid concentrations (10%-40%) and with bulk fluid (water $\rho_f = 992 \text{ kg/m}^3$) velocities ranging from 2-6 m/s.

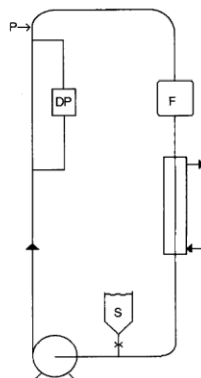


Figure IV.29 Experimental setup, F: flowmeter, S: standpipe, P: wall probe location, DP: wall friction transducer after [Shook and Bartosik, 1994]

The SIMMERE-V representation of the experiment consists of a one-dimensional vertical channel with the appropriate physical dimensions and adjusted fluid/solid properties in the code, visualized

in Figure IV.30. Grains are simulated by fuel particles and water is defined by an input option for coolant materials. Water and particles enter from the lower boundary with velocity boundary condition on water, and leave at the top outlet with constant pressure condition.

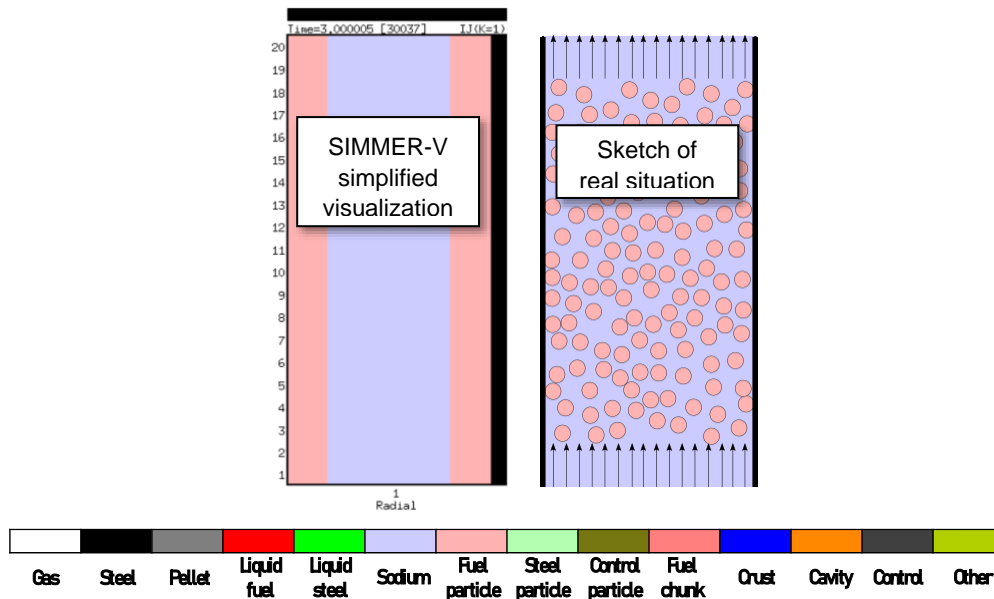


Figure IV.30 Schematic view of the hydraulic conveying

In the experiment, only bulk velocity was monitored by volumetric flow measurements and arguing that solid-fluid slip velocity was negligible compared to the global flow velocity. Thus, the comparison of experimental pressure losses with SIMMER-V results are based on liquid phase velocity. Firstly, to verify that the experimental conditions are well reproduced, SIMMER-V results for a fully developed flow are compared to the experimental pressure drop data with pure water in Figure IV.31. Since no particles are present in this calculation, SIMMER-V_{vo} and SIMMER-V_{vpd} give identical results. Experimental data is extracted from the publication of [Shook and Bartosik, 1994].

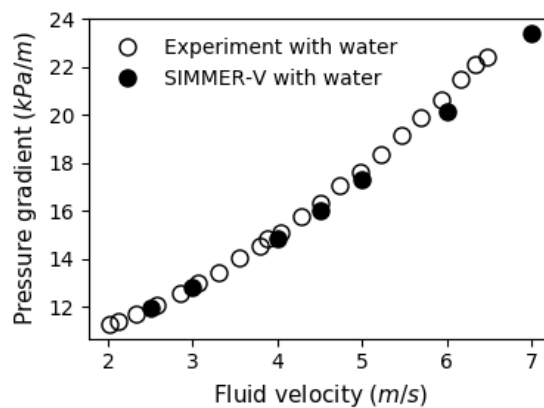


Figure IV.31 Experimental and SIMMER-V pressure drops with pure water

From the close agreement between the experiential and numerical curve in Figure IV.31, one can reasonably conclude that the experimental conditions are well recovered by SIMMER-V.

Following, the pressure drops with different polystyrene particle concentrations, 10% and 40% respectively to account for the different sets of rheology equations below and above 30% based on section III.7, are compared to the experimental values in Figure IV.32. The case of polystyrene grains

was chosen because it reveals the most the evidence of the effect of particles³⁰. We note that the results of SIMMER-V_vpd apply the adjustment of c_s parameter. The best fitting value for this experiment was found to be $c_s = 0.5$.

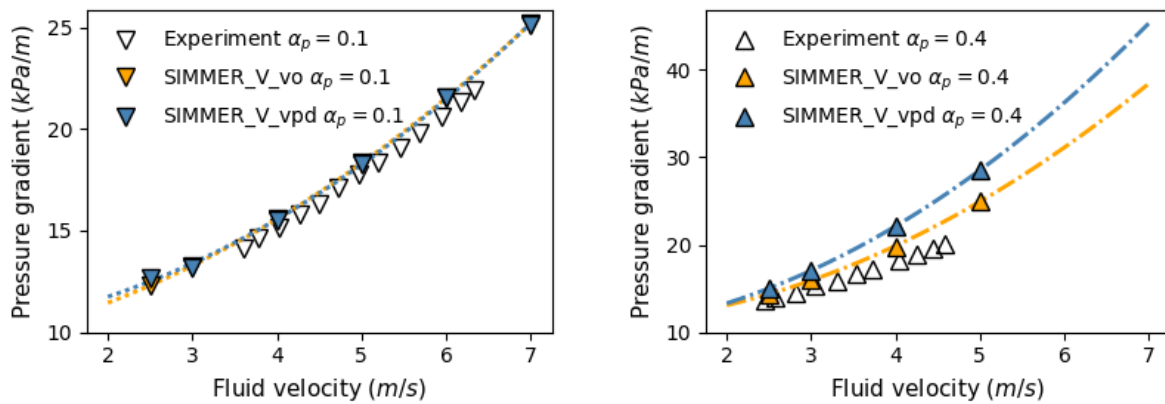


Figure IV.32 Frictional pressure drop with 10% (top left) and 40% (top right) concentration of 2.8 mm mono-disperse polystyrene ($\rho_p = 1045 \text{ kg/m}^3$) grains by experiment, SIMMER-V_vo and SIMMER-V_vpd

From Figure IV.32 left plot for 10% solid concentration, one can observe that both calculations predict almost identical pressure drops as a function of the varying fluid velocities, which is also in close agreement with the experimental data points according to which the fluid pressure drop is square proportional to the fluid velocity. The strong compliance between SIMMER-V_vo and SIMMER-V_vpd is expected since the form of shear stress equations below 30% are the same except for the solid friction factor, which has been adjusted through c_s in SIMMER-V_vpd to match experimental data. Regarding 40% particle concentration on the right plot of Figure IV.32, the same square proportionality is found, but with more pronounced differences between numerical predictions and experimental data. The general trend of SIMMER-V_vo and SIMMER-V_vpd agrees with the experimental points, however, both calculations overestimate the pressure drop. The overestimation becomes larger with increasing fluid velocity, and it is higher for SIMMER-V_vpd run in which rheology models for particle stresses are activated. We estimate that it arises partially from the empirical coefficients of the rheology equations. By adjusting these coefficients to better represent the experimental grain properties, (based on simulation results that are not displayed here) we postulate a better match between SIMMER-V_vpd numerical results and experimental values. Additionally, it is important to mention that the one dimensional modelling inherently brings the overestimation of frictional pressure loss. [Bartosik and Shook, 1995] reports that assuming radially uniform volume fraction over the pipe cross-section (1D approach) disregards the experimentally observed local depletion of particle concentration in the immediate vicinity of the wall, which would reduce the particle-wall interactions and consequently the fluid pressure drop. Similar to our results, they find increasing overestimations with higher solid content. The discrepancy between constant and real volume fraction distribution reaches 30% for coarse sand grains at 40% concentration. The SIMMER-V_vpd discrepancy does not exceed 24% at its maximum. To demonstrate the effect of particle concentration, the results for three different volume fractions are plotted together in Figure IV.33

³⁰ In some other tests, the complex interaction between particles and turbulent eddies enhancing or damping fluid phase turbulence affects the pressure drop. It takes place under certain conditions (grain size, density and concentration). In some cases, the pressure drop is found to be less with suspended particles than for clear water.

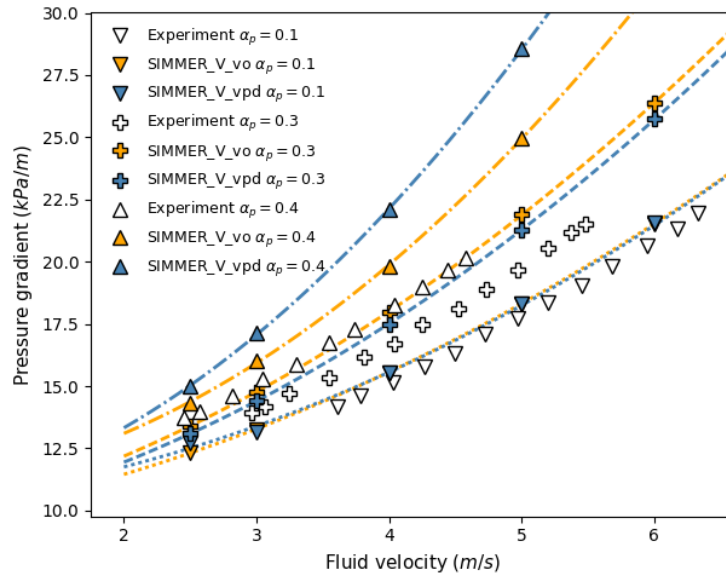


Figure IV.33 Frictional pressure drop with 10%, 30% and 40% concentration of 2.8 mm mono-disperse polystyrene grains by experiment, SIMMER-V_vo and SIMMER-V_vpd

From Figure IV.33, it is apparent, that when solid particles are added to the flow, the fluid pressure drop increases. According to the explanation of [Shook and Bartosik, 1994], it is associated to the appearance of Bagnold-like inter-particle stresses in the grain-inertia regime (see paragraph II.4.3). Such pressure drop increase with solid concentration is reproduced by both SIMMER-V_vo and SIMMER-V_vpd. Considering the previously observed overestimation of pressure drop, one can see that it switches between different SIMMER-V versions: at 30% solid concentration, SIMMER-V_vpd with rheology models are activated predicts pressure losses closer to the experimental values than SIMMER-V_vo, while it is the opposite at 40% particle volume fraction. It comes from the different functionality of solid concentration in the particle-structure momentum exchange term in SIMMER-V_vo and in the wall shear stress term in SIMMER-V_vpd. In SIMMER-V_vo, the particle-wall shear is linear proportional to the solid concentration (the fluid-structure momentum exchange function contains the viscosity multiplier that is non-linear); while in SIMMER-V_vpd it is a non-linear function. In the experimental paper of [Shook and Bartosik, 1994], based on the analysis for various grain diameters and densities, the non-linearity between particle concentration and fluid pressure drop is assigned to the solid-wall shear stress. In this view, even though quantitatively SIMMER-V_vpd results are further from experimental findings, we consider the qualitative estimation of pressure drop characteristic more representative.

In addition, [Shook and Bartosik, 1994] finds dependency of fluid pressure drop on the grain diameter: larger grains bring about higher pressure drops. Without exposing the numerical results, it is evident that SIMMER-V_vo is not able to account for such effect since wall stress equations do not depend on the particle diameter. On the other hand, the $\mu(I)$ dense granular rheology models of SIMMER-V_vpd are function of particle size: the wall shear rate is square proportional to the particle diameter, similar to Bagnold's grain-inertia regime. This is another strong argument towards the newly developed particle dynamic models in SIMMER-V_vpd.

In order to further examine the behavior of $\mu(I)$ dense granular rheology models, we consider the different contributors to the pressure drop. Assuming that the flow is fully developed and stationary, the pressure gradient in Figure IV.32 and Figure IV.33 emerges from the gravitational weight of the fluid-particle mixture, the fluid-wall shear stress and the particle phase stresses. This balance can be obtained by the addition of the two-fluid momentum equations. The terms obtained from SIMMER-V_vpd computation are plotted in Figure IV.34.

IV.8 Synthesis of results

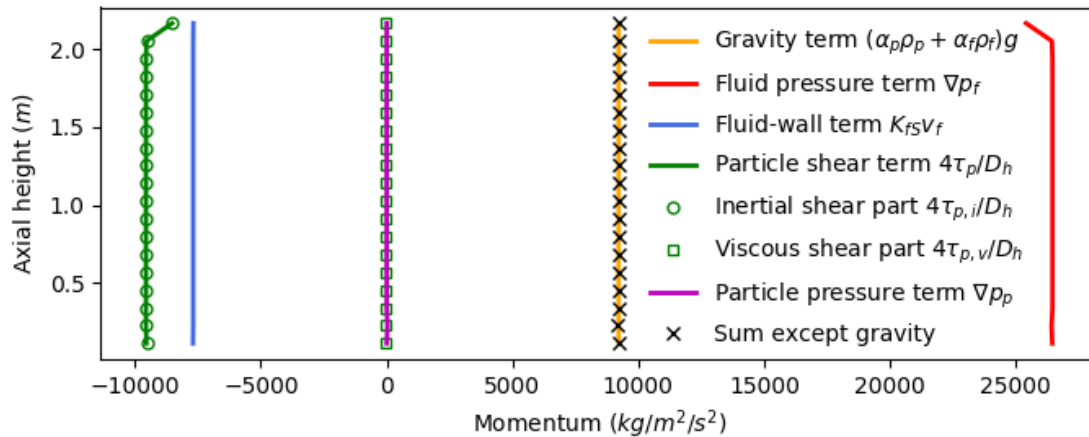


Figure IV.34 Momentum terms influencing the pressure drop during hydraulic conveying by 5 m/s fluid velocity of 40% concentration of 2.8 mm mono-disperse polystyrene grains by SIMMER-V_vpd

The balance of momentum terms in Figure IV.34 indicates that the highest contributor of the fluid pressure loss is indeed the particle phase shear stress term. It proves that particle-particle interactions dominate the global flow behavior. In agreement with the previously observed square velocity relations, the inertial part of the particle shear stress has an overwhelming influence over the viscous part with negligible importance. The particle pressure gradient is zero everywhere because of constant solid concentration through the pipe length. The fluid-structure friction term has a comparable magnitude to the particle shear term.

Overall, we conclude that the behavior of the hydraulic conveying experiment of [Shook and Bartosik, 1994] in terms of pressure loss increase with fluid velocity and solid concentration is well simulated by both SIMMER-V versions. Even though, SIMMER-V_vpd overestimates more the experimental data at higher concentrations (due to an acceptable degree of excess pressure loss), the experimentally confirmed non-linear dependence between pressure drop and solid concentration and the possibility to account for particle size effect supports the use of SIMMER-V_vpd.

IV.8 SYNTHESIS OF RESULTS

After analyzing every test case separately, we return to Table IV.2 summarizing the figure of merit and its characteristic behavior associated to each test. Based on the conclusions drawn from the comparative studies in the previous paragraphs, we reconstruct Table IV.2 by Table IV.5. Table IV.5 indicates whether the characteristic behavior of the figure of merit in liquid and gas is obtained by calculations of SIMMER-V_vo and of SIMMER-V_vpd.

Table IV.5 demonstrates that, by applying the newly developed particle dynamics models (section III.7), the characteristic behavior of the figure of merit is reproduced in each test case. It is valid in both liquid sodium and gaseous environments. In contrast to SIMMER-V_vo, calculations show considerable improvements, especially in case of fluidization by liquid sodium for which SIMMER-V_vo results are not interpretable and in case of jammed particle piles where SIMMER-V_vo models are insufficient to capture the physics of granular matter.

Table IV.5 Evaluation matrix of simplified test cases (+ reproduced, - not reproduced, ○ not interpretable, X not analyzed)

Test case	SIMMER-V_vo		SIMMER-V_vpd	
	Gas	Liquid	Gas	Liquid
Jammed particle pile (special situation)	-	X	+	X
	X	-	X	+
	X	-	X	+
Bin discharge	-	X	+	X
Flow through porous media	+	-	+	+
Fluidization transition	-	○	+	+
	-	○	+	+
Sedimentation	X	+	X	+
	X	+	X	+
	X	-	X	+
Hydraulic conveying	X	+	X	+

Chapter V. **INTEGRAL EFFECT TEST**

In this chapter, we move towards more complex scenarios that better correspond to the phenomena occurring during the discharge of degraded core through the mitigation transfer tubes. The objective is to evaluate the effect of model development related to particle dynamics in a multi-phase fluid environment besides heat and mass transfer. It is carried out by investigating the results of integral effect experimental programs.

V.1	Experimental programs on degraded core behavior.....	98
V.2	Synthetic description of EAGLE-1 tests.....	99
V.3	Modelling the test section in SIMMER-V	101
V.4	Simulation results of EAGLE-1 ID1 and FD with SIMMER-V	101
V.5	Comparison of discharged mass	104
V.6	Particle rheology in EAGLE-1 FD test	107
V.7	Sensitivity study	109
V.8	Discussion and perspectives	113

V.1 EXPERIMENTAL PROGRAMS ON DEGRADED CORE BEHAVIOR

Moving towards more complex scenarios, experimental data from integral effect tests is studied. Integral effect tests are carried out in scaled down facilities representative of real reactor conditions and dedicated to simulate the overall behavior of core materials during accident conditions. Available experimental knowledge on fuel degradation and its spatial relocation consists of international test programs that were performed in the past 30 years. The most relevant test programs providing quantitative evaluation and phenomena resolution of accidental scenarios are listed in Table V.1.

Table V.1 Experimental programs related to fuel degradation

Experimental program	Test	Phenomena of interest
SCARABEE [Kayser et al., 1998]	APL3	In-pile behavior of a volumetrically heated molten fuel pool resulting from a sub-assembly melting at full power. Sequence from initiating phase to fuel pellets fragmentation and its massive relocation.
	BF	In-pile physics of pure UO ₂ boiling in view of molten pool natural convection.
	PI-A	Melt propagation tests: propagation into inter-subassembly and neighboring sub-assembly respectively.
	PV-A BA	Phenomena inside the blocked subassembly.
THINA [Uršič and Leskovar, 2015]	TH561, TH652, TH654, TH567	Assessment of fuel-sodium interaction (out-of-pile). Melt front penetration into sodium followed by fuel thermal fragmentation, vaporization and rapid sodium condensation on the surface of the fragments.
GEYSER [Yamano and Tobita, 2008]	About 10 tests	Bulk freezing behavior of liquid fuel (out-of-pile) inserted upwards into a small vertical tube ($\varnothing=4$ mm). Focus on freezing morphology (particle formations and blockages) and the penetration length.
FARO [Le Belguet et al., 2012]	THERMOS-T1	Large-scale in-pile investigation of fuel-sodium coolant interaction and the related phenomena (jet breakup, fragmentation mechanisms and freezing).
EAGLE-1 [Konishi et al., 2007]	Out-of-pile series	Test with molten alumina to evaluating molten-fuel discharge behavior through the CRGT (control-rod guide tube)
	FD	In-pile test on the discharge of degraded fuel through an inner duct structure into voided channel
	ID1, ID2	In-pile test on the discharge of fuel through inner duct structure into a sodium filled channel (ID2 with reduced power insertion to achieve less pronounced fuel heating effect)
EAGLE-2	About 10 tests	In-pile and out-of-pile tests on molten fuel upward relocation behavior and heat transfer process from melt pool to inner duct wall
EAGLE-3	About 10 tests	Investigations of the molten-core relocation through the control rod guide tube (CRGT), on the coolability of relocated core material at the inlet coolant plenum and coolability of core-remaining materials by coolant re-entry after termination of relocation
SAIGA [Payot et al., 2018]	SAIGA-1	Future in-pile test on the discharge of molten fuel in a sodium-filled transfer tube in a ULOF scenario involving two small scale subassemblies of different power.
PLINIUS-2 [Journeau et al., 2019]	TR/FR/EXPLO SERUA/DROP	Future large scale (~100-300 kg material) out-of-pile tests planned at CEA for the study of fuel-sodium (or water) interaction controlling jet fragmentation and debris bed formation.

Among these, the EAGLE-1 (Experimental Acquisition of Generalized Logic to Eliminate recriticalities) in-pile test series is identified as most representative (at this moment) to the investigation of phenomena related to degraded core material discharge via dedicated duct. Another advantage is that CEA has access to the complete experimental documentation including data of

thermocouples, neutron detectors, pressure sensors etc. Upon that, extensive research at CEA is dedicated to the interpretation of such signals and their numerical reproducibility by SIMMER code series. The CEA reference calculation as a result of these analyses was performed by SIMMER-III. Therefore, we take advantage of the EAGLE-1 experimental program in evaluating the ability of newly developed particle models in SIMMER-V to predict the discharge dynamics on an integral level. In the next sections, we describe the global experimental setup and its numerical representation by SIMMER-V.

V.2 SYNTHETIC DESCRIPTION OF EAGLE-1 TESTS

The information presented in this work on EAGLE-1 tests is limited to the publicly available documentation. Due to the restricted CEA ownership, the use of precise experimental conditions and results are avoided to protect intellectual property. Henceforth, we do not intend to reflect precisely the experimental scenario. Our analysis focuses on tracing the major events and capturing the general experimental observations relevant to the scope of this work. The physical origin of such observations is discussed in internal CEA reports and they will not be communicated here.

The in-pile EAGLE-1 tests were conducted by JAEA, benefiting of the safety research facilities at the National Nuclear Center of the Republic of Kazakhstan. The experiments are performed in the central experimental channel of IGR (Impulse Graphite Reactor). The purpose of the EAGLE-1 test program is to gain experimental evidence for elimination of the re-criticality issue in SFRs in the event of excessive core degradation. It is achieved by demonstrating the effectiveness of early fuel escape from core center through an inner duct structure (FAIDUS approach [Tobita et al., 2008]) introduced into one of the sub-assemblies. Large-scale EAGLE-1 tests include “Fuel Discharge” (FD) and “Integral Demonstration” (ID1 and ID2) experiments. The test section geometries used in each of them are identical. The difference is that the inner duct contains Argon gas in FD test, while it is filled with liquid sodium in ID1 and ID2. The ID tests differ from each other only in terms of energy deposition [Toyooka et al., 2010]. The schematic view is shown in Figure V.1.

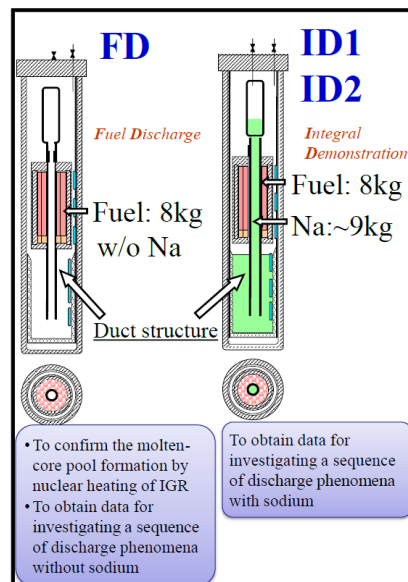


Figure V.1 Principle of FD, ID1 and ID2 in-pile tests conducted within the EAGLE-1 program after [Konishi et al., 2007]

The approximately 8 kg of fuel in form of uranium dioxide is loaded into a core-simulating vessel and arranged cylindrically in a 75-pin bundle (with steel cladding) around the center transfer duct. The duct is separated from the fuel assembly jacket (FAJ) by a 2 mm-thick steel wall. Its internal diameter

V.2 Synthetic description of EAGLE-1 tests

is 36 mm. In case of ID1/ID2 tests, it is filled with around 9 kg of liquid sodium. At the start of the experiment, a controlled power pulse from IGR is applied to the fuel bundle whose characteristic shape is shown in Figure V.2.

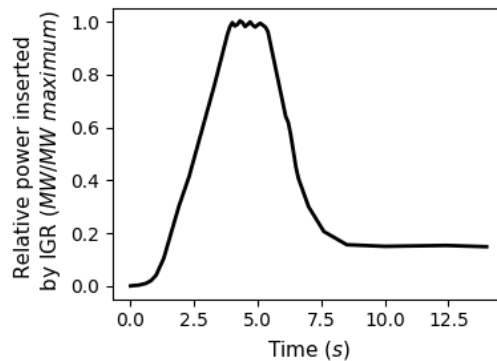


Figure V.2 Characteristic shape of power transient by IGR after [Konishi et al., 2007]

The energy insertion via the high neutron flux leads to clad melting and pin degradation, and subsequently to the formation of an UO₂-steel molten pool inside the fuel assembly jacket. The degraded/molten mixture comes in contact with the duct wall. Being exposed to large heat transfer, the duct wall heats up and eventually loses integrity by thermal failure. After duct opening, materials from the FAJ enter into the transfer duct and discharge towards the melt trap located below the test section [Kamiyama et al., 2014].

In line with our scope of interest, we focus on the discharge phase after duct wall failure. The sequence of events arriving to this point is disregarded. The important aspects originating from pre-discharge phase is the composition of degraded mixture flowing into the transfer channel. Ensuring that experimental conditions are well captured and that the global interpretation of the test is correct, we take into account the following figures of merit for the discharge process:

- 1) Duct wall thermal failure allows degraded mixture to enter into the duct.
- 2) Fuel freezes on the duct wall and forms crust. The crust protects the steel wall from melting such that it remains intact. (the information available on the state of the duct after the test is scarce: only post-test visualization suggests crust formation with varying thickness in ID1/ID2 and FD tests.)
- 3) Following a massive corium discharge, large fraction of fuel is removed from the FAJ and located in the lower trap. No permanent blockage was observed in the duct.

Our ultimate interest is to evaluate the discharged mass preferably, when the molten pool contains high fraction of solid debris. In this scenario, the mass flow rate inside the duct reflects the impact of particle dynamics. We acknowledge that establishing an appropriate mass balance is difficult due to the lack of data available for the precise calibration of neutron sensors. Therefore, we conduct a comparative analysis between CEA most recent best estimate calculations by SIMMER-III, SIMMER-V with original equations and default setting of modelling options (SIMMER-V_{vo}) and SIMMER-V with newly implemented particle dynamics models (SIMMER-V_{vpd}). The CEA best estimate calculation by SIMMER-III is supported by large research efforts on best fitting modelling parameters identified from sensitivity studies. Besides minor discrepancies, overall it is found to be in good agreement with experimental findings (however, the inner duct had to be radially meshed to avoid blockages due to particle accumulation inside the transfer duct). In the following, we focus on ID1 and FD tests since they account for the two distinctive cases of sodium and gas duct interior. The ID2 test shows similar behavior to ID1.

V.3 MODELLING THE TEST SECTION IN SIMMER-V

The numerical representation of the EAGLE-1 FD and ID1 test sections in SIMMER-V is shown in Figure V.3 with highlight on the three main regions: FAJ, Transfer Duct and Lower Ttrap. More details on the numerical representation of test section is not displayed for confidentiality reasons.

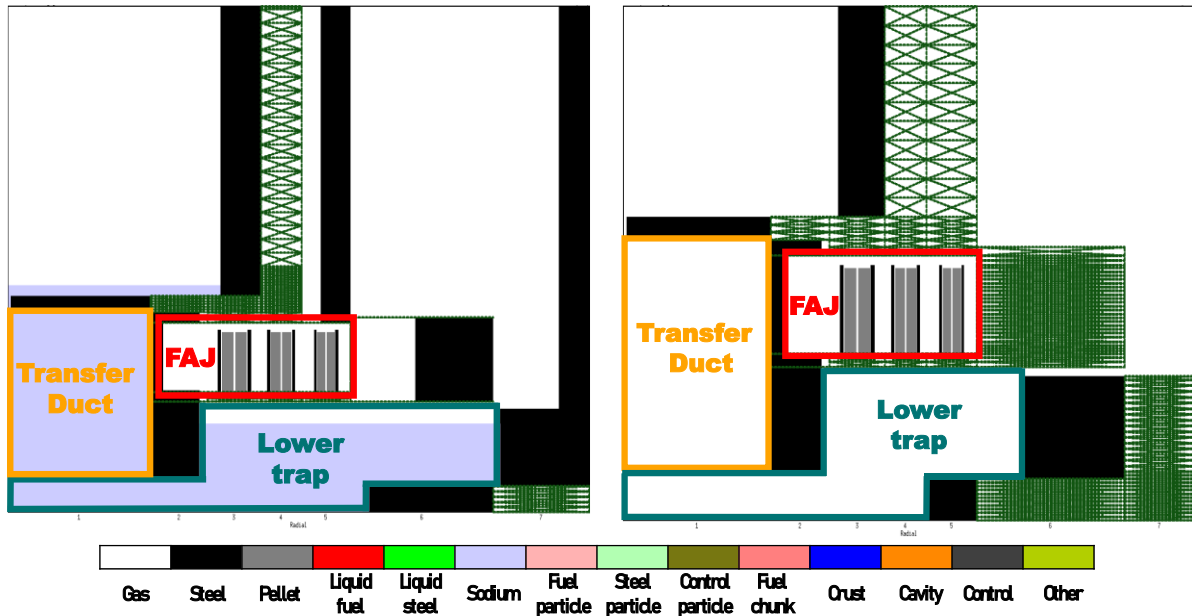


Figure V.3 r-z cut of test section ID1 (left) and FD (right) modelling in SIMMER-V (dark green areas are excluded from calculation). The symmetry axis is on the left side of each figure.

This simulation is performed by considering r- θ -z cylindrical coordinate system. The geometry of Figure V.3 is rotated 360° around theta direction. The FAJ (fuel assembly jacket) contains the total mass of fuel in form of pin structures. It is separated from the central duct by a 2 mm thick structure component. The transfer duct is modelled by one radial mesh in accordance with the one-dimensional flow map approach of SIMMER-V (section III.1). At the bottom of the test section, there is the lower melt trap. The duct and lower trap are filled with stagnant liquid sodium in ID1. As it was explained previously, particle diameter in SIMMER is a user choice. In the following simulations, it is set to be 1 mm uniform for all particulate components. The simulation by SIMMER-V_vpd includes the new input parameter RHEOLREG defining the regions for which newly implemented particle dynamics models are applied. RHEOLREG is initialized for the meshes of the Transfer Duct.

The geometry in SIMMER-III (without considering theta coordinate dependence) is the same as of Figure V.3 except that, in SIMMER-III, the duct is modelled by four radial meshes. It is identified as best estimate case that time by the development and validation team at CEA, following sensitivity studies showing strong dependence of discharge dynamics on the radial discretization of the inner duct. However, the need for a one-dimensional duct approach (in agreement with 1D SIMMER-V channel flows) has been identified.

V.4 SIMULATION RESULTS OF EAGLE-1 ID1 AND FD WITH SIMMER-V

In this part, we analyze the simulation results of SIMMER-V_vo and SIMMER-V_vpd in view of the criteria listed in section V.2.

1) Fuel degradation and duct wall failure

The degraded state of the FAJ at the instant before duct failure is illustrated in Figure V.4. Since the simulations of SIMMER-V_vo and SIMMER-V_vpd differ only when particulate components are present inside RHEOLREG meshes, the calculations give the same results on the phenomena

occurring inside the FAJ before duct opening. Thus, SIMMER-V_{vo} results are not plotted separately.

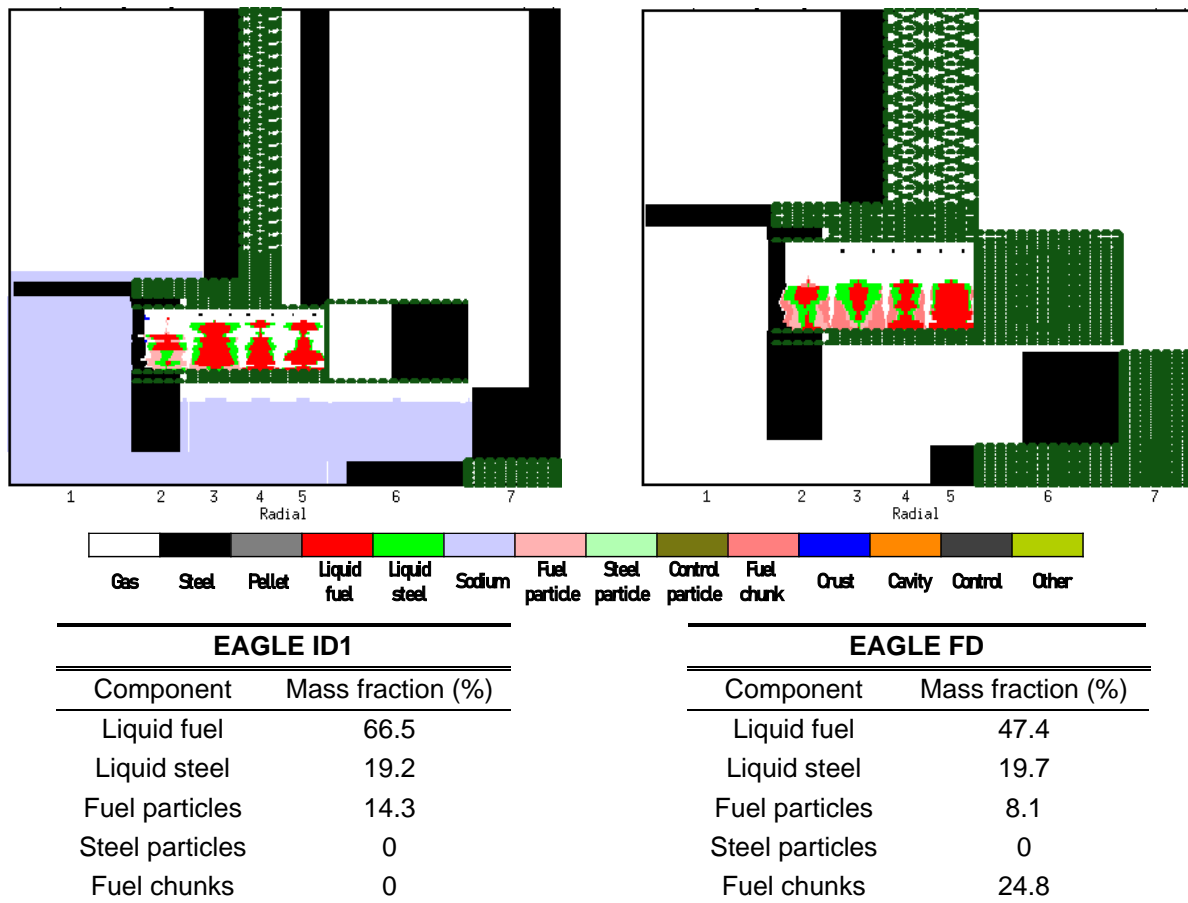


Figure V.4 Material distribution inside the FAJ in EAGLE-1 ID1 (left) and FD (right) tests by SIMMER-V_{vpd} just before duct failure

Figure V.4 indicates that all of the fuel pins inside the fuel assembly jacket are degraded in both tests. The cladding is completely melted (no steel particles) and it is present fully in form of liquid steel accounting for around 20% of the total FAJ mass. Regarding the state of fuel in ID1, approximately 80% is molten in the form of liquid (66.5% of total FAJ mass) and the remaining 20% (14.3% of total FAJ mass) is in form of fuel particles. For FD test, somewhat lower fraction, around 47% of total FAJ, reached melting temperature. Approximately one third of the initial FAJ mass (33%) is in particulate form, shared between fuel particles and chunks. The pellet disintegration mechanism defining the partitioning between fuel particles and chunks are controlled by input parameters selected in accordance with the conclusions (that differ from ID1 and FD) of the sensitivity study by SIMMER-III³¹. In case of FD, such high concentration of particulate components implies substantial effect of particle-particle interaction on the global discharge dynamics.

After the formation of molten pool, the duct wall is exposed to the high temperature mixture in both tests. In parallel, the wall surface temperature starts to increase rapidly, see Figure V.5. In the same time, part of the liquid steel inside the molten pool freezes on the wall surface and adds up to the thickness of the duct wall. Therefore, one observes an increased wall thickness in Figure V.5. When the wall heats up sufficiently approaching melting temperature (1700 K for steel), it begins to melt by reducing its thickness and eventually transforming into liquid steel. This conforms to the experimental observation according to which duct opens by its thermal failure. The physical phenomena in ID1

³¹ The fact that fuel chunks appear in EAGLE ID1 and not in EAGLE FD simulation is purely related to user input options.

and FD test are identical except that the internal side of the duct wall is cooled by liquid sodium and that wall failure takes place earlier in ID1 (presumably because of the larger power pulse).

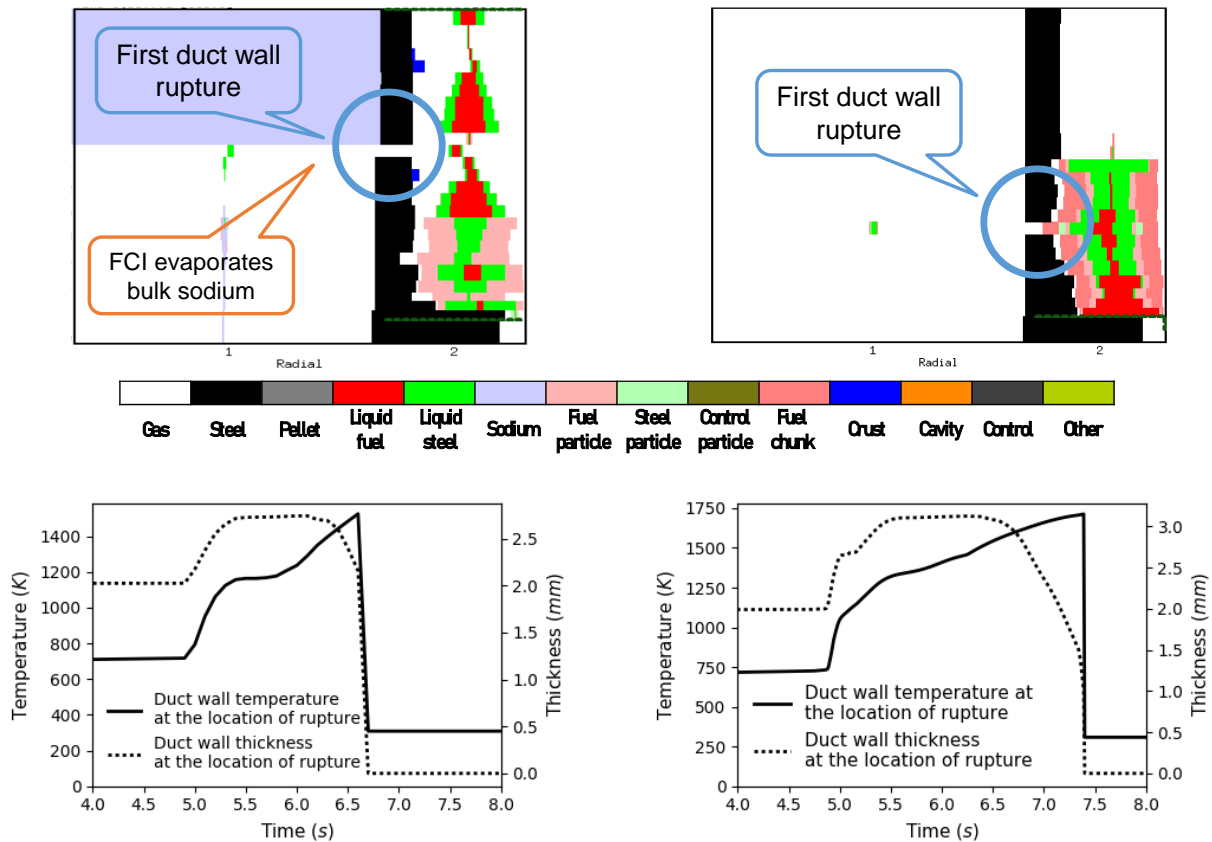


Figure V.5 First duct rupture view and wall temperature and thickness at this location by SIMMER-V_vpd in EAGLE ID1 (left) and EAGLE FD (right)

Consequently, one observes the disappearance of solid structures in SIMMER-V at the location of the rupture. At this point, the barrier between inner duct and FAJ disappears such that degraded materials are free to flow into the transfer channel. Afterwards, the rupture extends to several axial meshes increasing the cross-section for the inflow.

2) Crust formation

Post-experimental visual examination showed the formation of a crust on the duct wall surface (thick crust in FD and thin crust in ID1). Crust refers to the solidification of liquid fuel on structure surfaces. To decide whether this observation is well simulated, Figure V.6 shows the material distribution plots at the end of the calculation of ID1 and FD with SIMMER-V_vo and SIMMER-V_vpd respectively.

The simulation of ID1 test with SIMMER-V_vo does not predict crust formation inside the duct (there is some crust in the FAJ interior). It is because liquid fuel remains at FAJ height and it does not flow into the region where transfer duct is still intact (discussed in the next paragraph). The run of SIMMER-V_vpd shows for ID1 test a discontinuous crust along the intact tube surface. The average thickness is around 0.8 mm. The CEA reference calculation of ID1 test suggests an axially homogeneous crust of 0.4 mm on average at the end of the simulation.

V.5 Comparison of discharged mass

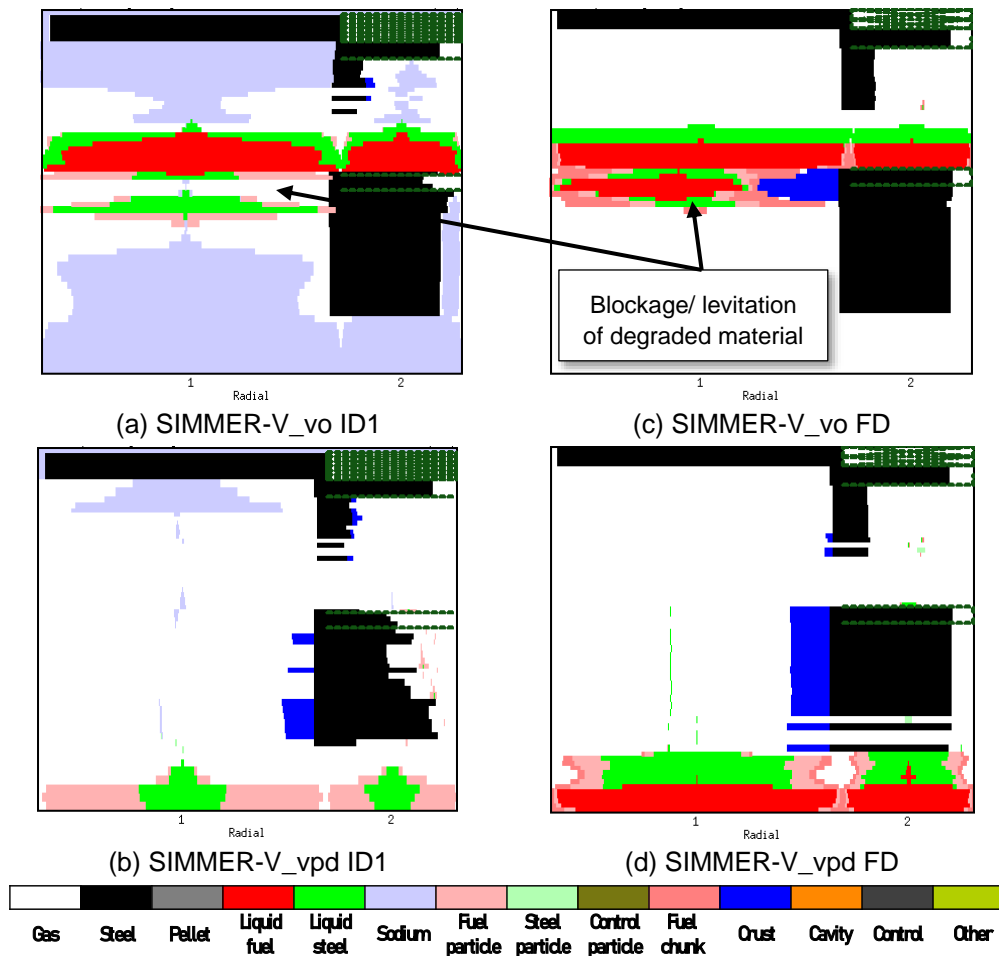


Figure V.6 Material distribution at the end of simulation for (a) ID1 test by SIMMER-V_vo, (b) ID1 test by SIMMER-V_vpd, (c) FD test by SIMMER-V_vo and (d) FD test by SIMMER-V_vpd

For FD test (see Figure 6 right plot), one can see that both SIMMER-V calculations predict crust formation on the duct wall surface. According to SIMMER-V_vo the crust is concentrated around the tube opening. Its thickness at the end of the simulation is around 3.8 mm. The fact that crust is only formed at upper duct locations is because the degraded mixture (liquid fuel) does not penetrate into lower duct regions. On the other hand, SIMMER-V_vpd predicts a relatively constant crust build-up along duct length with average thickness of 1.4 mm. This value coincides with the CEA reference calculation of SIMMER-III except that the latter run shows discontinuous crust formation. Altogether, in lack of sufficient experimental data available, we consider the SIMMER-V_vpd result of continuous crust with a reasonably close thickness to the one in CEA reference calculation, as an acceptable prediction.

The third point 3) stating that large fraction of FAJ materials is located in the lower melt trap is investigated in terms of the temporal evolution of masses in the next section.

V.5 COMPARISON OF DISCHARGED MASS

The temporal balance of masses inside the three main test regions of Figure V.3 are plotted in Figure V.7 for EAGLE ID-1 and FD. The results are obtained by SIMMER-III (CEA most recent best estimate run), by SIMMER-V_vo and by SIMMER-V_vpd.

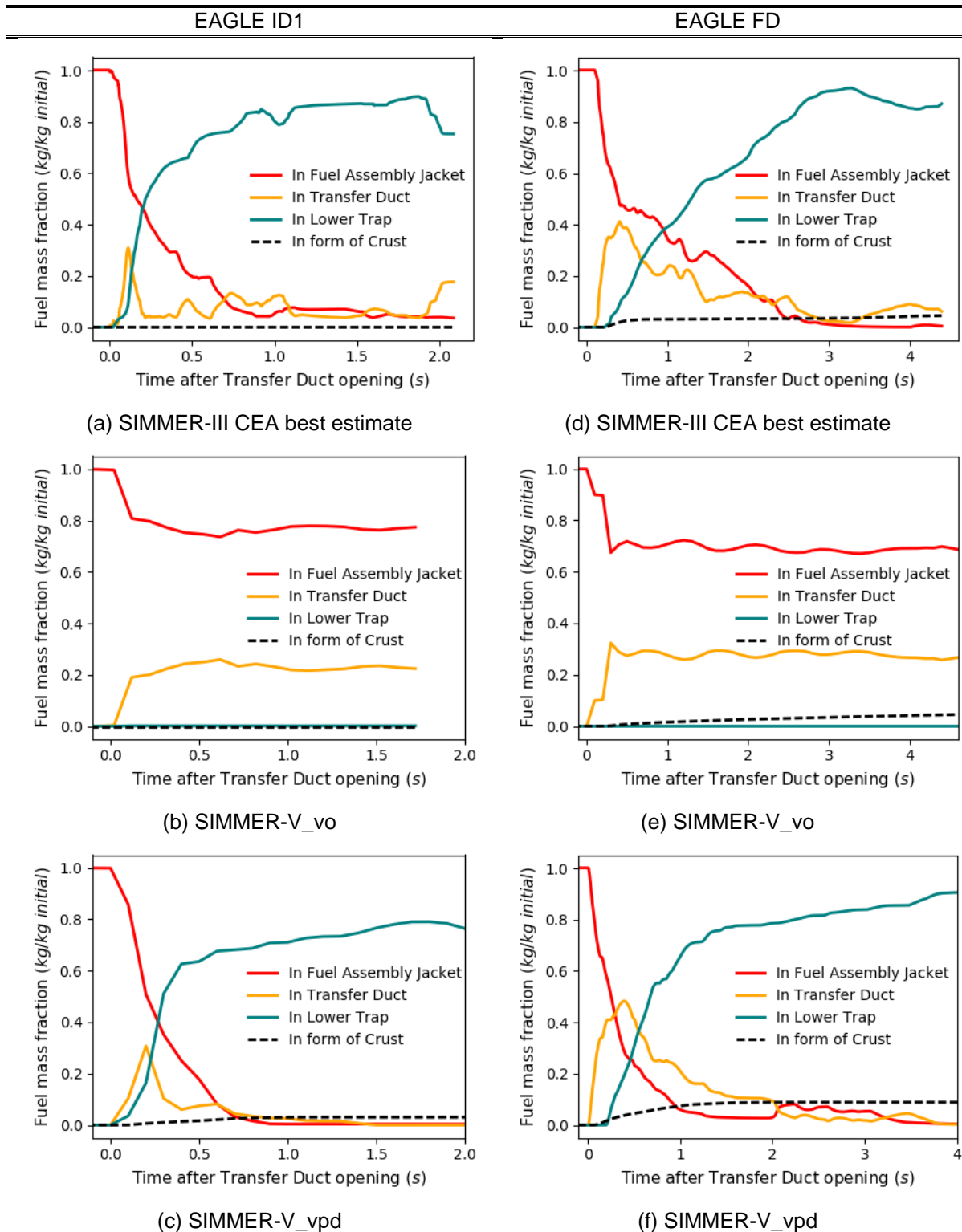


Figure V.7 Mass balance in the three main regions for EAGLE ID1 (left column) and for EAGLE FD (right column) with different SIMMER versions

In Figure V.7 for ID1 test, one observes that in the first instants after duct opening there is a sudden decrease of degraded fuel mass inside the FAJ. In parallel to this, mass builds up inside the transfer duct indicating material inflow from the FAJ. Such rapid transfer of mass results from the pressure difference between the FAJ and the duct before wall failure and from the effect of FCI. The FAJ pressure is approximately 4 bar above the duct pressure due to steel vaporization and Ar gas heat up during the degradation process. Just after wall failure, pressure pulse emerges from the interaction between the high temperature liquid steel/fuel and low temperature duct bulk sodium.

V.5 Comparison of discharged mass

The FCI evaporates liquid sodium around the failure location such that the subsequently arriving degraded mixture discharges in vapor environment. The downward motion in low-density vapor is considerably faster than in liquid sodium. This initial discharge phase is detected and nearly identical in each simulation by the different SIMMER versions, see Figure V.7 (a), (b) and (c). After this point, mass transfer rates differ significantly between the calculations in particular the SIMMER-V_vo from CEA best estimate run by SIMMER-III and SIMMER-V_vpd. The CEA best estimate and the SIMMER-V_vpd case predict a continuous and fast evacuation of degraded material from the FAJ. In about 1 second, more than 90% of initial mass is estimated to leave the FAJ by SIMMER-III. The FAJ evacuation by SIMMER-V_vpd is of similar duration but somewhat faster, around 0.7 second. In both simulations, the mass inside the transfer ducts decreases sharply after the initial build-up phase. In the same time, mass appears in the lower trap suggesting material inflow from the duct. In the remaining simulation period, large fraction of initial mass accumulates in the lower trap. The relocated mass is around 70% of the initial at the end of both calculations (2 seconds after duct opening). However, in the SIMMER-III run, the oscillations after 0.5 second between the duct and the lower trap as well as the 15% drop of lower trap mass just before 2 seconds imply that materials are still in motion and that stable final state has been reached. On the other hand, SIMMER-V_vpd results show no movement after materials are settled in the lower trap, approximately 1 second after duct wall rupture.

At the end of the simulation, the FAJ and the duct are completely depleted, small amount of the initial mass (~3%) is in the form of frozen crust on the duct surface, the largest fraction (~70%) is in the lower trap, and a minor but significant quantity (~25%) is ejected upwards into the side channel (represented by the seventh radial mesh in Figure V.4 and not accounted for in Figure V.7).

Opposite to this behavior, SIMMER-V_vo predicts quasi-constant masses inside the FAJ and in the duct during the whole simulation after the initial discharge phase. There is no material transfer into the lower trap indicating that a blockage has formed inside the duct avoiding the downward relocation. This observation contradicts the experimental finding according to which most of the initial FAJ mass is ejected into the lower trap.

Globally, both numerical predictions of SIMMER-III and SIMMER-V_vpd conform to the experiment in the sense that large amount of FAJ mass is found to be in the lower trap at the end of the test. Considering that SIMMER-V_vpd run ends with a stabilized state and that it applies single radial resolution (contrary to the 4 mesh resolution in SIMMER-III) of the transfer duct allow us to conclude on the preferable use of SIMMER-V_vpd with newly implemented particle dynamic models.

In Figure V.7 for FD test, the same large initial jump as in ID1 is observed expressing rapid material removal from the FAJ. The following discharge characteristics are again similar in SIMMER-III and SIMMER-V_vpd. There is a rapid increase of mass inside the duct, around 40% of FAJ mass enters immediately in SIMMER-III while it is approximately 50% in SIMMER-V_vpd. The succeeding transfer from the duct to the lower trap (indicated by the mass accumulation inside the lower trap) is slower in SIMMER-III, it takes around 3 seconds to evacuate 90%, than in SIMMER-V_vpd where only 2 seconds are necessary for the discharge of the same amount. In both simulations, minor fluctuations appear within the three regions. Their physical origin can be partially attributed³² to steel vaporization pushing materials upwards from the lower trap. At the end of the simulations, almost all initial fuel mass is located in the lower trap (more than 90%) or present in form of crust (somewhat less than 5%). SIMMER-III also predicts a small quantity of fuel that remains inside the duct.

The simulation of SIMMER-V_vo suggests again no transfer into the lower trap contradicting the experimental findings. Materials remain inside the FAJ and blocked inside the duct with minor built-up of fuel crust.

³² Although, we do not exclude the possibility that these fluctuations come from numerical models in SIMMER code.

In general, SIMMER-III and SIMMER-V_vpd reproduce well the experimental observations on the spatial distribution of fuel mass balance. In lack of available data on the exact temporal evolution of mass balances, it is not straightforward to judge which computation represents better the EAGLE FD tests. However, the same conclusion (preference towards SIMMER-V_vpd) can be drawn based on the correct duct meshing in SIMMER-V_vpd.

From Figure V.7, one can notice that the duct evacuation time is longer in general for FD than for ID1 test. It can be explained by the higher debris content of the entering degraded mixture in case of FD, which reduces flowability and hinders the relocation, or the presence of an additional driving due to FCI in ID1. Solid particles make up 14% only in ID1, while they constitute around 33% of total mass in FD. Such hindering effects in SIMMER-V_vo are taken into account through the particle viscosity factors (section II.2) while in SIMMER-V_vpd they are considered via the newly implemented particle rheology models.

V.6 PARTICLE RHEOLOGY IN EAGLE-1 FD TEST

In this section, the behavior of rheology models during the discharge phenomena through the transfer duct is investigated. In SIMMER-V_vpd, the effect of solid debris on the discharge dynamics is governed by the newly implemented particle normal pressure and shear stress. To study these terms, the temporal variations of the axial profile of total particle volume fraction, average velocity and rheology terms are plotted in Figure V.8. Only the first second of discharge is illustrated because, after this time interval, particle concentration does not reach 30% above which rheology models are activated³³. The axial profile is measured downward from the location of first duct wall failure. The lowest axial height corresponds to the bottom of the duct for which RHEOLREG is initialized. Out of the RHEOLREG region, particle pressure and shear stress are zero.

The plots of Figure V.8 are analyzed in consideration of the major characteristics of rheology parameters representing inter-particle collisions and friction, and their impact on solid concentration and velocity. We note that the variation of solid concentration results not only from dynamic phenomena but is also largely affected by heat and mass transfer processes that transform liquid to solid and vice versa.

Figure V.8 plot (a) shows that particles enter into the duct right after wall failure and move downwards with negative axial velocity in plot (b). In the first instants of the discharge, particle concentration is below 30%, meaning that $\mu(I)$ dense granular rheology variables are not computed. Particle volume fraction overpasses 30% in two jets shortly after the first inflow. The stream of two dense package of particles can be deduced from graphs (c) and (d) where inertial and viscous numbers are defined as well as from figures (e), (f), (g) and (h) where particle pressure and particle shear stress have values different from zero. It indicates the loss of particle phase momentum due to collisions and friction within the particulate debris. Comparing the magnitude of solid stresses in inertial and viscous flow regimes on plot (e) and (f), we observe that the inertial part is dominant over the negligible contribution of the viscous regime during the whole discharge. This trend is expected based on the average velocity of particles in (b) of around 4.5 m/s (corresponding to a large shear rate, large inertial particle pressure and thus a St number significantly greater than unity, see paragraph III.5.1), and considering that the relocation takes place in gaseous environment (low continuous phase viscosity further increases St number). The same can be concluded for the particle phase normal pressure comparing figures (g) and (h). We remark that such different magnitudes of internal and viscous stresses conform to our initial assumption on the predominance of one term over the other.

³³ Just to note, below 30% of particle concentration, the rheology models are not applied but we still experience application of new modified closure terms, see in section III.7.

V.6 Particle rheology in EAGLE-1 FD test

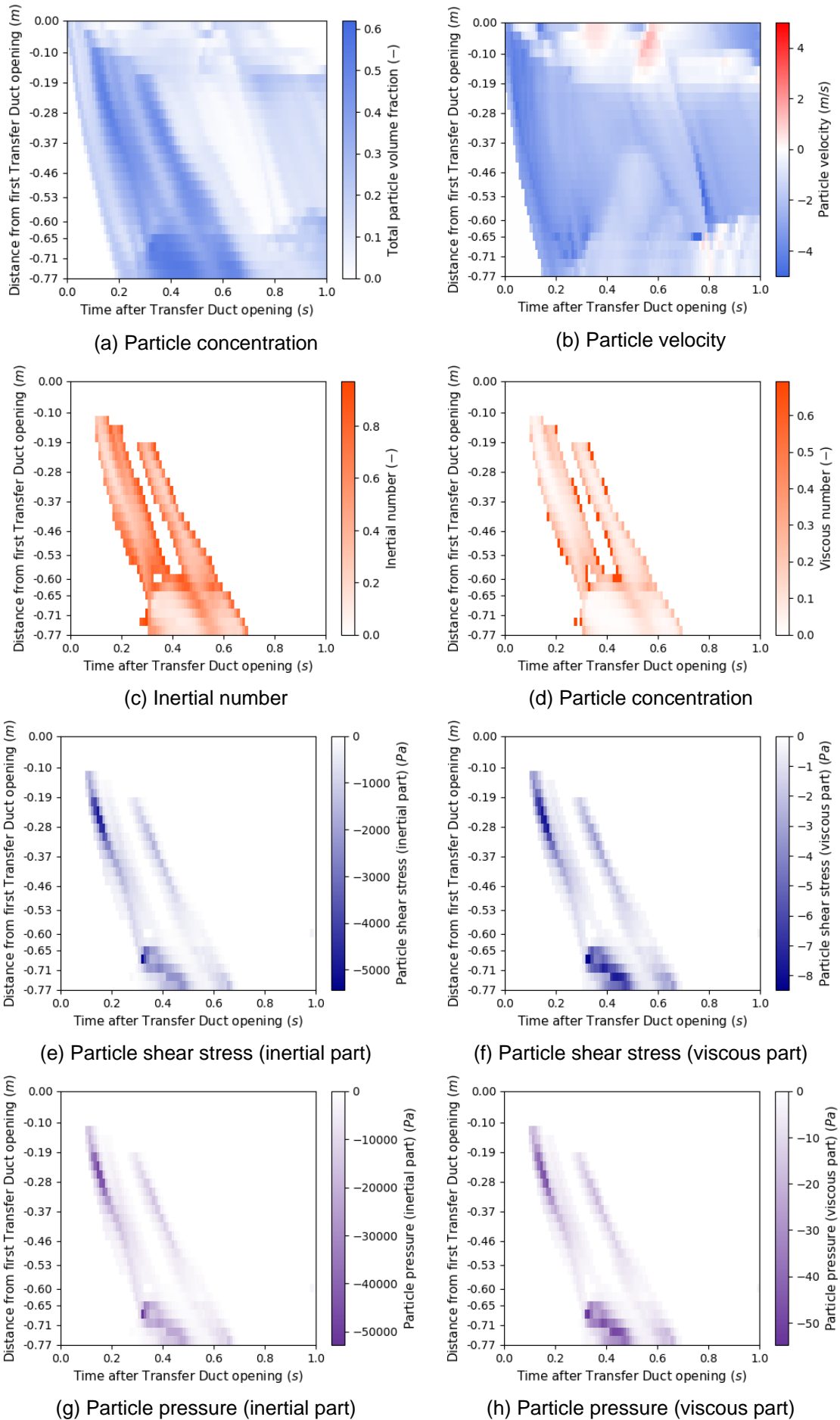


Figure V.8 Particle volume fraction, particle velocity and newly implemented rheology terms in SIMMER-V_vpd for EAGLE FD test

By looking at the color scale for shear and normal stress components, we observe their expected proportionality. The ratio of inertial shear (e) (and viscous (f)) and inertial (g) (and viscous (h)) normal stresses is governed by the macroscopic friction coefficient depending on the inertial (or viscous) number in (c) (or (d)) and the ratio between wall and vertical normal stresses. In the simulation of FD test, the ratio is found to be around 10 for inertial and around 6 for viscous regimes, indicating 10 and 6 times higher normal particle pressure than shear stress.

At the location and instant of the highest solid concentration of around 55% (-0.7 m below and 0.3 second after duct rupture), both shear and normal components³⁴ reach their largest absolute value. The localized debris built-up can be attributed to the production of fuel particles by liquid fuel solidification out of the heated test section. It brings about flow retardation and additional accumulation of solid debris. Following this instant and close to this location, the resultant reduction of particle velocity is visible in figure (b). In parallel, the particle concentration remains constant close to the initial value in figure (a). These previous two effects (lower shear and constant volume concentration) reduce again particle phase stresses that drop hindrance effects and continue the flow. This phenomenon is not pronounced during the relocation of the second dense debris jet most likely because of the lower amount of liquid fuel accompanying the motion of debris yet.

Overall, we conclude that the newly implemented rheology terms accounting for collisional and frictional interactions between solid debris particles have an impact on the discharge dynamics. The interplay of particle phase stresses with solid concentration and with particle velocity is coherent with the physically expected behavior. As a global result, rheology models predict a continuous discharge, which is in agreement with the experimental inspection.

V.7 SENSITIVITY STUDY

Following the reference calculation of EAGLE tests with SIMMER-V_vpd, this section presents a sensitivity study related to the rheology models in the frame of FD test. The sensitivity study is encouraged for two reasons. Firstly, because the derivation of $\mu(I)$ dense granular rheology equations in paragraph III.5.1 involves several empirical coefficients. The uncertainty of these parameters is unknown to the application for the prototypical debris of EAGLE tests (degraded reactor fuel and steel components) which have different physical properties from the particles used in the experiments to derive such parameters. To this category, we include the estimate of the shear rate from the average velocity since the coefficient expressing their functionality was also derived from experimental data. Secondly, because the lack of available quantitative knowledge on exact debris dimensions (such as size, size distribution and shape) brings an uncertainty on the equivalent diameter and maximum attainable solid concentration. In absence of this information, sensitivity analysis is necessary to investigate the impact of such parameters on the discharge phenomena. The parameters belonging to these two groups, their reference values and their range of variation considered in this work are summarized in Table V.2. The references for maximum and minimum values are indicated in footnotes. Where no reference is identified, values are chosen arbitrary based on engineering judgement.

Another philosophy behind such separation is to express that the first group of “Uncertain model coefficients of the $\mu(I)$ rheology” only influences the motion of particulate components inside the duct (RHEOLREG region), while the second group of “Uncertain particle properties” influences additionally the discharge dynamics of the whole degradation process inside the FAJ. They modify (among other physical quantities) the instant of wall failure and the material composition entering into the transfer duct that further affects the discharge phenomenon.

³⁴ Normal stress i.e. particle pressure impacts the relocation velocity through its gradient whose value is limited to $\pm 10^4 Pa$ to avoid numerical instabilities. Therefore, it is the particle shear stress, which has major influence in the momentum equation for particles.

V.7 Sensitivity study

Table V.2 Sensitivity study parameters and their analyzed range of variation

Parameter	Unit	Description	Reference	Minimum	Maximum
Uncertain coefficients of the $\mu(I)$ rheology models					
c_s	—	Proportionality coefficient of shear rate and average velocity	3.52	0.5	8 ³⁵
c_i	—	Coefficient of dilatancy law in inertial regime	0.667	0.31 ³⁶	—
δ	°	Internal angle of friction	35	11 ³⁷	57 ³⁸
Uncertain particle properties					
d_p	mm	Particle (degraded debris) diameter	1	0.5 ³⁹	2 ⁴⁰
α_{MP}	—	Maximum packing limit ⁴¹	0.62	0.58	0.64

Simulations with SIMMER-V_vpd are performed for EAGLE FD test shifting each uncertain parameter from its reference to its maximum or its minimum value while keeping all the others unchanged. The mass balances in the three different test regions obtained for the first group of coefficients are plotted in Figure V.9. The missing mass fraction is present in form of crust on the duct wall and somewhat varies between the computations. Since the crust formation is a dominantly thermal phenomenon, it not examined here.

Comparing the temporal evolution of fuel mass in the three test regions in Figure V.9, one can see that the initial rapid FAJ evacuation and the parallel fast material built-up in the duct are identical for each coefficient and they coincide with the reference case. Considering only the rate of fuel removal from the FAJ, the rheology coefficients have negligible impact. Even though the somewhat different evolution of the red curve (representing the highest considered proportionality between shear rate and average axial velocity), 90% of the initial fuel mass leaves the FAJ in around 1 second in all simulations. The independence of FAJ mass variation on the rheology coefficients is expected because they only play a role inside the transfer duct.

Accordingly, one can observe larger deviations (after the initial rapid inflow) on the second and third plots describing the mass transfer from the duct to the lower trap respectively. It is apparent that the maximum value of the proportionality coefficient between shear rate and average axial velocity ($c_s = 8$) produces the highest divergence. Materials stay in the duct for approximately 1 second longer and arrive to the lower trap at a considerably lower rate compared to all other simulations. It is because a larger proportionality coefficient at the same average particle velocity indicates higher shear rate. At higher shear rate, particles interact with each other more frequently bringing about increased solid stresses, and therefore a higher resistance for the downward motion.

Other uncertain rheology coefficients have minor influence on the global relocation dynamics. The only interpretable behavior can be seen when the fuel starts to discharge from the duct and in parallel accumulates in the lower trap. During this short period of time, the reduction of inertial dilatancy law coefficient ($c_i = 0.31$) and the lower shear proportionality coefficient ($c_s = 0.5$) produce faster fuel motion. It is in agreement with what we initially expected since both parameters reduce the

³⁵ Purely Newtonian velocity profile

³⁶ Maurin et al. (2016) for the turbulent bed-load transport of spherical particles

³⁷ Lubricated steel on steel contact

³⁸ Unlubricated UO₂ on steel

³⁹ Minimum diameter of particle-size reactor debris

⁴⁰ Maximum diameter that avoids solid bridge formation by $D_h/d_p > 15$

⁴¹ The maximum packing limit is not a particle property in the conventional sense but rather a measure of granular microstructure that depends on the particle properties.

magnitude of inertial stresses that facilitates the down flow. The value of the internal angle of friction follows closely the reference curve. It is again as predicted considering that it influences only the magnitude of particle pressure and its gradient, which is taken into account with a limited importance.

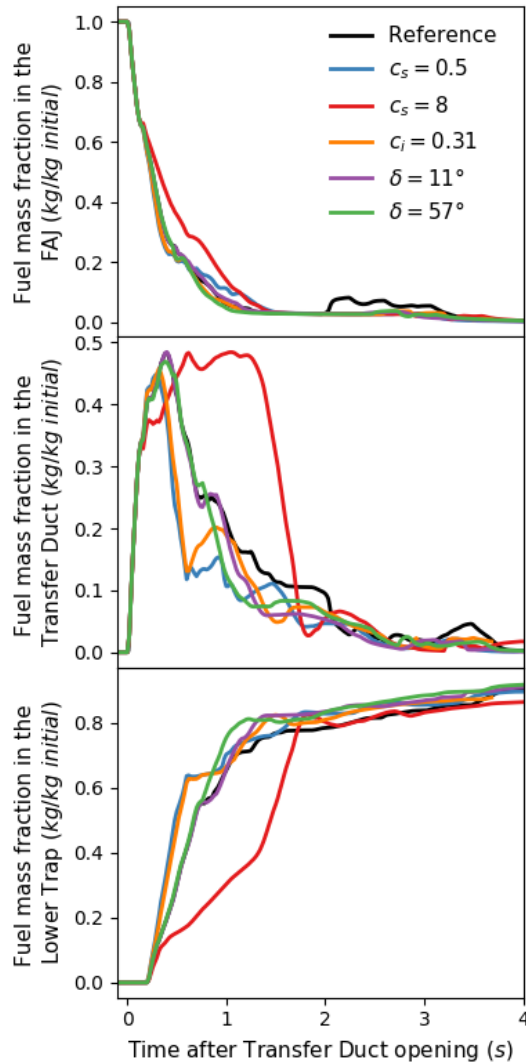


Figure V.9 Sensitivity study results for uncertain coefficients of the $\mu(I)$ rheology models

The mass balances in the three different test regions obtained for the second group of coefficients are plotted in Figure V.10 (Transfer Duct opening is different between the calculations). Figure V.10 illustrates also the composition of degraded FAJ entering into the duct. The origin of these compositions is not investigated in the following as it requires the identification and understanding of every physical model (heat-transfer correlations, structure disintegration mechanisms etc.) in SIMMER-V that involves particle size and maximum packing limit.

V.7 Sensitivity study

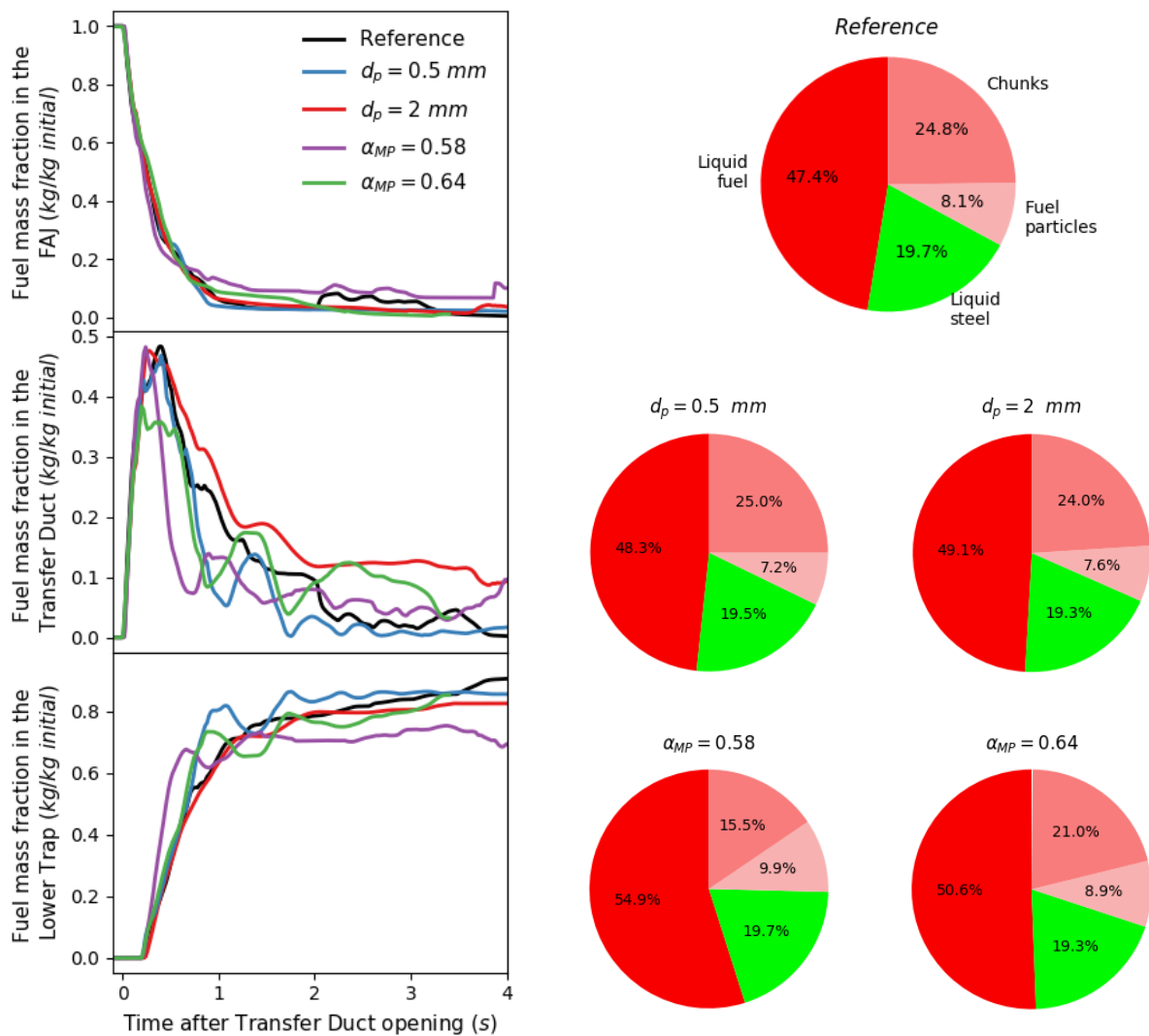


Figure V.10 Sensitivity study results for uncertain particle properties and their initial material composition

Looking at Figure V.10 uppermost graph, one can find again minor influence of uncertain particle properties on the FAJ evaluation process. The reasoning behind is the same as it was for Figure V.9. Deviations however are apparent during the fuel removal through the duct. In addition to the previously examined sensitivity cases, in order to perform a sound comparison, the varying fraction of entering particle concentration has to be included in the arguments.

Examining the effect of particle diameter, Figure V.10 middle plot suggests slower discharge rate with increasing particle diameters: the reference curve of $d_p = 1 \text{ mm}$ is in between the curves of maximum $d_p = 2 \text{ mm}$ (above) and minimum $d_p = 0.5 \text{ mm}$ (below) particle diameters. Such effect of particle size is explained by the leading contribution of inertial particle stresses (over viscous stresses identified in section V.6) having square proportionality with particle size. The total particle content is similar, around 32%.

Considering the effect of maximum packing fraction, one expects that a lower limit brings about higher stresses and thus delays mass transfers. It is opposite to Figure V.10 middle and lower figures suggesting that fuel leaves the duct and reaches the lower trap the earliest among all simulations. The reason for this is not fully attributed to the magnitude of particle stresses but rather to the smaller quantity of particulate components entering into the duct (25% of total FAJ mass). Besides this initial solid concentration, particle fraction inside the duct does not overpass 30% meaning that particle

pressure gradient is zero and shear stress component is according to the Fanning friction formula. Increasing the maximum packing limit produces as well less debris in comparison to the reference case. Even through this result is not so straightforward, we did not explore further this issue. The discharge dynamics differs from the reference calculation mostly during the passage through the duct. The fuel mass entering shortly after tube rupture is lower (we suppose it is because they are allowed to stay at higher volume with higher packing limit inside the FAJ) but it leaves faster in agreement with the reduced particle phase stresses being inversely proportional to the maximum packing limit. Globally, at the end of all simulations, large fraction (around 80% with a 20% span between the sensibility cases) of fuel has reached the lower trap. In terms of discharge duration, there is no considerable difference.

Concluding on the sensitivity study, we find that varying rheology model coefficients c_i and δ within the uncertainty range considered by Table V.2 imposes negligible divergence from the reference case. The uncertainty of these parameters does not affect the global dynamics of fuel removal under the conditions of EAGLE FD test. On the other hand, the uncertainty on shear rate - average velocity relation seems to contribute largely to variabilities in the simulation outcome (spatial distribution of mass balance). Therefore, special attention should be dedicated to the definition of c_s coefficients. The second part of the sensitivity study involving uncertainties on particle properties is less straightforward to conclude. It is because they not only influence particle motion but also the composition of degraded material and several other physical quantities and processes that indirectly affect the global dynamics. Altogether, we observe no outstanding fuel removal characteristic for any of the sensitivity cases on particle properties. Simulations with all sensitivity parameters of both groups show consistent dynamic behavior in SIMMER-V_vpd.

V.8 DISCUSSION AND PERSPECTIVES

In this chapter, the EAGLE ID1 and FD experiments were studied in SIMMER-V_vo and SIMMER-V_vpd. Our simulations took advantage of the preceding work at CEA in which the test section geometry, initial and boundary conditions are predefined, and the SIMMER modelling options following closest the experimental sequence of events are identified for both tests. Our main objective was to analyze whether the experimental observation revealing that large fraction of fuel is removed from the FAJ and located in the lower trap at the end of the test can be reproduced by the different SIMMER-V versions. The comparative analysis between SIMMER-V_vo, SIMMER-V_vpd and the CEA most recent best estimate calculation by SIMMER-III demonstrated that both SIMMER-V_vpd results and SIMMER-III calculations are in good agreement with this experimental finding. Considering that channel flows in the SIMMER architecture should be modelled by one radial mesh, the use of SIMMER-V_vpd is encouraged. On the contrary, SIMMER-V_vo (using 1 radial mesh for the duct) failed to predict the same experimental outcome due to the appearance of flow blockages inside the transfer duct.

The second objective was to investigate the behavior of the newly implemented particle dynamics models in SIMMER-V_vpd. For this, the FD test only is considered because of its higher particulate content. We found that particle stresses influence the discharge phenomena by introducing retardation effects that originate from particle collisions and inter-particle friction. The interplay between these effects and particle velocity/concentrations is corresponding to its physically expected behavior.

In the third part of this chapter, a sensitivity study was carried out. Uncertain parameters include empirical coefficients in the rheology models and particle properties. The most important finding is that the derivation of shear rate from average axial particle velocity, especially when their ratio is large, affects significantly the prediction of the temporal evolution of fuel mass distribution. Therefore, special attention should be paid when formulating one-dimensional shear rate correlations. In our model development, we used a constant proportionality coefficient with the average velocity as a

first approximation but, in reality, it can depend on several other parameters such as solid volume fraction, surrounding fluid features, particle properties etc. In this view, we conclude on the necessity to refine shear rate formulation.

Constraints to deeper analyze the experimental results were imposed partially by confidentiality issues but mostly by insufficient experimental data (lack of dedicated instrumentation) quantifying the effect of solid debris. This second constraint can be overcome by improving current or constructing new experimental platforms devoted to the analysis of dense debris flows in vertical ducts. In order to have a comprehensive evaluation/validation of the here presented $\mu(I)$ rheology models in the frame of reactor application, we identify the following quantities that are essential to measure (additionally to the ones in EAGLE-1 experiments) throughout future tests.

- Radial concentration and velocity profile of particulate debris to obtain more precise formulations for radially averaged quantities, most importantly regarding the shear rate equation.
- Axial velocity and concentration profile of degraded debris in order to interpret mass balances and validate particle stress terms.
- Debris properties including:
 - size and shape distributions in order to define an equivalent size and perhaps a shape factor in the numerical modelling,
 - average surface characteristics to obtain better estimation of the friction coefficients (μ_s, μ_2, δ in the rheology equations),
 - rigidity and elasticity in order to validate the applicability of the fundamental assumptions of $\mu(I)$ rheology.

As we have seen in ID1 test and some sensitivity cases of FD test, only a low fraction of degraded fuel was present in form of particles. Therefore, another perspective in future experiments is to achieve a degradation process that produces high fraction of solid components besides minor melting. In addition, since the EAGLE tests are representative to the discharge phenomena on the fuel pin scale (corresponding to the FAIDUS approach in paragraph I.3.1.1), future experiments should be dedicated to the fuel assembly scale discharge, corresponding more to the transfer tube approach. It is generally accepted that experiments demonstrating the mitigation performance have to be full scale in terms of transfer tube dimensions.

Besides validation purposes, from another point view, SIMMER-V_vpd can be used for the dimensioning of future PLINIUS-2 and SAIGA tests.

Chapter VI.

REACTOR SCALE APPLICATION

In this chapter, we return to the primary objective the thesis work, which is to improve the numerical estimation of the mitigation strategy during an ULOF accidental sequence in the ASTRID CFV core design. The model development in SIMMER-V_vpd on solid debris dynamics in Chapter III is devoted to the analysis of the mitigation scenario involving the controlled discharge of degraded core materials via the mitigation transfer tubes. Following the encouraging results of the simplified validation test cases and the experimental comparison, this chapter is dedicated to assess the global impact of the developed models on the numerical prediction of the discharge performance. In this context, the ULOF transient calculation is realized in SIMMER-V with the coupled thermo-hydraulic neutronics mode. The calculations are performed for the reference CFV core at beginning of life conditions (the fuel is not in an irradiated state)⁴². In the first part of this chapter, the SIMMER-V representation of the full reactor is explained together with its nominal state conditions. The second part describes the initiation of the ULOF transient and the following phenomena that lead eventually to massive core degradation. Up to this point, SIMMER-V_vo and SIMMER-V_vpd results are identical. It is only after the particulate debris enter into the transfer tubes that the newly implemented particle dynamics models are activated and play a role in the accident evolution. The relocation phase computed by SIMMER-V_vpd⁴³ is examined in the third part. The result of SIMMER-V_vo calculations is discussed in the last section in the frame of a comparative study carried out on the prediction of the discharge performance by different SIMMER versions. The comparison is made between SIMMER-III CEA reference calculation, SIMMER-V_vo and SIMMER-V_vpd.

VI.1	ASTRID conceptual design in SIMMER-V	116
VI.1.1	Reactor at nominal state	118
VI.2	ULOF transient in SIMMER-V	119
VI.2.1	Primary phase	119
VI.2.2	Transition phase.....	121
VI.2.3	Secondary phase	123
VI.2.4	Relocation phase in SIMMER-V_vpd.....	124
VI.3	Discharge performance by different SIMMER versions	127

⁴² The calculations for irradiated core have not been completed yet with SIMMER-V original models and thus beginning of life fuel and core conditions are selected for reference.

⁴³ To define cell face shear stress values, the “no-projection” method is used.

VI.1 ASTRID CONCEPTUAL DESIGN IN SIMMER-V

To model the ASTRID conceptual design in SIMMER-V a pseudo-3D approach in cylindrical $RZ\theta$ coordinates is used. The whole reactor geometry is created by initializing a 2D plane of meshes rotated axis-symmetrically 360° . Accordingly, the SIMMER visualization in Figure VI.1 shows half of the reactor with the left boundary being the axis of symmetry. The consequence of this modelling choice on the mitigation transfer tubes' geometry will be discussed later. The full reactor is simulated with 46 radial, 138 axial and a single circumferential thermal-hydraulic mesh. Neutronics meshes cover only the core region with a finer layout of 54 radial, 83 axial and 5 tangential meshes. Figure VI.1 displays also the main reactor regions and components, namely the core catcher, the diagrid/strongback, the transfer tubes, the core itself, the sodium plenum, the upper neutron protection, the upper core structures, the heat exchanger and the primary pump. The pump is represented by dedicated pump models in SIMMER-V. These models impose the internal pressure condition for the meshes specifying the pump.

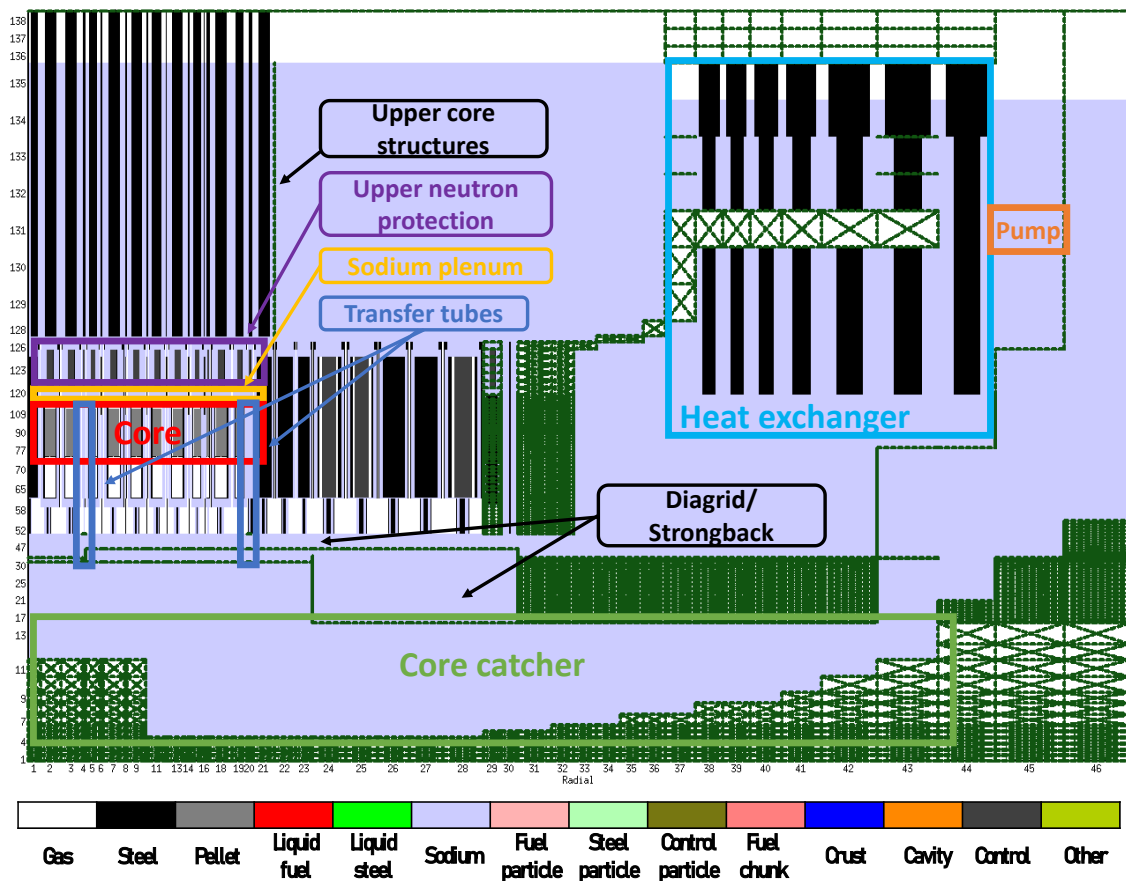


Figure VI.1 SIMMER-V illustration of ASTRID reactor with annotated regions

The CFV core configuration in SIMMER-V showing the different core zones and the locations of the 21 Control Rod Guide Tubes (CRGT) out of which 3 are scram rods of Prevention type; and the 21 mitigation transfer tubes is plotted in Figure VI.2. Fuel assemblies, CRGTs and transfer tubes are all represented in 1D mesh scheme.

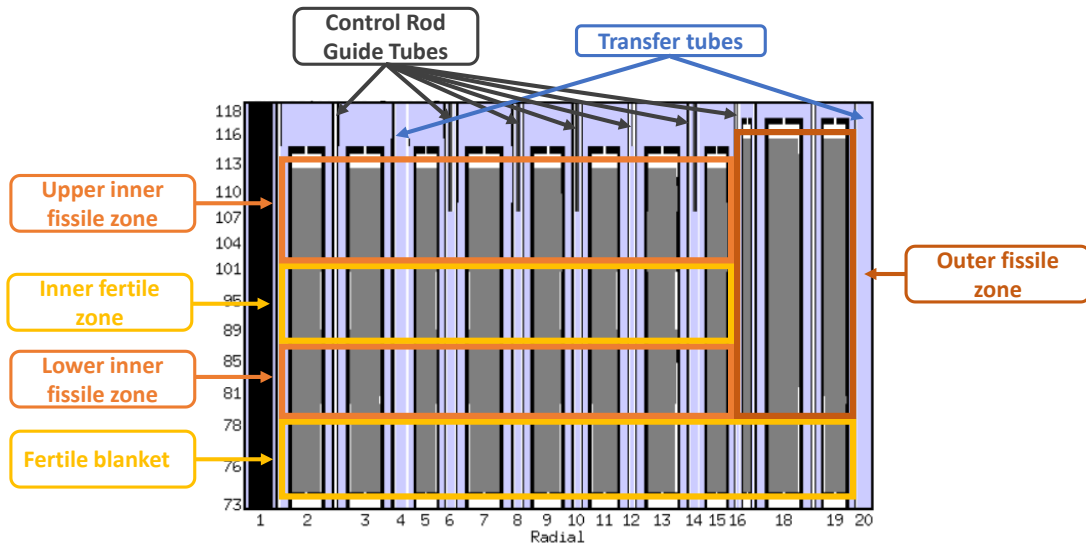


Figure VI.2 SIMMER-V illustration of ASTRID CFV core (radial-axial cut) with annotated regions

The 21 mitigation transfer tubes are placed in the axial slices of radial meshes 4 (accounting for 3 inner core tubes) and 20 (accounting for 18 tubes at core periphery) in terms of the thermal-hydraulic setup. The drawback of the 360° mesh rotation method is that the transfer tubes are modelled by annuluses. The volume between the concentric cylinders is defined in a way to correspond to 3 and 18 tubes in radial mesh slide 4 and 20 respectively. The hydraulic diameter associated with these meshes is the value of a single tube. This means that, in the simulation, one cannot differentiate among inner core tubes nor among the core periphery ones. The behavior of all inner and all outer tubes are treated identically. Another issue appears when connecting them to the core catcher region. The connection in SIMMER-V is realized by virtual walls through which no traverse flow can occur. Because each mesh forms a ring, extending the transfer tubes through the lower sodium plenum rotates also the virtual walls such that it closes the path for core inlet sodium flow. In order to avoid this problem, transfer tubes are connected to the core catcher only when sodium inflow becomes negligible after pump shutdown. The two types of connections are illustrated in Figure VI.3.

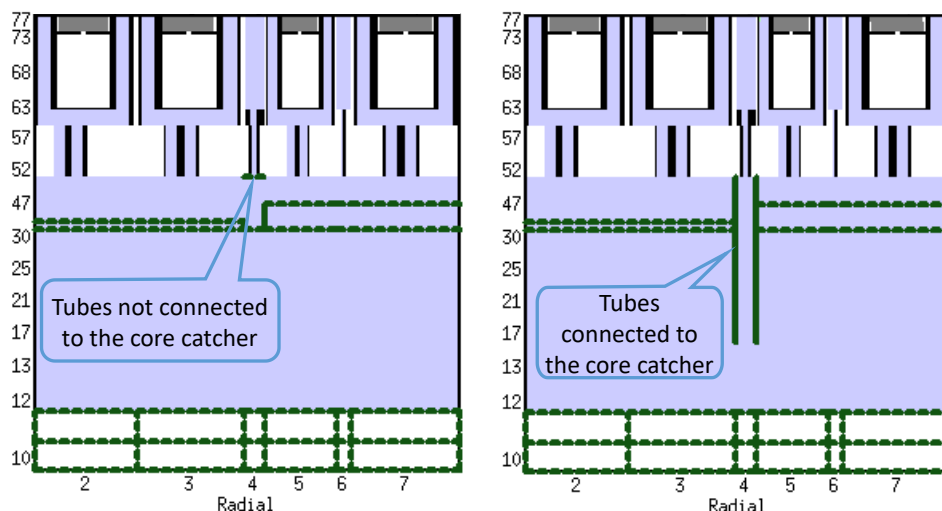


Figure VI.3 Transfer tube extension towards the core catcher: long before pump shutdown (left) and after sodium inflow to the core is negligible (right)

The mesh rotation method to achieve an axisymmetric reactor case in SIMMER-V has other drawbacks besides the need to manually extend transfer tubes towards the core catcher at the beginning of the primary phase. The fact that each mesh forms a ring containing a number of

subassemblies leads to symmetrical degradation processes for all subassemblies at the same radial location. Due to this coherency effect, the fuel compaction is overestimated and potentially the magnitude of power peaks as well. On the other hand, the axis symmetry causes the transfer tubes at the same radial position to open at the same time, and thus the overestimation of the discharged fuel quantity through them. Since these two effects are opposite, they can be assumed to cancel out.

VI.1.1 Reactor at nominal state

Before beginning the ULOF transient, the reactor must be initialized at nominal steady-state conditions in terms of both thermal-hydraulics (thermal power is 1500 MW) and neutronics (reactivity is 0\$)⁴⁴. The methodology to obtain the nominal state in SIMMER-V is not detailed here. However, it is important to verify whether the thermal-hydraulics state in SIMMER-V coincides with the design nominal conditions presented in paragraph I.1.2. With this purpose, Figure VI.4 left plot shows the sodium temperature profile across the core. In order to achieve radially homogenized sodium temperatures at the subassembly outlets, a specific feature of the ASTRID design is the spatial redistribution of power to sodium flow ratio (P/Q) between assemblies. In reality, it is managed by a distributor device inside the diagrid. This device adjusts the sodium flow rate below each subassembly to compensate for their inhomogeneous power generation. In SIMMER-V, orifice coefficients are introduced to tune sodium flow rates by imposing a controlled pressure drop to the inlet flow. Applying these coefficients, the core outlet temperatures in SIMMER-V are homogeneous and the inlet/outlet values in agreement with the design of 400/550 °C as can be seen in Figure VI.4.

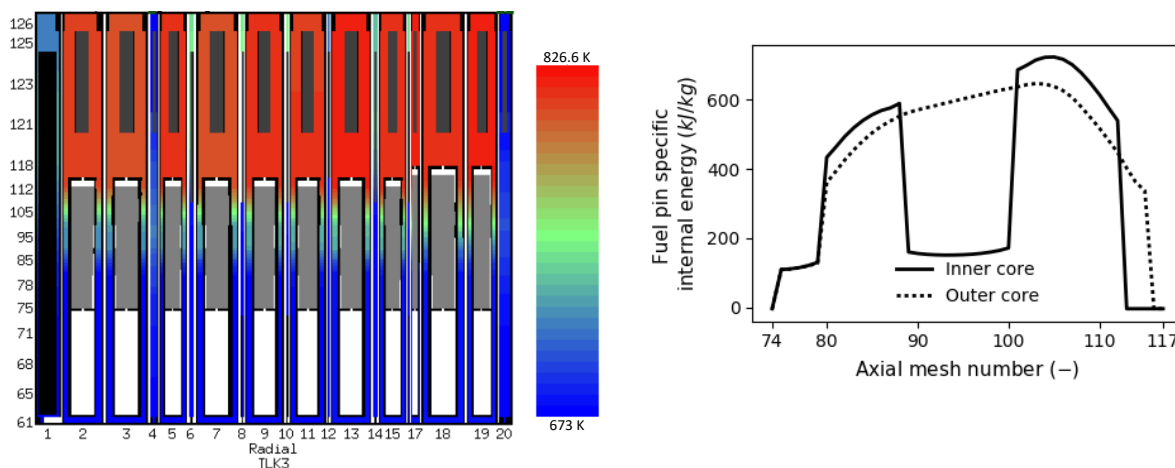


Figure VI.4 Sodium temperature profile across the core (left) Fuel internal energy axial profile (right)

The right hand plot of Figure VI.4 displays the fuel pin specific internal energy axial profile characteristic to subassemblies located in the inner and in the outer cores. The internal energy profile is representative of the power distribution. Based on the shape of the inner core curve, one can clearly identify the effect of the fissile and the fertile blankets. Inside the inner fertile blanket, the fuel internal energy is considerably lower while the highest energy production is shifted towards the upper fissile core (conformity of preventive design in paragraph I.1.2.1). The energy distribution inside the outer fissile zone is homogeneous. Besides sodium temperature distributions and fuel internal energy axial profile, other parameters were checked and found to be in agreement with the reference

⁴⁴ Steady-state conditions are achieved in two consecutive steps in SIMMER-V. In the first calculation, the nominal thermal and pumping power are imposed and kept constant without any neutronics feedback impact on power evolution. The aim is to reach nominal thermal-hydraulics state in a sense that temperatures and internal energies of all material components are stabilized. The second calculation stage compensates for the loss of reactivity due to the temperature increases by introducing an external reactivity ramp to criticality. The neutronics feedbacks are still prevented to influence the thermal-hydraulics. They are activated for transient calculation as we are focusing on the impact of reactivity evolution on power variation.

ones. Globally, we conclude that the reactor state in SIMMER-V matches with design nominal conditions.

VI.2 ULOF TRANSIENT IN SIMMER-V

This section describes the different ULOF transient phases (primary, transition and secondary following the SFR safety study approach in section 1.2) in chronological order starting from the nominal reactor state. Analogous to the simulation of the nominal state, the results are not differentiated between SIMMER-V_{vo} and SIMMER-V_{vpd} up to transfer tube opening in the secondary phase. Therefore, the ULOF transient phases in this section are described until transfer tubes start to perform their function. The discharge phenomena after this point are investigated in the last paragraph for SIMMER-V_{vpd}.

VI.2.1 Primary phase

The ULOF transient is initiated by the shutdown of the primary pump without actuation of any safety system that would cause reactor scram⁴⁵. Consequently, the transient starts at nominal power. In SIMMER-V, the shutdown is modelled by the gradual decrease of internal pressure condition for the pump meshes. The decrease is according to the pump's characteristic halving time, which reduces the core inlet sodium flow to its half in 10 s. The inlet flow evolution by SIMMER-V is shown in Figure VI.5.

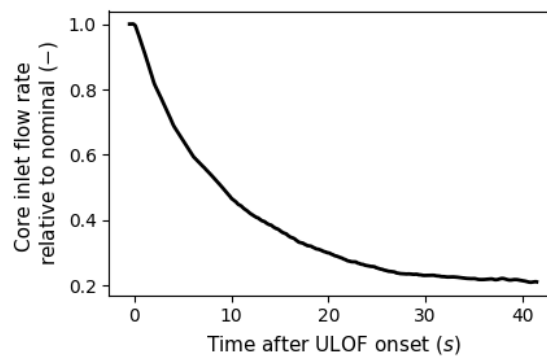


Figure VI.5 Core inlet sodium flow rate after pump shutdown in SIMMER-V

Once the pumping power is lost, only the hydrostatic pressure in the system plays a role such that natural convection establishes over the core. The loss of forced convection and the resulting lower heat transfer coefficient of sodium coolant lead to temperature variations of the different core materials (steel, fuel and sodium). Variations in the reactor state triggers reactivity feedbacks⁴⁶. The most important feedbacks in SFRs include the Doppler effect, sodium expansion effect including both expansion and/or voiding, the thermal expansion of solids (fuel, cladding, hexcan and diagrid), and the insertion of control rods into the core due to relative displacement of the rods driven by thermal expansion [Droin, 2016]. SIMMER neutronics does not take into account all of them (e.g. the axial expansion of fuel, cladding, CRGT and diagrid expansion are not simulated conservatively). Since the partial contribution of each simulated effect is not an output of SIMMER code and neither scope of this work, only the net reactivity evolution (being the global product of the different feedback effects and the direct indicator of nuclear fission power) is examined in the following. After pump shutdown, the balance of reactivity feedbacks is such that the net reactivity decreases gradually during the first 45 s of the ULOF scenario in Figure VI.6. In parallel, core power reduces to around 60% of its nominal value during this time interval.

⁴⁵ The scram is the emergency shutdown of the reactor achieved by immediately terminating the fission reaction.

⁴⁶ Reactivity is measure of the core's relative departure from a critical state in which the ongoing series of nuclear reactions can be sustained. Reactivity coefficients indicate the change of reactivity for a given change in of a parameter.

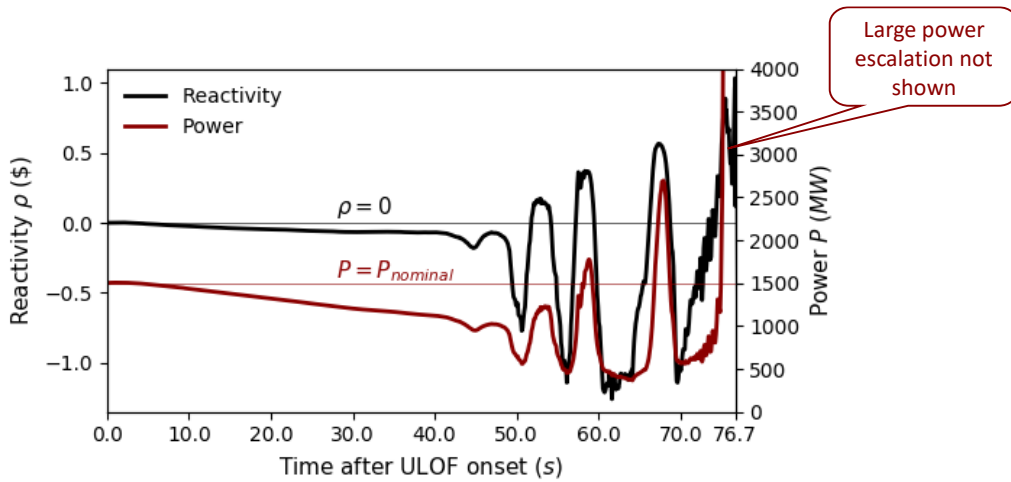


Figure VI.6 Reactivity and power evolution after ULOF onset (primary and transition phase)

Besides ongoing nominal nuclear heat generation, the primary sodium heats up and eventually reaches boiling temperature inside the highest neutron flux subassemblies. In the SIMMER-V calculation, it appears in the upper plenum above the 17th fuel assembly ring. Inherent to the CFV low sodium void worth design, voiding the upper sodium plenum inserts negative reactivity. However, when the boiling front penetrates into the positive void worth fuel assembly regions, the power rises and induces subsequent boiling phenomena inside other subassemblies. Since the boiling in other subassemblies takes place again in proximity of the upper sodium plenum, reactivity and power return to decline again. Another consequence of the upper plenum is that the large sodium reservoir fills up the voided regions leading alternating to boiling and reflooding phenomena as illustrated in Figure VI.7. The repeatedly occurring boiling/reflooding phenomena induce periodic reactivity spikes between 45 and 70 s in Figure VI.6. In spite of the reactivity oscillations linked to the boiling transient, the power continues to decrease globally.

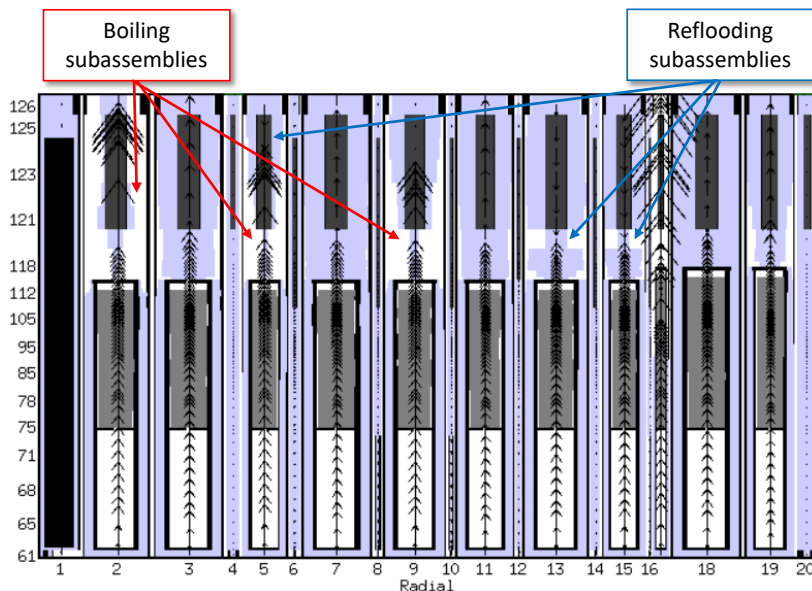


Figure VI.7 Illustration of boiling/reflooding phenomena (black arrows indicate sodium velocity directions and magnitudes)

The first fuel degradation occurs during the boiling and reflooding oscillatory pattern at 54.6 s after the ULOF onset. It takes place in the upper part of the 17th axial slice, which coincides with the appearance of the first boiling fronts. The degradation is caused by the complete dry-out of the clad surface and the resulting reduction of heat extraction capability from the fuel pins. The pin surface

temperature increases rapidly arriving to steel melting point at which the clad melts down. We note that the relocation of molten steel has an impact on the reactivity but we do not detail it here. Thanks to the previously explained reactivity characteristic of the CFV core, it happens at low core power (at around 800 MW) such that fuel-melting temperature is not reached. Consequently, the fuel remains in solid fragmented state after the loss of cladding. The fuel pellet disintegration mechanism in SIMMER-V is modelled by considering chunk formation whenever the solid cladding is lost following the sensitivity study of [Bachrata, 2015]. Alongside with the ongoing reactivity oscillations, the first degradation propagates axially over most part of the subassembly length. The propagation is accompanied by the hexagonal tube melting, which indicates the end of the primary phase (74.3 s after ULOF onset) according to the phenomenology of [Bertrand et al., 2018] in paragraph I.2.1.1. The degraded state at this point is visualized in Figure VI.8.

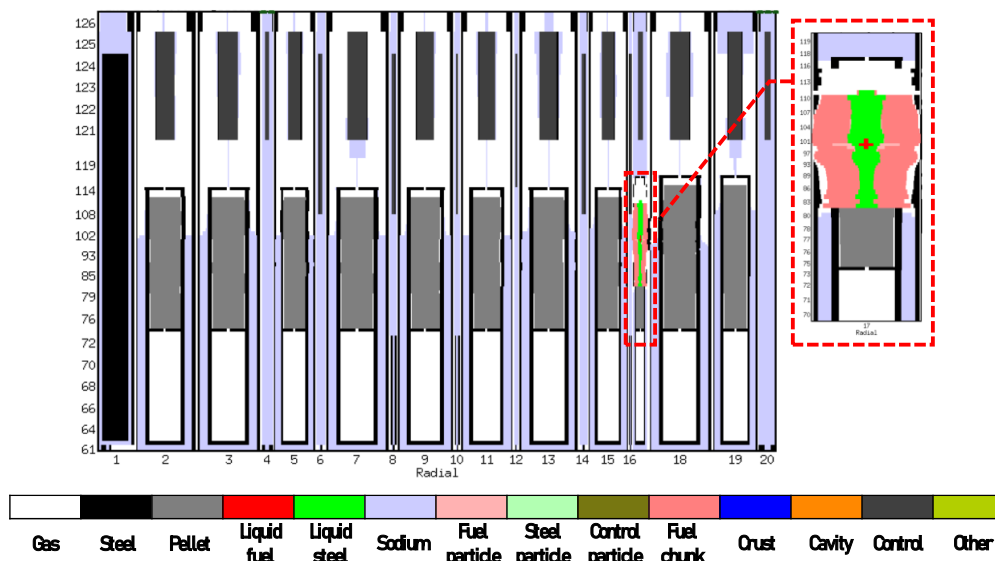


Figure VI.8 Core state at the end of the primary phase (74.3 seconds after ULOF onset)

In view of the reactivity and power evolution up to 74.3 s of the ULOF transient in Figure VI.6, we conclude that the primary phase terminates without large power escalations. It is attributed to the low energetic natural behavior of the CFV core that prevents large mechanical energy release.

VI.2.2 Transition phase

The transition phase starts when the degradation propagates radially over other subassemblies. Following the thermal failure of the hexcans, degraded materials of the 17th ring are ejected into the neighboring CRGT at 74.6 s. Opening a path for fuel evacuation brings about a favorable negative reactivity feedback. However, it is not sufficient to counterbalance the positive effect of the phenomena happening in parallel. Simultaneously, materials enter into the 18th neighboring fuel assembly slice and induce further damages there. Due to the merge of these subassemblies and the fuel compaction inside, the positive reactivity insertion becomes predominant. Correspondingly, we observe a net reactivity rise above super criticality in Figure VI.9.

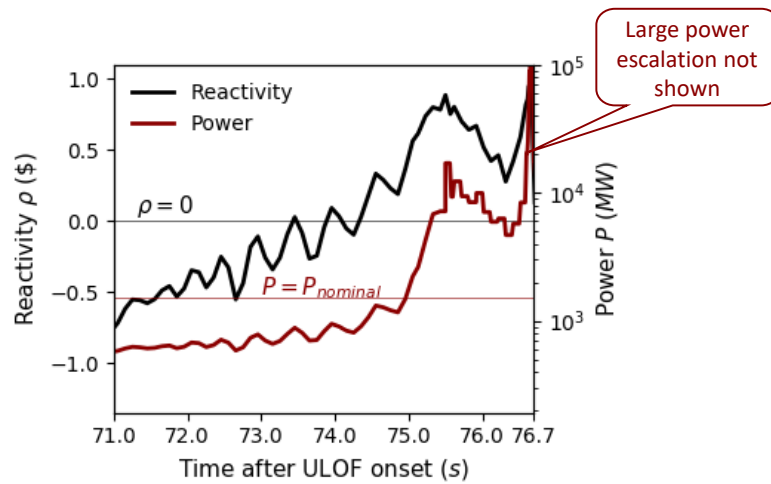


Figure VI.9 Reactivity and power evolution at the end of the primary and during the transition phase

The subsequent power increase triggers additional degradations in the internal core region. The degraded state posterior to the first power burst is illustrated on the left plot of Figure VI.10. Following, the reactivity drops due to the Doppler effect but degradations continue spreading both axially inside the individual subassemblies and radially over the whole core. It further increases reactivity such that eventually prompt criticality ($\rho = 1\$$) is attained at 76.7 s. Prompt criticality leads to large thermal energy deposition (the power burst is enhanced by the coherency effect of the pseudo-3D representation) causing excessive fuel melting and steel vaporization. The latter is responsible for significant pressure generation. The core state after prompt criticality is shown on the right plot of Figure VI.10.

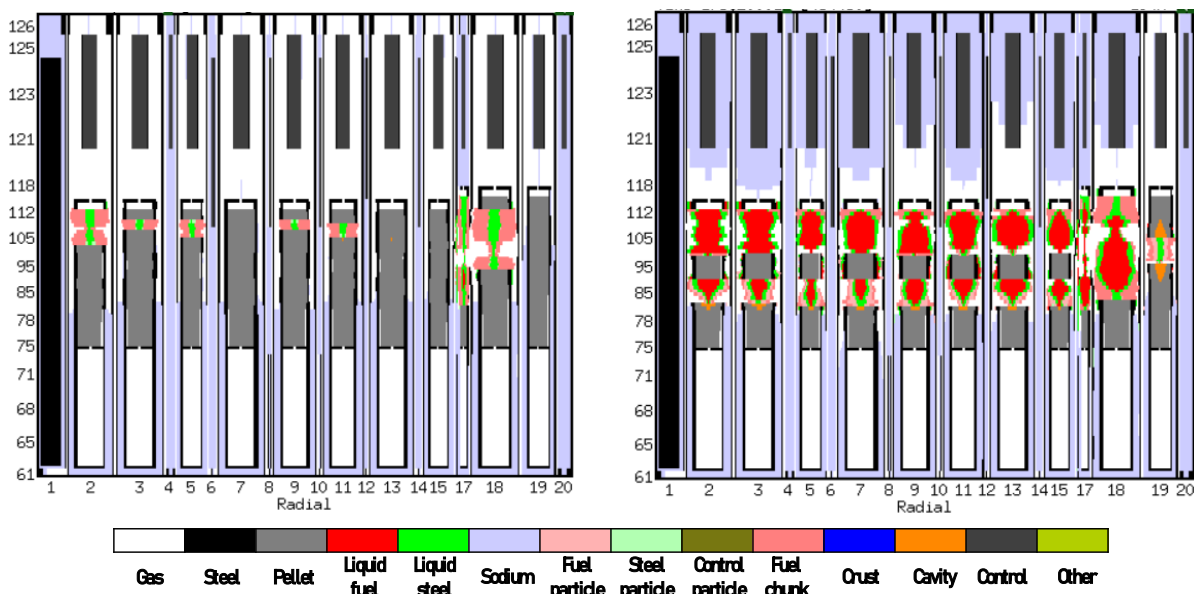


Figure VI.10 Core state shortly before (76.2 s) and after (76.7 s) first prompt criticality

We observe in Figure VI.10 that the upper and lower inner fissile zones of the CFV core are largely degraded and mostly comprised of liquid fuel. Similarly, the external fissile core is strongly degraded except the last ring of subassemblies where the degradation propagates slower due to the lower power exposure. Besides molten fuel, solid fuel debris (in pink) is present most abundantly in the lower internal and exterior core regions. On the other hand, the inner and lower fertile blankets stay mostly intact. This state is considered as the end of the transition phase in line with the phenomenology in paragraph I.2.1.2.

VI.2.3 Secondary phase

Having overpassed the first power escalation during the transition phase, the secondary phase begins when subassembly hexcans open up on a large scale and facilitate the formation of large molten/degraded pools. Fuel compaction inside these pools further augments reactivity and power increase at the beginning of the secondary phase. It can be seen during the first 0.2 s of the reactivity and power evolution in the secondary phase in Figure VI.11.

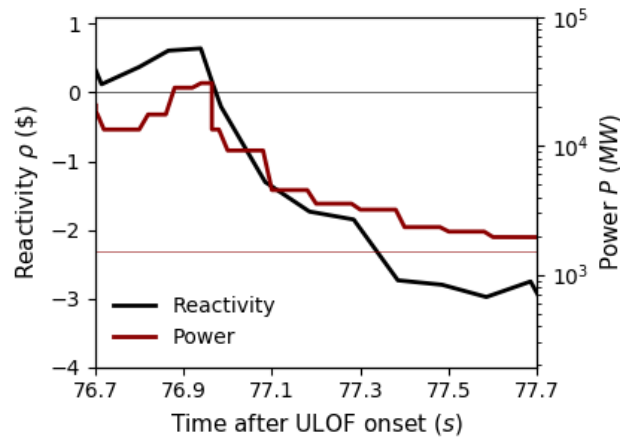


Figure VI.11 Reactivity and power evolutions during the secondary phase up to the transfer tube opening

The second part of Figure VI.11 showing declining trend is explained by the upward ejection of fissile fuel. The highly energetic encounter between molten reactor components and liquid sodium (CRGT internal) besides ongoing nuclear chain reaction produces high pressure. In presence of highly pressured core regions, upward material ejection takes place in some subassembly rings (most pronounced in the 5th) and in several CRGTs. In other subassemblies, the upper steel structures at the top of fuel pins remain intact avoiding upward fuel motion. The amount of fuel ejected upwards into the upper sodium plenum and upper neutron protection before transfer tube opening is around 12.5% of the total fuel mass. The evacuation of this fuel quantity from the high neutron flux core center region brings about considerable reactivity drop, see in Figure VI.11 after 70 s. However, as it will be shown later it is not sufficient to diminish further recriticalities. The material distribution and the upward ejection before transfer tube opening are displayed in Figure VI.12.

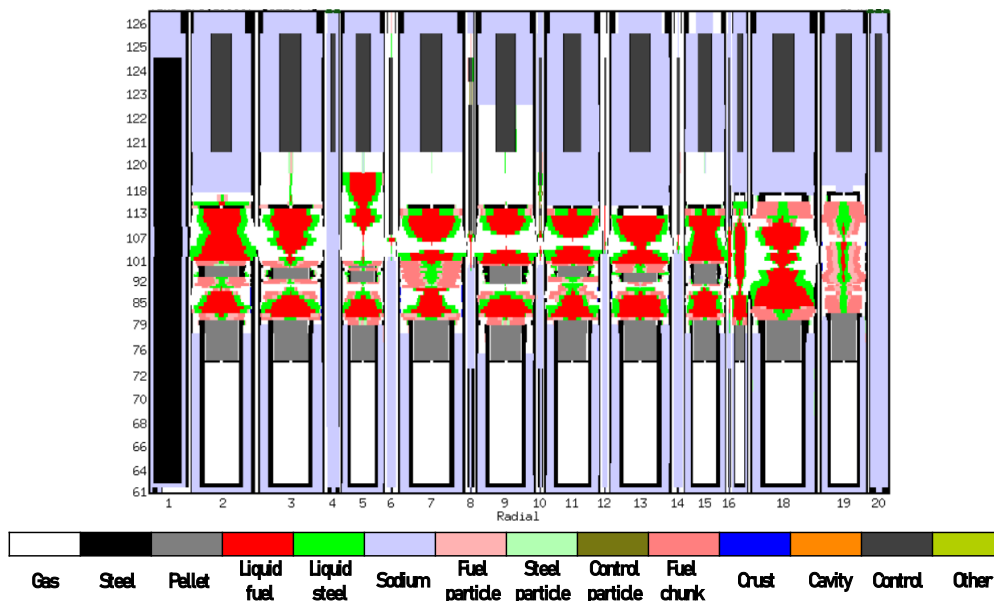


Figure VI.12 Material distribution before the transfer tube opening

Figure VI.12 indicates that also the inner fertile zone of some subassemblies is degraded. The fertile fuel in these regions is disintegrated mostly into chunk components. This leads to a global fuel debris content (sum of fuel particles and chunks) of 24.4% before the transfer tube opening.

VI.2.4 Relocation phase in SIMMER-V_vpd

After 77.7 s of ULOF transient initiation, the first transfer tube wall failure takes place. It happens to the inner core tubes at the height of the upper fissile zone. The failure is shown in Figure VI.12. In the first instants after the tube opening, the liquid steel and the liquid fuel enter into the sodium filled transfer tubes. The direct contact and the high temperature difference between these components bring about fuel-coolant interaction that evaporates the tube's sodium bulk and leads to the creation of small size re-solidified fuel/steel particles, see the highlight in Figure VI.12. We note here that at current state of the SIMMER code development, there are still ongoing studies to improve the understanding and to better reproduce numerically the FCI phenomena, in particular the thermal fragmentation behavior of molten core materials. Once these models are concluded, we expect even higher fragmentation rates (i.e. higher quantity of solid fragments).

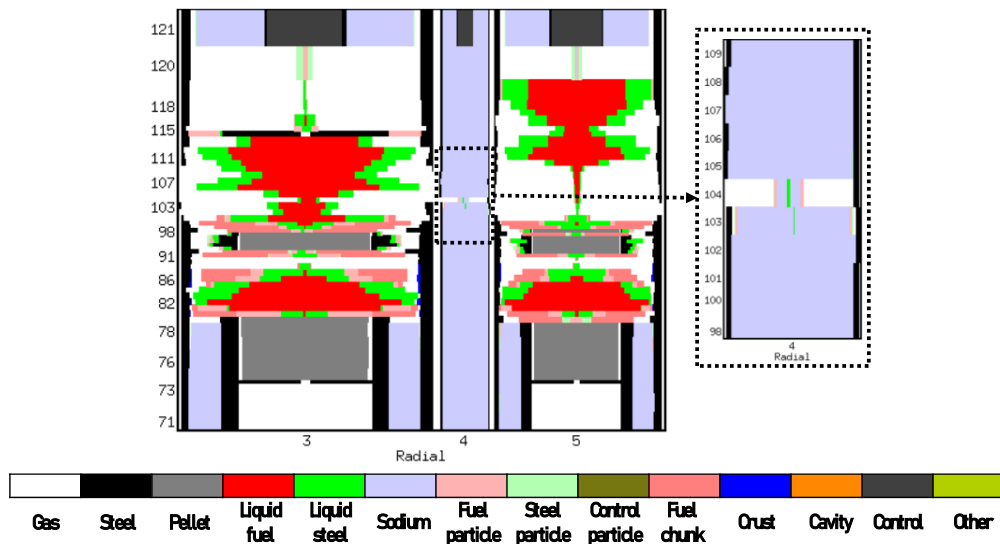


Figure VI.13 Material distribution around the first transfer tube opening in 4th subassembly ring

Simulation results starting from the first tube opening are distinguished between SIMMER-V_vo and SIMMER-V_vpd to account for the effects of different particle dynamic approaches. This paragraph focuses on the discharge characteristics predicted by SIMMER-V_vpd. The results of SIMMER-V_vo will be examined only in terms of discharge performance in the next section. Newly implemented particle dynamics models in SIMMER-V_vpd are activated for the motion of particulate components within RHEOLREG regions. RHEOLREG regions are defined for the location of mitigation transfer tubes in radial rings 4 and 20.

After the first tube failure, molten and degraded core components flow into the inner core transfer tubes. Because of the axis-symmetric one-dimensional modelling, transfer tubes at the same radial position are treated together in SIMMER-V (i.e. the volume of the mesh ring corresponds to 4 or 20 tubes) and thus the opening represents possible inflow into all 3 inner core tubes (non-conservative prediction). The transfer tubes at the core periphery open with a 3 s delay compared to the inner tubes. The phenomena inside the 20th ring of fuel assemblies are similar to the ones previously happening in the 4th ring. The FCI evaporates the bulk sodium and the discharge of molten/degraded core components commence. The following downward relocation in both ring of transfer tubes is driven by the pressure difference within degraded subassemblies and the initially unpressurized transfer tubes, and by gravity. The fuel mass evacuated by inner and outer core transfer tubes as a

function of time is plotted in Figure VI.14. The evacuated mass is obtained by integrating the mass flow rate at the bottom of each tube ring (after crossing the diaphragm).

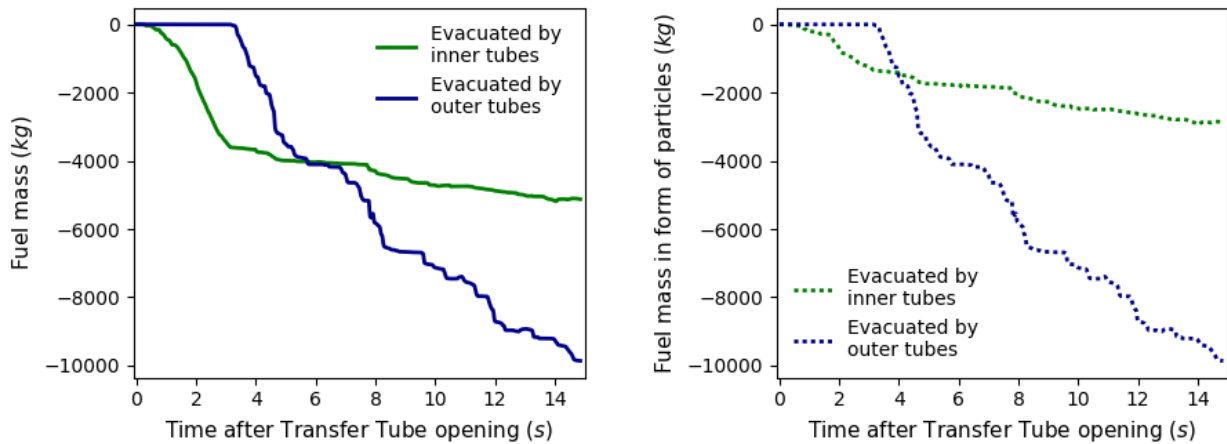


Figure VI.14 Total evacuated fuel mass (sum of liquid, particle and chunk components) (left), evacuated fuel mass and in form of particles (sum of particle and chunk components) (right) via inner/outer transfer tubes

In Figure VI.14 left plot, one can see that the ensemble of inner tubes evacuates around 3600 kg of fuel in around 3 s (1200 kg/s). This first steady fast discharge phase is followed by a slower (120 kg/s) evacuation accounting for an additional 1300 kg fuel removal until end of the simulation. The change in discharge rate is attributed partially to the equilibrated pressures giving rise to a gravitational fall but mostly the depletion of the degraded subassemblies, which are direct neighbors of the transfer tubes (the total fuel mass in the 3rd and 5th subassembly is approximately 3700 kg). Dividing the total evacuated mass (5100 kg) by three, each inner tube is responsible for around 1700 kg/tube fuel removal. Regarding the particle content, Figure VI.14 right plot shows that globally less than 50% of the total ejected fuel quantity by inner tubes is comprised of solid debris in form of particle and chunk components in SIMMER-V_vpd. The contribution of particulate components is more pronounced in the second half of the inner tube discharge. It is partially because liquid components have a higher mobility and partially because they solidify into particles with time.

The tubes at the core periphery open after the termination of the fast phase in the inner tubes. In Figure VI.14 right plot, we observe an even higher discharge rate 1640 kg/s up to around 4100 kg in 2.5 s reaching a small plateau a bit before 6 s. The plateau indicates the appearance of a potential flow blockage. However, it clears out quickly in less than half a second and the relocation continues. At the end of the simulation, the core periphery tubes evacuated around 10000 kg of reactive fuel. Even through their discharge is seemingly faster, the fuel removal by individual transfer tubes is only around 555 kg/tube. This observation is expected based on the lower energetic behavior at the core periphery (lower pressures), the fact that materials enter only from one side from 19th subassembly, and the higher particulate content of the relocating mixture, see the material distribution in the 19th ring in Figure VI.12. With all tubes together, 15100 kg of degraded/molten fuel in form of liquid, particles and chunk is evacuated during approximately 14 s from the reactive core center region. This corresponds to 33% of initial fuel inventory. In line with the material distribution before the tube opening, a large fraction of fuel manifests in form of solid debris. Consequently, the outer tube discharge materializes almost entirely in form of solid debris, as can be deduced by the close resemblance of Figure VI.14 right and left plots.

The discharge curves in Figure VI.14 imply rather continuous material outflow, especially for the inner tubes. However, the core periphery curve reveals minor flow interceptions. These variations emerge from the complex heat and mass transfer processes accompanying the fuel motion along the transfer tube length. Materials escaping the high power core region cool down and freeze into

mobile particles or immobile surface structures (liquid fuel becomes crust on the wall surface and liquid steel freezing locally increases the wall thickness). These phenomena impact the discharge dynamics from several points of view. First and most importantly the instantaneous appearance of refrozen particulate components can be such that the volume fraction of a computational mesh jumps quickly to maximum packing limit⁴⁷, which creates a temporary blockage for further downflow. It is temporary because whenever the pressure across the jammed particle structure overpasses their buoyant weight, they become fluidized and continue to flow analogous to the demonstration of the fluidization phenomena in section IV.5. The second important effect of heat and mass transfer arises from liquid solidification on the wall surface. It poses a cross section reduction that affects the particle rheology models through the hydraulic diameter. It also challenges the one-dimensional momentum approach, since particles accumulate into the corner of the reduction and their traverse motion into the new flow path makes the problem intrinsically two-dimensional. The same issue is encountered and even more pronounced at the location of the strongback where the transfer tubes diameter is reduced by a factor of two by design considerations, the visualization is shown in Figure VI.15.

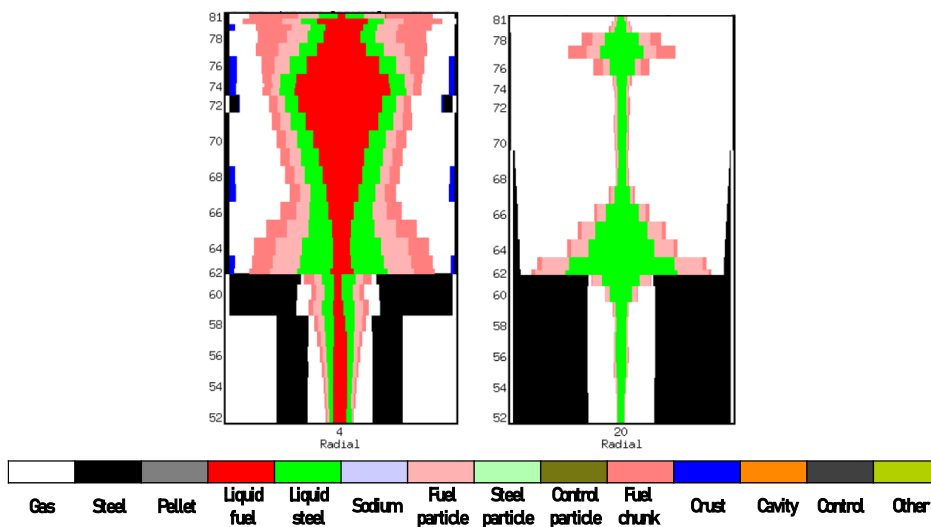


Figure VI.15 Illustration of the hydraulic diameter change in the transfer tube ring 4th (left) and ring 20th (right)

We have seen that 33% of the fuel inventory is evacuated in 14 seconds from the core center region via the mitigation transfer tubes. Although, the discharge performance and so the mitigation strategy can only be considered successful if such fuel removal rate is sufficient to avoid further re-criticalities and large power excursions. Therefore, Figure VI.16 compares the power evolution besides the global fuel removal characteristics. The reactivity is not plotted because it takes unreasonably large negative values due to the loss of fissile fuel in the core region where neutronics calculation is performed.

In Figure VI.16, we observe a power decrease already before the transfer tube opening. The reason for this was explained in paragraph VI.2.3. At the instant of first opening however, the power is still above its nominal value, around 1900 MW. The fuel removal via the collection of the mitigation transfer tubes inserts large negative reactivity, which leads to the gradually decrease of nuclear power. The core remains subcritical and the power continues to drop steadily until the end of the simulation, where it reaches around 20 MW. Since the evacuated fuel quantity is evaluated below the diagrid after which there is no flow obstacle, it can be reasonably concluded that all reactive fuel

⁴⁷ It might happen that the contribution of freezing is such that the total volume fraction of particles overpasses maximum packing limit. In this case, the particle phase stresses remain to be on their maximum value due to the numerical regularization technique preventing negative values in the dilatancy law by paragraph III.5.2.1. The maximum value of particle stresses inside a computational mesh prevents more particles to enter through the upper mesh edge but in the same time allows downward flow if the mesh below is not jammed.

arrives to the core catcher. In the core catcher, long-term cooling and re-criticality control shall be provided.

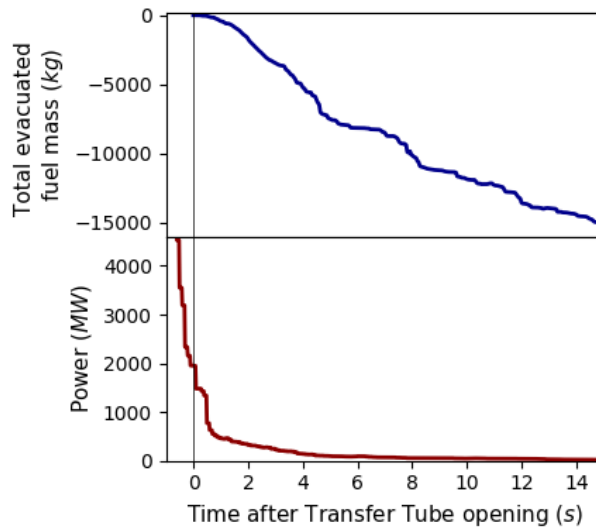


Figure VI.16 Total evacuated mass (top) and nuclear power (bottom) evolution

Overall, the scenario of controlled fuel relocation via the mitigation transfer tubes predicted by SIMMER-V_vpd supports that the goal of the mitigation strategy can be successfully achieved. Further power excursions are avoided and the reactor state is favorable to reach eventually safe conditions after a severe core disruptive ULOF accident.

VI.3 DISCHARGE PERFORMANCE BY DIFFERENT SIMMER VERSIONS

In this section, the discharge performance of SIMMER-V_vpd is compared to the prediction of SIMMER-V_vo and to the CEA reference ULOF transient by SIMMER-III. The calculation of SIMMER-V_vo is identical to SIMMER-V_vpd (pseudo-3D geometry, modelling options etc.) except that the state-of-the-art particle treatment is applied instead of the newly implemented particle dynamic models for the relocation mechanism inside the transfer tubes. The velocity field assignment, in line with CEA research directives, is the separate particle momentum approach. On the other hand, the CEA reference calculation has been performed by SIMMER-III in 2D geometry that brings about some minor differences in meshing compared to the pseudo-3D case, with separate particle momentum approach, and with identical modelling options except for particle viscosity. It is because already at that time, the applicability of the state-of-the-art physical models for the separate particle momentum approach was disputed. Therefore, in the best estimate reference computation based on engineering judgement, particle viscosity factors f_1, f_2 in Eq. II.4, Eq. II.5 in section II.2 are deactivated for chunks and other particles (the latter by extension of chunk models in the source code).

The discharge performance is assessed through the balance of remained and evacuated fuel mass from the core region. The core regions end above the diagrid assuming that such spatial dispersal is sufficient with a big margin to insert large negative reactivity, which prevents large mechanical energy releases. The evacuated quantity represents the fuel mass that reached the core catcher and can be controlled on the long-term in terms of cooling and re-criticality. The results obtained by SIMMER-III CEA reference run, SIMMER-V_vo and SIMMER-V_vpd are shown in Figure VI.17 together with the material distribution plot at the end of the simulations.

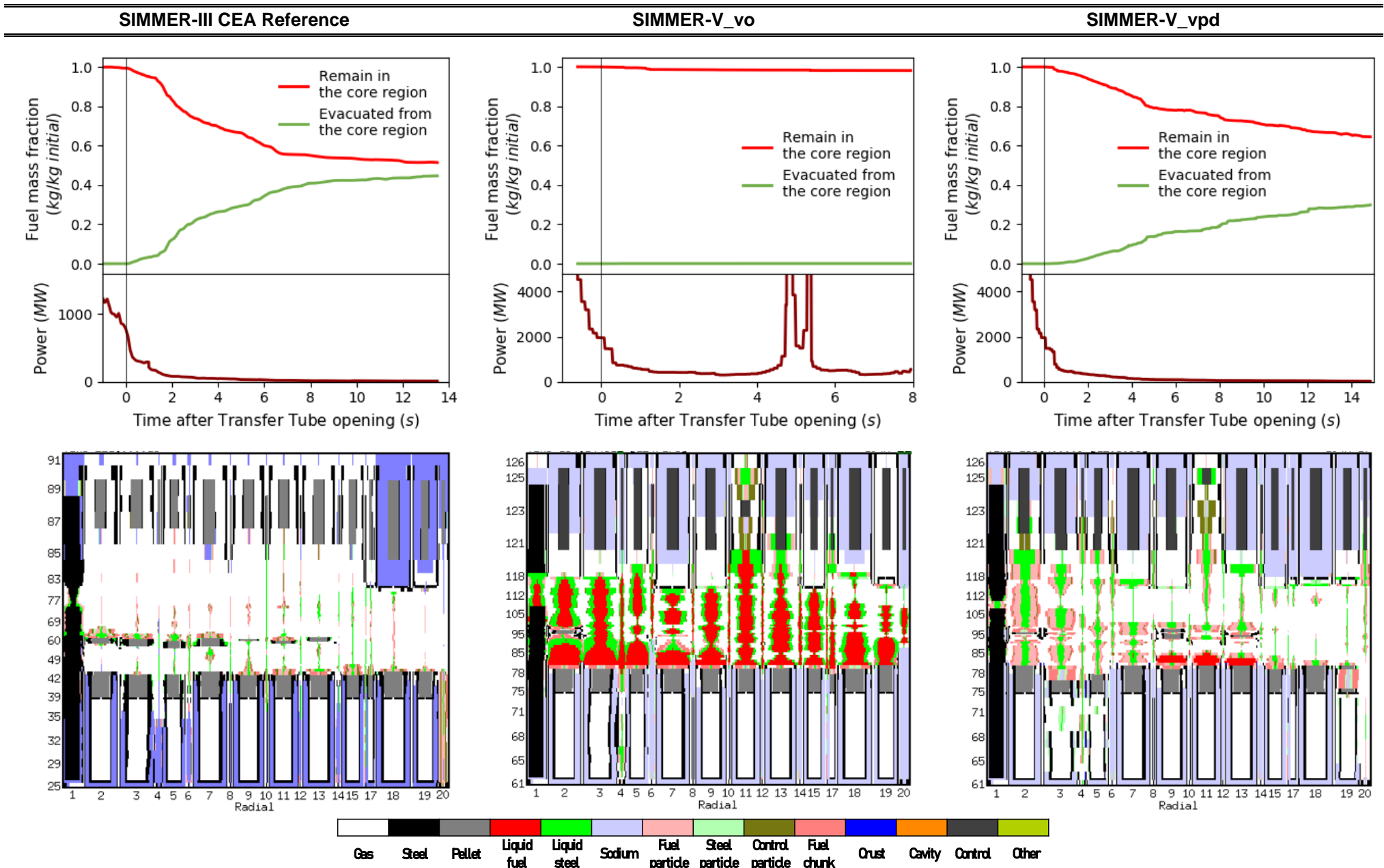


Figure VI.17 Temporal balance of fuel mass distribution and the total material distribution plot at the end of the simulation by different SIMMER versions

In case of SIMMER-III CEA reference calculation, around 45% of total fuel inventory is evacuated via both inner and core periphery tubes from the core region in a bit less than 14 s (3.2 %/s on average). Such inventory of fuel removed from the reactive core zone is largely sufficient to avoid further power escalations, power decreases gradually, and reaches strongly subcritical reactor state at the end of the simulation. In parallel, the material distribution plot shows a largely depleted core zone. One can conclude however that the fuel removal only reinforces negative reactivity and reduces power generation since already at the time of the first transfer tube opening the power is below its nominal value and it is decreasing.

Regarding the comparison to SIMMER-V runs, we note that the modifications on particle viscosity models lead to differences in material composition and distribution before transfer tube opening that affects the instant of wall failure and several other physical phenomena. Similar effects are attributed to the 2D geometrical representation. In view of these, a comparison cannot be quantitative but only qualitative. In addition, deactivating particle viscosity models means that the presence of particles is accounted for only through their gravity weight and interface momentum exchange via the use of apparent viscosity. In this method, there is no equation resolving the variation of fluid-particle or structure-particle exchange terms as a function of total particle content. It leads to the miscalculation of particle downflow and thus an overestimation of the fuel discharge rate.

In the second column of Figure VI.17, SIMMER-V_vo results are plotted. Similar to the case of SIMMER-V_vpd in paragraph VI.2.4, the power follows a decreasing trend but it is still above its nominal value at the instant of first tube opening. After transfer tube wall failure, degraded fuel flows into the newly available volume. Such fuel expansion inserts negative reactivity and maintains the power reduction. However, the temporal evolution of the fuel mass fraction indicates that more than 95% of initial fuel quantity stays in the core. Fuel evacuation from the reactive center region is inhibited by the formation of permanent particle blockages inside the transfer tubes. The inner core tubes remain blocked at the height of the lower tube restrictions til the end of the simulation, while material levitation is observed at the mid core height inside the outer tubes. These discharge obstacles facilitate the formation of large molten/degraded pools, which persist until the end of the computation based on the material distribution plot. Inside these pools, fuel compaction besides ongoing nuclear heat generation leads to re-criticalities and energetic power excursions (the magnitude of power peaks is not displayed in Figure VI.17 to avoid plot distortion). As a result, the inner fertile plate is degraded and the fuel is present predominantly in liquid form. Energetic power excursions have the potential to damage the integrity of safety barriers, and consequently to challenge safe accident termination without radioactivity release to the environment.

The third column of Figure VI.17 describes SIMMER-V_vpd results. Opposite to SIMMER-V_vo calculation, permanent particle blockages are not formed and a certain quantity of degraded fuel reaches the core catcher. The mass evacuated from the core region is around 33% in 14 second (2.35 % fuel mass/s on average). It is somewhat lower than the one predicted by SIMMER-III CEA reference calculation. Such relocation rate reduction is expected since the newly implemented particle rheology models in SIMMER-V_vpd account for direct particle-particle interactions and improve the estimation of particle-structure interactions (by incorporating the effect of total particle content). Even though the relocation rate is lower, it is still sufficient to prevent further power escalations in the simulated time frame, and analogous to SIMMER-III CEA reference calculation conclude on strongly subcritical reactor core state. The material distribution plot at the end of the calculation shows a rather large depleted central core zone with only minor fraction of liquid fuel and partly intact fertile plate similar to the reference case.

We conclude that SIMMER-V_vpd results are in agreement with SIMMER-III CEA reference calculation in terms of the main safety criterion, which is to avoid further re-criticalities. However, SIMMER-V_vpd conforms better with the conservatism required for nuclear safety studies. It provides a more detailed description of particle dynamic behavior that accounts more realistically for the hindering effect of particle concentration and incorporates the impact of particle level interactions.

Chapter VII.

CONCLUSIONS AND PERSPECTIVES

VII.1 SUMMARY AND CONCLUSIONS

This PhD work was outlined in the context of the safety evaluation of future generation Sodium-cooled Fast Reactors, in particular of the industrial scale technological demonstrator currently under research in the frame of the ASTRID project in France. Since improved safety is one of the main goals in the development of Generation IV nuclear systems, the domain of severe core disruptive accidents is addressed with a high importance. To comply with the higher safety standards, an innovative severe accident mitigation strategy has been developed by French teams. The strategy consists of the controlled discharge of degraded fuel from the core center region by applying special design transfer tubes and an in-vessel core catcher. At current state of research, the effectiveness of the mitigation scenario is being demonstrated through the best estimate calculations with the SIMMER code series. The simulations for the CFV reference core design of the ASTRID reactor showed significant amount of degraded fuel is present in form of solid particles. Consequently, the discharge performance and hence the success of the mitigation strategy were strongly influenced by the relocation mechanism of solid debris. Due to the importance of particle dynamics in the safety assessment of the mitigation devices, this thesis work was dedicated to improve the numerical modelling of particle-size solid debris in SIMMER-V code environment. The improvements were envisaged by considering a new momentum approach that separates particulate components from their liquid counterparts in terms of their velocity.

In this context, the state-of-the-art particle dynamic treatment in SIMMER was presented in **Chapter II**. The state-of-the-art physical models apply apparent viscosity and viscosity factors to account for the presence of solid bodies in the multi-phase multi-component flow. The physical foundation of such models inherently assumes that particles move fully suspended with the same velocity as their liquid form corresponding to a particle-liquid mixture momentum approach. Since the separate particle velocity concept does not comply with this assumption, we concluded on the necessity to elude their use and develop a new method to take into account the effect of solid debris on the relocation mechanism. In addition, the bibliographic review on immersed and dry granular media (being analogous to solid reactor debris in different fluid environment) revealed two important findings that are crucial to our scope of interest. Firstly, particulate systems possess unique dynamic features arising mainly from the inelastic nature of direct particle-particle collisions and inter-particle friction processes. Secondly, in dense configurations, these processes can be predominant over the hydrodynamic forces in shaping the macroscopic flow behavior. Following, we concluded that such particle level interactions have to be incorporated into the numerical modelling of dense debris flow in order to accurately simulate the discharge dynamics inside the transfer tubes. This conclusion was supported by a Phenomena Identification-Ranking Table (animated in the frame of the PhD) correlating the theoretical importance of multi-phase granular phenomena and the associated SIMMER modelling uncertainties.

Chapter III contains the core of the thesis work: the development of a comprehensive particle dynamics modelling set applicable over a wide range of solid volume fractions encountered in reactor applications. The model development has been carried out for a one-dimensional pressure due to phase changes and/or gravity driven particle flow in a multi-phase multi-component environment in a vertical tube potentially with cross section variations, and with tube to particle diameter ratio in the

VII.1 Summary and conclusions

order of a few hundred. The purpose was to improve the prediction of discharged fuel mass and evacuation time via the mitigation transfer tubes. The neutronics response of the reactor for fuel removal from the core center indicates whether further re-criticalities and large mechanical energy releases can be avoided. Therefore, the improved estimation of the mitigation performance is of high importance in SFR safety evaluation.

This model development constitutes the first level of conclusions related to physical modelling level. It consisted of the improvement of fluid-particle interphase momentum exchange terms and the newly incorporated effect of particle-particle interactions. The improvement of the interphase drag constitutive laws aimed to exclude the use of particle viscosity factors rooted in the mixture approach. It was carried out by replacing the original momentum exchange function with the Gidaspow drag function. The Gidaspow equation is a combination of the Wen & Yu and the Ergun correlations. The latter is widely recognized to be more representative to dense particle configurations, where correlations derived by the extension of single particle drag force (identical to the state-of-the-art SIMMER drag function) bring considerable uncertainties.

The second part of the model development involved the incorporation of direct particle-particle contacts, which were not modelled in original SIMMER versions. It was carried out by introducing a new particle phase stress term into the SIMMER momentum equation for particles. The constitutive laws for the solid stress (particle pressure and shear stress) were constructed by the recently developed $\mu(I)$ dense granular rheology. Our motivation towards this approach resulted from its capability to describe the intermediate fluid-like regime of granular flows in which particle collisions and friction have similar importance, its adaptability to formulate one-dimensional constitutive laws, and the fact that the equations are expressed in terms of macroscopic field variables.

The major strong point of implementing the $\mu(I)$ dense granular rheology into SIMMER is that it translates into a shear dependent frictional rheology through the shear rate dependent macroscopic friction coefficient. In addition, the rheology expresses the real three-dimensional nature of collisions and friction by correlating the normal and shear components of the solid stress. These previous two features bring an entirely new physics into the original fluid-like particle momentum description of SIMMER. In contrast to the simplest fluid-like continuum description, the new modelling set provides a more realistic view of dense particle flows by taking into account the heterogeneity of solid stresses and the shear dependent behavior.

To account for the different flow regimes in reactor applications, two stress scaling were adopted: inertial and viscous. Contrary to the original flow map topology in SIMMER, which neglects the influence of particle content, the new modelling set add another dimension to the flow topology that is now function of total particle concentration. Further accounting for the effect of particle content and extending the validity range of the particle level interaction models, the $\mu(I)$ dense granular rheology equations were augmented by percolation theory aspects (in the formulation of the dilatancy law) at high concentrations close to jamming transition. At lower concentrations, where $\mu(I)$ dense granular rheology has not been validated, the particle shear stress was formulated by the conventional Fanning equation with a solid friction factor derived from the $\mu(I)$ dense granular rheology to comply with continuity. Altogether, it makes the developed models multi-disciplinary. At the current stage of model development, the approach is proved to be satisfactory and the choices are justified. Some areas calling for future research and improvement will be detailed in the perspectives.

Following the aforementioned model development, **Chapter IV** contained their validation through simplified test cases. All test cases considered in this work were one-dimensional, purely dynamic without heat and mass transfer, two-phase (particle-liquid or particle-gas) and structure bounded set-ups. They all correspond to representative reactor conditions in which high concentration of particle-sized solid debris is likely to influence the dynamics of degraded core discharge via the mitigation transfer tubes. Test cases included static granular pile, bin discharge, flow through porous

media, fluidization, sedimentation and hydraulic conveying. Computations were performed with SIMMER-V_vo (state-of-the-art equations and default modelling options) and with SIMMER-V_vpd (newly implemented particle dynamic modelling set). The results with both calculations in every tests were compared to analytical solutions or empirical correlations in terms of the figure of merit. We concluded that applying the newly developed particle dynamics models provides encouraging results. The characteristic behavior of the figure of merit is reproduced in each test case. In contrast to SIMMER-V_vo, calculations with SIMMER-V_vpd showed remarkable improvements, especially in case of fluidization by liquid sodium for which SIMMER-V_vo results are not interpretable, and in case of jammed particle piles where SIMMER-V_vo models, in lack of solid stresses, are insufficient to capture the physics of granular matter.

Chapter V constitutes the second level of conclusions related to the experimental scale validation. This chapter confronts again SIMMER-V_vo and SIMMER-V_vpd results (also with the previous CEA best estimate run by SIMMER-III) but in case of a complex scenario with heat and mass transfer processes that better correspond to the phenomena occurring during the discharge process in a real reactor. The integral effect test used for this purpose was the EAGLE 1 FD and ID1 experimental programs. In spite of the restricted use of the precise experimental conditions and results, we were able to track the major events and to capture the general experimental observations relevant to the scope of this work. It included most importantly the observation on massive fuel removal from the fuel assembly jacket without sustained blockages inside the duct, and on the arrival of large fraction of initial fuel inventory into the lower trap. SIMMER-V_vo results indicated permanent particle blockages and unphysical material levitations that prevented massive fuel relocation in contradiction of both FD and ID1 test. On the other hand, the results of SIMMER-V_vpd were in close agreement with the CEA best estimate run, both predicting well the post experimental observation of fuel mass distribution in FD and ID1 tests. However, we encourage the use of SIMMER-V_vpd since the duct internal in SIMMER-III was represented in a non-satisfactory multi-mesh approach, opposed to the one-dimensional channel flow topology in SIMMER.

In order to have a better understanding of the behavior of particle rheology equations in a complex multi-phase multi-component environment, a separate section was dedicated to the analysis of particle stress terms in inertial and viscous regimes. By comparing their magnitude, we confirmed our initial assumption on their additivity by postulating the predominance of one over the other. Based on the spatial and temporal evolutions of normal and shear stresses, we deduced that their interplay with solid concentration and particle velocity is coherent with the physically expected behavior. In addition, to estimate the effect of uncertain empirical parameters in the rheology equations, a sensitivity study has been performed. The sensitivity analysis highlighted one parameter, the proportionality coefficient between the shear rate and average axial velocity, which has a substantial effect on the discharge dynamics.

The last chapter, **Chapter VI**, constitutes the third and most important level of conclusions related to the reactor scale applications. It is because the objective of the thesis work, through the development of particle dynamics models, was to predict the scenario of molten/degraded core discharge with a higher confidence and to contribute therefore to the safety evaluation of future generation SFRs. Consequently, the goal of this chapter was to evaluate the impact of the newly developed particle momentum approach on the numerically predicted performance of the severe accident mitigation strategy. The reactor scale application was studied through the simulation of the ULOF accidental sequence in the reference CFV ASTRID core and reactor design in pseudo-3D geometry. Following the whole ULOF accidental sequence in SIMMER-V, the low energetic natural behavior of the CFV core preventing significant mechanical energy release during the primary accidental phase was confirmed. Subsequent, the transfer tube discharge was analyzed with SIMMER-V_vo, SIMMER-V_vpd and through the results of the CEA reference calculation by SIMMER-III. We found that in the run of SIMMER-V_vo substantial fuel evacuation was inhibited by the formation of permanent particle blockages inside the transfer tubes. It led to large core powers, which would be unacceptable to

VII.2 Perspectives

establish reactor safety. However, based on the inaccurate predictions of SIMMER-V_vo for the simplified test cases in Chapter IV and for integral effect test results in Chapter V, we judged the original particle dynamics models of SIMMER-V_vo to be highly improved to be able to be applied for the separate particle velocity field approach. This statement was also supported by the conclusions drawn from the bibliographic study on dense granular flows. On the other hand, the comparative study showed that SIMMER-V_vpd results are in good qualitative agreement with SIMMER-III CEA reference calculation (that keeps 1D tube representation but first modifications on particle viscosity terms were applied already at that time, although they were far from the current stage of development summarized in this thesis). Both computations demonstrated that, by the massive and fast fuel extraction from the core center region, the core is in a strongly subcritical state that is favorable to avoid further re-criticalities and the corresponding large power escalations on the long term. This implies that the mitigation strategy by the given number and design of transfer tubes can be efficient in terms of the main safety criterion, which is to limit the likelihood and the amplitude of large mechanical energy releases. The fact that the core has been brought into a strongly subcritical state after a CDA is the first stage before other mitigation devices enter in action (core catcher, passive cooling devices etc.). A more elaborate analysis to conclude on a final safe reactor state requires the translation of our results into thermal and mechanical loading on safety barriers and on the core catcher. Such figures, even with their current large uncertainties, are of decisive interest for reactor designers.

The fruit of our work in face of the reference SIMMER calculations reveals in a more conservative and an improved physical prediction of the mitigation performance by SIMMER-V_vpd. It emerges from a detailed description of particle dynamic behavior accounting more realistically for the hindering effect of particle concentration and newly incorporated impact of particle level interactions. Even though the approach implemented is highly empirical and requires additional refinements, the new modelling tool is applicable to nuclear severe accidents. In the domain of severe accident, we do not intend to resolve phenomena on the finest physical level but to provide a sufficient degree of prediction to obtain a global figure of merit. In this view, the developed modelling set brings a more robust demonstration of SFR severe accident scenarios and consequently, it marks an important milestone in reactor safety analyses. Its added value to the reactor community can be further extended by the following future perspectives.

VII.2 PERSPECTIVES

The perspectives of this thesis work are organized into the same three levels as for the conclusions, namely the physical modelling level, the experimental level and the reactor scale level.

With respect to the **model development level**, we identify the following topics that could be advanced in the future. Part of them arises from the modelling shortcomings mentioned in the conclusions. The first area concerns the empirical coefficients of the rheology equations. These coefficients were deduced from experiments with specific particle and fluid properties. Therefore, the applicability of such coefficients for the description of reactor debris can be uncertain. This category includes the prior knowledge and formulation of the shear rate to adopt one-dimensional numerical treatment (found to be the highest influence uncertain modelling parameter in Chapter V). As a preliminary approach, we implemented a simple correlation, which is only the function of average axial velocity based on the pseudo-plastic behavior. To improve the shear rate equation and propose specific empirical coefficients for reactor debris, we suggest further investigations and dedicated experimental programs.

The second area proposed for future work is related to the rheological behavior of multi-component multi-phase flows. It is problematic because the stress scaling in the $\mu(I)$ dense granular rheology is established by the dimensional analysis of two-phase two-component systems. Although, we take refuge behind the little available experimental knowledge and modelling approach developed specifically for multi-component multi-phase flows. If in the future, well-established approaches and

correlations will be available for such systems, the implemented equations can be revisited and improved.

The third point that is worth of the most scientific attention in the future concerns the numerical implementation of the particle pressure gradient. It was implemented with explicit time treatment and first order downstream projection of cell edge variables as first approach. Even though, we experimented with various numerical schemes for spatial discretization, we did not manage to reach one that provides stable solution in all considered configurations. Consequently, we applied a numerical regularization technique that limits the magnitude of the gradient and resolves stability issues. Regarding the temporal discretization, we did not have a choice because the system of momentum equations in SIMMER is solved by first order Gaussian elimination supplemented with a Newtonian iteration for higher order terms. The iterative matrix method solves for momentum phase velocities at one given location. Including an implicit velocity dependent gradient term (velocity evaluation at different locations) into this system is a challenging task and extends above the limits of this PhD. Although, it would bring the advantage to match the temporal scheme of the particle pressure with the shear stress term, and we postulate that it could resolve instability problems. Therefore, we suggest to implement implicit time treatment for particle normal pressure. With this purpose, an internship is proposed recently at CEA (also aiming to further investigate the question of fluid pressure interpretation in SIMMER-V).

Besides corrective measures, the other category of improvements on the physical modelling level is to the upgrade the modelling capabilities, for example including the heat transfer phenomena in particulate systems or extending the dynamics into a three-dimensional domain. The first is necessary because the energy dissipation is a two-step process, and to account for such, heat transfer mechanisms in SIMMER-V have to be revisited and perhaps reconsidered. By extending the currently one-dimensional models into three-dimensional, they could be applied to the whole core reactor region and to the core catcher. Performing the extension, one could benefit from a more consistent particle dynamics approach and presumably more physical debris behavior over the whole simulation domain. The advantage of the $\mu(I)$ dense granular rheology approach is that the constitutive laws for solid stresses are relatively easily adaptable to a 3D modelling following the work of [Jop et al., 2006]. The previously mentioned internship topic also foresees this direction. Moreover, we emphasize that the particle momentum treatment developed in this work is not specific to SFRs, they can be applicable to other types of reactors where the motion of particles can be important.

Perspectives on the **experimental level** involve the more comprehensive separate and integral effect test validation of SIMMER-V_vpd models. Regarding separate effect tests focusing on elementary physical phenomena, the first tests of the PLINIUS2 (provisional name) platform are planned. For the construction of the PLINIUS2 prototypic experimental platform, there is a considerable investment at CEA at present with currently two propositions of small-scale separate effect tests. They could be complemented with a new test that involves the vertical flow of dense debris alone inside a tube structure (within a heated section to cancel the effect heat and mass transfer) aiming to validate the frictional and collisional dynamics of the $\mu(I)$ dense granular rheology. Preliminary calculations by SIMMER-V_vpd would help to construct the experimental section.

Concerning integral effect test, there are other experimental programs suitable to examine debris dynamics alongside other reactor phenomena. For instance, the EAGLE 1 out-of-pile test for which more precise mass balances are available, or the in-pile EAGLE 2/3 and SAIGA-1 future tests dedicated to the investigation of the discharge process. However, similarly to EAGLE 1 studied in this work, they consider the discharge at the pin level. For the integral effect validation of newly implemented particle dynamics models, we are more favorable towards the large-scale in-pile TR (Corium Relocation in Discharge Tubes) test planned at the new PLENIUS platform. It is because it uses prototypic materials and the test geometry is more representative to the transfer tube design: the length and cross-section of the discharge channel will be close to scale 1. Implementing

VII.2 Perspectives

dedicated instrumentation to monitor the composition (size and shape distribution) of degraded fuel, the radial profile of velocity and volume concentration, and the relocation characteristics (mass flow rate, appearance/disappearance of blockages) would benefit the validation of SIMMER-V_vpd models. From another point of view, SIMMER-V_vpd can be used to for pretest and posttest calculations. In the current pre-design phase, simulation results can help to approve or reconsider previously established configurations. All of these experiments (separate and integral effect tests) can be exploited not only for validation purposes but also to refine debris properties and better adjust the empirical model parameters.

The third level of perspectives concerns the **reactor scale application**. In our reactor simulations, the newly developed particle dynamics models were applied only to the transfer tube regions. However, it was apparent that fuel relocation inside the control-rod guide tubes has a significant reactivity effect as well. With the interest of better evaluating the effect of solid debris dispersal from the core center, we suggest the extension of new models for the CRGT regions. It can be done by simple user input modifications, the models are readily applicable.

Another improvement of the reactor case is to simulate the ULOF accidental sequence in real three-dimensional Cartesian coordinates in SIMMER-V, for which there is ongoing work already in process (the particle dynamics modelling set at its current state is applicable to Cartesian one-dimensional geometries). This computation resolves most of the geometrical deficiencies of the pseudo-3D runs, in particular that the transfer tubes at the same radial location can be treated separately. Eliminating the coherency effect arising from the rings of fuel assemblies, preliminary results show lower fuel enthalpies and consequently higher fraction of solid debris. Therefore, this run would underline even more the impact of new particle dynamic treatment in comparison to the pseudo-3D runs. In addition, they are extended to CRGT regions such that a new scope of analysis can be opened. Unfortunately, this computation is extremely time consuming (over 1 month of simulation time currently due to the large number of meshes), so we did not have the opportunity to present the results in this work. Furthermore, it is planned to examine the evolution of other accidental sequences (ULOF, USAF), and to investigate other design configurations (change of tube locations, number or geometry) if found necessary for the development of future SFRs.

References

- A Technology Roadmap for Generation IV Nuclear Energy Systems (No. GIF-002-00, 859029), 2002. . DOENE (USDOE Office of Nuclear Energy, Science and Technology (NE)), United States. <https://doi.org/10.2172/859029>
- Ancey, C., Coussot, P., Evesque, P., 1999. A theoretical framework for granular suspensions in a steady simple shear flow. *Journal of Rheology* 43, 1673–1699. <https://doi.org/10.1122/1.551067>
- Andreotti, B., Forterre, Y., Pouliquen, O., 2013. *Granular Media: Between Fluid and Solid*. Cambridge University Press.
- Aoyagi, M., Kamiyama, K., Tobita, Y., 2018. Improvement of a physical model for blockage formation of solid–liquid mixture flow with freezing for core safety evaluation of SFRs. *Journal of Nuclear Science and Technology* 55, 530–538. <https://doi.org/10.1080/00223131.2017.1417172>
- Azizi, J., Alexander, K.S., Dollimore, D., Murthy, A.S., Tata, S.S., 1992. The development of a permeability theory applied to concentrated suspensions. *Colloids and Surfaces* 62, 1–9. [https://doi.org/10.1016/0166-6622\(92\)80031-V](https://doi.org/10.1016/0166-6622(92)80031-V)
- Bachrata, A., 2015. Unprotected loss of flow simulation on ASTRID CFV-V3 reactor core, in: ICAPP 2015 Proceedings. Nice, France.
- Bachrata, A., Trotignon, L., Sciora, P., Saez, M., 2019. A three-dimensional neutronics – Thermalhydraulics Unprotected Loss of Flow simulation in Sodium-cooled Fast Reactor with mitigation devices. *Nuclear Engineering and Design* 346, 1–9. <https://doi.org/10.1016/j.nucengdes.2019.02.015>
- Bagnold, R.A., 1954. Experiments on a gravity-free dispersion of large solid spheres in a Newtonian fluid under shear. *Proceedings of the Royal Society of London. Series A. Mathematical and Physical Sciences*.
- Bartosik, A., 2020. Validation of friction factor predictions in vertical slurry flows with coarse particles. *Journal of Hydrology and Hydromechanics* 68, 119–127. <https://doi.org/10.2478/johh-2020-0005>
- Bartosik, A., 1996. Modelling the Bagnold stress effects in vertical slurry flow. *Journal of Hydrology and Hydromechanics* 1, 49–58.
- Bartosik, A.S., Shook, C.A., 1995. Prediction of vertical liquid solid pipe flow using measured concentration distribution. *Particulate Science and Technology* 13, 85–104. <https://doi.org/10.1080/02726359508906672>
- Beck, T., Blanc, V., Esclaine, J.-M., Haubensack, D., Pelletier, M., Phelip, M., Perrin, B., Venard, C., 2017. Conceptual design of ASTRID fuel sub-assemblies. *Nuclear Engineering and Design* 315, 51–60. <https://doi.org/10.1016/j.nucengdes.2017.02.027>
- Benavides, A., van Wachem, B., 2008. Numerical simulation and validation of dilute turbulent gas–particle flow with inelastic collisions and turbulence modulation. *Powder Technology, Granular Temperature* 182, 294–306. <https://doi.org/10.1016/j.powtec.2007.06.028>
- Berthoud, G., 2000. Vapor Explosions. *Annual Review of Fluid Mechanics* 32, 573–611. <https://doi.org/10.1146/annurev.fluid.32.1.573>
- Bertrand, F., Marie, N., Bachrata, A., Brun-Magaud, V., Droin, J.-B., Manchon, X., Herbreteau, K., Farges, B., Carlucci, B., Pomerouly, S., Lemasson, D., 2018. Status of severe accident studies at the end of the conceptual design of ASTRID: Feedback on mitigation features. *Nuclear Engineering and Design* 326, 55–64. <https://doi.org/10.1016/j.nucengdes.2017.10.019>
- Bertrand, F., Marie, N., Prulhière, G., Lecerf, J., Seiler, J.M., 2016. Comparison of the behaviour of two core designs for ASTRID in case of severe accidents. *Nuclear Engineering and Design* 297, 327–342. <https://doi.org/10.1016/j.nucengdes.2015.04.020>
- Beverloo, W.A., Leniger, H.A., van de Velde, J., 1961. The flow of granular solids through orifices. *Chemical Engineering Science* 15, 260–269. [https://doi.org/10.1016/0009-2509\(61\)85030-6](https://doi.org/10.1016/0009-2509(61)85030-6)
- Bohl, W.R., 1990. AFDM: An Advanced Fluid-Dynamics Model (No. LA-11692-MS-Vol.5). Los Alamos National Lab., NM (USA).
- Bouزيد, M., Izzet, A., Trulsson, M., Clément, E., Claudin, P., Andreotti, B., 2015. Non-local rheology in dense granular flows. *Eur. Phys. J. E* 38, 125. <https://doi.org/10.1140/epje/i2015-15125-1>
- Boyer, F., Guazzelli, É., Pouliquen, O., 2011. Unifying Suspension and Granular Rheology. *Physical Review Letters* 107. <https://doi.org/10.1103/PhysRevLett.107.188301>
- Campbell, C.S., 2006. Granular material flows – An overview. *Powder Technology* 162, 208–229. <https://doi.org/10.1016/j.powtec.2005.12.008>

- Campbell, C.S., 1989. Fluidization mechanism in slurry flow (No. DOE/PC/90 95 7—T8). Los Angeles, Ca.
- Cassar, C., Nicolas, M., Pouliquen, O., 2005. Submarine granular flows down inclined planes. *Physics of Fluids* 17, 103301. <https://doi.org/10.1063/1.2069864>
- Caulet, P.J.C., van der Lans, R.G.J.M., Luyben, K.Ch.A.M., 1996. Hydrodynamical interactions between particles and liquid flows in biochemical applications. *The Chemical Engineering Journal and the Biochemical Engineering Journal* 62, 193–206. [https://doi.org/10.1016/0923-0467\(96\)03086-2](https://doi.org/10.1016/0923-0467(96)03086-2)
- CEA Nuclear Energy Division, 2012. 4th Generation sodium-cooled fast reactors - The Astrid technological demonstrator.
- Chauchat, J., 2018. A comprehensive two-phase flow model for unidirectional sheet-flows. *Journal of Hydraulic Research* 56, 15–28. <https://doi.org/10.1080/00221686.2017.1289260>
- Chauchat, J., Médale, M., 2014. A three-dimensional numerical model for dense granular flows based on the $\mu(I)$ rheology. *Journal of Computational Physics* 256, 696–712. <https://doi.org/10.1016/j.jcp.2013.09.004>
- Chhabra, R., Basavaraj, M.G. [Eds.], 2019. Chapter 6 - Motion of Particles in a Fluid, in: Coulson and Richardson's Chemical Engineering (Sixth Edition). Butterworth-Heinemann, pp. 281–334. <https://doi.org/10.1016/B978-0-08-101098-3.00007-X>
- Clavier, R., Chikhi, N., Fichot, F., Quintard, M., 2015. Experimental investigation on single-phase pressure losses in nuclear debris beds: Identification of flow regimes and effective diameter. *Nuclear Engineering and Design* 292, 222–236. <https://doi.org/10.1016/j.nucengdes.2015.07.003>
- Clift, R., Grace, J.R., Weber, M.E., 2005. Bubbles, Drops, and Particles. Courier Corporation.
- Coussot, P., Ancey, C., 1999. Rheophysical classification of concentrated suspensions and granular pastes. *Physical Review E* 59, 4445–4457. <https://doi.org/10.1103/PhysRevE.59.4445>
- Dartevelle, S., 2004. Numerical modeling of geophysical granular flows: 1. A comprehensive approach to granular rheologies and geophysical multiphase flows: GEOPHYSICAL GRANULAR FLOWS, 1. *Geochemistry, Geophysics, Geosystems* 5. <https://doi.org/10.1029/2003GC000636>
- Deboeuf, A., Gauthier, G., Martin, J., Yurkovetsky, Y., Morris, J.F., 2009. Particle Pressure : A Bridge from Osmosis to Granular Dilatancy. *Physical Review Letters* 102. <https://doi.org/10.1103/PhysRevLett.102.108301>
- DeGiuli, E., Düring, G., Lerner, E., Wyart, M., 2015. Unified Theory of Inertial Granular Flows and Non-Brownian Suspensions. *Phys. Rev. E* 91, 062206. <https://doi.org/10.1103/PhysRevE.91.062206>
- Delannay, R., Valance, A., Mangeney, A., Roche, O., Richard, P., 2017. Granular and particle-laden flows: from laboratory experiments to field observations. *Journal of Physics D: Applied Physics* 50, 053001. <https://doi.org/10.1088/1361-6463/50/5/053001>
- Dey, S., Zeeshan Ali, S., Padhi, E., 2019. Terminal fall velocity: the legacy of Stokes from the perspective of fluvial hydraulics. *Proc. R. Soc. A* 475, 20190277. <https://doi.org/10.1098/rspa.2019.0277>
- Dharmarajah, A.H., 1982. Effect of particle shape on prediction of velocity-voidage relationship in fluidized solid-liquid systems (Doctor of Philosophy). Iowa State University, Digital Repository, Ames. <https://doi.org/10.31274/rtd-180813-5307>
- Droin, J.-B., 2016. Modélisation d'un transitoire de perte de débit primaire non protégé dans un RNR-Na (These de doctorat). Université Grenoble Alpes (ComUE).
- Düring, G., Lerner, E., Wyart, M., 2016. Effect of particle collisions in dense suspension flows. *Phys Rev E* 94, 022601. <https://doi.org/10.1103/PhysRevE.94.022601>
- Einstein, A., 1906. Eine neue Bestimmung der Moleküldimensionen. *Annalen der Physik* 324, 289–306. <https://doi.org/10.1002/andp.19063240204>
- Elghobashi, S., 1994. On predicting particle-laden turbulent flows. *Applied Scientific Research* 52, 309–329. <https://doi.org/10.1007/BF00936835>
- Enwald, H., Peirano, E., Almstedt, A.-E., 1996. Eulerian two-phase flow theory applied to fluidization. *International Journal of Multiphase Flow* 22, 46. [https://doi.org/10.1016/S0301-9322\(96\)90004-X](https://doi.org/10.1016/S0301-9322(96)90004-X)
- Forterre, Y., Pouliquen, O., 2009. Granular Flows, Séminaire Poincaré XIII. Marseille, France.
- Garić-Grulović, R., Kaluđerović Radoičić, T., Arsenijević, Z., Đuriš, M., Grbavčić, Ž., 2014. Hydrodynamic modeling of downward gas–solids flow. Part I: Counter-current flow. *Powder Technology* 256, 404–415. <https://doi.org/10.1016/j.powtec.2014.01.090>

- Garland, S., Gauthier, G., Martin, J., Morris, J.F., 2013. Normal stress measurements in sheared non-Brownian suspensions. *Journal of Rheology* 57, 71–88. <https://doi.org/10.1122/1.4758001>
- Garside, J., Al-Dibouni, M.R., 1977. Velocity-Voidage Relationships for Fluidization and Sedimentation in Solid-Liquid Systems. *Industrial & Engineering Chemistry Process Design and Development* 16, 206–214. <https://doi.org/10.1021/i260062a008>
- GDR MiDi, 2004. On dense granular flows. *The European Physical Journal E* 14, 341–365. <https://doi.org/10.1140/epje/i2003-10153-0>
- Ghigo, A.R., Lagrée, P.-Y., Fullana, J.-M., 2018. A time-dependent non-Newtonian extension of a 1D blood flow model. *Journal of Non-Newtonian Fluid Mechanics* 253, 36–49. <https://doi.org/10.1016/j.jnnfm.2018.01.004>
- Gidaspow, D., 1994. *Multiphase Flow and Fluidization: Continuum and Kinetic Theory Descriptions*. Academic Press.
- Guazzelli, É., Pouliquen, O., 2018. Rheology of dense granular suspensions. *Journal of Fluid Mechanics* 852. <https://doi.org/10.1017/jfm.2018.548>
- Haff, P.K., 1983. Grain flow as a fluid-mechanical phenomenon. *Journal of Fluid Mechanics* 134, 401. <https://doi.org/10.1017/S0022112083003419>
- Han, M., Kim, C., Kim, M., Lee, S., 1999. Particle migration in tube flow of suspensions. *Journal of Rheology - J RHEOL* 43, 1157–1174. <https://doi.org/10.1122/1.551019>
- Huilin, L., Gidaspow, D., 2003. Hydrodynamics of binary fluidization in a riser: CFD simulation using two granular temperatures. *Chemical Engineering Science* 58, 3777–3792. [https://doi.org/10.1016/S0009-2509\(03\)00238-0](https://doi.org/10.1016/S0009-2509(03)00238-0)
- Hunt, A., Ewing, R., Ghanbarian, B., 2014. Percolation Theory: Topology and Structure, in: Hunt, A., Ewing, R., Ghanbarian, B. (Eds.), *Percolation Theory for Flow in Porous Media*, Lecture Notes in Physics. Springer International Publishing, Cham, pp. 1–35. https://doi.org/10.1007/978-3-319-03771-4_1
- Internationale Atomenergie-Organisation [Ed.], 2015. *The Fukushima Daiichi accident*. International Atomic Energy Agency, Vienna.
- Ishii, M., Hibiki, T., 2010. *Thermo-Fluid Dynamics of Two-Phase Flow*. Springer Science & Business Media.
- Ishii, M., Zuber, N., 1979. Drag coefficient and relative velocity in bubbly, droplet or particulate flows. *AIChE Journal* 25, 843–855. <https://doi.org/10.1002/aic.690250513>
- Iwashita, K., Oda, M., 1999. *Mechanics of Granular Materials: An Introduction*. CRC Press.
- Jackson, R., 2000. *The Dynamics of Fluidized Particles*. Cambridge University Press.
- Jacquemain, D., 2015. *Nuclear Power Reactor Core Melt Accidents Current State of Knowledge*. 978-2-7598-1835-8, Place of publication not identified.
- Jaeger, H.M., Nagel, S.R., Behringer, R.P., 1996. Granular solids, liquids, and gases. *Reviews of Modern Physics* 68, 1259–1273. <https://doi.org/10.1103/RevModPhys.68.1259>
- Jenkins, J.T., Savage, S.B., 1983. A theory for the rapid flow of identical, smooth, nearly elastic, spherical particles. *Journal of Fluid Mechanics* 130, 187. <https://doi.org/10.1017/S0022112083001044>
- Jop, P., Forterre, Y., Pouliquen, O., 2006. A constitutive law for dense granular flows. *Nature* 441, 727–730. <https://doi.org/10.1038/nature04801>
- Jop, P., Forterre, Y., Pouliquen, O., 2005. Crucial role of sidewalls in granular surface flows: consequences for the rheology. *Journal of Fluid Mechanics* 541, 167–192. <https://doi.org/10.1017/S0022112005005987>
- Journeau, C., Aufore, L., Berge, L., Brayer, C., Cassiaut-Louis, N., Estre, N., Payot, F., Piluso, P., Prele, J.-C., Singh, S., Zabiégo, M., Pluyette, E., Serre, F., Teisseire, B., 2019. Corium-Sodium and Corium-Water Fuel-Coolant-Interaction Experimental Programs for the PLINIUS2 Prototypic Corium Platform. *Nuclear Technology* 205, 239–247. <https://doi.org/10.1080/00295450.2018.1479580>
- Journeau, C., Jeulain, G., Benyahia, L., Tassin, J.F., 2006. Rheology of mixtures in the solidification range 9, 12.
- Kalman, H., Portnikov, D., Gabrieli, O.G., Tripathi, N.M., 2019. What do pneumatic conveying and hydraulic conveying have in common? *Powder Technology* 354, 485–495. <https://doi.org/10.1016/j.powtec.2019.06.022>
- Kamiyama, K., Konishi, K., Sato, I., Toyooka, J., Matsuba, K., Zuyev, V.A., Pakhnits, A.V., Vityuk, V.A., Vurim, A.D., Gaidaichuk, V.A., Kolodeshnikov, A.A., Vassiliev, Y.S., 2014. Experimental studies on the upward fuel discharge for elimination of severe recriticality during core-disruptive

- accidents in sodium-cooled fast reactors. *Journal of Nuclear Science and Technology* 51, 1114–1124. <https://doi.org/10.1080/00223131.2014.912566>
- Kayser, G., Charpenel, J., Jamond, C., 1998. Summary of the SCARABEE-N Subassembly Melting and Propagation Tests with an Application to a Hypothetical Total Instantaneous Blockage in a Reactor. *Nuclear Science and Engineering* 128, 144–185. <https://doi.org/10.13182/NSE98-A1950>
- Khamseh, S., 2014. Rheophysics of granular materials with interstitial fluid : a numerical simulation study (phdthesis). Université Paris-Est.
- Kim, Y.C., Na, B.C., Hahn, D.H., 1997. Review of core disruptive accident analysis for liquid-metal cooled fast reactors (No. KAERI/AR--463/97). Korea Atomic Energy Research Institute.
- Kleinstreuer, C., Feng, Y., 2013. Computational Analysis of Non-Spherical Particle Transport and Deposition in Shear Flow With Application to Lung Aerosol Dynamics—A Review. *Journal of Biomechanical Engineering* 135. <https://doi.org/10.1115/1.4023236>
- Konishi, K., Toyooka, J.-I., Kamiyama, K., Sato, I., Kubo, S., Kotake, S., Koyama, K., Vurim, A.D., Gaidaichuk, V.A., Pakhnits, A.V., Vassiliev, Y.S., 2007. The result of a wall failure in-pile experiment under the EAGLE project. *Nuclear Engineering and Design* 237, 2165–2174. <https://doi.org/10.1016/j.nucengdes.2007.03.012>
- Kramer, O.J.I., de Moel, P.J., Baars, E.T., van Vugt, W.H., Padding, J.T., van der Hoek, J.P., 2019. Improvement of the Richardson-Zaki liquid-solid fluidisation model on the basis of hydraulics. *Powder Technology* 343, 465–478. <https://doi.org/10.1016/j.powtec.2018.11.018>
- Kwauk, M., Li, J., 1996. Fluidization regimes. *Powder Technology* 87, 193–202. [https://doi.org/10.1016/0032-5910\(96\)03089-6](https://doi.org/10.1016/0032-5910(96)03089-6)
- Landman, K.A., White, L.R., 1992. Determination of the hindered settling factor for flocculated suspensions. *AIChE Journal* 38, 184–192. <https://doi.org/10.1002/aic.690380203>
- Lazaro, A., Schikorr, M., Mikityuk, K., Ammirabile, L., Bandini, G., Darmet, G., Schmitt, D., Dufour, Ph., Tosello, A., Gallego, E., Jimenez, G., Bubelis, E., Ponomarev, A., Kruessmann, R., Struwe, D., Stempniewicz, M., 2014. Code assessment and modelling for Design Basis Accident analysis of the European Sodium Fast Reactor design. Part II: Optimised core and representative transients analysis. *Nuclear Engineering and Design* 277, 265–276. <https://doi.org/10.1016/j.nucengdes.2014.02.029>
- Le Belguet, A., Jeanne, T., Journeau, C., Bataille, F., 2012. A new analysis of the large scale fuel-sodium interaction in the FARO-TERMOS experiment with the SIMMER-III code. *International Youth Nuclear Congress* 3.
- Leung, L.S., Jones, P.J., 1986. Flow of Gas-Solid Mixtures through Standpipes and Valves, in: Hewitt, G.F., Delhay, J.M., Zuber, N. (Eds.), *Multiphase Science and Technology: Volume 2*. Springer, Berlin, Heidelberg, pp. 333–426. https://doi.org/10.1007/978-3-662-01657-2_5
- Liu, P., Yasunaka, S., Matsumoto, T., Morita, K., Fukuda, K., Tobita, Y., 2006. Simulation of the Dynamic Behavior of the Solid Particle Bed in a Liquid Pool: Sensitivity of the Particle Jamming and Particle Viscosity Models. *JOURNAL OF NUCLEAR SCIENCE AND TECHNOLOGY* 43, 10.
- Lun, C.K.K., Savage, S.B., Jeffrey, D.J., Chepurniy, N., 1984. Kinetic theories for granular flow: inelastic particles in Couette flow and slightly inelastic particles in a general flowfield. *Journal of Fluid Mechanics* 140, 223–256. <https://doi.org/10.1017/S0022112084000586>
- Lundberg, J., Halvorsen, B.M., 2008. A Review of Some Existing Drag Models Describing the Interaction Between Phases in a Bubbling Fluidized Bed.
- Malko, M.V., 2016. *The Chernobyl Reactor: Design Features and Reasons for Accident*. Kyoto University, Research Reactor Institute, Japan.
- Mankoc, C., Janda, A., Arévalo, R., Pastor, J.M., Zuriguel, I., Garcimartín, A., Maza, D., 2007. The flow rate of granular materials through an orifice. *arXiv:0707.4550 [cond-mat]*.
- Marie, N., Li, S., Marrel, A., Marquès, M., Bajard, S., Tosello, A., Perez, J., Grosjean, B., Gerschenfeld, A., Anderhuber, M., Geffray, C., Gorsse, Y., Mauger, G., MATTEO, L., 2021. VVUQ of a thermal-hydraulic multi-scale tool on unprotected loss of flow accident in SFR reactor. *EPJ N - Nuclear Sciences & Technologies* 7, 3. <https://doi.org/10.1051/epjn/2021002>
- Marshall, J.S., Li, S. [Eds.], 2014. *Fluid Forces on Particles*, in: *Adhesive Particle Flow: A Discrete-Element Approach*. Cambridge University Press, Cambridge, pp. 130–181. <https://doi.org/10.1017/CBO9781139424547.006>
- Maschek, W., Rineiski, A., Suzuki, T., Chen, X., Mori, M., Wang, S., Karlsruhe, F., Cadiou, T., Coste, P., 2003. *aaaThe SIMMER-III and SIMMER-IV Code Family: 2-D and 3-D Mechanistic Simulation Tools for Reactor Transients and Accidents*.

- Maschek, W., Roth, A., Kirstahler, M., Meyer, L., 1992. Simulation Experiments for Centralized Liquid Sloshing Motions (No. ISSN 0303-4003). Kernforschungszentrum Karlsruhe, Karlsruhe, Germany.
- Matsen, J.M., Grace, J.R., 2012. Fluidization: International Fluidization Conference. Springer Science & Business Media.
- Matsuba, K., Kamiyama, K., Toyooka, J., Tobita, Y., Zuyev, V.A., Kolodeshnikov, A.A., Vassiliev, Y.S., 2016. Experimental discussion on fragmentation mechanism of molten oxide discharged into a sodium pool. *Mechanical Engineering Journal* 3, 15-00595-15–00595. <https://doi.org/10.1299/mej.15-00595>
- Maurin, R., Chauchat, J., Frey, P., 2016. Dense granular flow rheology in turbulent bedload transport. *Journal of Fluid Mechanics* 804, 490–512. <https://doi.org/10.1017/jfm.2016.520>
- Mewis, J., Wagner, N.J., 2011. Colloidal Suspension Rheology, Cambridge Series in Chemical Engineering. Cambridge University Press, Cambridge. <https://doi.org/10.1017/CBO9780511977978>
- Mizua, H., 1974. Fragmentation of Uranium Dioxide after Molten Uranium Dioxide-Sodium Interaction. *Journal of Nuclear Science and Technology* 11, 480–487. <https://doi.org/10.1080/18811248.1974.9730698>
- Morita, K., Fischer, E.A., 1998. Thermodynamic properties and equations of state for fast reactor safety analysis: Part I: Analytic equation-of-state model. *Nuclear Engineering and Design* 183, 177–191. [https://doi.org/10.1016/S0029-5493\(98\)00175-7](https://doi.org/10.1016/S0029-5493(98)00175-7)
- Nedderman, R.M., Tüzün, U., Savage, S.B., Houlsby, G.T., 1982. The flow of granular materials—I: Discharge rates from hoppers. *Chemical Engineering Science* 37, 1597–1609. [https://doi.org/10.1016/0009-2509\(82\)80029-8](https://doi.org/10.1016/0009-2509(82)80029-8)
- Nezamabadi, S., Radjai, F., Averseng, J., Delenne, J.-Y., 2015. Implicit frictional-contact model for soft particle systems. *Journal of the Mechanics and Physics of Solids* 83, 72–87. <https://doi.org/10.1016/j.jmps.2015.06.007>
- OECD-NEA, 2018. Phenomena Identification and Ranking Table (No. 7443). Nuclear Energy Agency.
- OECD/NEA, 2016. Five Years after the Fukushima Daiichi Accident: Nuclear Safety Improvements and Lessons Learnt (No. 7284). Nuclear Energy Agency.
- Ogawa, S., 1978. Multitemperature theory of granular materials. Proc. of the US-Japan Seminar on Continuum Mechanical and Statistical Approaches in the Mechanics of Granular Materials, 1978 208–217.
- Ogawa, S., Umemura, A., Oshima, N., 1980. On the equations of fully fluidized granular materials. *Journal of Applied Mathematics and Physics (ZAMP)* 31, 483–493. <https://doi.org/10.1007/BF01590859>
- Onoda, G.Y., Liniger, E.G., 1990. Random loose packings of uniform spheres and the dilatancy onset. *Physical Review Letters* 64, 2727–2730. <https://doi.org/10.1103/PhysRevLett.64.2727>
- Pal, D., Ghoshal, K., 2013. Hindered settling with an apparent particle diameter concept. *Advances in Water Resources* 60, 178–187. <https://doi.org/10.1016/j.advwatres.2013.08.003>
- Pal, R., 2019. Teach Second Law of Thermodynamics via Analysis of Flow through Packed Beds and Consolidated Porous Media. *Fluids* 4, 116. <https://doi.org/10.3390/fluids4030116>
- Payot, F., Serre, F., Suteau, C., 2018. The SAIGA experimental program to support the ASTRID core assessment in severe accident conditions. International Atomic Energy Agency (IAEA) 1.
- Richardson, J.F., Zaki, W.N., 1997. Sedimentation and fluidisation: Part I. *Chemical Engineering Research and Design* 75, S82–S100. [https://doi.org/10.1016/S0263-8762\(97\)80006-8](https://doi.org/10.1016/S0263-8762(97)80006-8)
- Rodriguez, G., Amphoux, P., Plancq, D., Richebois, E., Varaine, F., Bignon, P., 2020. The knowledge management on the design of a generation IV sodium fast reactor project at CEA. The case and methodology applied on the Astrid project. *EPJ Nuclear Sci. Technol.* 6, 53. <https://doi.org/10.1051/epjn/2020016>
- Rouault, J., Abonneau, E., Settimo, D., 2015. ASTRID, The SFR GENIV Technology Demonstrator Project Where Are We, Where Do We Stand For? 9.
- Rumpf, H., 1975. Fundamental physical processes and particle metrology, in: Rumpf, H. (Ed.), Particle Technology, Powder Technology Series. Springer Netherlands, Dordrecht, pp. 56–135. https://doi.org/10.1007/978-94-011-7944-7_3
- Russel, W.B., 1983. Effects of Interactions between Particles on the Rheology of Dispersions, in: Meyer, R.E. (Ed.), Theory of Dispersed Multiphase Flow. Academic Press, pp. 1–34. <https://doi.org/10.1016/B978-0-12-493120-6.50006-4>

- Sato, I., Lemoine, F., Struwe, D., 2004. Transient Fuel Behavior and Failure Condition in the CABRI-2 Experiments. *Nuclear Technology* 145. <https://doi.org/10.13182/NT04-A3464>
- Schins, H., Gunnerson, F.S., 1986. Boiling and fragmentation behaviour during fuel-sodium interactions. *Nuclear Engineering and Design* 91, 221–235. [https://doi.org/10.1016/0029-5493\(86\)90077-4](https://doi.org/10.1016/0029-5493(86)90077-4)
- Schneiderbauer, S., Aigner, A., Pirker, S., 2012. A comprehensive frictional-kinetic model for gas–particle flows: Analysis of fluidized and moving bed regimes. *Chemical Engineering Science* 80, 279–292. <https://doi.org/10.1016/j.ces.2012.06.041>
- Schulze, D., 2007. *Powders and Bulk Solids: Behavior, Characterization, Storage and Flow*. Springer Science & Business Media.
- Scott, G.D., Kilgour, D.M., 1969. The density of random close packing of spheres. *J. Phys. D: Appl. Phys.* 2, 863–866. <https://doi.org/10.1088/0022-3727/2/6/311>
- Serre, F., Bertrand, F., Journeau, C., Suteau, C., Verwaede, D., Schmitt, D., Farges, B., 2015. Status of the French R/D program on the severe accident issue to develop Gen IV SFRs - 15373, in: *The International Congress on Advances in Nuclear Power Plants (ICAPP)*. Presented at the The International Congress on Advances in Nuclear Power Plants (ICAPP), Nice, France.
- Shen, H., Ackermann, N.L., 1982. Constitutive Relationships for Fluid-Solid Mixtures. *Journal of the Engineering Mechanics Division* 108, 748–763.
- Shi, H., Vescovi, D., Singh, A., Roy, S., Magnanimo, V., Luding, S., 2017. Granular Flow: From Dilute to Jammed States. *Granular Materials*. <https://doi.org/10.5772/intechopen.68465>
- Shook, C.A., Bartosik, A.S., 1994. Particle—wall stresses in vertical slurry flows. *Powder Technology* 81, 117–124. [https://doi.org/10.1016/0032-5910\(94\)02877-X](https://doi.org/10.1016/0032-5910(94)02877-X)
- Simpson, M., Janna, W., 2008. Newtonian and Non-Newtonian Fluids: Velocity Profiles, Viscosity Data, and Laminar Flow Friction Factor Equations for Flow in a Circular Duct. Presented at the ASME International Mechanical Engineering Congress and Exposition, Proceedings. <https://doi.org/10.1115/IMECE2008-67611>
- Singh, S., 2019. Radioscopie X pour les interactions corium-sodium lors d'un scénario d'accident grave. Ph.D. Thesis at Université Paris-Saclay
- Singh, S., Cassiaut-Louis, N., Journeau, C., Zabiégo, M., Estre, N., Tamagno, L., 2018. Modelling of X-Ray Radioscopy for Phase Topology Estimation During Corium Sodium Interaction, in: *Volume 9: Student Paper Competition*. Presented at the 2018 26th International Conference on Nuclear Engineering, American Society of Mechanical Engineers, London, England, p. V009T16A084. <https://doi.org/10.1115/ICONE26-82400>
- Song, C., Wang, P., Makse, H.A., 2008. A phase diagram for jammed matter. *Nature* 453, 629–632. <https://doi.org/10.1038/nature06981>
- Sperl, M., 2006. Experiments on corn pressure in silo cells – translation and comment of Janssen's paper from 1895. *Granular Matter* 8, 59–65. <https://doi.org/10.1007/s10035-005-0224-z>
- Sumner, R.J., McKibben, M., Shook, C.A., 1991. Concentration and velocity distribution in turbulent vertical slurry flow. *J. Solid Liquid Flow* 2, 33–42.
- Tagami, H., Tobita, Y., 2014. Numerical Simulation for Debris Bed Behavior in Sodium Cooled Fast Reactor 12.
- Tentner, A.M., Parma, E., Wei, T., Wigeland, R., Sni, Inl, 2010. Severe accident approach - final report. Evaluation of design measures for severe accident prevention and consequence mitigation. (No. ANL-GENIV-128, 973483). <https://doi.org/10.2172/973483>
- Three Mile Island accident, 2021. . Wikipedia.
- Tobita, Y., 1991. Interfacial area modeling for a multiphase, multicomponent fluid-dynamics code. undefined.
- Tobita, Y., Yamano, H., Sato, I., 2008. Analytical study on elimination of severe recriticalities in large scale LMFBRs with enhancement of fuel discharge. *Nuclear Engineering and Design* 238, 57–65. <https://doi.org/10.1016/j.nucengdes.2007.04.014>
- Toomey, 2018. Pressure and bed height vs superficial velocity in a fluidized bed [WWW Document]. URL https://commons.wikimedia.org/wiki/File:Pressure_vs_superficial_velocity_in_fluidized_beds.png (accessed 1.17.22).
- Toyooka, J.-I., Kamiyama, K., Konishi, K., Tobita, Y., Sato, I., 2010. SIMMER-III analysis of eagle-1 in-pile tests focusing on heat transfer from molten core material to steel-wall structure. *Proceedings of 7th Korea-Japan Symposium on Nuclear Thermal Hydraulics and Safety (NTHAS-7) (CD-ROM)* 7.

- Trulsson, M., Andreotti, B., Claudin, P., 2012. Transition from the Viscous to Inertial Regime in Dense Suspensions. *Phys. Rev. Lett.* 109, 118305. <https://doi.org/10.1103/PhysRevLett.109.118305>
- Uršič, M., Leskovar, M., 2015. Analyses of THINA melt-sodium interaction experiments with MC3D 8.
- van Leer, B., 1979. Towards the ultimate conservative difference scheme. V. A second-order sequel to Godunov's method. *Journal of Computational Physics* 32, 101–136. [https://doi.org/10.1016/0021-9991\(79\)90145-1](https://doi.org/10.1016/0021-9991(79)90145-1)
- Varaine, F., Marsault, P., Chenaud, M.S., Bernardin, B., Conti, A., Sciora, P., Venard, C., Fontaine, B., Devictor, N., Martin, L., Scholer, A.C., Verrier, D., 2012. Pre-conceptual design study of ASTRID core. Proceedings of the 2012 International Congress on Advances in Nuclear Power Plants - ICAPP '12.
- WebSVN, 2021. , Online Subversion repository browser. WebSVN.
- Wilhelm, D., 1990. AFDM: An Advanced Fluid-Dynamics Model (No. LA--11692-MS-VOL.2). Los Alamos National Lab.
- Yamano, H., Fujita, S., Tobita, Y., Kamiyama, K., Kondo, S., Morita, K., Fischer, E.A., 2003. SIMMER-III: A Computer Program for LMFR Core Disruptive Accident Analysis. Internal JNC Report 340.
- Yamano, H., Tobita, Y., 2008. R&D of the Next Generation Safety Analysis Methods for Fast Reactors With New Computational Science and Technology: 4 — Experimental Analyses by SIMMER-III for the Integral Verification of COMPASS, in: Volume 2: Fuel Cycle and High Level Waste Management; Computational Fluid Dynamics, Neutronics Methods and Coupled Codes; Student Paper Competition. Presented at the 16th International Conference on Nuclear Engineering, ASME, Orlando, Florida, USA, pp. 307–314. <https://doi.org/10.1115/ICONE16-48385>
- Zegzulka, J., Gelnar, D., Jezerska, L., Ramirez-Gomez, A., Necas, J., Rozbroj, J., 2018. Internal Friction Angle of Metal Powders. *Metals* 8, 255. <https://doi.org/10.3390/met8040255>
- Zhang, J., Yan, S., Yuan, D., Alici, G., Nguyen, N.-T., Ebrahimi Warkiani, M., Li, W., 2016. Fundamentals and applications of inertial microfluidics: a review. *Lab on a Chip* 16, 10–34. <https://doi.org/10.1039/C5LC01159K>
- Zhu, Z., Wang, H., Peng, D., Dou, J., 2019. Modelling the Hindered Settling Velocity of a Falling Particle in a Particle-Fluid Mixture by the Tsallis Entropy Theory. *Entropy* 21, 55. <https://doi.org/10.3390/e21010055>

Annexe A

Code manual

New form of the momentum equation for particles in one-dimension (axial direction z runs along the tube length) writes as Eq. A.1 (variables are according to the nomenclature of the main text) with red highlights on the modified terms, namely the σ_p solid stress tensor representing direct particle-particle interactions and the K_{pq} particle-fluid interphase momentum exchange terms.

$$\frac{\partial(\bar{\rho}_p v_p)}{\partial t} + \sum_{m \in p} \nabla(\bar{\rho}_m v_p v_p) = -\alpha_p \frac{\partial p}{\partial z} - \frac{\partial \sigma_p}{\partial z} + \bar{\rho}_p g + \sum_q K_{pq}(v_q - v_p) \quad \text{Eq. A.1}$$

We recall that mobile components in SIMMER-V comprise liquid fuel 1, liquid steel 2, liquid sodium 3, fuel particles 4, steel particles 5, control particles 6, chunks 7 and gas 8. In the following, the numerical implementation of these two terms into SIMMER-V code will be detailed (SIMMER-V is written in FORTRAN language). The description is dedicated to SIMMER users and it adopts the current code architecture and terminology [Yamano et al., 2003]. Attributions added in the frame of this work are detailed in the following.

These new terms are applied exclusively to meshes that are labeled as “transfer tubes” via a new input parameter RHEOLREG. This variable is defined under the NAMELIST XMXF class. It defines three-dimensional rectangular regions by the following terminology:

\XMXF

$$\text{RHEOLREG}(x,y) = i_{\min}, k_{\min}, j_{\min}, i_{\max}, k_{\max}, j_{\max}$$

where x index defines the coordinates of the region where new models are applied and y index indicates the region number (max 30). An illustration is provided on Figure A.1.

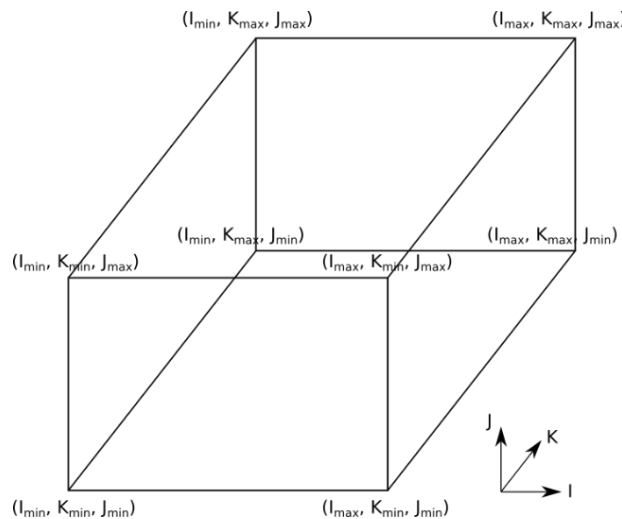


Figure A.1 Interpretation of RHEOLREG new input parameter in a Cartesian frame of reference

During the model development in SIMMER-V, all modifications are implemented by the MXFOPT option control flag. Option control flags are special integer inputs in the NAMELIST XCNTL class that allow switching between different models, numerical schemes etc. through the user input file. This provides flexibility in activating or deactivating the newly developed particle dynamics models. The summary of new options is listed in Table A.1.

Table A.1 New option control flags

Variable	Value	Description	Comments	Implementation
MXFOPT(28)	1	Downstream projection of shear stress coefficients to cell faces	Recommendation based on physical arguments but warning, proves unstable for reactor case	Variation of already existing MCFOPT(27) option in mxf.f subroutine in STEP1 algorithm
	2	No projection of shear stress coefficients to cell faces	Recommended for full reactor calculation	Variation of already existing MXFOPT(27) option in mxf.f subroutine in STEP1 algorithm
MXFOPT(32)	1	Apply Gidaspow drag function for continuous liquid – particle component momentum exchange functions	Recommended for high volume concentration particle flows	Variation of already existing interphase momentum exchange terms in mxf.f subroutine in STEP1 algorithm
MXFOPT(33)	6	Apply shear stress term according to $\mu(l)$ dense granular rheology for particle - structure momentum exchange	Recommended to use together with MXFOPT(36) = 1	Variation of already existing fluid - structure momentum exchange terms in mxf.f subroutine in STEP1 algorithm
MXFOPT(34)	1	Omit particle viscosity factors from continuous liquid - structure component momentum exchange functions	Recommended when applying separate momentum field for particles and when applying MXFOPT(33) = 6	IF condition on the continuous liquid viscosity in bubbly flow regime in mxf.f subroutine in STEP1 algorithm
MXFOPT(36)	1	Apply particle pressure gradient term according to $\mu(l)$ dense granular rheology for inter particle interactions	Recommended to use together with MXFOPT(33) = 6	New subroutines to compute the axial gradient of the particle pressure that is called in STEP2 and STEP4 algorithm
MXFOPT(37)	1	Omit particle viscosity factors from continuous phase – liquid droplet component momentum exchange functions	Recommended when applying separate momentum field for particles and when applying MXFOPT(32) = 1	IF condition on the continuous liquid viscosity in bubbly and dispersed flow regimes in mxf.f subroutine in STEP1 algorithm

To implement the above-mentioned options to switch between particle dynamics models involve the modification of already existing subroutines and the creation of new ones in the fluid-dynamics module of SIMMER-V. Modified subroutines comprise `mx.f`, `step2.f`, `vitevp.f`, `step4.f` and `vitev.f`. Newly created subroutines comprise `cvepqp.f` and `cvepqp2.f`. Their function and connection to the main code architecture are indicated in Figure A.2.

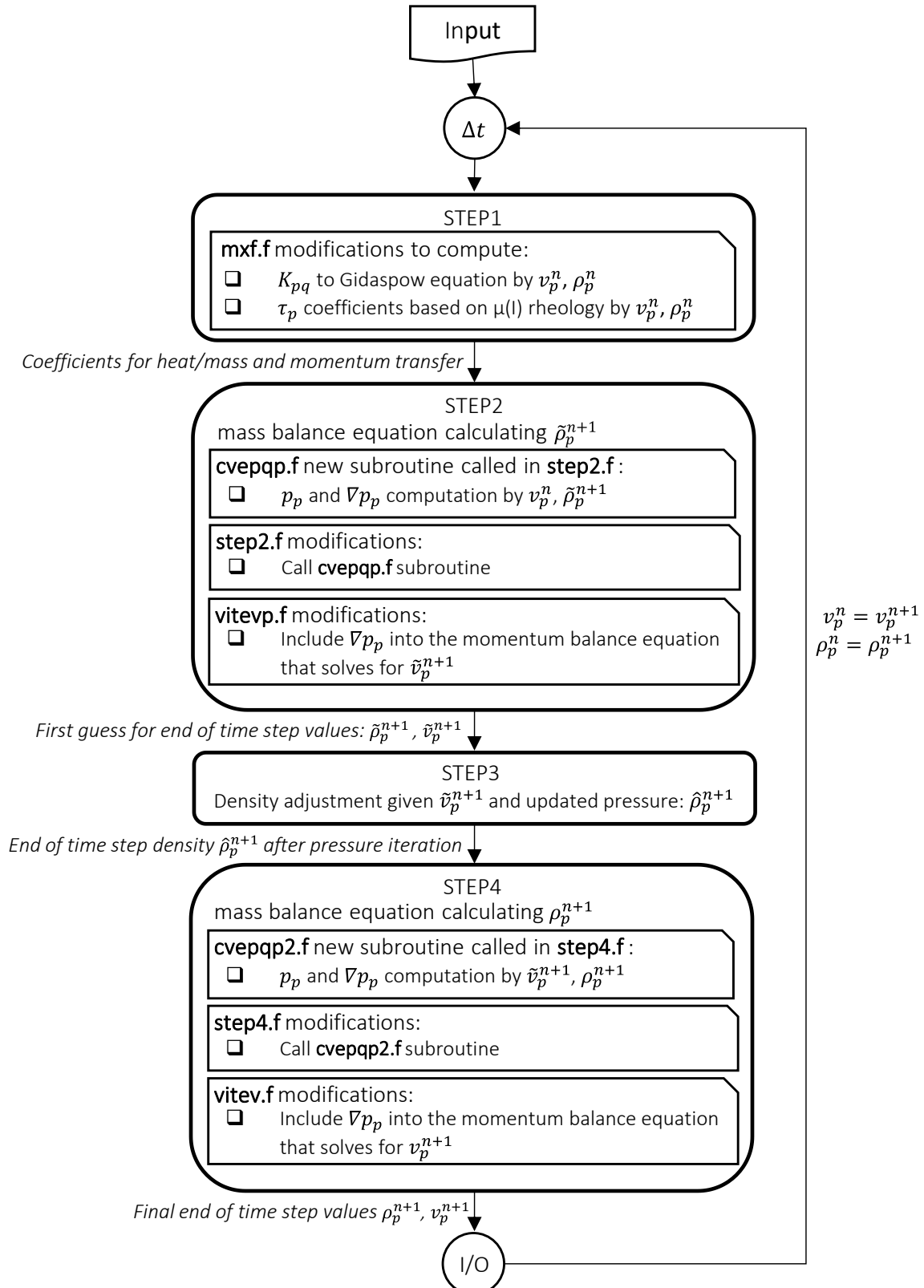


Figure A.2 Code modifications related to model development on particle dynamics

Annexe B

Solid stress tensor in one-dimension

In reality, particle-particle direct interactions are inherently three-dimensional. Therefore, the solid stress arising from such writes in a three-dimensional tensor form. Considering cylindrical coordinates with directions r, θ, z and following the second-order Cauchy stress tensor, the tensor is decomposed into nine components by Eq. B.1:

$$\sigma_p = \begin{bmatrix} p_{p,r} & \tau_{p,r\theta} & \tau_{p,rz} \\ \tau_{p,\theta r} & p_{p,\theta} & \tau_{p,\theta z} \\ \tau_{p,zr} & \tau_{p,z\theta} & p_{p,z} \end{bmatrix} \quad \text{Eq. B.1}$$

where p represents normal component and τ stands for shear components with the first subscript index denoting the plane to which the stress component is normal and the second subscript index indicating the direction of the stress component. These components are illustrated for a cylinder slice in Figure B.1 (without p subscript for simplicity).

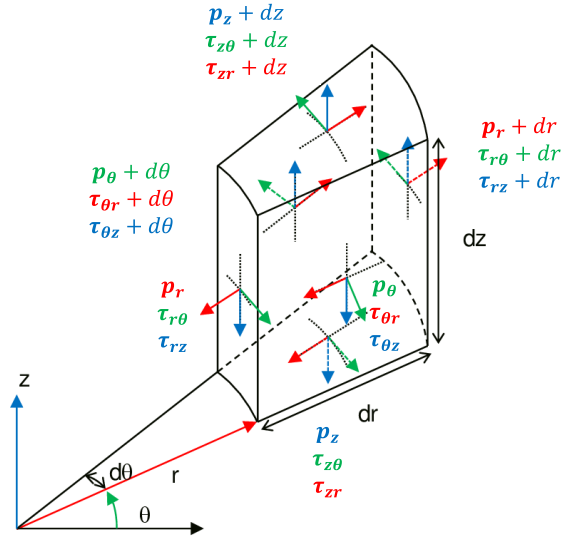


Figure B.1 Cylindrical volume with stresses exerted on all faces in cylindrical coordinates (modification of [Molker et al., 2017])

In line with the one-dimensional flow topology in SIMMER-V, which imposes the constraint to represent mitigation transfer tubes as 1D channels with changes only along the axial direction, the stress tensor has to be reduced into a one-dimensional form. By applying a single lateral mesh, meaning that the domain is rotated 360° around the z axis, variables depending on θ disappear. By applying a single radial mesh, meaning that dr represents the distance between the centerline and the tube wall $D_h/2$, variables depending on r disappear except the shear on the wall surface $\tau_{p,rz}$ which integrates over the wall surface area. Altogether, the axial gradient of the solid stress tensor reduces to Eq. B.2:

$$\frac{\partial \sigma_p}{\partial z} = \frac{\partial p_{p,z}}{\partial z} + \frac{4\tau_{p,rz}}{D_h} \quad \text{Eq. B.2}$$

with $p_{p,z}$ particle pressure and $\tau_{p,rz}$ shear stress term acting on the wall surface both in the flow direction. This form is applied in the core of this document.